

**Characterization of Two-Dimensional High
Frequency Microstrip and Dielectric
Interconnects**

Tahera Emilie van Deventer

1992

CHARACTERIZATION OF TWO-DIMENSIONAL HIGH FREQUENCY MICROSTRIP AND DIELECTRIC INTERCONNECTS

by

Tahera Emilie van Deventer

A dissertation submitted in partial fulfillment
of the requirements for the degree of
Doctor of Philosophy
(Electrical Engineering)
in The University of Michigan
1992

Doctoral Committee:

Associate Professor Pisti B. Katehi, Chairperson
Associate Professor Eduard Harabetian
Professor Dimitris Pavlidis
Assistant Research Scientist Kamal Sarabandi
Professor Fawwaz T. Ulaby

To the engineers in my family,
my grandfather Jan Emile,
my father Eric and
my brother Jan Arselan

ACKNOWLEDGEMENTS

I would like to thank my committee members and in particular my advisor, Professor Linda P.B. Katehi for her guidance and support throughout the course of this work and my mentor and former advisor, Professor Fawwaz Ulaby.

My deepest thanks go to the faculty and staff members of the Radiation Laboratory, and in particular to Professor Gabriel Rebeiz and to Doctor John Bryant. On technical cooperation, I would like to acknowledge Professors Andreas Cangelaris and Nikolaos Uzunoglu and Doctor Jack Josefowicz.

Also, I thank my colleagues who contributed to this work through many interesting discussions: Messrs. Nihad Dib, Yioryos Eleftheriades, Andrew Engel, Kazem Sabetfakhri, Ms. Rhonda Drayton, and Drs. Lawrence Dunleavy, William Harokopus, Thomas Livernois and Norman VandenBerg. The moral support of some special friends; the late Dr. Matthias Weiss, Mr. Kok Hwe Koh, Dr. Jaganatha Rao and Dr. Leonard Rexberg; helped me through this endeavor. Thanks also to Master Han Won Lee who directed my outbursts of frustration into meaningful forms.

The path that has led me to higher education in the United States has some cornerstones which I would like to acknowledge here and that include Professor Kaldjian who encouraged me to apply to the University of Michigan, H.I.M.F.P. and Mr. Niels Brüel for their financial support during my undergraduate years, and of course my parents who always insisted on a solid education.

Finally I thank my family for their indulgent and patient support.

This work was supported by the Army Research Office under contract projects DAAL03-91-G-0116 and DAAL03-K-0088(23836-EL) and by the NASA/Center for Space Terahertz Technology at the University of Michigan.

TABLE OF CONTENTS

DEDICATION	ii
ACKNOWLEDGEMENTS	iii
LIST OF FIGURES	ix
LIST OF TABLES	xvi
LIST OF APPENDICES	xvii
CHAPTER	
I. INTRODUCTION	1
1.1 Motivation	2
1.2 Objectives	5
1.3 Full-wave approach	7
1.4 Overview	8
II. THE ELECTRIC FIELD INTEGRAL EQUATION TECH- NIQUE	11
2.1 Overview and assumptions	11
2.2 Formulation of the integral equation	14
2.2.1 Single integral representation	15
2.2.2 Fredholm integral equation of the second kind	16
2.3 Derivation of the Green's function	18
2.3.1 Notation	18
2.3.2 Vector potential formulation	20
2.3.3 Representation of multi-layered structures	23
2.3.4 Solution to the boundary value problem	26
2.4 Method of moments	32
2.4.1 Overview of the method	32
2.4.2 Matrix formulation	35
III. MICROSTRIP LINES: THEORETICAL STUDY OF LOSSES	38

3.1	Introduction and background	38
3.2	Description of the theoretical method	40
3.3	Derivation of the equivalent surface impedance	43
3.3.1	Quasi-static integral equation for the current distribution in conductors	43
3.3.2	Evaluation of the resistance and inductance matrices	47
3.3.3	Derivation of the surface impedance	50
3.4	Integral equation formulation	52
3.5	Application of the Method of Moments	54
3.5.1	Basis functions expansion	58
3.5.2	Testing functions	59
3.6	Determination of the propagation characteristics	64
3.6.1	Propagation constant	64
3.6.2	Equivalent current density and field distributions	65
3.6.3	Characteristic impedance	66
3.7	Time domain analysis	75
3.7.1	Theory	76

IV. MICROSTRIP LINES: NUMERICAL CONSIDERATIONS AND RESULTS 78

4.1	Numerical considerations	79
4.1.1	Algorithm	79
4.1.2	Determination of the propagation constant	79
4.1.3	Convergence considerations	86
4.2	Dispersion analysis	89
4.2.1	Single microstrip line	90
4.2.2	Multiple microstrip lines	92
4.3	Substrate loss analysis	97
4.4	Conductor loss analysis	103
4.4.1	Skin effect	104
4.4.2	Multiple metallization and roughness	110
4.4.3	Ground plane contribution	111
4.4.4	Experimental verification	113
4.4.5	Multiple coupled strips	114
4.5	Time domain analysis	123

V. LOSSES IN HIGH TEMPERATURE SUPERCONDUCTING THIN-FILM LINES 128

5.1	Motivation and approach	128
5.2	Theory	130
5.2.1	Fabrication	133
5.2.2	Measurement of the surface impedance	133

5.2.3	Calculation of the superconducting current	135
5.3	Results	136
5.3.1	Temperature variation	138
5.3.2	Permittivity variation	142
5.3.3	Line width and substrate thickness variation	142
VI. DIELECTRIC LINES: THE GENERALIZED INTEGRAL EQUATION METHOD		149
6.1	Motivation and background	149
6.2	Approach	152
6.3	Description of the problem	155
6.3.1	Polarization formulation	156
6.3.2	Equivalent planar problem	158
6.4	Application of the boundary conditions	160
6.4.1	Outside the strip	161
6.4.2	At the strip interfaces	161
6.5	Formulation of the modified integral equation	164
6.6	Modified Green's function for the shielded case	166
VII. DIELECTRIC LINES: NUMERICAL CONSIDERATIONS AND RESULTS		170
7.1	Method of moments solution	170
7.1.1	Matrix formulation	171
7.1.2	Expansion and testing functions	171
7.2	Algorithm	173
7.3	Convergence considerations	179
7.3.1	Number of basis functions	179
7.3.2	Modal summations	180
7.4	Validation and limitations of the method	186
7.4.1	Parallel polarization	186
7.4.2	Perpendicular polarization	188
7.5	Numerical results	190
7.5.1	Single strip	191
7.5.2	Multiple strips	194
VIII. CONCLUSIONS AND RECOMMENDATIONS		199
8.1	Summary of achievements	200
8.1.1	Microstrip lines	200
8.1.2	Superconducting lines	201
8.1.3	Dielectric lines	202
8.2	Recommendation for future work	202
8.2.1	VLSI interconnects	202

8.2.2 Dielectric interconnects 203

APPENDICES 205

BIBLIOGRAPHY 271

LIST OF FIGURES

<u>Figure</u>		
1.1	Metallic transmission line interconnects	3
1.2	Dielectric transmission line interconnects	6
2.1	Shielded microstrip line configuration	12
2.2	Multilayered structure	24
2.3	Basis Functions	34
3.1	Geometry of a multilevel microstrip line system in a shielded environment	41
3.2	System of N_c z -directed multiconductor lines above a ground plane	45
3.3	Magnitude of current density inside a rectangular strip at a height of 3 mils above a perfectly conducting ground ($W = 3$ mils, $\sigma = 4 \times 10^7$ S/m, $f = 1$ GHz, $t = 0.2$ mils)	48
3.4	Geometry for entire domain basis functions	58
3.5	Multilevel lines in the source region	72
4.1	Variation of the determinant versus β for a single strip ($a = b = 12.7$ mm, $w = 0.635$ mm, $h = 1.27$ mm, $\epsilon_r = 8.875$)	82
4.2	Variation of the determinant versus β for edge-coupled strips ($a = b = 12.7$ mm, $w_1 = w_2 = h = 1.27$ mm, $s = 1.27$ mm, $\epsilon_r = 8.875$, $f = 5$ GHz)	83
4.3	Impedance elements as a function of β ($a = b = 12.7$ mm, $w = h = 1.27$ mm, $\epsilon_r = 8.875$, $f = 5$ GHz)	86

4.4	Convergence of the impedance elements with respect to the modal index m ($a = b = 12.7$ mm, $w = 0.635$ mm, $h = 1.27$ mm, $\epsilon_r = 8.875$, $f = 10$ GHz)	87
4.5	Convergence of the propagation characteristics with respect to the truncation modal number M ($a = 2.1$ mm, $b = 2$ mm, $w = 73$ μm , $d = 100$ μm , $\epsilon_r = 12.9$, $\sigma = 2 \times 10^7$ S/m, $t = 1$ μm , $f = 10$ GHz)	88
4.6	Convergence with respect to the number of basis functions ($a = 10$ mm, $b = 20$ mm, $d = 1$ mm, $\epsilon_r = 10$, $f = 1$ GHz)	89
4.7	Dispersion curves for the even modes propagating along a single shielded microstrip ($a = b = 12.7$ mm, $w = 0.635$ mm, $h = 1.27$ mm, $\epsilon_r = 8.875$)	91
4.8	Dispersion curves for the LSE and LSM modes in an inhomogeneously-filled waveguide ($a = b = 12.7$ mm, $h = 1.27$ mm, $\epsilon_r = 8.875$)	92
4.9	Geometry of coplanar and non-coplanar coupled strips	93
4.10	Example of applications for edge-coupled strips : symmetrical and assymetrical 3-dB microstrip couplers, 3-line microstrip directional coupler	94
4.11	Field distribution for the even and odd modes of symmetric edge-coupled strips	96
4.12	Propagation characterisitcs of two-coupled lines versus frequency ($a = b = 12.7$ mm, $w_1 = w_2 = h = 1.27$ mm, $s = 1.27$ mm, $\epsilon_r = 8.875$)	97
4.13	Field distribution for the even and odd modes of broadside coupled strips	97
4.14	Propagation characteristics of broadside-coupled lines as a function of horizontal separation ($b = 400$ mm, $\epsilon_{r1} = \epsilon_{r2} = \epsilon_{r3} = 1$, $\sigma = 3.33 \times 10^7$ S/m, $t = 3\mu\text{m}$, $d_1 = d_3 = 31$ mm, $d_2 = 10$ mm, $w_1 = w_2 = 5$ mm, $f = 1$ GHz)	98
4.15	Propagation characteristics of broadside-coupled lines as a function of frequency : present method (lines), Carin (points) ($a = b = 2.54$ cm, $\epsilon_{r1} = 1$, $\epsilon_{r2} = \epsilon_{r3} = 12$, $d_2 = d_3 = 127\mu\text{m}$, $s = 381\mu\text{m}$)	99
4.16	Dielectric loss of the dominant mode of a single microstrip versus frequency ($a = b = 20$ mm, $w = h = 0.5$ mm, $\epsilon_r = 10$, $\mu_r = 1$)	101

4.17	Dielectric losses of a single strip versus strip width ($a = 10$ mm, $b = 20$ mm, $d = 1$ mm, $\epsilon_r = 10$, $\tan\delta = 2 \times 10^{-4}$, $f = 1$ GHz)	102
4.18	Dielectric losses of coupled strips versus line separation s/d ($a = 10$ mm, $b = 20$ mm, $W = d = 1$ mm, $\epsilon_r = 10$, $\tan\delta = 2 \times 10^{-4}$, $f = 1$ GHz)	103
4.19	Conductor losses of a single strip versus strip width ($a = 10$ mm, $b = 20$ mm, $d = 1$ mm, $\epsilon_r = 10$, $\sigma = 3.33 \times 10^7$ S/m, $\tan\delta = 2 \times 10^{-4}$, $f = 1$ GHz, $t = 10$ μ m)	105
4.20	Effect of thickness on the ohmic attenuation constant ($a = 10$ mm, $b = 20$ mm, $d = 1$ mm, $\epsilon_r = 10$, $\sigma = 3.33 \times 10^7$ S/m, $f = 1$ GHz)	106
4.21	Propagation constant of a single lossy strip as a function of frequency ($a = 2.1$ mm, $b = 2$ mm, $W = 73$ μ m, $d = 100$ μ m, $\epsilon_r = 12.9$, $\sigma = 2 \times 10^7$ S/m, $t = 1$ μ m)	108
4.22	Characteristic impedance of a single lossy strip as a function of frequency ($a = 2.1$ mm, $b = 2$ mm, $W = 73$ μ m, $d = 100$ μ m, $\epsilon_r = 12.9$, $\sigma = 2 \times 10^7$ S/m, $t = 1$ μ m)	109
4.23	Comparison between dielectric and conductor losses as a function of frequency ($a = b = 500$ μ m, $W = d = 50$ μ m, $\epsilon_r = 10$, $\sigma = 3.33 \times 10^7$ S/m, $t = 5$ μ m)	110
4.24	Geometry for a microstrip made of multiple metallization	111
4.25	Effect of roughness on the ohmic attenuation constant as a function of frequency ($a = 10$ mm, $b = 20$ mm, $W = d = 280$ μ m, $T = 70$ μ m, $r = 1.5$ μ m, $\epsilon_r = 10$, $\sigma = 4 \times 10^7$ S/m, $t = 6$ μ m)	112
4.26	Effect of ground plane resistivity on the ohmic attenuation constant ($a = 10$ mm, $b = 20$ mm, $d = 1$ mm, $\epsilon_r = 10$, $\sigma = 3.33 \times 10^7$ S/m, $f = 1$ GHz)	113
4.27	Equivalent surface resistivity R_l and ground resistivity R_g versus frequency ($a = b = 500$ μ m, $W = d = 50$ μ m, $\epsilon_r = 10$, $\sigma = 3.33 \times 10^7$ S/m, $t = 5$ μ m)	114
4.28	Comparison between theory and experiment for a single microstrip on a GaAs substrate ($a = 2.1$ mm, $b = 2$ mm, $W = 73$ μ m, $d = 100$ μ m, $\epsilon_r = 12.9$, $\sigma = 3.33 \times 10^7$ S/m, $\tan\delta = 16 \times 10^{-4}$, $t = 2$ μ m)	115

4.29	Conductor losses of coupled strips versus line separation ($a = 10$ mm, $b = 20$ mm, $W = d = 1$ mm, $\epsilon_r = 10$, $\sigma = 3.33 \times 10^7$ S/m, $\tan\delta = 2 \times 10^{-4}$, $f = 1$ GHz, $t = 0.01$ mm)	117
4.30	Two edge-coupled lines ($\epsilon_{r1} = 1$, $\epsilon_{r2} = \epsilon_{r3} = 4$, $\sigma = 4.8 \times 10^7$ S/m, $t = 4\mu\text{m}$, $d_1 = 40\mu\text{m}$, $d_2 = 20\mu\text{m}$, $w_1 = w_2 = 20\mu\text{m}$, $s = 40\mu\text{m}$) . . .	118
4.31	Frequency dependence of the characteristic modal impedances Z_{ij} .	119
4.32	Effect of strip spacing on the surface resistance for even and odd modes ($a = 1$ mm, $b = 2$ mm, $d_1 = 0.1$ mm, $\epsilon_{r1} = 1$, $\epsilon_{r2} = \epsilon_{r3} = 4$, $\sigma = 3.33 \times 10^7$ S/m, $t = 4\mu\text{m}$, $d_3 = 100\mu\text{m}$, $w_1 = w_2 = 100\mu\text{m}$, $f = 5$ GHz)	120
4.33	Effect of strip spacing on the propagation constant of the dominant microstrip mode ($a = 1$ mm, $b = 2$ mm, $d_1 = 0.1$ mm, $\epsilon_{r1} = 1$, $\epsilon_{r2} = \epsilon_{r3} = 4$, $\sigma = 3.33 \times 10^7$ S/m, $t = 4\mu\text{m}$, $d_3 = 100\mu\text{m}$, $w_1 = w_2 = 100\mu\text{m}$, $f = 5$ GHz)	122
4.34	Equivalent circuit for the active and sense lines	124
4.35	Voltages at the near-end and far-end points for the active line . . .	125
4.36	Voltages at the near-end and far-end points for the sense line . . .	126
5.1	Superconducting microstrip line configuration	130
5.2	Surface resistance of a $YBa_2Cu_3F_xO_y$ microstrip line on a $LaAlO_3$ substrate as a function of the strip width to substrate thickness ratio ($\epsilon_r = 22$, $h = 0.5$ mm, $t = 0.5 \mu\text{m}$, $a = b = 2.5$ mm, $T = 4$ K, $f = 5$ GHz)	132
5.3	Attenuation constant vs. frequency for (a)normal strips ($\sigma = 3.33 \times 10^7$ S/m, $T = 300$ K) and (b) superconducting strips ($T = 70$ K)	137
5.4	Current flow in normal and superconductors	138
5.5	Effect of temperature on the attenuation constant of the dominant microstrip mode as a function of frequency ($\epsilon_r = 22$, $w = 250 \mu\text{m}$, $h = 0.5$ mm, $t = 0.5 \mu\text{m}$, $a = b = 2.5$ mm)	139
5.6	Comparison of attenuation constant for post-annealed and in-situ thin film lines ($\epsilon_r = 22$, $w = 250 \mu\text{m}$, $h = 0.5$ mm, $t = 0.5 \mu\text{m}$, $a = b = 2.5$ mm, $f = 5$ GHz)	141

5.7	Attenuation constant vs. frequency as a function of permittivity ($w = 250 \mu\text{m}$, $h = 0.5 \text{ mm}$, $t = 0.5 \mu\text{m}$, $a = b = 2.5 \text{ mm}$)	143
5.8	Phase constant of the dominant microstrip mode ($\epsilon_r = 22$, $\tan\delta = 5 \times 10^{-5}$, $t = 0.5 \mu\text{m}$, $R_s = 1 \text{ m}\Omega$)	144
5.9	Attenuation constant of the dominant microstrip mode ($\epsilon_r = 22$, $\tan\delta = 5 \times 10^{-5}$, $t = 0.5 \mu\text{m}$, $R_s = 1 \text{ m}\Omega$)	145
5.10	Characteristic Impedance of the dominant microstrip mode ($\epsilon_r = 22$, $\tan\delta = 5 \times 10^{-5}$, $t = 0.5 \mu\text{m}$, $R_s = 1 \text{ m}\Omega$)	146
5.11	Attenuation constant vs. frequency using the present method and the PEM method ($\epsilon_r = 3.9$, $\tan\delta = 10^{-4}$, $w = 2 \mu\text{m}$, $h = 1 \mu\text{m}$, $a = b = 50 \mu\text{m}$, $T = 77 \text{ K}$)	147
6.1	General configuration of low-loss ridged waveguides using heterostructures	150
6.2	General configuration of dielectric waveguides	151
6.3	Approach used in the derivation of the GIE method	153
6.4	Geometry of the analyzed structure	155
6.5	Equivalent polarization current	157
6.6	Equivalent dipole moment per unit surface	159
7.1	Geometry for subsectional basis functions	172
7.2	Modified impedance matrix elements as a function of k_z for a single strip ($a = 5 \text{ cm}$, $b = 2 \text{ cm}$, $h_1 = 2.625 \text{ cm}$, $h_2 = 0.5 \text{ cm}$, $h_3 = 1.875 \text{ cm}$, $w = 1 \text{ cm}$, $\epsilon_{strip} = 12$, $\epsilon_{substrate} = 2$, $f = 3\text{GHz}$)	175
7.3	Variation of the determinant versus the propagation constant for a single strip ($a = 5 \text{ cm}$, $b = 2 \text{ cm}$, $h_1 = 2.625 \text{ cm}$, $h_2 = 0.5 \text{ cm}$, $h_3 = 1.875 \text{ cm}$, $w = 1 \text{ cm}$, $\epsilon_{strip} = 12$, $\epsilon_{substrate} = 2$, $f = 3\text{GHz}$)	176
7.4	Geometry and notation of a partially-filled waveguide	178
7.5	Convergence of the Ξ_{ij} terms as a function of the modal index m ($a = 5 \text{ cm}$, $b = 2 \text{ cm}$, $h_1 = 2.625 \text{ cm}$, $h_2 = 0.5 \text{ cm}$, $h_3 = 1.875 \text{ cm}$, $w = 1 \text{ cm}$, $\epsilon_{strip} = 12$, $\epsilon_{substrate} = 2$, $f = 3\text{GHz}$)	183

7.6	Comparison between the GIE method and the modal expansion method ($w = 0.5$ mm, $h = 62.5$ μ m, $s = 250$ μ m, $\epsilon_{strip} = 2$, $\epsilon_{substrate} = 12$)	187
7.7	Comparison between the GIE method and the polarization current formulation ($a = 5$ cm, $b = 2$ cm, $h_1 = 2.5$ cm, $y_o = 0.75$ cm, $h_2 = 0.2$ cm, $h_3 = 2.3$ cm, $\epsilon_{strip} = 12$, $\epsilon_{substrate} = 2$, $f = 15$ GHz)	189
7.8	Comparison between the GIE method and the modal expansion method ($a = 2$ cm, $b = 5$ cm, $h_1 = 1.8$ cm, $h_2 = 0.2$ cm, $t = 0.1$ cm, $\epsilon_{strip} = 12$, $\epsilon_{substrate} = 2$, $f = 3$ GHz)	190
7.9	Phase constant as a function of strip width compared to a partially-filled waveguide structure ($f = 3$ GHz)	192
7.10	Effect of strip thickness on the propagation characteristics ($a = 5$ cm, $b = 2$ cm, $h_1 = 2.3$ cm, $h_2 = 0.2$ cm, $h_3 = 2.3$ cm, $w = 2$ cm, $\epsilon_{strip} = 12$, $\epsilon_{substrate} = 2.2$, $f = 3$ GHz)	193
7.11	Frequency dependence of a single strip for different widths ($a = 5$ cm, $b = 2$ cm, $h_1 = 4.5$ cm, $h_2 = 0.5$ cm, $t = 0.2$ cm, $\epsilon_{strip} = 12$, $\epsilon_{substrate} = 2.2$)	194
7.12	Normalized phase constant of the propagating modes as a function of frequency ($a = 1.25$ mm, $b = 500$ μ m, $w_1 = w_2 = 125$ μ m, $h = h_1 = h_2 = 50$ μ m, $t = 50$ μ m, $s = 125$ μ m, $\epsilon_l = 12$, $\epsilon_{sub} = 2.2$)	195
7.13	Propagation constant as a function of permittivity of the line ($a = 5$ cm, $b = 2$ cm, $w_1 = w_2 = 5$ mm, $h_1 = h_2 = 2$ mm, $s = 5$ mm, $\epsilon_{sub} = 2.2$, $f = 15$ GHz)	196
7.14	The normalized phase constant as a function of strip separation ($a = 5$ cm, $b = 2$ cm, $w_1 = w_2 = 5$ mm, $h_1 = h_2 = 2$ mm, $\epsilon_l = 12$, $\epsilon_{sub} = 2.2$, $f = 15$ GHz)	197
7.15	The normalized coupling length for total power transfer versus strip separation	198
A.1	Green's function geometry	207
A.2	Geometry of the source layer	211
A.3	Current point sources	211
A.4	Notation for multiple layers	226

C.1	Chebyshev family of orthogonal polynomials	236
D.1	Pulse function	246
E.1	Geometry of the problem	260
F.1	Reflection and transmission of a vertically polarized plane wave in a slab	262

LIST OF TABLES

Table

3.1	Chebyshev basis functions and the resulting moments integrals for the first three orders $p = 1, 2, 3$	60
3.2	Chebyshev testing functions and the resulting moments integrals for the first three orders $p = 1, 2, 3$	63
4.1	Coupling Coefficient for edge-coupled and broadside-coupled lines .	123
B.1	Integration in the layers around the source region	232
B.2	Integration in the source region	232
C.1	Coefficients A_{lm} for the expansion of $\sin m\theta$ in terms of Legendre polynomials of order l , P_l	241

LIST OF APPENDICES

Appendix

A.	DERIVATION OF THE GENERALIZED GREEN'S FUNCTIONS OF A MULTILAYERED WAVEGUIDE	206
A.1	Green's functions in the source layer	210
A.1.1	Application of the boundary conditions of the waveguide structure	210
A.1.2	Application of the boundary conditions at the source	214
A.2	Green's functions in the surrounding layers	224
B.	EVALUATION OF POWER INTEGRALS	230
B.1	Around the source region	231
B.2	In the source region	232
C.	EVALUATION OF ENTIRE DOMAIN MOMENTS INTEGRALS	234
C.1	Chebychev polynomials	234
C.2	Integration over the basis functions	237
C.2.1	Evaluation of $\mathcal{I}_n^{(1)}$	238
C.2.2	Evaluation of $\mathcal{I}_n^{(2)}$	239
C.3	Integration over the testing functions	240
C.3.1	Evaluation of $\mathcal{I}_m^{(3)}$	240
C.3.2	Evaluation of $\mathcal{I}_m^{(4)}$	243
C.4	Integration over the conductor term	243
D.	EVALUATION OF SUBSECTIONAL MOMENTS INTEGRALS	245
D.1	Pulse functions	245
D.2	Integration over the expansion functions	246
D.3	Integration over the conductor term	247
E.	GENERAL BOUNDARY CONDITIONS BETWEEN TWO HOMOGENEOUS, ISOTROPIC MEDIA	248
E.1	Initial boundary conditions	249

E.2	First-order boundary conditions	250
E.3	Higher-order boundary conditions	254
E.4	SUMMARY	258
F.	REFLECTION AND TRANSMISSION BY AN INFINITE SLAB . .	261
F.1	Classical Derivation	261
F.2	Alternate Derivation	263
G.	HARMONIC CLOSED FORM EXPRESSIONS	267
G.1	Evaluation of the (A) term	268
G.2	Evaluation of the (B) term	269
G.3	Evaluation of the (C) term	270

CHAPTER I

INTRODUCTION

Microwave circuits are integrated on many different dielectric substrates using hybrid or monolithic techniques. In hybrid circuits, both active and passive components are fabricated separately and attached to the substrate by any of several bonding methods. Monolithic circuits differ from the above IC's in that the active devices are fabricated together with the passive elements in a single semi-conductor wafer. In both cases, however, the active devices are connected through various types of transmission lines. These lines form an integral part of high frequency circuits since their primary role is to confine and transmit the electromagnetic waves with as low loss as possible. Also, these lines can be designed to serve as passive components such as capacitors and inductors, and as circuit elements such as filters and directional couplers. For practical purposes, most MMIC's are enclosed in a shielded housing which prevents radiation and surface wave losses and suppresses electromagnetic interference from the environment. The shielding structure also provides hermetic sealing, mechanical strength, ease of handling and allows for the mounting of connectors. In view of the importance of shielded transmission lines, it is necessary to have a good understanding of their performance and limitations. To that end, this dissertation addresses the characterization of two-dimensional metallic and

dielectric interconnects integrated in a multilayered shielded environment.

1.1 Motivation

Transmission line structures commonly used in microwave integrated circuits consist of thin conducting layers of gold, copper or high temperature superconductor on a dielectric substrate and are backed by a conducting ground plane (Figure 1.1). Circuits realized using planar geometries have several advantages such as light weight, small size, low cost, reliability and reproduceability. They also allow for easy integration with active elements and are compatible with planar antennas. At microwave and millimeter-wave frequencies up to 110 GHz, the most widely used type of printed transmission line interconnect is the microstrip line due to its simple construction. However, to design such interconnects in the frequency range of interest, a full-wave description of these lines is required where both dispersion and losses have to be accounted for as they impose a limit on the overall performance of the circuits.

Another application of microwave integrated circuit technology can be seen in digital logic circuits. With the development of gigabit-rate logic circuits, more emphasis is placed on design and modeling to obtain higher densities on the substrate and higher yields of the circuits. As the speed of digital integrated circuits increases, the pulse rise and fall times become shorter (< 50 ps) and therefore the frequency spectrum extends in the microwave region. At microwave frequencies, dispersion on the line is a well-known phenomenon, which leads to pulse distortion and cross-talk. An additional factor that cannot be neglected at high frequencies is the frequency dependent ohmic loss, which not only attenuates the signal but also adds to the dispersion of the propagating pulse.

Recently, interest has been focused on the potential use of high temperature su-

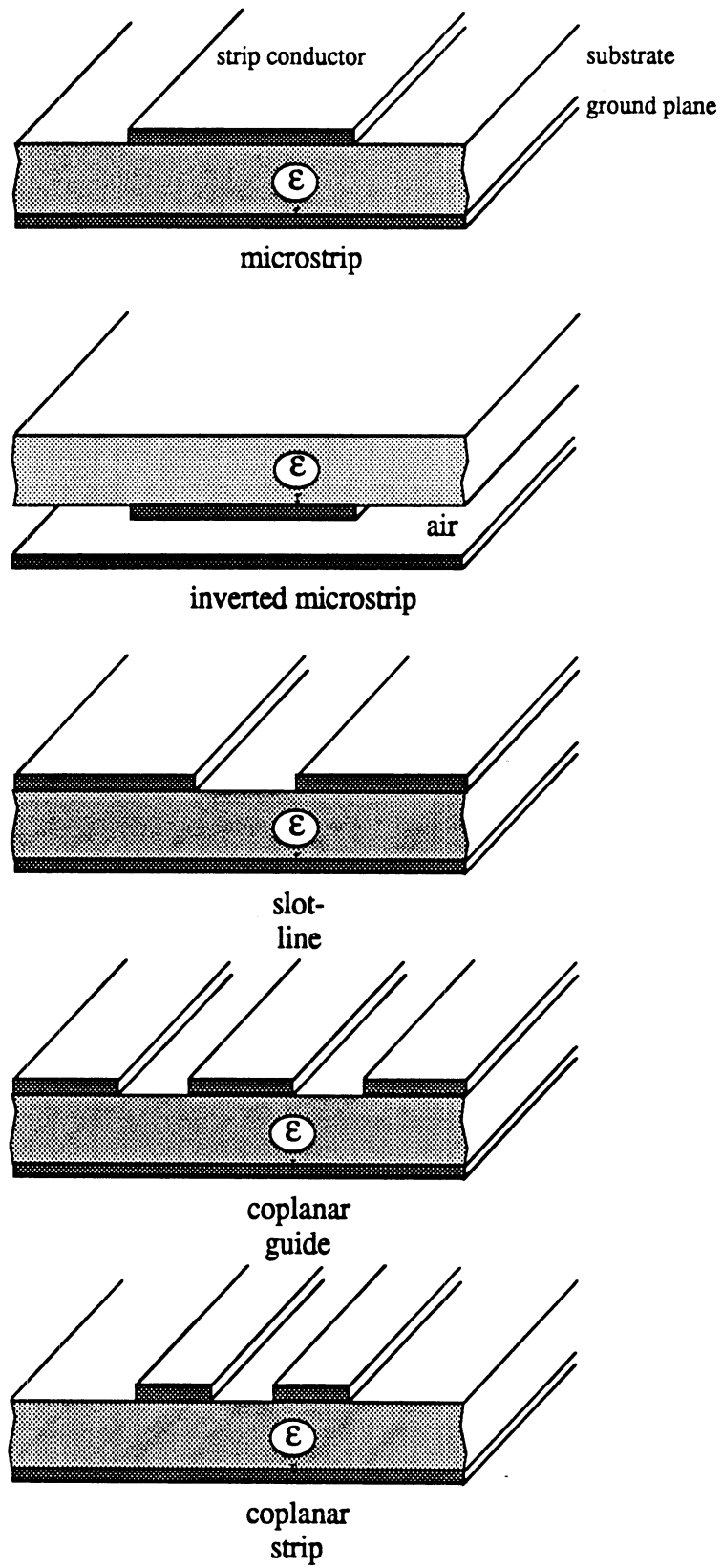


Figure 1.1: Metallic transmission line interconnects

perconductors, such as YBCO, as transmission line materials. Unlike the microstrip lines mentioned above, superconducting lines have negligible ohmic losses and dispersion for frequencies up to several tens of GHz. For high frequency applications, the major advantage of high critical temperature (T_c) superconductors is the reduced surface resistance of the lines as compared to normally conducting metal strips. This, in turn, decreases conductor loss significantly in microwave circuits where ohmic losses can be an important limitation. Also, the use of superconducting transmission lines in VLSI circuits will lead to higher switching speeds, higher data bandwidth, low cross-talk, high packing density and reduced resistive heating. The lines, as they are currently developed, are made of thin films which have a thickness large compared to λ , the penetration depth of the magnetic field into the superconductor. Their low-loss properties make them good candidates for most microwave circuit applications where power loss is usually a limiting factor.

The millimeter-wave and terahertz frequency region is becoming increasingly important for scientific and military applications, such as landing systems for airplanes in heavy fog, radiometric systems for monitoring the upper atmosphere and ozone depletion, and radio-astronomical receivers for studying the chemical composition of our universe. Since, at these frequencies, conductor lines display prohibitively high ohmic losses, a new type of waveguiding structure is needed. A novel monolithic guiding interconnect made of a combination of dielectric layers of different permittivities has been proposed [1]. This type of dielectric line exhibits several advantages over more conventional conducting lines such as low ohmic losses, electrically small size (fraction of a guided wavelength), good guiding properties by appropriate combination of layers, easy fabrication, and monolithic nature that allows for easy construction of passive circuit elements as well as simple integration of active de-

vices. These lines can be made of very low-loss dielectric materials (e.g. Si/Glass, GaAs/AlAs or InP/AlInAs) with thickness a fraction of the wavelength in the dielectric and appear to be suitable for millimeter waveguiding applications (Figure 1.2).

1.2 Objectives

The main objective of this research is to characterize accurately microstrip and dielectric transmission line interconnects for high frequency applications. During the past two decades, several numerical techniques have been developed to investigate planar microwave transmission line circuits with arbitrary metallization for microwave applications. For an accurate description of the circuits, it is now of interest to study second order effects such as cross-talk, packaging effects and losses, and to understand their influence on the propagation characteristics of normal and superconducting interconnects as well as dielectric lines. Because all interconnects studied in this thesis are within a shielded environment, losses due to surface waves, leakage and radiation are not present, and therefore only dissipative losses, including conductor loss and dielectric loss, are considered.

The main objectives of this study are summarized as follows:

1. Derive a generalized model to account for electromagnetic coupling between multiple microstrip lines printed on different planar interfaces which are in close proximity. The method addresses geometries involving multilayered structures with any number of substrates or superstrates since today's MMIC technology uses a combination of multiple thin passivation films and thick dielectric layers.
2. Develop accurate theoretical methods for the analysis of ohmic losses in shielded structures. Unlike planar hybrid transmission line circuits where metallization

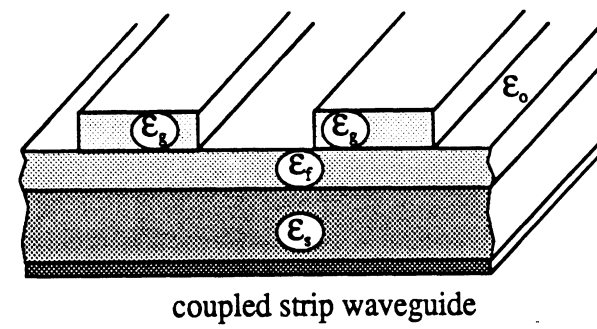
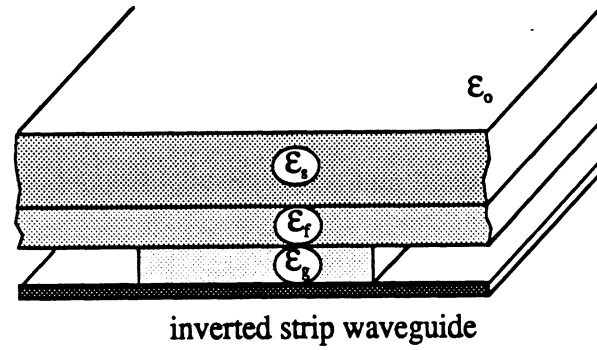
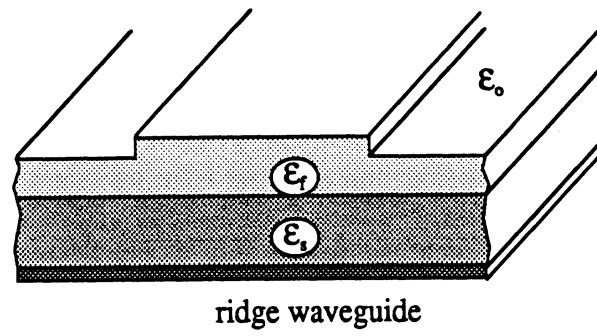
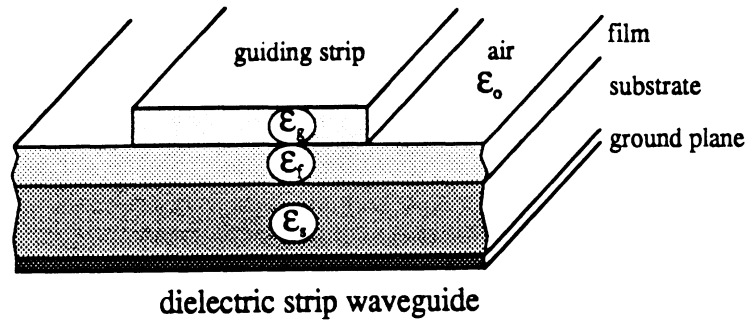


Figure 1.2: Dielectric transmission line interconnects

thicknesses are of the order of several skin depths, the conductor thickness of MMIC's is of the order of magnitude of the skin depth. The goal is therefore to calculate the effect of losses on the propagation characteristics of multiple microstrip lines with thickness ranging from a fraction of the skin depth δ to several skin depths.

3. Investigate the importance of conductor losses relative to dielectric losses in high temperature superconducting thin films. Because the values found in the literature for loss tangent and other electrical parameters needed to characterize these films are not consistent with each other, a parametric study of the transmission characteristics is to be performed as functions of frequency, temperature, permittivity and geometry of the structure.
4. Develop an analytical method to study thin dielectric lines at terahertz frequencies in a manner that allows for easy and accurate characterization of their propagation parameters. This method should also allow for a straightforward extension to three dimensional problems without increasing the complexity of the solution.

1.3 Full-wave approach

In the present work, we are interested in studying interconnects at microwave, millimeter-wave and terahertz frequencies, and therefore it is important to develop accurate full-wave analysis methods and validate their need as compared to the simpler TEM and quasi-TEM or dispersive techniques which have a limited frequency range.

Several static or TEM methods, such as modified conformal mapping [2], finite-difference [3] and integral equation techniques [4] have been used extensively in the

past to study transmission lines where the circuit parameters are determined through the use of electrostatic capacitances and low frequency inductances. A TEM mode of propagation assumes no longitudinal fields and no dispersion and is therefore limited in frequency to a few Gigahertz. These methods are adequate for the analysis of circuits where the strip width and substrate thickness are much smaller than the guided wavelength.

As the frequency increases, quasi-TEM or dispersive techniques, such as the planar-waveguide[5] and ridge waveguide models [6], are used because they provide a frequency dependent solution and yield convenient analytical formulations which are represented by semi-empirical formulas. Although their frequency range of validity extends beyond the TEM models, their accuracy is still frequency limited because they assume negligible longitudinal components and ignore shielding effects.

In order to provide accurate modeling of transmission lines at the frequencies of interest in this work, fullwave analysis techniques are needed which account for all components of the fields in the transmission line structure. These methods include differential techniques (finite-difference and finite element methods [7]) which require the solution of the wave equation and solve the variational problem purely numerically. Integral equation techniques have also been implemented in the space domain [8] and the spectral domain [9], and have the advantage of providing a physical insight in the problem. This dissertation describes the use of a space domain integral equation technique for the characterization of two-dimensional interconnects.

1.4 Overview

In this thesis, two-dimensional microstrip and dielectric transmission line interconnects are studied. The analysis of these two-dimensional passive elements pro-

vides the basic properties for the study of more complex three-dimensional circuits.

In Chapter 2, we introduce an integral equation formulation to analyze a broad class of microstrip and dielectric interconnects. This integral equation provides an exact formulation for the electric field, and has several advantages over conventional differential formulations. Boundary conditions are incorporated in a general manner in the Green's function kernel, and include all the possible modes in the guiding structure. Although different approaches are used to model the metallic and dielectric transmission lines studied in this thesis, some common points apply and are given in Chapter 2, namely the derivation of the generalized dyadic Green's function for a generic multilayered shielded structure, the formulation of a Fredholm integral equation of the second kind, and its solution by the method of moments.

The influence of dielectric and conductor losses on the propagation characteristics of microstrip lines with thickness of the order of the skin depth δ is studied in Chapter 3 using a modified electric field integral equation that accounts for both loss and dispersion. The electromagnetic fields are expressed by an integral equation which is solved independently inside the conducting strips and in the surrounding region. The solution for the fields inside the conductors provide the surrounding region with a relation between tangential electric and magnetic fields on the surface of the strips which serves as an additional boundary condition. This boundary condition is satisfied by an equivalent infinitesimally thin impedance surface which then replaces the lossy conducting strips. The resulting integral equation is then solved to calculate the complex propagation constants, current distribution and characteristic impedance of multiple line geometries. From these results derived in the frequency domain, the effect of losses on pulse dispersion and cross-talk in coupled microstrip lines can be obtained in the time domain by an inverse Fourier transformation. The

method presented in Chapter 3 is implemented numerically in Chapter 4 to quantify the effects of dispersion and losses in conductors with thickness comparable to the skin depth. Examples illustrating the validity and accuracy of the present method are shown for multiple conductors on several layers where dielectric losses in the substrate and conductor losses in the strips and ground plane are considered.

In Chapter 5, an integral equation approach is applied to calculate the propagation characteristics of high temperature thin-film superconducting lines at high frequencies. To evaluate losses in these lines, the superconducting strips are replaced by frequency-dependent surface impedance boundaries. The values of these surface impedances are measured experimentally by a stripline resonator technique. Using this method, phase and attenuation constants as well as impedance of the lines are evaluated and presented as functions of frequency, temperature and several other geometrical parameters.

A novel method is developed in Chapter 6 to calculate the propagation characteristics of dielectric ridge structures in high frequency monolithic integrated circuits. First, the electric field in the dielectric ridge is expressed in terms of a polarization current from which an equivalent surface current density is defined. Generalized boundary conditions are then enforced in order to provide a simple integral equation. The validation of this method for both polarizations is discussed in Chapter 7 and results are reported where comparison to numerical methods is made.

Several appendices can be found at the end of this dissertation. They collect the more lengthy derivations and calculations that are intentionally omitted to simplify the flow of the text. These appendices are included not only for completeness, but are also intended to those who may extend the scope of this work.

CHAPTER II

THE ELECTRIC FIELD INTEGRAL EQUATION TECHNIQUE

2.1 Overview and assumptions

This chapter presents the general technique used in the present work to obtain the fundamental properties of two-dimensional transmission lines in a multilayered dielectric configuration within a shielded environment (Figure 2.1). The theoretical methodology described here serves as building block to the analysis of both types of interconnects studied in this thesis, i.e. metallic microstrip lines and ridge dielectric waveguides.

An electric field integral equation technique (EFIE) is used to derive the propagation characteristics of shielded lines. The approach is based on a full-wave analysis that employs an **integral equation** to relate the electric currents to the electromagnetic fields inside a waveguide with any number of dielectric layers. The appropriate boundary conditions for the problem at hand are applied to establish a **dyadic Green's function** derived for an electric point source in the waveguide structure. By expanding the unknown electric currents into basis functions and applying the **method of moments**, the integral equation is transformed into a system of linear equations. The solution of this system provides information on the propagation

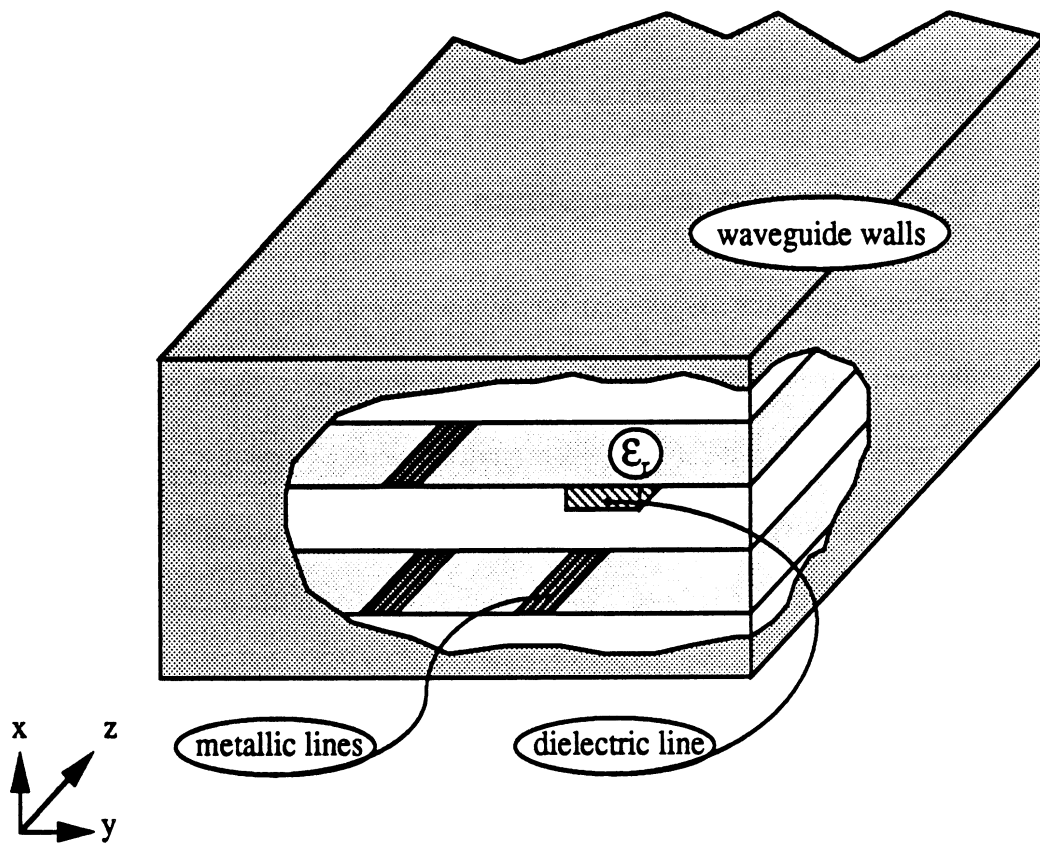


Figure 2.1: Shielded microstrip line configuration

characteristics of the structure, i.e. the phase and attenuation constants of the excited modes, the characteristic impedance of the lines and the current distribution. These frequency-dependent parameters can then be utilized to solve for the fields in the structure or for a time domain analysis. The integral equation method derived in this chapter can be applied to more general problems for the characterization of lossy microstrip lines (Chapters 3, 4) and superconducting lines (Chapter 5), and of dielectric lines (Chapters 6, 7).

Consider an infinitely long inhomogeneously-filled waveguide along the z -direction, with several lines on different levels in a multilayered configuration as shown in Figure 2.1. Cartesian coordinates are used with x the direction perpendicular to the interfaces. In the two-dimensional problem, the z -dependence will be of the form $e^{-\gamma_z z}$ where γ_z is the complex propagation constant for the given mode¹. The development considers lossy dielectric layers, as well as finite conducting strips and ground planes. However, the side walls of the waveguide are assumed to be perfect conductors. In the past, many formulations considered the case of narrow strips with widths small compared to the strip wavelength so that only the longitudinal component of current needed to be accounted for. In this work, there is no restriction on the width of the strips as both longitudinal and transverse components are included in the presentation *and* in the computational implementation. Also, no assumptions have been made which limit the validity of the technique with respect to the operating frequency, the number of strips or their location within the shielded structure.

¹In this derivation, the sinusoidal time dependence is chosen to be $e^{j\omega t}$ and is suppressed throughout the text

2.2 Formulation of the integral equation

Let us assume the waveguide structure to be excited by an impressed electric field \vec{E}^i which can be supported by an assumed aperture distribution or a current probe in the waveguide. The impressed field induces a current or dipole moment \vec{J} on the line resulting in a scattered field \vec{E}^s . At any point \vec{r} , the total field is the sum of the impressed and scattered fields ($\vec{E} = \vec{E}^i + \vec{E}^s$), or

$$\vec{E}(\vec{r}) = \vec{E}^i(\vec{r}) + \int \int \int_V \bar{\bar{G}}^e(\vec{r}/\vec{r}') \cdot \vec{J}(\vec{r}') dv'. \quad (2.1)$$

For two-dimensional guided-wave problems, we are searching for solutions to the source-free or eigenvalue problem. To that end, the impressed field \vec{E}^i is set to zero, yielding

$$\vec{E}(\vec{r}) = \int \int \int_V \bar{\bar{G}}^e(\vec{r}/\vec{r}') \cdot \vec{J}(\vec{r}') dv'. \quad (2.2)$$

The kernel of the integral, $\bar{\bar{G}}^e$, represents the electric dyadic Green's function for the problem and is obtained by solving the boundary-value problem of the structure excited by an infinitesimal source. Equation (2.2) allows one to obtain the electromagnetic fields excited anywhere in the structure by an arbitrary surface current $\vec{J}(\vec{r}')$ and is derived by applying the Green's theorem between \vec{E} and $\bar{\bar{G}}^e$ and by making use of the boundary and radiation conditions. A similar integral equation can be derived for the magnetic field

$$\vec{H}(\vec{r}) = \int \int \int_V \bar{\bar{G}}^h(\vec{r}/\vec{r}') \cdot \vec{J}(\vec{r}') dv' \quad (2.3)$$

where $\bar{\bar{G}}^h$ represents the magnetic dyadic Green's function.

2.2.1 Single integral representation

In the two-dimensional problem, the Green's function must represent outward-propagating waves to infinity, as

$$G(z) = \begin{cases} C_1 e^{-jk_z z} & , z > z' \\ C_2 e^{jk_z z} & , z < z' \end{cases} \quad (2.4)$$

where we require $G(z)$ to be continuous at $z = z'$. In the above, the eigennumber in the z -direction is given by $k_z = \sqrt{k^2 - k_x^2 - k_y^2}$. In addition, we can synthesize the spectrum of plane waves propagating in the z -direction by using a one-dimensional Fourier transform with respect to z as

$$\delta(z - z') = \frac{1}{2\pi} \int_{-\infty}^{\infty} e^{-jk_z(z-z')} dk_z. \quad (2.5)$$

The Green's function may therefore be written in terms of an eigenfunction expansion with respect to the z -direction, and since the components are separable in \vec{r} and \vec{r}' , we get

$$\bar{\bar{G}}(\vec{r}/\vec{r}') = \frac{1}{2\pi} \int_{-\infty}^{\infty} \bar{\bar{G}}(x, y/x', y') e^{-jk_z(z-z')} dk_z \quad (2.6)$$

where ($\bar{\bar{\cdot}}$) is used to denote the transverse dependence of $\bar{\bar{G}}$. The induced current \vec{J} is assumed separable with respect to the variables x' , y' and z' , and is written as

$$\vec{J}(\vec{r}') = \vec{J}(x', y') e^{-jk'_z z'} \quad (2.7)$$

where k'_z is the unknown current propagation constant on the line.

Substituting (2.6) and (2.7) into Pocklington's integral equation (2.2), the electric field due to a current \vec{J} can be expressed as

$$\vec{E} = \int \int \int \int_{-\infty}^{\infty} \frac{1}{2\pi} \bar{\bar{G}}^e(x, y/x', y') e^{-jk_z(z-z')} \cdot \vec{J}(x', y') e^{-jk'_z z'} dx' dy' dz' dk_z \quad (2.8)$$

where the z -dependence of both the Green's function and the current is shown explicitly. Since the dyadic function contains the exponential $e^{-jk_z(z-z')}$, the integration

with respect to k_z can be evaluated in closed form by the method of contour integration. However, equation (2.8) may be written at any cross-section $z = c$, and therefore at $z = 0$ it becomes

$$\vec{E} = \frac{1}{2\pi} \int \int \int \int_{-\infty}^{\infty} \tilde{\tilde{G}}^e(x, y/x', y') \cdot \vec{J}(x', y') e^{-j(k'_z - k_z)z'} dx' dy' dz' dk_z. \quad (2.9)$$

Using the sifting property of the Fourier transform, i.e.

$$\int_{-\infty}^{\infty} e^{-j(k'_z - k_z)z'} dz' = 2\pi \delta(k'_z - k_z), \quad (2.10)$$

the electric field becomes

$$\vec{E} = \int \int_{S_w} \tilde{\tilde{G}}^e(x, y/x', y') \cdot \vec{J}(y') dx' dy' |_{k_z = k'_z} \quad (2.11)$$

where S_w is the cross-section of the line. Discrete modes with propagation constants $k_z = k'_z$ form the spectrum of the surface currents. As will be seen later, the poles of the integrand never occurs for $k_z = k'_z$, and therefore the sifting property of the impulse function can be used. The above expression satisfies all boundary conditions except the ones on the lines, as discussed next.

2.2.2 Fredholm integral equation of the second kind

In this thesis, the propagation characteristics of two-dimensional metallic and dielectric lines are evaluated by solving the appropriate boundary-value problems which are formulated in terms of Fredholm integral equations of the second kind of the form

$$\phi(x) = f(x) + \lambda \int_{\Omega} G(x, y)\phi(y)dy. \quad (2.12)$$

Here $f(x)$ and $G(x, y)$ are known functions defined at every point x of the domain, and the unknown function ϕ appears both under the integral and outside, as opposed

to the integral equation of the first kind where the unknown appears only under the integral sign

$$\int_{\Omega} N(x, y)\phi(y)dy = f(x). \quad (2.13)$$

Also, the domain of integration is fixed in this type of problem unlike Volterra integral equations where the upper limit of integration is variable.

Lossy Microstrip Lines

For perfectly conducting strips Dirichlet condition of vanishing tangential electric field on the surface of the line is enforced

$$\hat{n} \times \vec{E} = 0 \quad (2.14)$$

and can be cast in the form of a Fredholm integral equation of the first kind (2.13). For the general case of strips with finite thickness and finite conductivity this condition is not applicable since the fields can penetrate inside the strips. As further discussed in Chapter 3, we approximate the strips with equivalent non-zero frequency-dependent surface boundaries extending over the surface of the strips and derived from a quasi-TEM analysis of the field penetration. The resulting integral equation is derived from the recognition that the total field on the strip is given by

$$\hat{n} \times \vec{E} = \hat{n} \times \vec{\bar{Z}} \cdot \vec{J} \quad (2.15)$$

where $\vec{\bar{Z}}$ represents the dyadic surface impedance of the lossy metallic line. The integral equation may then be written as a homogeneous integral equation of the second kind

$$\hat{n} \times \vec{\bar{Z}} \cdot \vec{J}(y) = \int_{C_w} \hat{n} \times \vec{\bar{G}}^e(x, y/x', y') \cdot \vec{J}(y') dy' \Big|_{k_z=k'_z} \quad (2.16)$$

where the unknown function is the current distribution $\vec{J}(y)$.

Dielectric Lines

A novel method is developed in Chapter 6 to calculate the propagation characteristics of dielectric ridge structures in high frequency monolithic integrated circuits. First, the electric field in the dielectric ridge is expressed in terms of a polarization current from which an equivalent planar dipole moment \vec{P} is defined. Further, generalized boundary conditions are enforced to provide the following Fredholm integral equation

$$\vec{P}(y) = \int_{C_w} \bar{\bar{G}}_{mod}^e(y/y') \cdot \vec{P}(y') dy' \Big|_{k_x=k'_x} \quad (2.17)$$

where the unknown function is the equivalent dipole moment $\vec{P}(y)$, and where $\bar{\bar{G}}_{mod}$ is a modified dyadic Green's function which includes the generalized higher order electric field boundary conditions at the surfaces of the dielectric strip.

2.3 Derivation of the Green's function

In this section, the kernel $\bar{\bar{G}}^e$ of equation (2.2) is presented for a shielded multilayered dielectric configuration where a vector potential formulation is used to derive electric and magnetic Green's functions as detailed in Appendix A. A generalized impedance boundary formulation is introduced to enforce the boundary conditions at the planar dielectric interfaces in a simple way, leading to a compact formulation of all nine components of the dyadic Green's functions.

2.3.1 Notation

Assuming the time dependence to be $e^{j\omega t}$, the three independent Maxwell's equations are

$$\vec{\nabla} \times \vec{E} = -j\omega\mu\vec{H} \quad , \text{ Faraday's law} \quad (2.18)$$

$$\vec{\nabla} \times \vec{H} = \vec{J} + j\omega\epsilon\vec{E} \quad , \text{ Maxwell-Ampere's law} \quad (2.19)$$

$$\vec{\nabla} \cdot (\vec{J}) = -j\omega\rho \quad , \text{ equation of continuity} \quad (2.20)$$

with auxiliary equations

$$\vec{\nabla} \cdot (\mu\vec{H}) = 0 \quad , \text{ Gauss's law magnetic} \quad (2.21)$$

$$\vec{\nabla} \cdot (\epsilon\vec{E}) = \rho \quad , \text{ Gauss's law} \quad (2.22)$$

where, in an isotropic and homogeneous medium, $\vec{D} = \epsilon\vec{E}$ and $\vec{B} = \mu\vec{H}$ have been used. Taking the curl of (2.18) and substituting $\vec{\nabla} \times \vec{H}$ from (2.19), we obtain the vector wave equation

$$\vec{\nabla} \times \vec{\nabla} \times \vec{E} - k^2\vec{E} = -j\omega\mu\vec{J} \quad (2.23)$$

where $k = \omega\sqrt{\epsilon\mu}$. The concept of dyadic Green's function $\vec{\vec{G}}$ has been developed to find the solutions for this type of equations with various boundary conditions and may be defined as a solution to

$$\vec{\nabla} \times \vec{\nabla} \times \vec{\vec{G}}(\vec{r}/\vec{r}') - k^2\vec{\vec{G}}(\vec{r}/\vec{r}') = -\vec{\vec{I}}\delta(\vec{r} - \vec{r}') \quad (2.24)$$

with $\vec{\vec{I}}$ the idem dyad $\vec{\vec{I}} = \hat{x}\hat{x} + \hat{y}\hat{y} + \hat{z}\hat{z}$. Each component of current gives rise to a vector field and associated vector potentials, and therefore the general linear relation between the current and the field is a dyadic relation. Thus for vector fields, the Green's function is a dyadic quantity which can be represented in its most general form in rectangular coordinates as a tensor

$$\vec{\vec{G}} = \begin{pmatrix} G_{xx}\hat{x}\hat{x} + G_{xy}\hat{x}\hat{y} + G_{xz}\hat{x}\hat{z} \\ G_{yx}\hat{y}\hat{x} + G_{yy}\hat{y}\hat{y} + G_{yz}\hat{y}\hat{z} \\ G_{zx}\hat{z}\hat{x} + G_{zy}\hat{z}\hat{y} + G_{zz}\hat{z}\hat{z} \end{pmatrix} \quad (2.25)$$

where G_{ij} is the i th component of the field due to a unit j -directed current source.

We can define dyadic Green's functions for electric as well as magnetic fields due

to electric or fictitious magnetic current sources. In this work, we will only be interested in the electric-type Green's function $\bar{\bar{G}}^e(\vec{r}/\vec{r}')$ and magnetic-type Green's function $\bar{\bar{G}}^h(\vec{r}/\vec{r}')$ due to electric current sources, where

$$\vec{\nabla} \times \vec{\nabla} \times \bar{\bar{G}}^e(\vec{r}/\vec{r}') - k^2 \bar{\bar{G}}^e(\vec{r}/\vec{r}') = \bar{I} \delta(\vec{r} - \vec{r}') \quad (2.26)$$

$$\vec{\nabla} \times \vec{\nabla} \times \bar{\bar{G}}^h(\vec{r}/\vec{r}') - k^2 \bar{\bar{G}}^h(\vec{r}/\vec{r}') = \vec{\nabla} \times \bar{I} \delta(\vec{r} - \vec{r}'). \quad (2.27)$$

Equation (2.19) shows that the following relation holds between $\bar{\bar{G}}^e$ and $\bar{\bar{G}}^h$

$$k^2 \bar{\bar{G}}^e = \vec{\nabla} \times \bar{\bar{G}}^h - \bar{I} \delta(\vec{r} - \vec{r}'). \quad (2.28)$$

Therefore, from the knowledge of the magnetic Green's function $\bar{\bar{G}}^h$, the electric Green's function $\bar{\bar{G}}^e$ can be determined in a straightforward manner through the use of (2.28).

2.3.2 Vector potential formulation

The Green's function is derived by applying the boundary conditions to the problem of Figure 2.1 for an infinitesimal current source with all three components. There are several approaches in solving boundary value problems of this type, such as the field expansion method using vector wave functions [10]-[11], the scattering superposition method with Hertz potentials [12] or vector potential functions [13], or the mixed potential formulation [14], to name just a few. In this chapter, the dyadic Green's function is derived through the use of vector potentials.

Introducing the concept of vector potential functions \vec{A} and \vec{F} simplifies the problem when fields generated by sources inside the region of interest are considered. The magnetic vector potential \vec{A} is derived from the current source and is subsequently used to compute the electromagnetic fields. Since the definition of any vector requires

the specification of both its curl and divergence, we define the curl of \vec{A} as

$$\vec{B} = \mu\vec{H} = \nabla \times \vec{A}, \quad (2.29)$$

whereas the choice of the divergence of \vec{A} is taken such as to simplify the problem, and is commonly referred to as the *Lorentz's gauge* [15], yielding

$$\vec{H} = \frac{1}{\mu} \nabla \times \vec{A} \quad (2.30)$$

$$\vec{E} = -j\omega\vec{A} + \frac{\nabla\nabla\cdot\vec{A}}{j\omega\epsilon\mu}. \quad (2.31)$$

Substituting (2.29) and (2.31) into (2.18) yields

$$\begin{aligned} \vec{\nabla} \times \vec{\nabla} \times \vec{A} &= -\vec{\nabla}^2 \vec{A} + \nabla(\nabla \cdot \vec{A}) \\ &= \mu\vec{J} + k^2\vec{A} + \nabla\nabla \cdot \vec{A} \end{aligned} \quad (2.32)$$

which reduces to the inhomogeneous vector Helmholtz equation :

$$\nabla^2 \vec{A} + k^2 \vec{A} = \mu\vec{J}. \quad (2.33)$$

Similarly, the vector electric potential \vec{F} is given by

$$\vec{D} = \nabla \times \vec{F}, \quad (2.34)$$

for which we get

$$\vec{E} = \frac{1}{\epsilon} \nabla \times \vec{F} \quad (2.35)$$

$$\vec{H} = j\omega\vec{F} - \frac{\nabla\nabla\cdot\vec{F}}{j\omega\epsilon\mu}, \quad (2.36)$$

and

$$\nabla^2 \vec{F} + k^2 \vec{F} = 0. \quad (2.37)$$

In microstrip problems, the current is carried by the strip and can be decomposed into a longitudinal and transverse component. As shown by Sommerfeld, for a

current source parallel to a dielectric interface, continuity at the boundary requires two components of the vector magnetic potential \vec{A} , one parallel to the interface, the other perpendicular to the interface (see Sommerfeld's derivation for a horizontal antenna over an arbitrary earth, p. 257 [16]). Instead of deriving the electromagnetic fields through the vector magnetic potential \vec{A} with these components, it is possible to derive \vec{E} and \vec{H} through both \vec{A} and \vec{F} potentials. Any two components of \vec{A} and \vec{F} can define the electromagnetic fields anywhere but a judicious choice of the two components can greatly simplify the derivations by producing a set of decoupled equations [17]. The vector wave potentials having only one component in the direction of propagation produce a formulation of the electromagnetic fields in terms of TE and TM waveguide modes. On the other hand, when $\vec{A} = A_x \hat{x}$ and $\vec{F} = F_x \hat{x}$, the fields are then written in terms of longitudinal section electric LSE modes and longitudinal section magnetic LSM modes to the x -direction. This formulation is usually referred to as the Hertz potentials. In view of (2.30)-(2.31) and (2.35)-(2.36), an (A_x, F_x) formulation yields electromagnetic fields of the form

$$\vec{E} = -j\omega A_x \hat{x} + \frac{1}{j\omega\epsilon\mu} \frac{\partial^2}{\partial x \partial y} A_x \hat{y} + \frac{1}{j\omega\epsilon\mu} \frac{\partial^2}{\partial x \partial z} A_x \hat{z} \quad (2.38)$$

$$\vec{H} = \frac{1}{\mu} \frac{\partial}{\partial z} A_x \hat{y} - \frac{\partial}{\partial y} A_x \hat{z} \quad (2.39)$$

for LSM modes, and

$$\vec{E} = \frac{1}{\epsilon} \frac{\partial}{\partial z} F_x \hat{y} - \frac{\partial}{\partial y} F_x \hat{z} \quad (2.40)$$

$$\vec{H} = j\omega F_x \hat{x} - \frac{1}{j\omega\epsilon\mu} \frac{\partial^2}{\partial x \partial y} F_x \hat{y} - \frac{1}{j\omega\epsilon\mu} \frac{\partial^2}{\partial x \partial z} F_x \hat{z} \quad (2.41)$$

for LSE modes. The total fields at any point are the sum of both contributions

$$\vec{E} = \vec{E}|_{LSE} + \vec{E}|_{LSM} \quad (2.42)$$

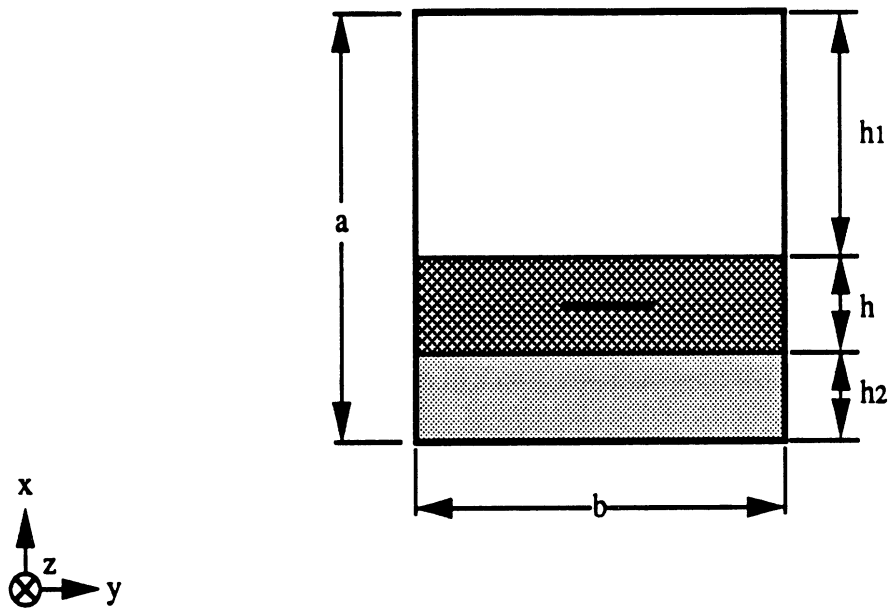
$$\vec{H} = \vec{H}|_{LSE} + \vec{H}|_{LSM}. \quad (2.43)$$

2.3.3 Representation of multi-layered structures

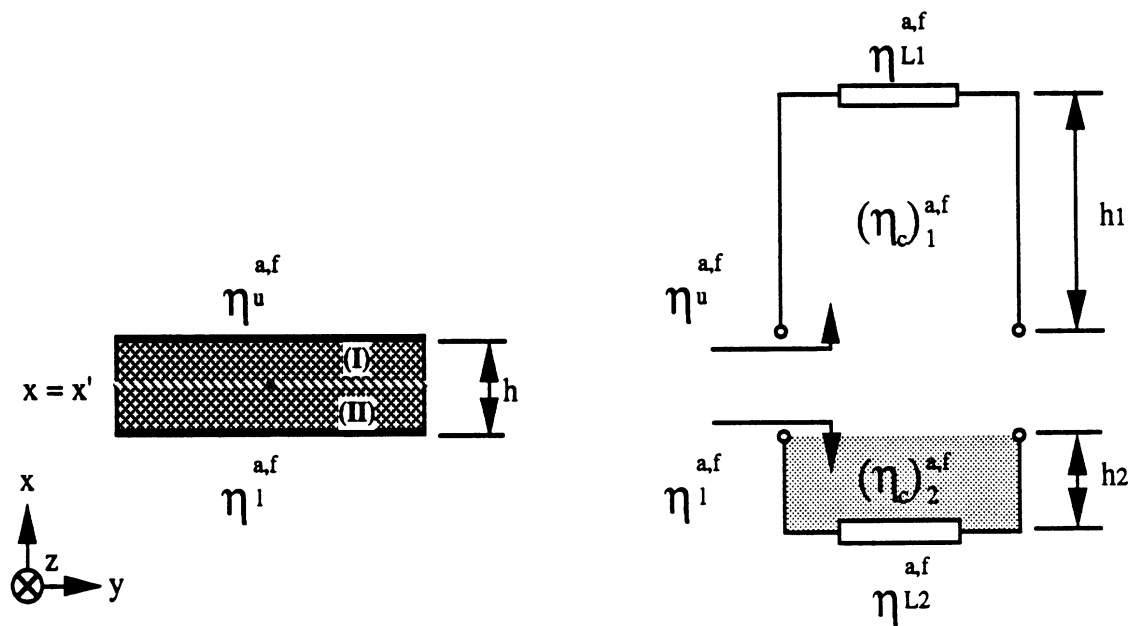
In the present derivation, the Green's function is formulated in a generalized way that can be applied to analyze structures involving multiple substrates and superstrates made of a combination of materials. For such structures, the boundary value problem is usually solved by satisfying the boundary conditions of continuity of tangential electric and magnetic fields at the interface between each of n dielectric regions separately [18]. This approach leads to a linear set of $4(n+1)$ equations which has to be solved analytically in order to find the unknown potentials. In the present formulation, the problem is simplified by considering equivalent boundary conditions on the dielectric interfaces. In this manner, we are able to decrease the complexity of the solution and solve for the electromagnetic fields within the source region only. This formalism has been applied extensively in the past to open structures [19]. This approach results in a simpler formulation of the problem and has the advantage that there is no theoretical limit to the number of dielectric layers that can be treated.

From the uniqueness theorem, we know that *a field in a lossy region is uniquely specified by the sources within the region plus the tangential components of E over the boundary, or the tangential components of H over the boundary, or the former over part of the boundary and the latter over the rest of the boundary* [20]. Therefore, we can derive the Green's function for the source layer alone (layer s) with impedance boundaries η_u and η_l at the upper and lower interfaces, respectively, as shown in Figure 2.2. The fields in the other layers are solved by applying the continuity of tangential fields at the interfaces and can be cast in a simple and compact form as shown in Appendix A. These fields are not needed for the solution of the eigenvalue problem, but are required for the calculation of the characteristic impedance.

The impedance boundaries η_u and η_l are found by introducing the concept of wave



a. Generic cross section of a single shielded line



b. Equivalent transmission line problem

Figure 2.2: Multilayered structure

impedances. Wave impedances can be defined at the planar dielectric interfaces in terms of a simple relationship between the tangential electric and magnetic fields existing on them

$$\vec{E}_t = \hat{x} \times \eta \vec{H}_t \quad (2.44)$$

or, in other terms

$$\eta = \frac{\hat{y} \cdot \vec{E}}{\hat{z} \cdot \vec{H}}. \quad (2.45)$$

These components are chosen such that $\hat{y} \times \hat{z} = \hat{x}$ is the direction of power flow [21]. The boundary conditions at the upper and lower interfaces are enforced separately for each LSE and LSM modes [18] as

$$\eta_l^{a,f} = \left(\frac{E_y}{H_z} \right)_{LSM,LSE}, \quad @ \ x = 0 \quad (2.46)$$

$$\eta_u^{a,f} = \left(\frac{E_y}{H_z} \right)_{LSM,LSE}, \quad @ \ x = h \quad (2.47)$$

where the subscripts l and u represent the lower and upper interfaces and the superscripts a and f are associated with the LSM and LSE modes, respectively. To simplify the notation, we define normalized wave impedances as

$$\tilde{\eta}_u = \frac{\eta_u}{(\eta_c)^s}, \quad \tilde{\eta}_l = \frac{\eta_l}{(\eta_c)^s} \quad (2.48)$$

where the characteristic impedances $(\eta_c)^s$ correspond to the TM and TE impedances in the source layer. In any layer i , we can define

$$(\eta_c)_f^i = \frac{\omega \mu_i}{k_{z_i}}, \quad \text{for LSE modes} \quad (2.49)$$

$$(\eta_c)_a^i = \frac{k_{z_i}}{\omega \epsilon_i}, \quad \text{for LSM modes.} \quad (2.50)$$

The interface complex impedance η_i is equivalent to the impedance of a transmission line i with characteristic impedance $(\eta_c)^i$ terminated by a load impedance which

may be a lumped impedance (such as the surface resistance of the ground plane) or the impedance presented by another substrate layer (Figure 2.2b). The normalized impedance $\tilde{\eta}$ is calculated by the impedance transformation formula for transmission lines using an iterative scheme from the upper and lower walls towards the source region s :

$$\tilde{\eta}_i^{a,f} = \frac{(\eta_c)_{a,f}^i}{(\eta_c)_{a,f}^{i-1}} \frac{\tilde{\eta}_{i-1}^{a,f} + j \tan k_{x_{i-1}} h_{i-1}}{1 + j \tilde{\eta}_{i-1}^{a,f} \tan k_{x_{i-1}} h_{i-1}}, \quad i < s \quad (2.51)$$

$$\tilde{\eta}_i^{a,f} = \frac{(\eta_c)_{a,f}^i}{(\eta_c)_{a,f}^{i+1}} \frac{\tilde{\eta}_{i+1}^{a,f} - j \tan k_{x_{i+1}} h_{i+1}}{1 - j \tilde{\eta}_{i+1}^{a,f} \tan k_{x_{i+1}} h_{i+1}}, \quad i > s \quad (2.52)$$

2.3.4 Solution to the boundary value problem

The homogeneous scalar wave equations for A_x and F_x are solved in regions (I) for $x > x'$ and (II) for $x < x'$ inside the equivalent structure. The solution of the fields in each region amounts to applying first the boundary conditions of the structure at the waveguide walls and the interfaces, and then to solving three independent problems with an excitation in the form of an electric current dipole with an x , y and z component respectively.

Applying the method of separation of variables to the wave equations (2.33) and (2.37) yields

$$A_x = \mathcal{X}_a(x) \mathcal{Y}_a(y) \mathcal{Z}_a(z) \quad (2.53)$$

$$F_x = \mathcal{X}_f(x) \mathcal{Y}_f(y) \mathcal{Z}_f(z) \quad (2.54)$$

for which a general solution may be put in the form

$$\phi = A \cos k_\xi \xi + B \sin k_\xi \xi \quad (2.55)$$

where $\xi = x, y$, or z , $\phi = \mathcal{X}, \mathcal{Y}$, or \mathcal{Z} and k_ξ is complex in general. The eigenvalues

are related by

$$k^2 = k_x^2 + k_y^2 + k_z^2. \quad (2.56)$$

First, boundary conditions at the walls and interfaces of the structure need to be enforced. Since the waveguide walls are assumed to be perfectly conducting, the tangential components of the electric field must vanish at the side walls

$$E_x(y = 0, b) = 0 \quad (2.57)$$

$$E_z(y = 0, b) = 0. \quad (2.58)$$

These boundary conditions are satisfied by choosing the following eigenfunction solutions for the y -dependence

$$\mathcal{Y}_a(y) = \sin k_y y \quad (2.59)$$

$$\mathcal{Y}_f(y) = \cos k_y y \quad (2.60)$$

with

$$k_y = \frac{m\pi}{b}, \quad m = 0, 1, 2, \dots \quad (2.61)$$

To completely characterize the shielded multilayered structure, the boundary conditions on the lower and upper interfaces (2.46) and (2.47) of the source layer have to be enforced, as described in the previous section, by setting

$$\left(\frac{\tilde{E}_y}{\tilde{H}_z} \right)_{a,f}^i = \eta_u^{a,f}, \quad x = h \quad (2.62)$$

$$\left(\frac{\tilde{E}_y}{\tilde{H}_z} \right)_{a,f}^i = \eta_l^{a,f}, \quad x = 0. \quad (2.63)$$

Making use of (2.38)-(2.41), it is shown in Appendix A that the eigenfunction solution for the x -dependence can be written as

$$\mathcal{X}_a^{(I)}(x) = A^{(I)} [\cos k_x(x - h) - j\tilde{\eta}_u^a \sin k_x(x - h)] \quad (2.64)$$

$$\mathcal{X}_f^{(I)}(x) = D^{(I)} [\sin k_x(x - h) + j\tilde{\eta}_u^f \cos k_x(x - h)] \quad (2.65)$$

for region (I), and as

$$\mathcal{X}_a^{(II)}(x) = A^{(II)} [\cos k_x x - j\tilde{\eta}_l^a \sin k_x x] \quad (2.66)$$

$$\mathcal{X}_f^{(II)}(x) = D^{(II)} [\sin k_x x + j\tilde{\eta}_l^f \cos k_x x] \quad (2.67)$$

for region (II).

The four unknown coefficients $A^{(I)}$, $D^{(I)}$, $A^{(II)}$, $D^{(II)}$ in (2.64)-(2.67) are determined by the application of the boundary conditions at the source. To that end, we consider an infinitesimal current source located at \vec{r}' with unit amplitude and components in the x , y and z direction. To account for the electric current source, continuity of the electric fields needs to be satisfied at the interface $x = x'$. An infinitesimal two-dimensional current source in the y and z directions yields a discontinuity in the magnetic field components as follows

$$\hat{n} \times (\vec{H}^{(I)} - \vec{H}^{(II)}) = \hat{y} \delta(\vec{r} - \vec{r}')|_{x=x'} \quad (2.68)$$

$$\hat{n} \times (\vec{H}^{(I)} - \vec{H}^{(II)}) = \hat{z} \delta(\vec{r} - \vec{r}')|_{x=x'}. \quad (2.69)$$

For an x -directed electric dipole, the wave equation is used

$$\nabla^2 \vec{A} + k^2 \vec{A} = -\mu \hat{x} \delta(\vec{r} - \vec{r}')|_{x=x'} \quad (2.70)$$

to derive the coefficients of the \vec{A} potential (2.53)-(2.54) as detailed in Appendix A. Except at the source point, the eigenfunction expansion of the Green's function is well-behaved. It should be noted that the potential formulation of the problem leads to a singular term in the normal xx -component of the Green's function. However, for the characterization of planar structures where the current sources are assumed to have only y and z components, the xx component of the Green's function is not needed.

Electric Green's function

The components of the dyadic electric-type Green's function $\bar{\bar{G}}^e$ are given below for the source layer, where \tilde{G}_{jk}^e represents the j component of the electric field due to a k directed current dipole. In the following, ϵ_s^* is the complex permittivity of the source layer and i represents the region above (I) or below (II) the point source.

$$\begin{aligned} (\tilde{G}_{xx}^e)^i &= \frac{j}{\omega\epsilon_s^*} \left[-\delta(\vec{r} - \vec{r}') \right. \\ &\quad \left. + \sum_{m=0}^{\infty} \frac{\delta_m}{b} \frac{(k_y^2 + k_z^2)}{k_x} \frac{1}{\mathcal{D}_a} \varsigma_a^i(x) v_a^i(x') \sin k_y y \sin k_y y' \right] \end{aligned} \quad (2.71)$$

$$(\tilde{G}_{xy}^e)^i = -\frac{j}{\omega\epsilon_s^*} \sum_{m=0}^{\infty} \frac{\delta_m}{b} k_y \frac{1}{\mathcal{D}_a} \varsigma_a^i(x) \varphi_a^i(x') \sin k_y y \cos k_y y' \quad (2.72)$$

$$(\tilde{G}_{xz}^e)^i = \frac{1}{\omega\epsilon_s^*} \sum_{m=0}^{\infty} \frac{\delta_m}{b} k_z \frac{1}{\mathcal{D}_a} \varsigma_a^i(x) \varphi_a^i(x') \sin k_y y \sin k_y y' \quad (2.73)$$

$$(\tilde{G}_{yx}^e)^i = -\frac{j}{\omega\epsilon_s^*} \sum_{m=0}^{\infty} \frac{\delta_m}{b} \frac{1}{\mathcal{D}_a} k_y \psi_a^i(x) v_a^i(x') \cos k_y y \sin k_y y' \quad (2.74)$$

$$\begin{aligned} (\tilde{G}_{yy}^e)^i &= j \sum_{m=0}^{\infty} \frac{\delta_m}{b} \frac{1}{k_y^2 + k_z^2} \cos k_y y \cos k_y y' \\ &\quad \left[k_y^2 (\eta_c)_a^s \frac{1}{\mathcal{D}_a} \psi_a^i(x) \varphi_a^i(x') + k_z^2 (\eta_c)_f^s \frac{1}{\mathcal{D}_f} \psi_f^i(x) \varphi_f^i(x') \right] \end{aligned} \quad (2.75)$$

$$\begin{aligned} (\tilde{G}_{yz}^e)^i &= \sum_{m=0}^{\infty} \frac{\delta_m}{b} \frac{k_y k_z}{(k_y^2 + k_z^2)} \cos k_y y \sin k_y y' \\ &\quad \left[-(\eta_c)_a^s \frac{1}{\mathcal{D}_a} \psi_a^i(x) \varphi_a^i(x') + (\eta_c)_f^s \frac{1}{\mathcal{D}_f} \psi_f^i(x) \varphi_f^i(x') \right] \end{aligned} \quad (2.76)$$

$$(\tilde{G}_{zx}^e)^i = -\frac{1}{\omega\epsilon_s^*} \sum_{m=0}^{\infty} \frac{\delta_m}{b} k_z \frac{1}{\mathcal{D}_a} \psi_a^i(x) v_a^i(x') \sin k_y y \sin k_y y' \quad (2.77)$$

$$\begin{aligned} (\tilde{G}_{zy}^e)^i &= \sum_{m=0}^{\infty} \frac{\delta_m}{b} \frac{k_y k_z}{(k_y^2 + k_z^2)} \sin k_y y \cos k_y y' \\ &\quad \left[(\eta_c)_a^s \frac{1}{\mathcal{D}_a} \psi_a^i(x) \varphi_a^i(x') - (\eta_c)_f^s \frac{1}{\mathcal{D}_f} \psi_f^i(x) \varphi_f^i(x') \right] \end{aligned} \quad (2.78)$$

$$\begin{aligned}
(\tilde{G}_{zz}^e)^i &= j \sum_{m=0}^{\infty} \frac{\delta_m}{b} \frac{1}{k_y^2 + k_z^2} \sin k_y y \sin k_y y' \\
&\quad \left[k_z^2 (\eta_c)_a^s \frac{1}{\mathcal{D}_a} \psi_a^i(x) \varphi_a^i(x') + k_y^2 (\eta_c)_f^s \frac{1}{\mathcal{D}_f} \psi_f^i(x) \varphi_f^i(x') \right] \quad (2.79)
\end{aligned}$$

where

$$k_s = \omega \sqrt{\epsilon_s^* \mu_0} \quad (2.80)$$

$$k_y = \frac{m\pi}{b} \quad (2.81)$$

$$k_{x_s} = \sqrt{k_s^2 - k_y^2 - k_z^2}. \quad (2.82)$$

and δ_m is the Neumann delta defined by

$$\delta_m = \begin{cases} 1 & , m = 0 \\ 2 & , m \neq 0 \end{cases} \quad (2.83)$$

The x dependence is given by

$$\zeta_{a,f}^I(x) = \cos k_x(x-h) - j\tilde{\eta}_u^{a,f} \sin k_x(x-h) \quad (2.84)$$

$$\zeta_{a,f}^{II}(x) = \cos k_x x - j\tilde{\eta}_l^{a,f} \sin k_x x \quad (2.85)$$

$$\psi_{a,f}^I(x) = \sin k_x(x-h) + j\tilde{\eta}_u^{a,f} \cos k_x(x-h) \quad (2.86)$$

$$\psi_{a,f}^{II}(x) = \sin k_x x + j\tilde{\eta}_l^{a,f} \cos k_x x, \quad (2.87)$$

and the x' dependence may be written as

$$\varphi_{a,f}^I(x') = \sin k_x x' + j\tilde{\eta}_u^{a,f} \cos k_x x' \quad (2.88)$$

$$\varphi_{a,f}^{II}(x') = \sin k_x(x'-h) + j\tilde{\eta}_l^{a,f} \cos k_x(x'-h) \quad (2.89)$$

$$v_{a,f}^I(x') = \cos k_x x' - j\tilde{\eta}_u^{a,f} \sin k_x x' \quad (2.90)$$

$$v_{a,f}^{II}(x') = \cos k_x(x'-h) - j\tilde{\eta}_l^{a,f} \sin k_x(x'-h) \quad (2.91)$$

with

$$\mathcal{D}_{a,f} = \sin k_x h \left(1 - \tilde{\eta}_u^{a,f} \tilde{\eta}_l^{a,f} \right) + j \cos k_x h \left(\tilde{\eta}_l^{a,f} - \tilde{\eta}_u^{a,f} \right). \quad (2.92)$$

As further discussed in Chapter 7, the equations $\mathcal{D}_a = 0$ and $\mathcal{D}_f = 0$ are the characteristic equations for the waveguide modes of the TM and TE types, respectively, propagating in the corresponding multilayered inhomogeneously-filled waveguide. The contribution of the LSE and LSM terms is expressed clearly through the x and x' dependence of the individual components. For the vertical component of the field, only LSM modes are present. All the terms of $\bar{\bar{G}}^e$ are eigenmode expansions with respect to the y direction, resulting in a single summation over the modes m . It is interesting to note that the $m = 0$ term only contributes to the summation for the yy -component since it is the product of two cosines.

The dyadic Green's function components are given here for the regions just above and below the source. By applying the boundary conditions at the different dielectric interfaces, the Green's function can be derived in any layer as shown in Appendix A.

Magnetic Green's function

The components of the magnetic Green's function are needed for the evaluation of the characteristic impedance and are given below

$$\left(\tilde{G}_{xx}^h \right)^i = 0 \quad (2.93)$$

$$\left(\tilde{G}_{xy}^h \right)^i = -j \sum_{m=0}^{\infty} \frac{\delta_m}{b} \frac{k_z}{k_x} \frac{1}{\mathcal{D}_f} \psi_a^i(x) \varphi_a^i(x') \cos k_y y \cos k_y y' \quad (2.94)$$

$$\left(\tilde{G}_{xz}^h \right)^i = - \sum_{m=0}^{\infty} \frac{\delta_m}{b} \frac{k_y}{k_x} \frac{1}{\mathcal{D}_f} \psi_a^i(x) \varphi_a^i(x') \cos k_y y \sin k_y y' \quad (2.95)$$

$$\left(\tilde{G}_{yx}^h \right)^i = \frac{j}{\omega \mu} \sum_{m=0}^{\infty} \frac{\delta_m}{b} k_z (\eta_c)_a^s \frac{1}{\mathcal{D}_a} \zeta_a^i(x) v_a^i(x') \sin k_y y \sin k_y y' \quad (2.96)$$

$$\begin{aligned}
(\tilde{G}_{yy}^h)^i &= j \sum_{m=0}^{\infty} \frac{\delta_m}{b} \frac{k_y k_z}{k_y^2 + k_z^2} \sin k_y y \cos k_y y' \\
&\quad \left[-\frac{1}{\mathcal{D}_a} \varsigma_a^i(x) \varphi_a^i(x') + \frac{1}{\mathcal{D}_f} \varsigma_f^i(x) \varphi_f^i(x') \right] \quad (2.97)
\end{aligned}$$

$$\begin{aligned}
(\tilde{G}_{yy}^h)^i &= \sum_{m=0}^{\infty} \frac{\delta_m}{b} \frac{1}{k_y^2 + k_z^2} \sin k_y y \sin k_y y' \\
&\quad \left[k_z^2 \frac{1}{\mathcal{D}_a} \varsigma_a^i(x) \varphi_a^i(x') + k_y^2 \frac{1}{\mathcal{D}_f} \varsigma_f^i(x) \varphi_f^i(x') \right] \quad (2.98)
\end{aligned}$$

$$(\tilde{G}_{zz}^h)^i = \frac{1}{\omega \mu} \sum_{m=0}^{\infty} \frac{\delta_m}{b} k_y (\eta_c)_a^s \frac{1}{\mathcal{D}_a} \varsigma_a^i(x) v_a^i(x') \cos k_y y \sin k_y y' \quad (2.99)$$

$$\begin{aligned}
(\tilde{G}_{zy}^h)^i &= - \sum_{m=0}^{\infty} \frac{\delta_m}{b} \frac{1}{k_y^2 + k_z^2} \cos k_y y \cos k_y y' \\
&\quad \left[k_y^2 \frac{1}{\mathcal{D}_a} \varsigma_a^i(x) \varphi_a^i(x') + k_z^2 \frac{1}{\mathcal{D}_f} \varsigma_a^i(x) \varphi_a^i(x') \right] \quad (2.100)
\end{aligned}$$

$$\begin{aligned}
(\tilde{G}_{zz}^h)^i &= j \sum_{m=0}^{\infty} \frac{\delta_m}{b} \frac{k_y k_z}{k_y^2 + k_z^2} \cos k_y y \sin k_y y' \\
&\quad \left[-\frac{1}{\mathcal{D}_a} \varsigma_a^i(x) \varphi_a^i(x') + \frac{1}{\mathcal{D}_f} \varsigma_f^i(x) \varphi_f^i(x') \right]. \quad (2.101)
\end{aligned}$$

2.4 Method of moments

The generalized integral equation (2.11) can only be solved numerically because of the complexity of the integrand. The Method of Moments is particularly well-suited for the solution of integral equations of this type [22] and is adopted here to calculate the current distribution on the lines. This technique transforms the integral equation into a matrix algebraic equation that can be easily solved on a computer.

2.4.1 Overview of the method

Let us consider the operator equation (2.2) as

$$\mathcal{L}(\vec{J}) = g(\vec{E}) \quad (2.102)$$

where \mathcal{L} is an integral operator (which includes the Green's function and certain boundary conditions), $g(\vec{E})$ is a known excitation function and \vec{J} is the unknown

function to be found. Equation (2.102) can be solved by applying the method of moments. The first step in this approach involves approximating the unknown current by a series of functions as

$$\vec{J}(y') = \sum_p \vec{I}_{zp} \cdot \vec{b}_p(y') \quad (2.103)$$

where the components of \vec{I}_p are the unknown constants to be determined and the components of $\vec{b}_p(y')$ are known expansion functions which form a suitable basis. The basis functions may be either entire domain bases defined over the entire domain of the operator (e.g. Chebychev polynomials) or subsectional bases which only exist over subsections of the domain (e.g. pulses) as shown in Figure 2.3. In this work, both types of basis functions have been used.

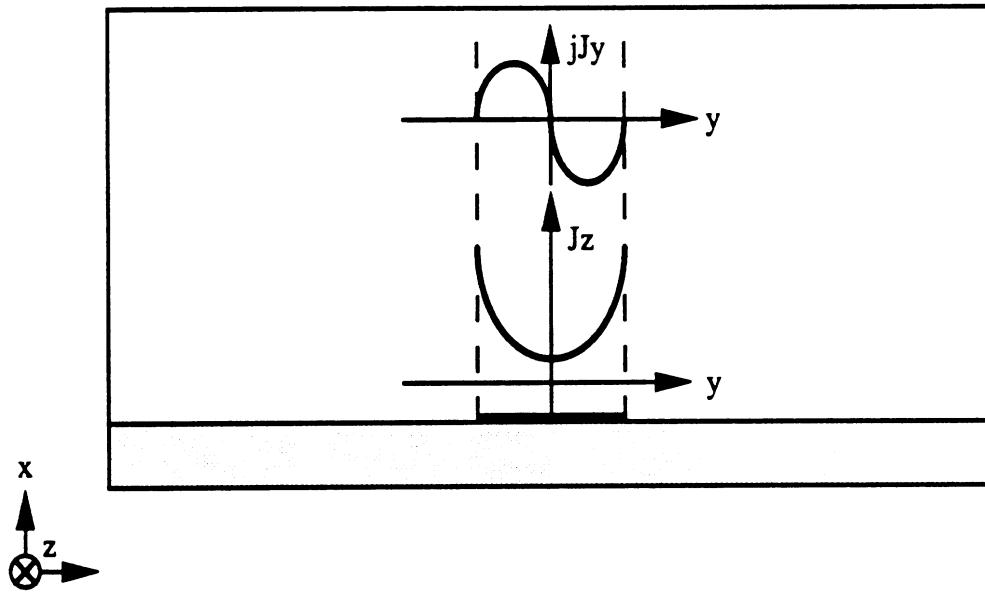
For exact solutions, (2.103) is usually an infinite summation and \vec{b}_p form a complete set of basis functions. For approximate solutions, (2.103) is a finite summation which is truncated after insuring proper convergence. In addition, the expansion in (2.103) has to satisfy the boundary conditions as required by the original equation (2.102) where, upon substitution, we obtain

$$\sum_p^P \vec{I}_p \cdot \mathcal{L}(\vec{b}_p) \simeq g(\vec{E}). \quad (2.104)$$

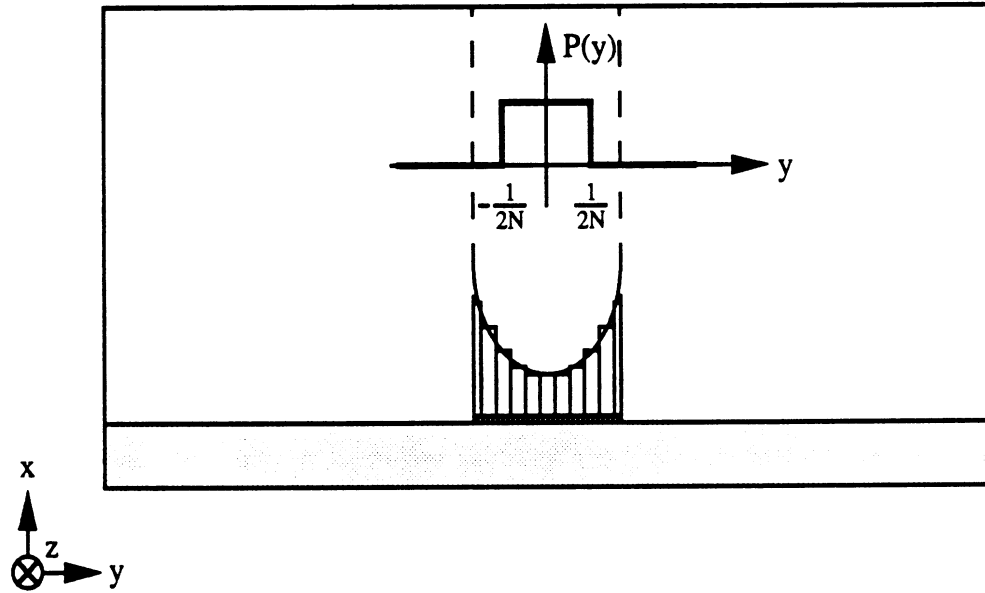
The second step in the moments method is to compute the coefficients $\{I_{lp}\}$ so that the approximate equation (2.104) is satisfied in some average sense. The subscript l denotes the x , y or z component of the unknown constants. To that end, we define the inner product

$$\langle \vec{f}, \vec{g} \rangle = \int_W \vec{f} \cdot \vec{g} dy \quad (2.105)$$

where the integration is taken in the y direction along the width W of the strip. Next, we take the inner product of (2.104) with some suitable weighting functions



a. Entire Domain Bases



b. Subsectional Bases

Figure 2.3: Basis Functions

\vec{w}_q , $q = 1, \dots, Q$, which form a functional basis, defined on the same domain as the unknown current, i.e. the source coordinates. In Galerkin's method, the weighting functions are taken to be the same as the basis functions $w_n = b_n$. Thus we obtain a set of linear equations in $\{\vec{I}_p\}$:

$$\sum_p^P \vec{I}_p \langle \vec{w}_q, \mathcal{L}(\vec{b}_p) \rangle \simeq \langle \vec{w}_q, g(\vec{E}) \rangle, \quad q = 1, \dots, Q \quad (2.106)$$

which can be solved for $\{I_{lp}\}$ by using either direct methods (Gaussian elimination, or LU transform) or iterative methods (conjugate-gradient method), which are suitable for large systems of equations.

2.4.2 Matrix formulation

The application of the inner product to (2.102) reduces the integral equation to a matrix equation given by

$$[\mathcal{Z}][\mathcal{I}] = [\mathcal{V}] \quad (2.107)$$

where $[\mathcal{Z}]$ is the impedance matrix, $[\mathcal{I}]$ is the current vector of unknown x, y, z amplitudes and $[\mathcal{V}]$ is the excitation vector.

The impedance matrix $[\mathcal{Z}]$ contains 9 sub-matrices as shown below

$$[\mathcal{Z}] = \begin{bmatrix} [\mathcal{Z}_{xx}] & [\mathcal{Z}_{xy}] & [\mathcal{Z}_{xz}] \\ [\mathcal{Z}_{yx}] & [\mathcal{Z}_{yy}] & [\mathcal{Z}_{yz}] \\ [\mathcal{Z}_{zx}] & [\mathcal{Z}_{zy}] & [\mathcal{Z}_{zz}] \end{bmatrix} \quad (2.108)$$

with individual components given by

$$\mathcal{Z}_{kl}(q, p) = \langle w_{kq}, \mathcal{L}(b_{lp}) \rangle \quad (2.109)$$

$$= \int_{W_q} dy \int_{W_p} dy' \tilde{G}_{ij}^e(x, y/x', y') b_{jp}(y') w_{iq}(y). \quad (2.110)$$

In the above, W_q and W_p represent the width of the testing and basis cells, respectively. Integration is performed over the total width of the strip when entire domain

bases are chosen to represent the current, and over subsections of the strip width for subsectional basis functions.

The elements of the excitation vector are of the form

$$[\mathcal{V}] = \begin{bmatrix} [\mathcal{V}_x(q)] \\ [\mathcal{V}_y(q)] \\ [\mathcal{V}_z(q)] \end{bmatrix}, \quad (2.111)$$

where

$$\mathcal{V}_k(q) = \int_{W_q} dy E_k(y) w_{kq}(y) \quad , k = x, y, z. \quad (2.112)$$

When the boundary conditions on the strip are imposed, either in the case of lossy conductors or dielectric lines, the resulting integral equation is a Fredholm integral of the second kind (see section 2.2.2). Therefore the unknown current appears under the integral as well as on the right hand side of equation (2.107). In view of equation (2.12), equation (2.112) takes the form

$$\begin{aligned} \mathcal{V}_x(q) &= \int_{W_q} dy C_x J_x(y) w_{xq}(y) \\ \mathcal{V}_y(q) &= \int_{W_q} dy C_y J_y(y) w_{yq}(y) \\ \mathcal{V}_z(q) &= \int_{W_q} dy C_z J_z(y) w_{zq}(y) \quad , q = 1, \dots, Q \end{aligned} \quad (2.113)$$

where C_x, C_y, C_z are functions of the boundary conditions on the line and independent of y . In the above equations the current is the only unknown and can be written in terms of the expansion (2.103) as

$$\begin{aligned} \mathcal{V}_x(q) &= C_x \sum_p I_{xp} \int_{W_q} dy b_{xp}(y) w_{xq}(y) \\ \mathcal{V}_y(q) &= C_y \sum_p I_{yp} \int_{W_q} dy b_{yp}(y) w_{yq}(y) \\ \mathcal{V}_z(q) &= C_z \sum_p I_{zp} \int_{W_q} dy b_{zp}(y) w_{zq}(y) \quad , q = 1, \dots, Q \end{aligned} \quad (2.114)$$

The resulting expressions can be moved to the left hand side of equation (2.107) and incorporated in the impedance matrix. The resulting excitation vector is zero for the solution of two-dimensional eigenvalue problems [23].

CHAPTER III

MICROSTRIP LINES: THEORETICAL STUDY OF LOSSES

3.1 Introduction and background

Shielded microstrip lines are widely used in microwave integrated circuits where they perform a great variety of functions. It is therefore very important to have an accurate knowledge of their characteristics, i.e. phase velocity, characteristic impedance and losses as a function of geometry and frequency. Although dissipative losses are often considered a second order effect, they can impose a major limitation on the performance of microstrip interconnects, passive circuits and radiating elements in high frequency circuits. It is therefore of interest to improve loss analysis, whereby effects of substrate and non-perfectly conducting strips can be treated individually. In the context of shielded microwave and millimeter-wave printed circuits, ohmic losses due to the finite conductivity of the strips are the prevalent loss effect and have been studied by several authors during the past fifty years but have been limited to lower frequencies and electrically thick strips.

The *incremental-inductance rule* derived by Wheeler [24] is the foundation for calculating the surface resistivity of conductive strips. From the knowledge of the resistivity, attenuation due to conductor losses has been evaluated by analytic dif-

ferentiation [25], [26] and numerical integration [27]. The perturbation method is also frequently used in quasi-static techniques such as the boundary-element method [28], the finite-element method [29] as well as in spectral domain fullwave analyses [30], [31]. These methods are based on the electromagnetic field distribution of a loss-free environment and are useful for hybrid circuits with relatively small losses in conductors with cross-sectional dimensions much larger than the skin-depth.

In the approaches mentioned above, explicit formulas are given as a function of the width to thickness ratio of the strip. However, these techniques are strictly limited to electrically thick conducting strips, i.e. they assume that the conductors have a thickness much greater than the skin depth at the frequency of interest. The thickness is usually taken into account by a modification of the strip width [27], [32]. In monolithic microwave and millimeter wave integrated circuits, however, the metallization thickness is of the order of a few μm , and the skin depth δ varies between about $3\mu\text{m}$ at 1 GHz to $0.3\mu\text{m}$ at 100 GHz. Thus the conductor thickness and skin depth are of the same order of magnitude and therefore the skin effect becomes an important issue. In the past few years, several researchers have studied the above problem using variational formulations [33], [34]. Since the publication of the present work to the scientific community in 1989 [35]-[36], several new approaches have been employed, ranging from quasi-static techniques (Green's function method [37]) to semi-empirical methods ('phenomenological loss equivalence method' [38]) and full-wave approaches (mode matching method [39], finite-difference method [40], and the method of lines [41]). In the present method the influence of conductor losses is evaluated using an integral equation method. In this mathematical formulation, the fields are computed inside the conductors and are utilized to define an equivalent impedance on the surface of the strips. This surface impedance is used as a boundary

condition for the solution of the electromagnetic problem outside the conductors.

3.2 Description of the theoretical method

This chapter represents an approach to evaluate dispersion and losses in a system of multiconductor microstrip lines printed on multilayer substrates and surrounded by a shielding cavity. The system is uniform in the direction perpendicular to the $x - y$ plane. An arbitrary number N_c of conductors are embedded in an arbitrary number N_d of dielectric layers (Figure 3.1). The conductor strips are assumed to have a uniform, rectangular cross-section, finite conductivity σ and thickness t . For microstrip lines used in microwave and millimeter wave applications, the strip thickness is in many cases small compared to the width of the strip. However, VLSI interconnections with strip aspect ratios less than five (width/thickness < 5) are commonly encountered in state-of-the-art, high-speed, high-density packages. Also, in practical circuits the strips are usually at least two widths away from the side walls of the waveguide to avoid coupling, therefore losses of the shielding can be ignored since most of the fields are concentrated below the strips. However, the effect of a lossy ground plane is included. Dielectric losses are accounted for by assuming a complex permittivity for each layer which in turn implies that the propagation constant $\gamma_z \equiv jk_z$ is a complex quantity whose real part represents the attenuation due to the finite conductivity of the strips and dielectric losses. Both conducting and dielectric regions are assumed to be nonmagnetic with free-space permeability μ_0 . The theory can be extended to multilayered isotropic magnetic media in a straightforward manner by the concept of duality [20]. In the case of anisotropic materials, the electrical parameters have to be described as permittivity and permeability tensors.

The approach consists of a generalized integral equation formulation where fields

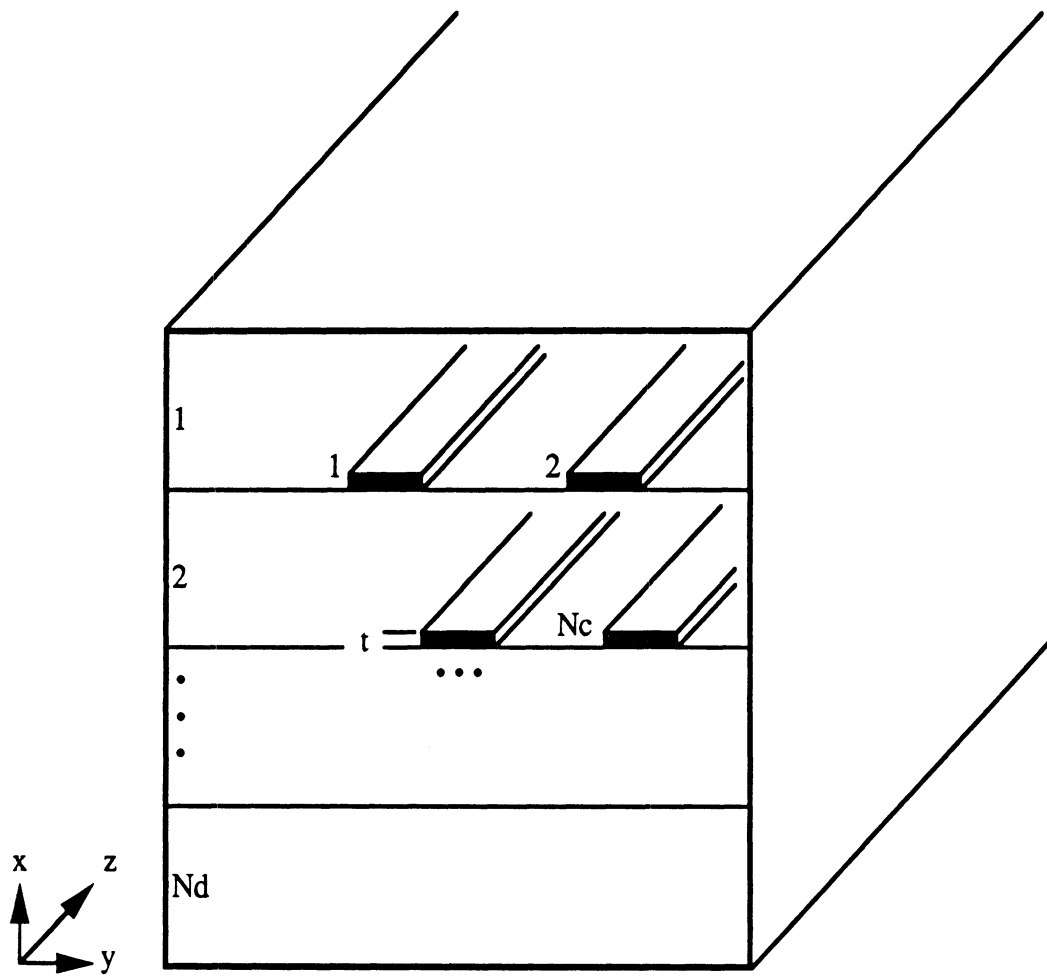


Figure 3.1: Geometry of a multilevel microstrip line system in a shielded environment

are computed independently in different dielectric regions as well as inside the conductors. The field behavior inside the conductor is described by a quasi-TEM analysis where the magnetic vector potential is related to the unknown current distribution by a static Green's function. This method allows for the computation of the per unit length resistance $R(f)$ and the per unit length internal inductance of the strip $L_{in}(f)$ as function of frequency. An equivalent surface impedance is then defined which describes, in a physical equivalent sense, the frequency-dependent field penetration in the lossy strips and serves as the boundary condition on the strips. In the case of N_c coupled strips, there are N_c modes associated with the structure. Each line is therefore represented by N_c surface impedances corresponding to each mode. The fields in the dielectric region, which consists of an arbitrary number of layers parallel to the ground plane, are computed by a method of moments solution of Pocklington's integral equation subject to the new introduced boundary condition.

The novelty of this method resides in the application of the boundary conditions on the strip where the tangential electric field is related to the finite current in the microstrip line by the surface impedance described above. The resulting general integral equation that accounts for both dielectric and conductor losses is solved to calculate the complex propagation constant, current distribution and characteristic impedance. From these results derived in the frequency domain, pulse dispersion and cross-talk effects are obtained in the time domain by an inverse Fourier transformation. The numerical implementation of this method is discussed in the following chapter where example results are presented for copper-polyimide interconnections embedded in various substrates.

3.3 Derivation of the equivalent surface impedance

In today's VLSI and MMIC circuits where the cross-sectional dimensions of the lines are comparable to the skin depth, conductor losses are of particular concern. In order to examine the importance of skin-effect, it is necessary to derive the current distribution inside of the conductors. An exact analysis of this case requires Maxwell's equations to be solved throughout the entire domain, i.e., in the dielectric regions and inside the lossy strips. Such an analysis is very involved and actually needs not been undertaken for the frequency range of interest. Inside the lossy strips, the much simpler quasi-TEM approximation discussed below will be shown to be valid up to millimeter wave frequencies. The quasi-TEM integral equation formulation used here for the frequency-dependent current distributions in the lossy strips has been derived in [42], [43] and will be repeated here for completeness. From the knowledge of the current density distribution and energy considerations, the per-unit-length inductance and resistance matrices of the multiconductor transmission line system can be calculated. An equivalent infinitesimally thin impedance is then defined which replaces the lossy conducting strip. This impedance provides the surrounding region with a relation between tangential electric and magnetic fields on the surface of the strip and serves as an additional boundary condition.

3.3.1 Quasi-static integral equation for the current distribution in conductors

Assuming that the cross-sectional dimensions of the strips are small compared to the wavelength λ in the frequency range of interest, the fields in the strips can be considered to be quasi-TEM allowing the use of transmission line circuit-theory parameters. The multiconductor transmission line system can be described in the

frequency domain by the telegrapher equations

$$\frac{dV(z)}{dz} = -([R] + j\omega[L]) I \quad (3.1)$$

$$\frac{dI(z)}{dz} = -([G] + j\omega[C]) V \quad (3.2)$$

where $[R]$, $[L]$, $[G]$ and $[C]$ are the per-unit-length resistance, inductance, conductance and capacitance matrices, respectively. All these quasi-TEM matrices are of dimensions $N_c \times N_c$ where N_c is the number of conductors in the system. The parameters V and I are the complex voltage and current vectors and ω is the angular frequency.

Because of the finite conductivity of the lines and their small cross-sectional dimensions, a longitudinal component of the electric field E_z exists inside the conductors. However it has been shown [44] that this component is still very small compared to the transverse E_t component inside the lossy conductors throughout the millimeter wave frequency range and, as a result, the quasi-TEM approximation remains valid. The field penetration in the strips is dependent on the frequency of operation and therefore the $[R]$ and $[L]$ matrices, which are of interest in this work, will also be frequency-dependent.

In the derivation of the quasi-static integral equation for the current, the system of multiconductors is above an infinite perfectly conducting ground plane as shown in Figure 3.2. At frequencies up to the millimeter wave region, the displacement currents inside the conductors can be neglected compared to conduction currents ($\omega\epsilon \ll \sigma$) for good conductors such as copper. From Maxwell's equations, and under quasi-TEM conditions, the longitudinal component of the electric field is given by

$$E_z(x, y) = -j\omega A_z(x, y) - \nabla\Phi \quad (3.3)$$

where \vec{A} is the magnetic vector potential and Φ is the scalar electric potential. As-

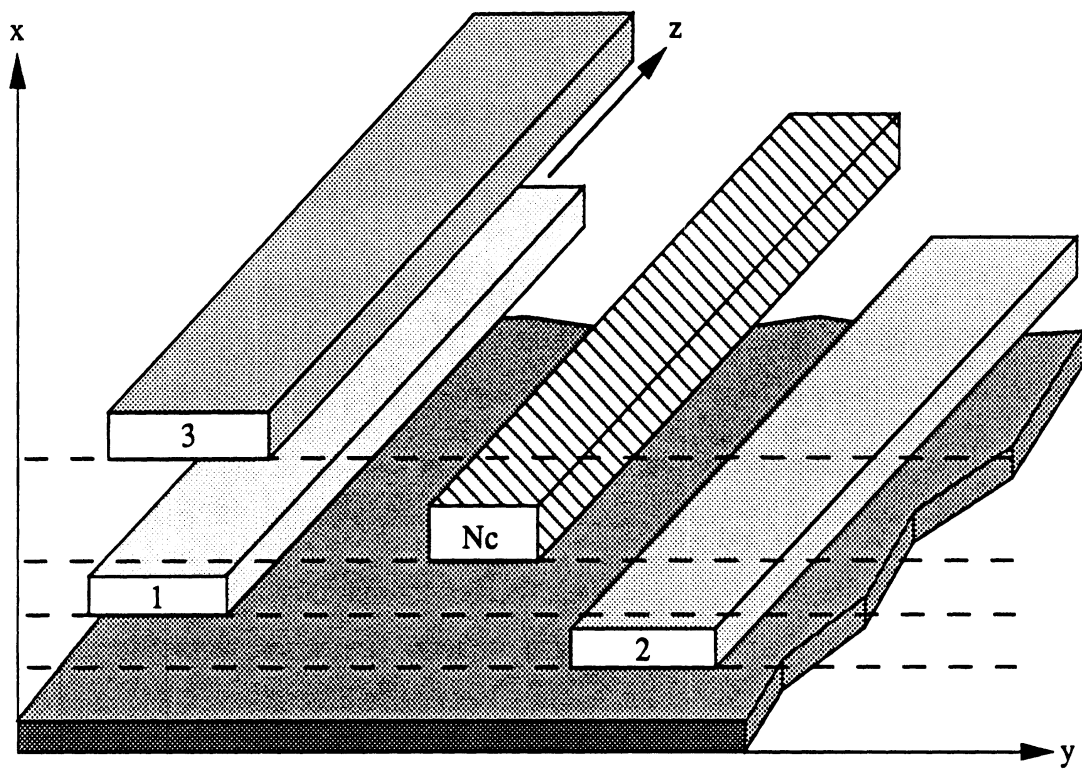


Figure 3.2: System of N_c z -directed multiconductor lines above a ground plane

suming that the voltage drop inside the conductor is only in the z direction, we can write

$$\vec{\nabla}\Phi = \hat{z}\frac{\partial\Phi}{\partial z}. \quad (3.4)$$

Using the fact that for any scalar quantity $\vec{\nabla} \times \vec{\nabla}\Phi \equiv 0$, it follows that $\frac{d\Phi}{dz} = C$.

Applying Ohm's law ($\vec{J} = \sigma\vec{E}$) to (3.3), we get

$$J_z(x, y) = -j\omega\sigma A_z(x, y) - \sigma\frac{d\Phi}{dz}. \quad (3.5)$$

By integration of equation (3.5) over the cross-section of the m th conductor, the constant $\frac{d\Phi}{dz}$ can be determined as

$$-\frac{d\Phi}{dz} = \frac{1}{S_m\sigma} \int \int_{S_m} J_z ds + \frac{j\omega}{S_m} \int \int_{S_m} A_z ds \quad (3.6)$$

where the first integral represents the total current flowing through the cross-section of the m th conductor and the second integral can be seen as the average magnetic potential over the strip and will be denoted by \tilde{A}_m

$$\tilde{A}_m = \frac{1}{S_m} \int \int_{S_m} A_z ds. \quad (3.7)$$

This leads to

$$J_z(x, y) = -j\omega\sigma A_z(x, y) + j\omega\sigma \tilde{A}_m + \frac{1}{S_m} \int \int_{S_m} J_z(x, y) ds. \quad (3.8)$$

The magnetic potential A satisfies the inhomogeneous equation

$$\nabla_t^2 A_z = -\mu J_z(x, y) \quad (3.9)$$

whose general solution has the form

$$A_z(x, y) = \mu \int \int_S J_z(x', y') G(x, y; x', y') dx' dy'. \quad (3.10)$$

The two main assumptions in this derivation are that the gradient of the electric potential has only a z component which is a constant (3.4), and that the current \vec{J} may be related to the magnetic vector potential \vec{A} through a quasi-static Green's function. In (3.10), the quasi-static Green's function G is dependent upon the geometry considered and can be written as

$$G(x, y; x', y') = -\frac{1}{4\pi} \ln \left[\frac{(x - x')^2 + (y - y')^2}{(x - x')^2 + (y + y')^2} \right] \quad (3.11)$$

for an infinite ground plane [45]. Upon substitution of (3.10) in (3.8), we can write the final integral equation for the current density distribution inside of the lossy strips as

$$\begin{aligned} J_z(x, y) = & -j\omega\sigma\mu_o \int \int_{S_T} J_z(x', y') G(x, y; x', y') dx' dy' + \int \int_{S_m} J_z(x, y) ds \\ & + j\omega\sigma\mu_o \frac{1}{S_m} \int \int_{S_m} \left[\int \int_{S_T} J_z(x', y') G(x, y; x', y') dx' dy' \right] ds \end{aligned} \quad (3.12)$$

where $S_T = \sum_{n=1}^{N_c}$ is the total cross section of all conductors. The integral equation (3.12) has been solved by the Method of Moments using pulse basis functions over the cross-section of the strips [45]. Figure 3.3 illustrates the results of this formulation by showing the magnitude of the current density along the width of a metallic strip plotted for four different distances s_1, s_2, s_3 and s_4 from the bottom side of the strip.

3.3.2 Evaluation of the resistance and inductance matrices

Resistance matrix

Once the current distribution inside the conductors has been computed, the per unit length resistance $R(f)$ is found by considering the time average power dissipated

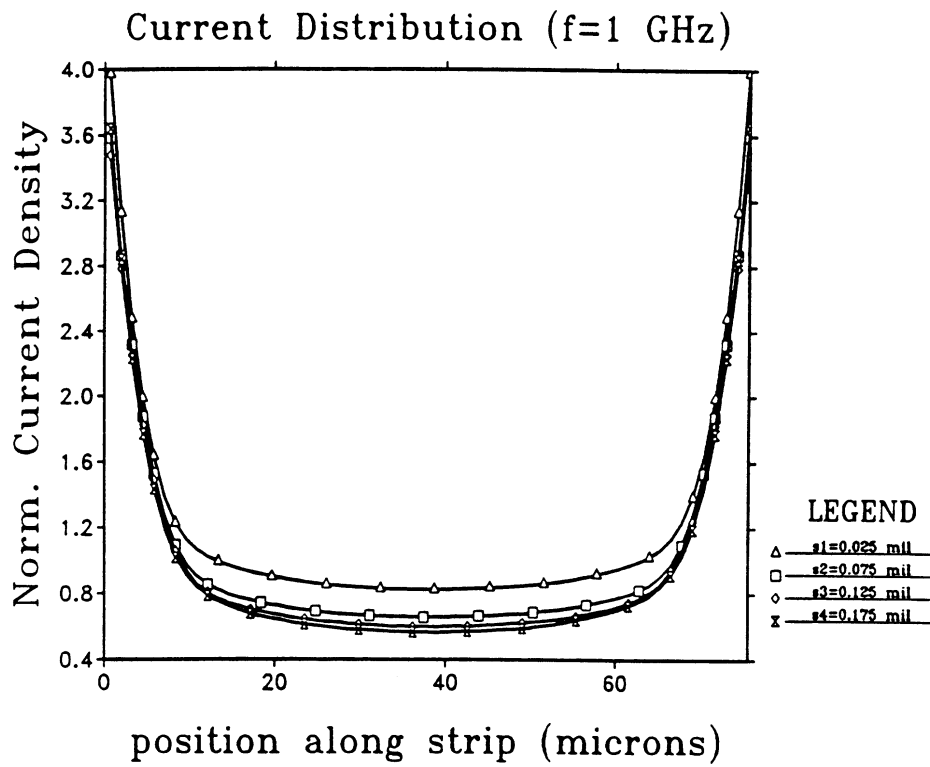


Figure 3.3: Magnitude of current density inside a rectangular strip at a height of 3 mils above a perfectly conducting ground ($W = 3$ mils, $\sigma = 4 \times 10^7$ S/m, $f = 1$ GHz, $t = 0.2$ mils)

in the conductor due to ohmic losses on the line:

$$P_{av} = \frac{1}{2} \text{Re} \left\{ \int_S \vec{J} \cdot \vec{E}^* ds \right\}. \quad (3.13)$$

Using Ohm's law ($\vec{J} = \sigma \vec{E}$), we get

$$P_{av} = \frac{1}{2\sigma} \text{Re} \left\{ \int_S \vec{J} \cdot \vec{J}^* ds \right\} = \frac{1}{2\sigma} \text{Re} \left\{ \int_S |J|^2 ds \right\}. \quad (3.14)$$

The power can also be written in terms of the per-unit-length resistance matrix as

$$P_{av} = \frac{1}{2} R |I|^2 = \frac{1}{2} R \left| \left(\int_S J ds \right) \right|^2 \quad (3.15)$$

where $I = \int_S J ds$. The component R_{ij} of the resistance matrix $[R]$ represents the per-unit resistance of the j th conductor due to a current in the i th conductor and is expressed as

$$R_{ij} = \frac{1}{\sigma_i} \frac{\int_{S_i} |J_i|^2 ds}{\left| \left(\int_{S_j} J_j ds \right) \right|^2}. \quad (3.16)$$

Inductance matrix

The per-unit-length inductance $L(f)$ can be derived by examining the energy stored in the inductors used to represent the lines. The magnetic energy stored inside of a conductor is given by

$$U_m = \frac{1}{4} \text{Re} \left\{ \int_{S_T} \vec{J}^* \cdot \vec{A} ds \right\} \quad (3.17)$$

where \vec{A} is the magnetic vector potential. The magnetic energy U_m can also be expressed in terms of mutual and self inductances as

$$U_m = \frac{1}{4} \sum_{i=1}^{N_c} \sum_{j \neq i}^{N_c} L_{ij} I_i I_j \quad (3.18)$$

where L_{ij} is the component of the per-unit-length inductance matrix for a system when only the i th and j th conductors are excited, and I_i and I_j are the amplitudes

of the currents on the respective lines. The case where only the i th conductor is excited yields

$$U_m^{ii} = \frac{1}{4} L_{ii} I_i^2. \quad (3.19)$$

From (3.19) and after expanding (3.18), we get

$$L_{ii} = 4 \frac{U_m^{ii}}{I_i^2} \quad (3.20)$$

$$L_{ij} = 2 \frac{U_m^{ij} - U_m^{ii} - U_m^{jj}}{I_i I_j}. \quad (3.21)$$

3.3.3 Derivation of the surface impedance

From the knowledge of the per-unit length resistance and inductance matrices, a longitudinal surface impedance is defined that relates these quantities to the tangential magnetic field H_y and the tangential electric field E_z . A transverse component of the current also exists, and thus a transverse surface impedance Z_t may be defined as discussed below.

Longitudinal component

The per unit length internal inductance of the strip is computed as

$$L_{in}(f) = L(f) - L_\infty, \quad (3.22)$$

where L_∞ is the per unit length inductance of the strip in the limit $\sigma \rightarrow \infty$, in which case the current flows on the surface of the strip and there is no field penetration. Knowledge of the per unit length strip resistance and internal inductance allows us to express the per unit length voltage drop ΔV along the lossy strip as

$$-\Delta V = [R(f) + j2\pi f L_{in}(f)] I \quad (V/m) \quad (3.23)$$

where I is the total current flowing in the strip.

In order to derive the desirable surface impedance we start with the standard definition for the surface impedance of an imperfect conductor as the ratio of the tangential component of the electric field to the surface current density at the conductor surface

$$E_z(\tau) = Z(\tau)J_{zs}(\tau) = Z(\tau)H_y(\tau), \quad (3.24)$$

where τ is the transverse coordinate along the surface of the conductor. Integrating (3.24) along the side of the strip we have

$$\int_0^W E_z(\tau)d\tau = \int_0^W Z(\tau)H_y(\tau)d\tau, \quad (3.25)$$

where W is the width of the strip. From (3.25) using the mean value theorem for Riemann integration [46] we can write

$$\int_0^W E_z(\tau)d\tau = Z(\tau_0) \int_0^W H_y(\tau)d\tau, \quad (3.26)$$

where $\tau_0 \in [0, W]$. Dividing both sides of (3.26) by W and recognizing the integral on the right-hand side as the total current flowing on the surface we can write

$$\tilde{E}_z = Z(\tau_0) \frac{I}{W}, \quad (3.27)$$

where \tilde{E}_z is the average value of the longitudinal component of the electric field on the strip. Obviously, this value can be thought of as the negative of the per unit length average voltage drop along the strip, in which case (3.23) and (3.27) lead to the relation

$$Z(\tau_0) = W [R(f) + j\omega L_{in}(f)]. \quad (3.28)$$

This is the desirable expression for the surface impedance of the equivalent impedance surface to be used in place of the lossy strip. In what follows, we shall denote this surface impedance as $Z_l(f)$ where the subscript l suggests its relation to

the longitudinal current on the strip.

$$\frac{E_z}{H_y} \equiv Z_l(f). \quad (3.29)$$

Transverse component

For most practical purposes, the dominant part of the conductor loss is due to the longitudinal component of the current, for which an accurate longitudinal surface impedance $Z_l(f)$ has been proposed. However, as the frequency of interest becomes higher and/or the width of the strip increases, the transverse component of the current becomes more significant and needs to be accounted for. This is being done using the standard surface impedance for an infinite resistive plane as

$$-\frac{E_y}{H_z} \equiv Z_t = (1 + j)\frac{1}{\sigma\delta}, \quad (3.30)$$

where σ is the conductivity of the strip and δ the skin depth at the frequency of interest. Even if the width of the strip is finite, use of (3.30) is justified by the fact that the strip is assumed to be infinite in the direction perpendicular to the flow of the transverse component of the current.

3.4 Integral equation formulation

As discussed in Chapter 2, the electric field excited by an electric current source depends upon the surface current density \vec{J} as follows

$$\vec{E}(\vec{r}) = \int \int \int_V \vec{G}^e(\vec{r}/\vec{r}') \cdot \vec{J}(\vec{r}') dv'. \quad (3.31)$$

The above expression satisfies all boundary conditions except the ones on the surface of the strip conductors. For perfectly conducting strips we enforce the Dirichlet condition of vanishing tangential electric field on the surface of the line. This

boundary condition is applied to (2.11), and is satisfied for discrete values of k_z^{MS} corresponding to the dominant and possible higher-order modes, depending on the operating frequency. For the general case of strips with finite thickness and finite conductivity this condition is not applicable anymore. We follow here the alternative, approximate method based on an equivalent representation of the lossy strips by the impedance surfaces derived above.

In planar microstrip problems, the current sources are assumed to have both longitudinal and transverse components which, in turn, implies that only four out of the nine Green's function components need to be considered (G_{yy}, G_{yz}, G_{zy} and G_{zz}). In view of (3.29) and (3.30), equation (3.31) takes the following form on the surface of the strip

$$\vec{E}_t(\vec{r}) = \int \int \int_V \hat{n} \times \vec{G}^e(\vec{r}/\vec{r}') \cdot \vec{J}(\vec{r}') dv' = -\hat{n} \times \vec{\bar{Z}} \cdot (\vec{H} \times \hat{n}) \quad (3.32)$$

where \vec{E}_t represents the transverse electric field and $\vec{\bar{Z}}$ is a dyadic quantity that we call *the dyadic surface impedance* given by

$$\vec{\bar{Z}} = Z_t \hat{y}\hat{y} + Z_l \hat{z}\hat{z}. \quad (3.33)$$

Recognizing the boundary condition for the magnetic field as

$$\hat{n} \times \vec{H} = \vec{J} \quad (3.34)$$

and recalling (2.11), equation (3.32) becomes

$$\int_{C_w} \hat{n} \times \vec{G}^e(x, y/x', y') \cdot \vec{J}(y') dy' - \hat{n} \times \vec{\bar{Z}} \cdot \vec{J}(y) \Big|_{k_z=k_z^{MS}} = 0 \quad (3.35)$$

In a multiconductor system, the above equation can be generalized to a Fredholm integral equation of the second kind

$$\sum_{j=1}^{N_c} \int_{C_{w_j}} \hat{n} \times \vec{G}^{ij}(x, y/x', y') \cdot \vec{J}^j(y') dy' - \hat{n} \times \vec{\bar{Z}}^i \cdot \vec{J}^i(y) = 0 \Big|_{k_z=k_z^{MS}} \quad (3.36)$$

, $i = 1, \dots, N_c$

where \bar{Z}^i is the surface impedance of the i th strip and \tilde{G}^{ij} is the Green's function at the i th strip due to a current \vec{J}^j on the j th strip.

3.5 Application of the Method of Moments

The integral equation (3.36) is solved by the Method of Moments [22]. The cross-section of the strips has been replaced by an infinitesimal impedance surface. Let N_c be the number of conductors and N_b the number of entire domain basis functions that are used to represent the current on the surface of the strip. The total number of elements, N_T , is then given by $N_T = \sum_{i=1}^{N_c} N_b = N_c \times N_b$.

The two-dimensional surface current on the i th strip may be written as

$$\vec{J}^i(y') = J_y^i(y')\hat{y} + J_z^i(y')\hat{z} \quad (3.37)$$

where $J_y^i(y')$ and $J_z^i(y')$ are functions of y' given by

$$\begin{aligned} J_y^i(y') &= \sum_{p=1}^{N_b} I_{yp}^i b_{yp}^i(y') \\ J_z^i(y') &= \sum_{p=1}^{N_b} I_{zp}^i b_{zp}^i(y') \end{aligned} \quad (3.38)$$

and I_{yp}^i, I_{zp}^i are unknown current coefficients. Inserting the expression for $\vec{J}(y)$ from equation (3.38) into equation (3.36) we get

$$\begin{aligned} \sum_{j=1}^{N_c} \sum_{p=1}^{N_b} I_{yp}^j \int_{C_{w_j}} dy' \tilde{G}_{yy}^{ij}(x, y/x', y') b_{yp}^j(y') + \\ I_{zp}^j \int_{C_{w_j}} dy' \tilde{G}_{yz}^{ij}(x, y/x', y') b_{zp}^j(y') &= -Z_t^i \sum_{p=1}^{N_b} I_{yp}^i b_{yp}^i(y) \\ \sum_{j=1}^{N_c} \sum_{p=1}^{N_b} I_{yp}^j \int_{C_{w_j}} dy' \tilde{G}_{zy}^{ij}(x, y/x', y') b_{yp}^j(y') + \\ I_{zp}^j \int_{C_{w_j}} dy' \tilde{G}_{zz}^{ij}(x, y/x', y') b_{zp}^j(y') &= Z_l^i \sum_{p=1}^{N_b} I_{zp}^i b_{zp}^i(y) \\ &, i = 1, \dots, N_c. \end{aligned} \quad (3.39)$$

After applying the weighted averages, the system of equations (3.39) becomes

$$\begin{aligned}
& \sum_{p=1}^{N_b} \sum_{j=1}^{N_c} I_{yp}^j \int_{C_{w_j}} dy' \int_{C_{w_i}} dy \tilde{G}_{yy}^{ij}(x, y/x', y') b_{yp}^j(y') w_{yq}^i(y) \\
& + I_{zp}^j \int_{C_{w_j}} dy' \int_{C_{w_i}} dy \tilde{G}_{yz}^{ij}(x, y/x', y') b_{zp}^j(y') w_{yq}^i(y) \\
& = -Z_t^i \sum_{p=1}^{N_b} I_{yp}^i \int_{C_{w_i}} dy b_{yp}^i(y) w_{yq}^i(y) \\
& \sum_{p=1}^{N_b} \sum_{j=1}^{N_c} I_{yp}^j \int_{C_{w_j}} dy' \int_{C_{w_i}} dy \tilde{G}_{zy}^{ij}(x, y/x', y') b_{yp}^j(y') w_{zq}^i(y) \\
& + I_{zp}^j \int_{C_{w_j}} dy' \int_{C_{w_i}} dy \tilde{G}_{zz}^{ij}(x, y/x', y') b_{zp}^j(y') w_{zq}^i(y) \\
& = Z_l^i \sum_{p=1}^{N_b} I_{zp}^i \int_{C_{w_i}} dy b_{zp}^i(y) w_{zq}^i(y)
\end{aligned}$$

for $i, j = 1, \dots, N_c$ and $p, q = 1, \dots, N_b$. (3.40)

The set of equations (3.40) may be rewritten as

$$\sum_{p=1}^{N_b} \left[Z_t^i I_{yp}^i \mathcal{I}_{pq}^{(5)} + \sum_{j=1}^{N_c} \sum_{m=0}^{\infty} \left(I_{yp}^j \mathcal{I}_p^{(1)} \mathcal{I}_q^{(3)} \mathcal{F}_{yy}(m, x_i, x'_j) + I_{zp}^j \mathcal{I}_p^{(2)} \mathcal{I}_q^{(3)} \mathcal{F}_{yz}(m, x_i, x'_j) \right) \right] = 0 \quad (3.41)$$

$$\sum_{p=1}^{N_b} \left[Z_l^i I_{zp}^i \mathcal{I}_{pq}^{(6)} - \sum_{j=1}^{N_c} \sum_{m=0}^{\infty} \left(I_{yp}^j \mathcal{I}_p^{(1)} \mathcal{I}_q^{(4)} \mathcal{F}_{zy}(m, x_i, x'_j) + I_{zp}^j \mathcal{I}_p^{(2)} \mathcal{I}_q^{(4)} \mathcal{F}_{zz}(m, x_i, x'_j) \right) \right] = 0 \quad (3.42)$$

for $i, j = 1, \dots, N_c$ and $p, q = 1, \dots, N_b$

In the above, the $\mathcal{F}(m, x_i, x'_j)$ are given, according to the notation defined in Chapter 2, by

$$\mathcal{F}_{yy}(m, x_i, x'_j) = j \frac{\delta_m}{b} \frac{1}{k_y^2 + k_z^2} \left[k_y^2 (\eta_c)_a^s \psi_a(x_i) \varphi_a(x'_j) + k_z^2 (\eta_c)_f^s \psi_f(x_i) \varphi_f(x'_j) \right] \quad (3.43)$$

$$\mathcal{F}_{yz}(m, x_i, x'_j) = \frac{\delta_m}{b} \frac{k_y k_z}{(k_y^2 + k_z^2)} \left[-(\eta_c)_a^s \psi_a(x_i) \varphi_a(x'_j) + (\eta_c)_f^s \psi_f(x_i) \varphi_f(x'_j) \right] \quad (3.44)$$

$$\mathcal{F}_{zy}(m, x_i, x'_j) = \frac{\delta_m}{b} \frac{k_y k_z}{(k_y^2 + k_z^2)} \left[(\eta_c)_a^s \psi_a(x_i) \varphi_a(x'_j) - (\eta_c)_f^s \psi_f(x_i) \varphi_f(x'_j) \right] \quad (3.45)$$

$$\mathcal{F}_{zz}(m, x_i, x'_j) = j \frac{\delta_m}{b} \frac{1}{k_y^2 + k_z^2} \left[k_z^2 (\eta_c)_a^s \psi_a(x_i) \varphi_a(x'_j) + k_y^2 (\eta_c)_f^s \psi_f(x_i) \varphi_f(x'_j) \right] \quad (3.46)$$

The terms \mathcal{I}_p 's represent the moments integrals resulting from the application of the method of moments and are dependent on the choice of basis and weighting functions through the following definitions

$$\mathcal{I}_p^{(1)} = \int_{C_{w_j}} dy \cos k_y y b_{yp}^j(y) \quad (3.47)$$

$$\mathcal{I}_p^{(2)} = \int_{C_{w_j}} dy \sin k_y y b_{zp}^j(y) \quad (3.48)$$

$$\mathcal{I}_p^{(3)} = \int_{C_{w_j}} dy \cos k_y y w_{yp}^j(y) \quad (3.49)$$

$$\mathcal{I}_p^{(4)} = \int_{C_{w_j}} dy \sin k_y y w_{zp}^j(y) \quad (3.50)$$

$$\mathcal{I}_{pq}^{(5)} = \int_{C_{w_j}} dy b_{yp}^j(y) w_{yq}^j(y) \quad (3.51)$$

$$\mathcal{I}_{pq}^{(6)} = \int_{C_{w_j}} dy b_{zp}^j(y) w_{zq}^j(y). \quad (3.52)$$

The set of equations (3.40) can be further reduced to a matrix equation of the form

$$[\mathcal{Z}][I] = [0]. \quad (3.53)$$

For the general case of N_c strips on two levels of interconnects, the impedance matrix $[\mathcal{Z}]$ can be represented as a $[2N_b N_c \times 2N_b N_c]$ matrix

$$\begin{bmatrix}
\mathcal{Z}_{yy}^{11} & \mathcal{Z}_{yz}^{11} & \mathcal{Z}_{yy}^{12} & \mathcal{Z}_{yz}^{12} & \dots & \mathcal{Z}_{yy}^{1N_c} & \mathcal{Z}_{yz}^{1N_c} \\
\mathcal{Z}_{yy}^{21} & \mathcal{Z}_{yz}^{21} & & & \dots & \mathcal{Z}_{yy}^{2N_c} & \mathcal{Z}_{yz}^{2N_c} \\
\dots & \dots & & & & & \\
\dots & \dots & & & & & \\
\mathcal{Z}_{yy}^{N_c 1} & \mathcal{Z}_{yz}^{N_c 1} & \dots & \dots & \dots & \mathcal{Z}_{yy}^{N_c N_c} & \mathcal{Z}_{yz}^{N_c N_c} \\
\\
\mathcal{Z}_{zy}^{11} & \mathcal{Z}_{zz}^{11} & \mathcal{Z}_{zy}^{12} & \mathcal{Z}_{zz}^{12} & \dots & \mathcal{Z}_{zy}^{1N_c} & \mathcal{Z}_{zz}^{1N_c} \\
\mathcal{Z}_{zy}^{21} & \mathcal{Z}_{zz}^{21} & & & \dots & \mathcal{Z}_{zy}^{2N_c} & \mathcal{Z}_{zz}^{2N_c} \\
\dots & \dots & & & & & \\
\dots & \dots & & & & & \\
\mathcal{Z}_{zy}^{N_c 1} & \mathcal{Z}_{zz}^{N_c 1} & \dots & \dots & \dots & \mathcal{Z}_{zy}^{N_c N_c} & \mathcal{Z}_{zz}^{N_c N_c}
\end{bmatrix} \quad (3.54)$$

where the individual \mathcal{Z}^{ij} are themselves $N_b \times N_b$ submatrices, whose elements are defined by

$$\mathcal{Z}_{yy}^{ij}(p, q) = \sum_{m=0}^{\infty} \mathcal{I}_p^{(1)} \mathcal{I}_q^{(3)} \mathcal{F}_{yy}(m, x_i, x'_j) + \delta(i, j) Z_t \mathcal{I}_{pq}^{(5)} \quad (3.55)$$

$$\mathcal{Z}_{yz}^{ij}(p, q) = \sum_{m=0}^{\infty} \mathcal{I}_p^{(2)} \mathcal{I}_q^{(3)} \mathcal{F}_{yz}(m, x_i, x'_j) \quad (3.56)$$

$$\mathcal{Z}_{zy}^{ij}(p, q) = \sum_{m=0}^{\infty} \mathcal{I}_p^{(1)} \mathcal{I}_q^{(4)} \mathcal{F}_{zy}(m, x_i, x'_j) \quad (3.57)$$

$$\mathcal{Z}_{zz}^{ij}(p, q) = \sum_{m=0}^{\infty} \mathcal{I}_p^{(2)} \mathcal{I}_q^{(4)} \mathcal{F}_{zz}(m, x_i, x'_j) - \delta(i, j) Z_l \mathcal{I}_{pq}^{(6)} \quad (3.58)$$

where $\delta(i, j)$ is the Kronecker delta,

$$\delta(i, j) = \begin{cases} 1 & , \text{ for } i = j \\ 0 & , \text{ for } i \neq j. \end{cases} \quad (3.59)$$

It is important to choose the basis functions \vec{b} to be as close as possible to the physical current on the strip for numerical efficiency and rapid convergence. If the first few basis functions represent the current reasonably well, the necessary size of the matrix can be kept small for a given accuracy of the solution, so that CPU time is minimized. Therefore, the formulation of \vec{J} should take into account the

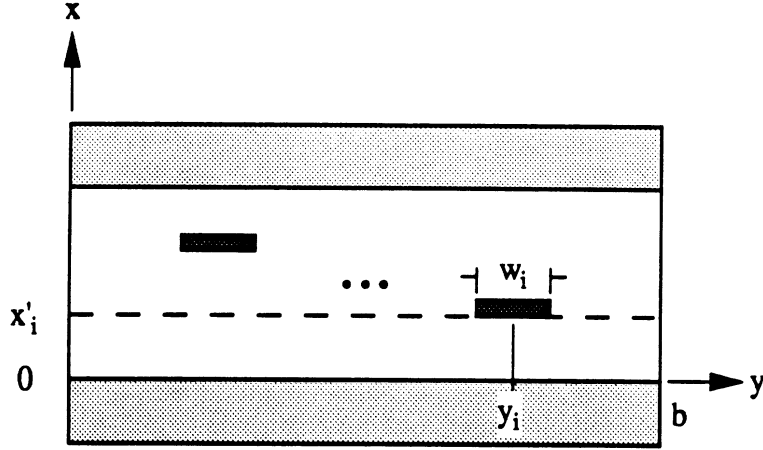


Figure 3.4: Geometry for entire domain basis functions

singularities of the charge distribution at the edges of the strip. In this study, we have investigated the use of entire domain functions to approximate the behavior of the current distribution.

3.5.1 Basis functions expansion

Entire domain basis functions are chosen to approximate the behavior of the current distribution. The longitudinal current is represented by Chebychev polynomials of the first kind T_p multiplied by their respective weighting functions in order to satisfy the edge conditions

$$J_z^i(y') = \sum_{p=1}^{N_b} I_{zp}^i \frac{T_{p-1}\left(\frac{2}{W_i}(y - y_i)\right)}{\sqrt{1 - \left(\frac{2}{W_i}(y - y_i)\right)^2}}. \quad (3.60)$$

with N_b the total number of basis functions, W_i the width of the i th strip and y_i the distance from the origin to the center of the strip as shown in Figure 3.4.

For narrow strips, the zeroth order polynomial T_0 is usually sufficient to describe the variation of the longitudinal current J_z in the transverse direction with good accuracy. Indeed, this variation corresponds to that derived by Maxwell for the

surface charge density distribution on an isolated strip [47]

$$\sigma(y') = \begin{cases} \frac{\sigma_0}{\pi \sqrt{1 - \left(\frac{2}{W_i}(y-y_i)\right)^2}} & , \text{ for } |y - y_i| < \frac{W_i}{2} \\ 0 & , \text{ for } |y - y_i| > \frac{W_i}{2} \end{cases}. \quad (3.61)$$

For the dominant quasi-TEM mode, the transverse current J_y is zero at the center of the strip and is an odd function about the center. The current $I_y(y)$ can be obtained analytically through the use of the continuity equation [48] and has been described in the past by closed-form trigonometric functions [49], [50]. In this work, the transverse current J_y is approximated by Chebychev polynomials of the second kind U_i multiplied by their own weighting function

$$J_y^i(y') = \sum_{p=1}^{N_b} I_{yp}^i U_p \left(\frac{2}{W_i}(y - y_i) \right) \sqrt{1 - \left(\frac{2}{W_i}(y - y_i) \right)^2}. \quad (3.62)$$

The first order ($p = 1$) corresponds to an odd function over the strip which satisfies the edge conditions and approximates accurately the current distribution on the microstrip. Introducing these expressions for the basis functions into equation (3.36) results in closed-form integrals of the form

$$\mathcal{I}_p^{(1)} = \int_{y_i - \frac{W_i}{2}}^{y_i + \frac{W_i}{2}} U_p \left(\frac{2}{W_i}(y - y_i) \right) \sqrt{1 - \left[\frac{2}{W_i}(y - y_i) \right]^2} \cos(k_y y) dy \quad (3.63)$$

$$\mathcal{I}_p^{(2)} = \int_{y_i - \frac{W_i}{2}}^{y_i + \frac{W_i}{2}} \frac{T_{p-1} \left(\frac{2}{W_i}(y - y_i) \right)}{\sqrt{1 - \left[\frac{2}{W_i}(y - y_i) \right]^2}} \sin(k_y y) dy \quad (3.64)$$

that simplify to Bessel functions of integer order as shown in Table 3.1. The derivation of these integrals can be found in Appendix C.

3.5.2 Testing functions

In the choice of appropriate testing functions, care has to be taken to fulfill certain mathematical requirements. The testing functions should be chosen so that the inner products are independent of the excitation. Some additional factors may

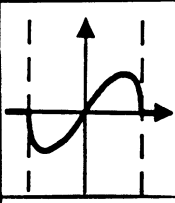
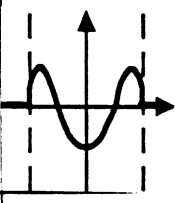
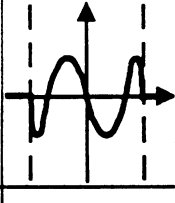
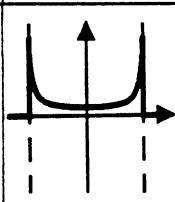
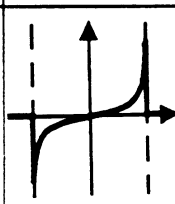
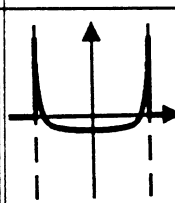
Basis Functions		Moments Integrals		
$J_y(y)$ where $Y = \frac{2}{W}(y - y_i)$				
$b_{yp}(Y)$		$\mathcal{I}_p^{(1)}$		
	$2Y\sqrt{1-Y^2}$ 0	, if $ Y \leq 1$, if $ Y > 1$	$-\frac{2b}{m} J_2(k_y \frac{W}{2}) \sin(k_y y_i)$ 0	, if $m \neq 0$, if $m = 0$
	$(4Y^2 - 1)\sqrt{1-Y^2}$ 0	, if $ Y \leq 1$, if $ Y > 1$	$-\frac{3b}{m} J_3(k_y \frac{W}{2}) \cos(k_y y_i)$ 0	, if $m \neq 0$, if $m = 0$
	$4Y(2Y^2 - 1)\sqrt{1-Y^2}$ 0	, if $ Y \leq 1$, if $ Y > 1$	$\frac{4b}{m} J_4(k_y \frac{W}{2}) \sin(k_y y_i)$ 0	, if $m \neq 0$, if $m = 0$
$J_z(y)$ where $Y = \frac{2}{W}(y - y_i)$				
$b_{zp}(Y)$		$\mathcal{I}_p^{(2)}$		
	$\frac{1}{\sqrt{1-Y^2}}$ 0	, if $ Y \leq 1$, if $ Y > 1$	$\frac{W}{2} \pi J_0(k_y \frac{W}{2}) \sin(k_y y_i)$	
	$\frac{Y}{\sqrt{1-Y^2}}$ 0	, if $ Y \leq 1$, if $ Y > 1$	$\frac{W}{2} \pi J_1(k_y \frac{W}{2}) \cos(k_y y_i)$	
	$\frac{2Y^2-1}{\sqrt{1-Y^2}}$ 0	, if $ Y \leq 1$, if $ Y > 1$	$-\frac{W}{2} \pi J_2(k_y \frac{W}{2}) \sin(k_y y_i)$	

Table 3.1: Chebyshev basis functions and the resulting moments integrals for the first three orders $p = 1, 2, 3$

influence the selection, and in particular the ease of evaluating the inner products: computational considerations require to find closed-form expressions that can be easily implemented numerically. Galerkin's method, which assumes the testing and basis functions to be identical, is applicable to the solution of the integral equation in the case of lossless strips. When adding conductor losses, however, the unknown current appears on both sides of the Fredholm integral equation. The application of weighted averages to the right hand side of (3.39) implies the solution of an additional integral of the type

$$\langle w_{yq}^i, J_y^i(y) \rangle = \sum_p^{N_b} I_{yp}^i \int w_{yq}^i(y) b_{yp}^i(y) \quad , q = 1, \dots, N_b \quad (3.65)$$

$$\langle w_{zq}^i, J_z^i(y) \rangle = \sum_p^{N_b} I_{zp}^i \int w_{zq}^i(y) b_{zp}^i(y) \quad , q = 1, \dots, N_b. \quad (3.66)$$

For the case of Galerkin's procedure, we would choose

$$w_{zq}^i(y) = \frac{T_{q-1} \left(\frac{2}{W_i} (y - y_i) \right)}{\sqrt{1 - \left(\frac{2}{W_i} (y - y_i) \right)^2}} \quad (3.67)$$

which results in undetermined integrals of the form

$$\int_0^\pi \left(\frac{\cos(q+p)\theta}{\sin \theta} + \frac{\cos(q-p)\theta}{\sin \theta} \right) d\theta. \quad (3.68)$$

Another type of testing function was considered

$$w_{zq}^i(y) = T_{q-1} \left(\frac{2}{W_i} (y - y_i) \right) \sqrt{1 - \left(\frac{2}{W_i} (y - y_i) \right)^2} \quad (3.69)$$

which yields closed-form expressions. However, this set of testing functions is zero at the ends of the domain of solution and therefore should be avoided since a finite current cannot be synthesized at the edges with such a choice. In mathematical terms, the residual may be large near the end points and so may be the error in the solution [51]. Using the above guidelines, the following testing functions have been

chosen

$$w_{yq}^i(y) = U_q \left(\frac{2}{W_i} (y - y_i) \right) \quad (3.70)$$

$$w_{zq}^i(y) = T_{q-1} \left(\frac{2}{W_i} (y - y_i) \right). \quad (3.71)$$

This method is a variation of Galerkin's procedure where the testing functions \vec{w}_q differ from the basis functions \vec{b}_p by the Chebychev weighting functions, i.e. $(1 - Y_i^2)^{\frac{1}{2}}$ and $(1 - Y_i^2)^{-\frac{1}{2}}$ for the y and z components, respectively.

The integrals resulting from the weighted averages are given by

$$\mathcal{I}_p^{(3)} = \int_{y_i - \frac{w_i}{2}}^{y_i + \frac{w_i}{2}} U_p \left(\frac{2}{W_i} (y - y_i) \right) \cos(k_y y) dy \quad (3.72)$$

$$\mathcal{I}_p^{(4)} = \int_{y_i - \frac{w_i}{2}}^{y_i + \frac{w_i}{2}} T_{p-1} \left(\frac{2}{W_i} (y - y_i) \right) \sin(k_y y) dy \quad (3.73)$$

and summarized in Table 3.2. These moments integrals result in closed-form expressions involving the family of spherical Bessel functions j_p of p th order and are derived in Appendix C.

Using the testing functions defined in (3.70)-(3.71) the moments integrals introduced by the conductor loss term in (3.65)-(3.66) may be written as

$$\begin{aligned} \mathcal{I}_{pq}^{(5)} &= \int_{y_i - \frac{w_i}{2}}^{y_i + \frac{w_i}{2}} U_p \left(\frac{2}{W_i} (y - y_i) \right) \sqrt{1 - \left[\frac{2}{W_i} (y - y_i) \right]^2} U_q \left(\frac{2}{W_i} (y - y_i) \right) dy \\ &= W_i \begin{cases} \frac{\pi}{4} & , \text{ for } p = q \\ 0 & , \text{ for } p \neq q. \end{cases} \end{aligned} \quad (3.74)$$

$$\begin{aligned} \mathcal{I}_{pq}^{(6)} &= \int_{y_i - \frac{w_i}{2}}^{y_i + \frac{w_i}{2}} \frac{T_{p-1} \left(\frac{2}{W_i} (y - y_i) \right)}{\sqrt{1 - \left[\frac{2}{W_i} (y - y_i) \right]^2}} T_{q-1} \left(\frac{2}{W_i} (y - y_i) \right) dy \\ &= W_i \begin{cases} \frac{\pi}{2} & , \text{ for } p = q = 1 \\ \frac{\pi}{4} & , \text{ for } p = q \neq 1 \\ 0 & , \text{ for } p \neq q \end{cases} \end{aligned} \quad (3.75)$$

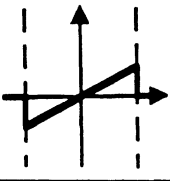
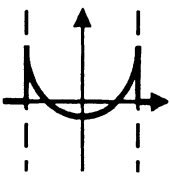
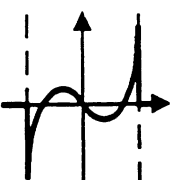
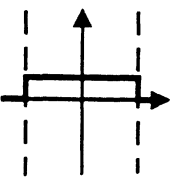
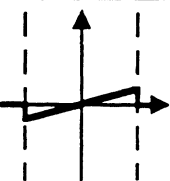
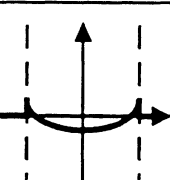
Testing Functions		Moments Integrals	
$J_y(\mathbf{y})$ where $Y = \frac{2}{W}(y - y_i)$			
$w_{yp}(Y)$		$\mathcal{I}_n^{(3)}$	
	$2Y$ 0 , if $ Y \leq 1$, if $ Y \geq 1$	$-2W j_1(k_y \frac{W}{2}) \sin(k_y y_i)$	
	$4Y^2 - 1$ 0 , if $ Y \leq 1$, if $ Y \geq 1$	$\frac{W}{3} \{j_0(k_y \frac{W}{2}) - 8j_2(k_y \frac{W}{2})\} \cos(k_y y_i)$	
	$4Y(2Y^2 - 1)$ 0 , if $ Y \leq 1$, if $ Y \geq 1$	$-\frac{4W}{5} \{j_1(k_y \frac{W}{2}) - 4j_3(k_y \frac{W}{2})\} \sin(k_y y_i)$	
$J_z(\mathbf{y})$ where $Y = \frac{2}{W}(y - y_i)$			
$w_{zp}(Y)$		$\mathcal{I}_n^{(4)}$	
	1 0 , if $ Y \leq 1$, if $ Y \geq 1$	$W j_0(k_y \frac{W}{2}) \sin(k_y y_i)$	
	Y 0 , if $ Y \leq 1$, if $ Y \geq 1$	$W j_1(k_y \frac{W}{2}) \cos(k_y y_i)$	
	$2Y^2 - 1$ 0 , if $ Y \leq 1$, if $ Y \geq 1$	$-\frac{W}{3} \{j_0(k_y \frac{W}{2}) + 4j_2(k_y \frac{W}{2})\} \sin(k_y y_i)$	

Table 3.2: Chebychev testing functions and the resulting moments integrals for the first three orders $p = 1, 2, 3$

3.6 Determination of the propagation characteristics

Using the method of moments solution detailed above, the integral equation (3.36) results in a homogeneous system of simultaneous algebraic equations which can be solved by setting the determinant of the impedance matrix $[\mathcal{Z}]$ equal to zero

$$\text{Det}(\mathcal{Z}) = 0. \quad (3.76)$$

The resulting homogeneous equation is solved for the microstrip propagation constant of the dominant quasi-TEM mode and higher order microstrip modes. In the study of losses, however, interest is focused on the dominant microstrip mode for which the surface impedance \bar{Z} was derived. The above expression (3.76) can be easily programmed on a personal computer to evaluate the roots of the determinant. Expressions for the elements of $[\mathcal{Z}]$ involve a summation over the modes of the inhomogeneously filled waveguide along the y -direction. The number of modes considered is enough to insure convergence as discussed in the next chapter.

3.6.1 Propagation constant

When considering lossy metallic lines or lossy dielectrics, the propagation constant k_z is a complex quantity defined as

$$k_z = -j \gamma_z = \beta - j \alpha \quad (3.77)$$

where β is called the phase constant and α the attenuation constant.

The real part of the propagation constant β is given, in the lossless case, by

$$\beta = \frac{2\pi}{\lambda_g} \quad [\text{rad/meter}] \quad (3.78)$$

where λ_g is the microstrip wavelength. In the lossy case, the phase constant is simply defined as the real part of the propagation constant as described in (3.77).

The imaginary part of the propagation constant α is the sum of an ohmic attenuation factor α_c and a dielectric attenuation factor α_d . Conductor losses are represented through the surface impedance defined in equation (3.33). Dielectric losses are considered by assuming a complex permittivity for each layer as

$$\epsilon_i = \epsilon_{r_i} \epsilon_o (1 - j \tan \delta) \quad (3.79)$$

where the loss tangent $\tan \delta$ is given by

$$\tan \delta = \frac{1}{\omega \epsilon_{r_i} \epsilon_o \rho} \quad (3.80)$$

with ϵ_{r_i} the relative permittivity of layer i and ρ the resistivity of the substrate.

3.6.2 Equivalent current density and field distributions

Once the propagating modes on the lines are found, the current distribution on the strips is derived in a straightforward manner by back-substitution of k_z into $[\mathcal{Z}]$. Since we are solving a two-dimensional problem, there is no source in the excitation vector and therefore the excitation vector $[V] = 0$, and the current vector $[I]$ is of the form

$$\left[[I_y^1], [I_z^1], [I_y^2], [I_z^2], [I_y^3], [I_z^3], \dots, [I_y^{N_c}], [I_z^{N_c}] \right]^T \quad (3.81)$$

where each submatrix $[I_i^j]$ can be decomposed as

$$\left[I_i^j(1), I_i^j(2), I_i^j(3), \dots, I_i^j(N_b) \right]^T. \quad (3.82)$$

From (3.53), the unknown current coefficients can be normalized with respect to one of them, e.g. $I_y^1(1)$. Bringing the first column of (3.53) to the other side of the equality leads to an $N_T \times (N_T - 1)$ overdetermined linear system, which is solved to obtain the normalized current vector $[I_{norm}]$. Using the Golub Householder algorithm

(QR method) [52], we need to solve the following system

$$[\mathcal{Z}'] [I_{norm}] = [b], \quad (3.83)$$

where \mathcal{Z}' is an $N_T \times (N_T-1)$ matrix, b is an $N_T \times 1$ vector, and I_{norm} is the $N_T \times 1$ vector of unknowns which is to be found such that $[\mathcal{Z}'] [I_{norm}]$ is the best approximation to $[b]$. The dispersion analysis provides only the relative amplitude coefficients with respect to each one of them, therefore a value of 1 is set for the normalization factor ($I_y^1(1)$), and the other ones are obtained from (3.83).

Once the propagation constant and the relative amplitude coefficients of the surface current density distributions are known, the field components at any point in the structure can be calculated in a straightforward manner by using (3.31).

3.6.3 Characteristic impedance

Among the parameters of interest in circuit design of high frequency interconnects is the characteristic impedance Z_o . To study the effects of pulse dispersion and losses, it is important to determine the frequency dependence of the characteristic impedance and to define a TEM equivalent in terms of current and voltage at each frequency. In the microwave and millimeter-wave frequency range, the characteristic impedance is not defined uniquely for non-TEM structures such as microstrip lines. This is due to the fact that, at higher frequencies, the longitudinal components of the electric and magnetic field are not negligible, and therefore the conductor voltages and currents cannot be calculated by line integrals in a simple way. For a single microstrip line, several definitions for Z_o are used,

$$Z_o = \frac{V}{I} \quad (3.84)$$

$$Z_o = \frac{|V|^2}{2P^*} \quad (3.85)$$

$$Z_o = \frac{2P}{|I|^2} \quad (3.86)$$

namely the voltage-current, the power-voltage and the power-current definition, respectively. In the above, (*) denotes complex conjugation, P is the total power transferred across the reference transverse plane and I is the total longitudinal current carried by the strip. All these definitions give the same results in the low frequency limit. The power-current relation is particularly well-suited for microstrip problems, whereas the power-voltage definition is preferred for slot problems. It is therefore customary to choose the characteristic impedance definition (3.86) for the microstrip line. For the case of two symmetric coupled lines, the power is split between the two conductors ($P_1 = P_2 = 1/2P$) and therefore the line characteristic impedance is half the one of a single strip $Z_{even,odd} = \frac{P}{|I|^2}$. When considering larger systems of conductors, the power-current definition needs to be extended to account for multiconductor transmission lines.

In a general configuration involving N_c conducting strips over a ground plane or in a shielded environment, there exists N_c modes which combine together to form the actual field around the strips and satisfy all boundary conditions. For multiconductor systems, each mode k is described by its phase velocity and by the total power transported along the system of conductors. This total mode power P_k can be decomposed into partial powers associated with each strip P_{kj} where

$$P_k = \sum_{j=1}^{N_c} P_{kj} \quad (3.87)$$

and

$$P_{kj} = \int \vec{E}_k^{tot} \times \vec{H}_{kj}^* \cdot d\vec{s}. \quad (3.88)$$

In the above, the integral is evaluated over the cross-section of the waveguide with

\vec{E}_k^{tot} the total electric field due to mode k and \vec{H}_{kj} the magnetic field due to the current on strip j for mode k .

Based on (3.86) and (3.88), the partial power characteristic impedance definition was proposed as [53]

$$Z_{kj} = \frac{P_{kj}}{|i_{kj}|^2}, \quad (3.89)$$

where i_{kj} is defined as the surface current on line j for mode k with

$$i_{kj} = \int_{W_j} (J_z)_{kj} dy \quad (3.90)$$

and represents an element of the $N_c \times N_c$ eigencurrent matrix $[I]$. In the same manner, an $N_c \times N_c$ eigenvoltage matrix $[V]$ is introduced with components $V_{kj} = Z_{kj} i_{kj}$.

The formulation of Z_{kj} given in (3.89) is widely used as it seems to give consistent results with measurements [54], but it does not strictly satisfy the necessary reciprocity conditions at higher frequencies [55]. To that end, another definition of the modal characteristic impedance has been proposed which is based on the orthogonality of the eigenvoltage and the eigencurrent vectors of the different modes. The relation is described by

$$V_k^T I_l = P_k \delta_{kl} \quad , \quad \text{for } k, l = 1, 2, \dots, N_c \quad (3.91)$$

where V_k and I_l are the k th and l th column vectors of $[V]$ and $[I]$, respectively. This provides a set of N_c^2 equations that are solved for the new modal characteristic impedances Z_{kj} as a function of the total modal power and the modal currents.

In circuit design, one is generally mostly interested in the total characteristic impedance $[Z_c]$ which includes a superposition of all the modes and is defined as

$$[Z_c] = [V] [I]^{-1}. \quad (3.92)$$

The components of $[Z_c]$ must all have positive values, which is not necessarily the case for the modal characteristic impedances Z_{kj} .

Evaluation

In the evaluation of the partial modal power P_{kj} , integrals of the form

$$\begin{aligned} P_{kj} &= \int \vec{E}_k^{tot} \times \vec{H}_{kj}^* \cdot d\vec{s} \\ &= \int dx \int dy \left[(E_k^{tot})_x (H_{kj})_y^* - (E_k^{tot})_y (H_{kj})_x^* \right] \end{aligned} \quad (3.93)$$

have to be performed over the whole cross-section of the waveguide. The total transverse electric field due to mode k is expressed as

$$E_x^{tot} = \sum_{i=1}^{N_c} (E_{ki})_x \quad (3.94)$$

$$E_y^{tot} = \sum_{i=1}^{N_c} (E_{ki})_y \quad (3.95)$$

and the general formulation of the electric and magnetic fields associated with each mode k is given by

$$(E_{kj})_x = \int_{W_j} dy' \left[\widetilde{G}_{xy}^{e kj}(x, y/x'_j, y') J_y^j(y') + \widetilde{G}_{xz}^{e kj}(x, y/x'_j, y') J_z^j(y') \right] \quad (3.96)$$

$$(E_{kj})_y = \int_{W_j} dy' \left[\widetilde{G}_{yy}^{e kj}(x, y/x'_j, y') J_y^j(y') + \widetilde{G}_{yz}^{e kj}(x, y/x'_j, y') J_z^j(y') \right] \quad (3.97)$$

$$(H_{kj})_x = \int_{W_j} dy' \left[\widetilde{G}_{xy}^{h kj}(x, y/x'_j, y') J_y^j(y') + \widetilde{G}_{xz}^{h kj}(x, y/x'_j, y') J_z^j(y') \right] \quad (3.98)$$

$$(H_{kj})_y = \int_{W_j} dy' \left[\widetilde{G}_{yy}^{h kj}(x, y/x'_j, y') J_y^j(y') + \widetilde{G}_{yz}^{h kj}(x, y/x'_j, y') J_z^j(y') \right] \quad (3.99)$$

In each dielectric layer r , the electromagnetic fields may be written as

$$(E_{kj})_x = -\frac{1}{\omega \epsilon_r} \sum_{m=0}^{\infty} \frac{\delta_m}{b} \frac{1}{\mathcal{D}_r^a} \sin k_y y \left[j k_y C_y^{kj} - k_z C_z^{kj} \right] \zeta^a(x) \varphi^a(x'_j) \quad (3.100)$$

$$\begin{aligned} (E_{kj})_y &= \sum_{m=0}^{\infty} \frac{\delta_m}{b} \frac{1}{k_y^2 + k_z^2} \cos k_y y \\ &\left\{ \left(\frac{k_{xr}}{\omega \epsilon_r} \right) \frac{1}{\mathcal{D}_r^a} \left[j k_y^2 C_y^{kj} - k_y k_z C_z^{kj} \right] \psi^a(x) \varphi^a(x'_j) \right. \\ &\left. + \left(\frac{\omega \mu_r}{k_{xr}} \right) \frac{1}{\mathcal{D}_r^f} \left[j k_z^2 C_y^{kj} + k_y k_z C_z^{kj} \right] \psi^f(x) \varphi^f(x'_j) \right\} \end{aligned} \quad (3.101)$$

and

$$(H_{kj})_x = - \sum_{m=0}^{\infty} \frac{\delta_m}{b} \frac{1}{D_r^f k_{xr}} \cos k_y y \left[j k_z C_y^{kj} + k_y C_z^{kj} \right] \psi^f(x) \varphi^f(x'_j) \quad (3.102)$$

$$(H_{kj})_x = \sum_{m=0}^{\infty} \frac{\delta_m}{b} \frac{1}{k_y^2 + k_z^2} \sin k_y y \left\{ \left(\frac{k_{xr}}{\omega \epsilon_r} \right) \frac{1}{D_r^a} \left[-j k_y k_z C_y^{kj} + k_z^2 C_z^{kj} \right] \varsigma^a(x) \varphi^a(x'_j) + \left(\frac{\omega \mu_r}{k_{xr}} \right) \frac{1}{D_r^f} \left[j k_y k_z C_y^{kj} + k_y^2 C_z^{kj} \right] \varsigma^f(x) \varphi^f(x'_j) \right\} \quad (3.103)$$

where $\psi^{a,f}$, $\varphi^{a,f}$ and $\varsigma^{a,f}$ are defined in Appendix A for each layer. In the above, the y' dependence is incorporated in the modal coefficients C^{kj} resulting from the method of moments solution

$$C_y^{kj}(m) = \sum_{p=1}^{N_b} I_y^{kj}(p) \mathcal{I}_{pj}^{(1)}(m) \quad (3.104)$$

$$C_z^{kj}(m) = \sum_{p=1}^{N_b} I_z^{kj}(p) \mathcal{I}_{pj}^{(2)}(m) \quad (3.105)$$

where I^{kj} are the current coefficients on line j for the mode k . Also $\mathcal{I}_{pj}^{(1)}$ and $\mathcal{I}_{pj}^{(2)}$ given by (3.47)-(3.52) are the moments integrals and depend on the choice of the current expansion functions.

The modal power (3.93) is evaluated analytically by integrating the Poynting vector over the waveguide cross-section and may be decomposed into two terms as follows

$$\begin{aligned} \mathcal{P}_1 &= \int_r (E_{ki})_x (H_{kj})_y^*(r) dx \\ &= -\frac{1}{\omega \epsilon_r} \sum_{m=0}^{\infty} \left(\frac{\delta_m}{b} \right) \left(\frac{1}{k_y^2 + k_z^2} \right)^* \frac{1}{D_r^a} \\ &\quad \int_r dx \left\{ \left[j k_y C_y^{ki} - k_z C_z^{ki} \right] \varsigma^a(x) \varphi^a(x'_i) \right\} \\ &\quad \left\{ \left(\frac{k_{xr}}{\omega \epsilon_r} \right) \frac{1}{D_r^a} \left[-j k_y k_z C_y^{kj} + k_z^2 C_z^{kj} \right] \varsigma^a(x) \varphi^a(x'_j) \right. \\ &\quad \left. + \left(\frac{\omega \mu_r}{k_{xr}} \right) \frac{1}{D_r^f} \left[j k_y k_z C_y^{kj} + k_y^2 C_z^{kj} \right] \varsigma^f(x) \varphi^f(x'_j) \right\}^* \end{aligned} \quad (3.106)$$

$$\begin{aligned}
\mathcal{P}_2 &= \int_r (E_{ki})_y (H_{kj})_x^*(r) dx \\
&= - \sum_{m=0}^{\infty} \left(\frac{\delta_m}{b} \right) \frac{1}{k_y^2 + k_z^2} \left(\frac{1}{\mathcal{D}_r^f} \frac{1}{k_{xr}} \right)^* \\
&\quad \int_r dx \left\{ \left(\frac{k_{xr}}{\omega \epsilon_r} \right) \frac{1}{\mathcal{D}_r^a} [j k_y^2 C_y^{ki} - k_y k_z C_z^{ki}] \psi^a(x) \varphi^a(x'_i) \right. \\
&\quad \left. + \left(\frac{\omega \mu_r}{k_{xr}} \right) \frac{1}{\mathcal{D}_r^f} [j k_z^2 C_y^{ki} + k_y k_z C_z^{ki}] \psi^f(x) \varphi^f(x'_i) \right\} \\
&\quad \left\{ [j k_z C_y^{kj} + k_y C_z^{kj}] \psi^f(x) \varphi^f(x'_j) \right\}^* . \tag{3.107}
\end{aligned}$$

In the above, orthogonality has been used to simplify the integration over the y direction as

$$\int_0^b dy \cos \frac{m\pi}{b} y \cos \frac{n\pi}{b} y = \begin{cases} b & , \text{for } m = n = 0 \\ \frac{b}{2} & , \text{for } m = n \neq 0 \\ 0 & , \text{for } m \neq n \end{cases} \tag{3.108}$$

and

$$\int_0^b dy \sin \frac{m\pi}{b} y \sin \frac{n\pi}{b} y = \begin{cases} \frac{b}{2} & , \text{for } m = n \neq 0 \\ 0 & , \text{for } m \neq n \end{cases} \tag{3.109}$$

The integration over the x direction is more involved and requires the evaluation of complex-valued functions of the real variable x . For all layers except the source layer, the electric and magnetic field components E_x and H_y (E_y and H_x) associated with lines i and j have the same x dependence. The integration over layer r involves the following integrals

$$\int_r dx \zeta^{a,f}(x) (\zeta^{a,f}(x))^* = \int_r dx |\zeta^{a,f}(x)|^2 \tag{3.110}$$

$$\int_r dx \psi^{a,f}(x) (\psi^{a,f}(x))^* = \int_r dx |\psi^{a,f}(x)|^2 \tag{3.111}$$

where

$$|\zeta^{a,f}(x)|^2 = \begin{cases} \left| \cos k_{xr} \left(x - h - \sum_{l=1}^r h_l \right) - j \tilde{\eta}_r^{a,f} \sin k_{xr} \left(x - h - \sum_{l=1}^r h_l \right) \right|^2, & x \geq h \\ \left| \cos k_{xr} \left(x + \sum_{l=1}^r h_l \right) - j \tilde{\eta}_r^{a,f} \sin k_{xr} \left(x + \sum_{l=1}^r h_l \right) \right|^2, & x \leq 0 \end{cases}$$

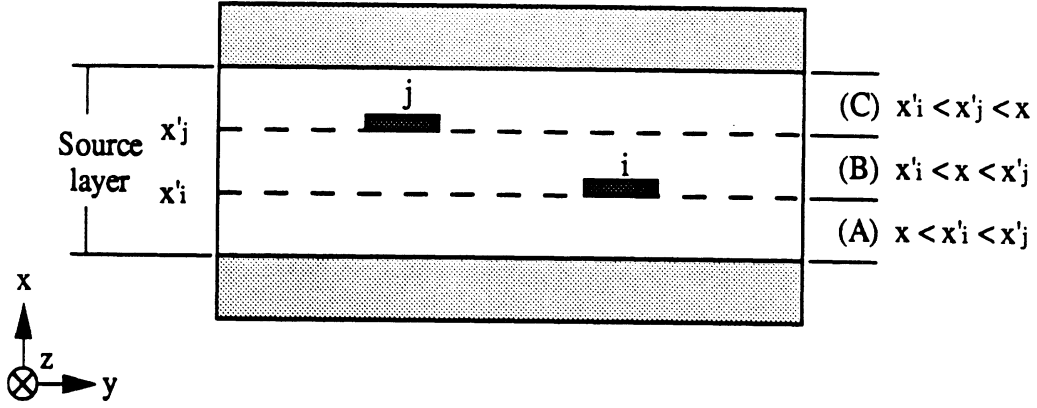


Figure 3.5: Multilevel lines in the source region

$$|\psi^{a,f}(x)|^2 = \begin{cases} \left| \sin k_{xr} \left(x - h - \sum_{l=1}^r h_l \right) + j \tilde{\eta}_r^{a,f} \cos k_{xr} \left(x - h - \sum_{l=1}^r h_l \right) \right|^2, & x \geq h \\ \left| \sin k_{xr} \left(x + \sum_{l=1}^r h_l \right) + j \tilde{\eta}_r^{a,f} \cos k_{xr} \left(x + \sum_{l=1}^r h_l \right) \right|^2, & x \leq 0. \end{cases} \quad (3.112)$$

The integrals (3.110)-(3.111) are derived in Appendix B and yield

$$\begin{aligned} \int_r dx |\zeta^{a,f}(x)|^2 &= \frac{\{(1 + \tilde{\eta}_r \tilde{\eta}_r^*) \sinh 2\Im(k_{xr}) h_r \mp (\tilde{\eta}_r + \tilde{\eta}_r^*) (\cosh 2\Im(k_{xr}) h_r - 1)\}}{4\Im(k_{xr})} \\ &+ \frac{\{(1 - \tilde{\eta}_r \tilde{\eta}_r^*) \sin 2\Re(k_{xr}) h_r \mp j (\tilde{\eta}_r - \tilde{\eta}_r^*) (\cos 2\Re(k_{xr}) h_r - 1)\}}{4\Re(k_{xr})} \\ \int_r dx |\psi^{a,f}(x)|^2 &= \frac{\{(1 + \tilde{\eta}_r \tilde{\eta}_r^*) \sinh 2\Im(k_{xr}) h_r \mp (\tilde{\eta}_r + \tilde{\eta}_r^*) (\cosh 2\Im(k_{xr}) h_r - 1)\}}{4\Im(k_{xr})} \\ &- \frac{\{(1 - \tilde{\eta}_r \tilde{\eta}_r^*) \sin 2\Re(k_{xr}) h_r \mp j (\tilde{\eta}_r - \tilde{\eta}_r^*) (\cos 2\Re(k_{xr}) h_r - 1)\}}{4\Re(k_{xr})} \end{aligned}$$

where $\Re(k_{xr})$ and $\Im(k_{xr})$ represent the real and imaginary part of the wave number k_{xr} , respectively. In the source layer, the expressions for the x -integrals depend on the vertical position of line j with respect to i . Let line j be at $x = x'_j$ and line i at $x = x'_i$, with $x'_j > x'_i$ as shown in Figure 3.5. We can define three distinct regions : (A) $x'_j > x'_i > x$, (B) $x'_j > x > x'_i$ and (C) $x > x'_j > x'_i$. The x dependence in the

different regions is given by,

$$\begin{aligned}
(A)_{ij}^{\zeta} &= \left\{ \cos k_x x - j \tilde{\eta}_l^{a,f} \sin k_x x \right\} \left\{ \cos k_x x - j \tilde{\eta}_l^{a,f} \sin k_x x \right\}^* \\
(B)_{ij}^{\zeta} &= \left\{ \cos k_x x - j \tilde{\eta}_l^{a,f} \sin k_x x \right\} \left\{ \cos k_x (x - h) - j \tilde{\eta}_u^{a,f} \sin k_x (x - h) \right\}^* \\
(C)_{ij}^{\zeta} &= \left\{ \cos k_x (x - h) - j \tilde{\eta}_u^{a,f} \sin k_x (x - h) \right\} \left\{ \cos k_x (x - h) - j \tilde{\eta}_u^{a,f} \sin k_x (x - h) \right\}^*
\end{aligned} \tag{3.113}$$

for \mathcal{P}_1 , and

$$\begin{aligned}
(A)_{ij}^{\psi} &= \left\{ \sin k_x x + j \tilde{\eta}_l^{a,f} \cos k_x x \right\} \left\{ \sin k_x x + j \tilde{\eta}_l^{a,f} \cos k_x x \right\}^* \\
(B)_{ij}^{\psi} &= \left\{ \sin k_x x + j \tilde{\eta}_l^{a,f} \cos k_x x \right\} \left\{ \sin k_x (x - h) + j \tilde{\eta}_u^{a,f} \cos k_x (x - h) \right\}^* \\
(C)_{ij}^{\psi} &= \left\{ \sin k_x (x - h) + j \tilde{\eta}_u^{a,f} \cos k_x (x - h) \right\} \left\{ \sin k_x (x - h) + j \tilde{\eta}_u^{a,f} \cos k_x (x - h) \right\}^*
\end{aligned} \tag{3.114}$$

for \mathcal{P}_2 . The integration over the source layer becomes

$$\int_0^{x'_i} (A)_{ij} dx + \int_{x'_i}^{x'_j} (B)_{ij} dx + \int_{x'_j}^h (C)_{ij} dx, \tag{3.115}$$

where

$$\begin{aligned}
&\int_0^{x'_i} (A)_{ij}^{\zeta} dx = \\
&= \frac{1}{4\Im(k_x)} \left\{ (1 + \tilde{\eta}_l \tilde{\eta}_l^*) \sinh 2\Im(k_x) x'_i + (\tilde{\eta}_l + \tilde{\eta}_l^*) (\cosh 2\Im(k_x) x'_i - 1) \right\} \\
&+ \frac{1}{4\Re(k_x)} \left\{ (1 - \tilde{\eta}_l \tilde{\eta}_l^*) \sin 2\Re(k_x) x'_i + j (\tilde{\eta}_l - \tilde{\eta}_l^*) (\cos 2\Re(k_x) x'_i - 1) \right\} \\
&\int_{x'_i}^{x'_j} (B)_{ij}^{\zeta} dx = \\
&= \frac{1}{4\Im(k_x)} \left\{ \sinh 2\Im(k_x) \Big|_{x'_i}^{x'_j} [\cos^* k_x h (1 + \tilde{\eta}_u \tilde{\eta}_l^*) - j \sin^* k_x h (\tilde{\eta}_u + \tilde{\eta}_l^*)] \right. \\
&\quad \left. + \cosh 2\Im(k_x) \Big|_{x'_i}^{x'_j} [\cos^* k_x h (\tilde{\eta}_u + \tilde{\eta}_l^*) - j \sin^* k_x h (1 + \tilde{\eta}_u \tilde{\eta}_l^*)] \right\} \\
&+ \frac{1}{4\Re(k_x)} \left\{ \sin 2\Re(k_x) \Big|_{x'_i}^{x'_j} [\cos^* k_x h (1 - \tilde{\eta}_u \tilde{\eta}_l^*) + j \sin^* k_x h (\tilde{\eta}_u - \tilde{\eta}_l^*)] \right. \\
&\quad \left. + \cos 2\Re(k_x) \Big|_{x'_i}^{x'_j} [-\sin^* k_x h (1 - \tilde{\eta}_u \tilde{\eta}_l^*) + j \cos^* k_x h (\tilde{\eta}_u - \tilde{\eta}_l^*)] \right\}
\end{aligned}$$

$$\begin{aligned}
& \int_{x'_j}^h (C)^\zeta dx = \\
&= \frac{1}{4\Im(k_x)} \left\{ (1 + \tilde{\eta}_u \tilde{\eta}_u^*) \sinh 2\Im(k_x)|_{x'_j}^h - (\tilde{\eta}_u + \tilde{\eta}_u^*) \cosh 2\Im(k_x)|_{x'_j}^h \right\} \\
&+ \frac{1}{4\Re(k_x)} \left\{ (1 - \tilde{\eta}_u \tilde{\eta}_u^*) \sin 2\Re(k_x)|_{x'_j}^h - j (\tilde{\eta}_u - \tilde{\eta}_u^*) \cos 2\Re(k_x)|_{x'_j}^h \right\} \quad (3.116)
\end{aligned}$$

for \mathcal{P}_1 , and

$$\begin{aligned}
& \int_0^{x'_i} (A)^\psi dx = \\
&= \frac{1}{4\Im(k_x)} \left\{ (1 + \tilde{\eta}_l \tilde{\eta}_l^*) \sinh 2\Im(k_x)x'_i + (\tilde{\eta}_l + \tilde{\eta}_l^*) (\cosh 2\Im(k_x)x'_i - 1) \right\} \\
&- \frac{1}{4\Re(k_x)} \left\{ (1 - \tilde{\eta}_l \tilde{\eta}_l^*) \sin 2\Re(k_x)x'_i - j (\tilde{\eta}_l - \tilde{\eta}_l^*) (\cos 2\Re(k_x)x'_i - 1) \right\}
\end{aligned}$$

$$\begin{aligned}
& \int_{x'_i}^{x'_j} (B)^\psi dx = \\
&= \frac{1}{4\Im(k_x)} \left\{ \sinh 2\Im(k_x)|_{x'_i}^{x'_j} [\cos^* k_x h (1 + \tilde{\eta}_u \tilde{\eta}_l^*) - j \sin^* k_x h (\tilde{\eta}_u + \tilde{\eta}_l^*)] \right. \\
&\quad \left. + \cosh 2\Im(k_x)|_{x'_i}^{x'_j} [\cos^* k_x h (\tilde{\eta}_u + \tilde{\eta}_l^*) - j \sin^* k_x h (1 + \tilde{\eta}_u \tilde{\eta}_l^*)] \right\} \\
&- \frac{1}{4\Re(k_x)} \left\{ \sin 2\Re(k_x)|_{x'_i}^{x'_j} [\cos^* k_x h (1 - \tilde{\eta}_u \tilde{\eta}_l^*) + j \sin^* k_x h (\tilde{\eta}_u - \tilde{\eta}_l^*)] \right. \\
&\quad \left. + \cos 2\Re(k_x)|_{x'_i}^{x'_j} [\sin^* k_x h (1 + \tilde{\eta}_u \tilde{\eta}_l^*) + j \cos^* k_x h (\tilde{\eta}_u - \tilde{\eta}_l^*)] \right\}
\end{aligned}$$

$$\begin{aligned}
& \int_{x'_j}^h (C)^\psi dx = \\
&= \frac{1}{4\Im(k_x)} \left\{ (1 + \tilde{\eta}_u \tilde{\eta}_u^*) \sinh 2\Im(k_x)|_{x'_j}^h - (\tilde{\eta}_u + \tilde{\eta}_u^*) \cosh 2\Im(k_x)|_{x'_j}^h \right\} \\
&+ \frac{1}{4\Re(k_x)} \left\{ (1 - \tilde{\eta}_u \tilde{\eta}_u^*) \sin 2\Re(k_x)|_{x'_j}^h - j (\tilde{\eta}_u - \tilde{\eta}_u^*) \cos 2\Re(k_x)|_{x'_j}^h \right\} \quad (3.117)
\end{aligned}$$

for \mathcal{P}_2 .

For edge-coupled lines, the sources are on the same planar level $x'_i = x'_j$, and therefore the integral of region (B) disappears. In the case of broadside-coupled lines, $x'_i = 0$ and $x'_j = h$, and therefore integrals of (A) and (C) are not needed. Note

that the following relations apply

$$(A)_{ij} = (A)_{ji} \quad (3.118)$$

$$(B)_{ij} = (B)_{ji}^* \quad (3.119)$$

$$(C)_{ij} = (C)_{ji} \quad (3.120)$$

Once the partial modal power P_{jk} is computed, the characteristic impedance is found through the use of (3.89) or (3.91).

3.7 Time domain analysis

As the speeds of signals on modern VLSI interconnections increase, with projected rise times $< 50ps$, the need arises for quantifying the effects of dispersion on overall pulse degradation. Such dispersion effects are of great importance in cross-talk phenomena, since the amount of cross-talk in a symmetric coupled microstrip depends on the difference between the frequency-dependent propagation constants of the even and odd modes of the line. Moreover, as we are moving toward higher device densities, with the interconnection cross-sectional dimensions shrinking to values of a few microns, conductor losses are becoming an important factor. Naturally, questions have been raised about the effect of the longitudinal component of the electric field inside the lossy conductor on the field distribution of the fundamental microstrip mode, especially for the case of very thin conductors with high current densities. Furthermore, due to faster rise-times and clock-frequencies, these losses exhibit a frequency-dependence which, in addition to attenuating the propagation pulses, cause further degradation to their rise and fall times.

While the effect of conductor losses to the frequency-dependence of the propagation and attenuation constant as well as the characteristic impedance of single

microstrip has been studied extensively [36], very little is available on their influence on cross-talk effects in coupled microstrip interconnections. In this section, the full-wave analysis presented above is used for the parametric study of such effects.

3.7.1 Theory

In order to implement the frequency-domain analysis presented above for the study of pulse propagation, cross-talk, and dispersion effects on VLSI interconnections, the equivalent circuit model for the terminated hybrid-mode multiconductor transmission lines presented in [56] is used.

For a given frequency ω , the total voltages and currents at any point z on a multiconductor transmission line can be written as

$$[I] \{i\} = \{i_T\} \quad (3.121)$$

$$[V] \{v\} = \{v_T\} \quad (3.122)$$

where $[I]$ is an $N_c \times N_c$ matrix with columns the N_c eigencurrents corresponding to the N_c eigenmodes of the line, $[V]$ is an $N_c \times N_c$ matrix with elements $i_{kj}Z_{kj}$ (row k , column j) with Z_{kj} as defined in (3.89), $\{i_T\}$ and $\{v_T\}$ are N_c -dimensional column vectors with elements the total currents and voltages on the lines at point z , respectively. In the above, $\{v\}$ and $\{i\}$ are N_c -dimensional column vectors with elements that are dependent on the spatial position. For the case of semi-infinite lines, these are given by

$$v_j = a_j \exp(-\gamma_j z) \quad (3.123)$$

$$i_j = a_j \exp(-\gamma_j z). \quad (3.124)$$

For terminated lines, the analysis uses a model consisting of uncoupled lines with

unit characteristic impedance and elements of the form

$$v_j = a_j^{(+)} \exp(-\gamma_j z) + a_j^{(-)} \exp(+\gamma_j z) \quad (3.125)$$

$$i_j = a_j^{(+)} \exp(-\gamma_j z) - a_j^{(-)} \exp(+\gamma_j z) \quad (3.126)$$

where $j = 1, 2, \dots, N_c$ and γ_j is the propagation constant for mode j calculated using the full-wave analysis described previously. The coefficients $a_j^{(+)}$, $a_j^{(-)}$, $j = 1, 2, \dots, N_c$ are found by applying the boundary conditions for the total voltages and currents at the terminating networks, i.e. at the ends of the lines $z = 0$ and $z = l$. The uncoupled lines are then coupled at the input and output ends of the lines by (3.121).

The waveform simulation procedure involves the solution of the above system of equations for a set of discrete frequencies dictated by the characteristics of the exciting signal. The excitation is at $z = 0$ of line 1, and may be either a pulse or a sine wave. Pulse functions are usually treated as trapezoidal functions with finite rise and fall-times. For each of these frequencies, the frequency-dependent propagation constants and characteristic modal impedances needed for the solution are obtained using the frequency-domain method described in the previous sections. Finally, with the restriction of linear terminating networks, the frequency-domain data are converted to the time domain via standard inverse Fourier transform procedures.

CHAPTER IV

MICROSTRIP LINES: NUMERICAL CONSIDERATIONS AND RESULTS

The need to increase the speed of analog and digital circuits has led to advances in the design and use of interconnects operating in the millimeter-wave range. This, in turn, requires the understanding of signal propagation in microstrip transmission lines at these frequencies. The study of broad-bandwidth waveform propagation in microstrip transmission lines is of importance to understand signal distortion which is attributed to two factors, namely the frequency-dependent phase velocity due to modal dispersion, and the frequency-dependent attenuation due to the skin-effect in the conductors. The theory developed in the previous chapter incorporates both mechanisms of dispersion and losses.

The present chapter is organized into two main parts. First, the numerical implementation of the full-wave method of Chapter 3 is addressed. A practical algorithm is implemented to calculate the propagation characteristics of microstrip lines. Convergence requirements are discussed and a description of the impedance matrix is further detailed. In the second part, the effects of modal dispersion, dielectric properties of the substrate and frequency dependence of the conductors are analyzed for single and multiple coupled microstrip lines as a function of geometry and the oper-

ating frequency. Finally, using these frequency-dependent results, the effects of pulse dispersion are illustrated.

4.1 Numerical considerations

4.1.1 Algorithm

Based on the theory derived in the previous chapter, a FORTRAN 77 computer program has been developed to calculate the propagation characteristics of lossy microstrip lines, and the algorithm used is summarized here. The code consists of three separate modules: input, processing and output. The geometry of the two-dimensional structure is read into the program from either the screen or an input file. Several computational parameters and conditional flags are also inputted from this file. Following the calculations, results are printed on the screen and stored in an output file as well.

The processing module can be subdivided in three parts: the search of the roots corresponding to the complex propagation constant of the modes, the calculation of the current distribution on the strips and the computation of the characteristic impedance of the lines. Once the lossy root $k_z = \beta - j\alpha$ is determined, the current distribution and the characteristic impedance of each strip are found in a straightforward manner as described in Chapter 3. Therefore only the root searching process is detailed here.

4.1.2 Determination of the propagation constant

The knowledge of the propagation constant k_z is needed for the computation of the current distribution, the characteristic impedance and the field distribution. Therefore the accuracy of the key transmission line parameters depends directly on

the precision of k_z . The search routine for finding the roots of $Det(k_z) = 0$ is two-fold. First, the propagating modes are found for the lossless structure, and then, the values are used as initial approximations for determining the roots when ohmic and dielectric losses are added.

The lossless case amounts to determining the real roots β of the nonlinear equation $Det(\beta) = 0$. To that end, the determinant is computed for successive values of k_z within an interval (k_{z0}, k_{z1}) where the lower and upper bounds k_{z0} and k_{z1} , and the increment Δ are provided as input parameters. Since the problem consists of finding the propagation constant in a shielded waveguide, the normalized phase constant may vary between $k_{z0} = 0$ and $k_{z1} = \sqrt{\epsilon_r}$, where ϵ_r is the permittivity of the substrate. In a first step, the roots are located roughly to within the accuracy of the interval Δ by checking for the condition $Det(\beta).Det(\beta + \Delta) < 0$. Then, these roots are used as initial guesses to determine the roots with a more rapidly convergent method. Rather than using recursive methods, such as the bisection method [52], which are slowly converging, we can attain significantly faster convergence using more refined methods, such as the Muller's method with deflation, which require initial approximations close to the desired root. Muller's algorithm was chosen because it can be applied to solve both real and complex zeros of an analytic complex function, and thus allows the characterization of both lossless and lossy structures.

Next, dissipative losses are incorporated in the formulation by assuming metallic lines with finite conductivity and dielectric layers with complex permittivity. Using Muller's algorithm with deflation, the IMSL routine ZANLYT calculates the complex zeros of the analytic complex function $Det(k_z)$ with the lossless roots as initial guesses. The attenuation constant α is found as the imaginary part of the resulting root by solving (3.76). In the case of large losses, (such as $\tan\delta = 1$), an iterative

procedure is followed. First, the roots are found for the lossless case (such as $\tan\delta = 0.001$) and these roots are then used as initial guess for the next iteration ($\tan\delta = 0.01$). The iteration cycle is repeated until the loss value ($\tan\delta = 1$) is reached. This method proved to be a rather sensitive function of the initial guesses, therefore it is crucial to verify the stability of the final results.

Variation of the determinant

In the lossless case, the matrix elements of the impedance matrix $[\mathcal{Z}]$ become either purely real ($\mathcal{Z}_{yz}, \mathcal{Z}_{zy}$) or imaginary ($\mathcal{Z}_{yy}, \mathcal{Z}_{zz}$) for real phase constants β . The inversion of the $[\mathcal{Z}]$ matrix and the calculation of its determinant are computed by NAAS routines for complex matrices. The zeros of the corresponding real determinant indicate the existence of propagating modes.

The variation of the determinant is dependent upon the geometrical parameters of the structure and the operating frequency. Figure 4.1 illustrates the behavior of the determinant of a typical microstrip on a dielectric substrate as a function of β . In this example, only the dominant quasi-TEM mode propagates with a phase constant of $2.45 k_0$ at an operating frequency of 5 GHz. When the operating frequency extends into the millimeter-wave region, the circuit package becomes electrically large enough to allow package resonances. The existence of higher order modes results into multiple roots of the determinant as illustrated in Figure 4.1 b) where the dominant and three higher order modes propagate at 20 GHz. Also, above the cut-off frequency of the waveguide, the determinant exhibits poles corresponding to the propagation constants of the LSE and LSM modes of the dielectrically-loaded guide. The poles result in a change of sign of the determinant but are ignored in the computer program since they do not represent a propagating mode on the microstrip line.

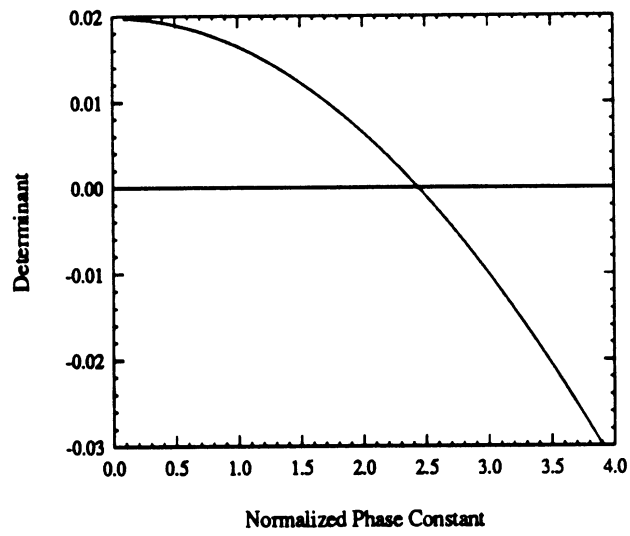
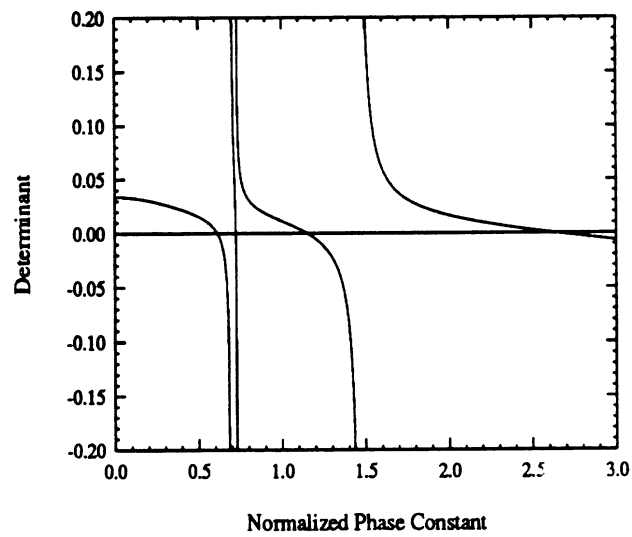
a. $f = 5$ GHzb. $f = 20$ GHz

Figure 4.1: Variation of the determinant versus β for a single strip ($a = b = 12.7$ mm, $w = 0.635$ mm, $h = 1.27$ mm, $\epsilon_r = 8.875$)

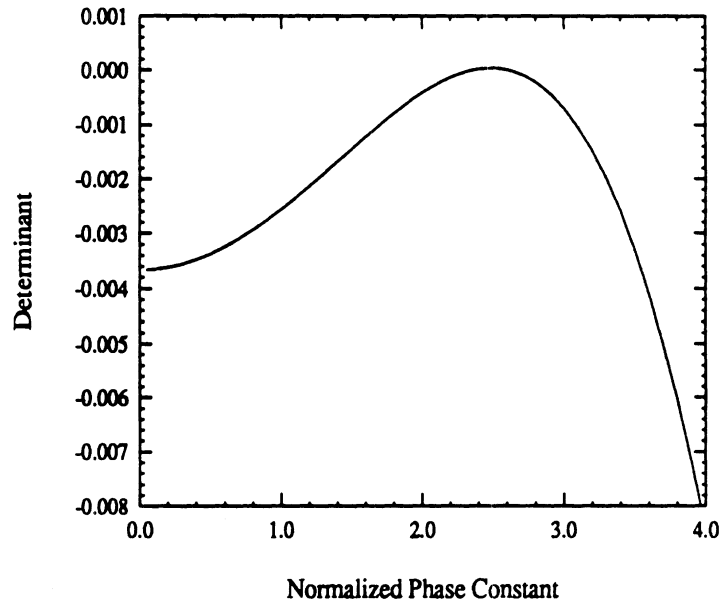


Figure 4.2: Variation of the determinant versus β for edge-coupled strips ($a = b = 12.7$ mm, $w_1 = w_2 = h = 1.27$ mm, $s = 1.27$ mm, $\epsilon_r = 8.875$, $f = 5$ GHz)

Another case where more than one zero crossing of the determinant occurs is for an N-dimensional conductor system which results in N dominant degenerate modes. Figure 4.2 shows the behavior of the determinant for two edge-coupled microstrip lines at an operating frequency of 5 GHz. The determinant is a smooth function of β where the roots correspond to the dominant quasi-TEM even and odd microstrip modes.

Impedance matrix elements

To derive the propagation constant we must first compute the elements of the impedance matrix \mathcal{Z}_{qp} . The formulation for these elements, given in Chapter 3, are put in a form more convenient for programming below. This is important because 70% of the computation time is spent on evaluating the elements of the matrix

\mathcal{Z} . The components \mathcal{Z}_{yy} , \mathcal{Z}_{yz} , \mathcal{Z}_{zy} and \mathcal{Z}_{zz} given in (3.55)-(3.58) involve modal summations of the form

$$\sum_{m=0}^M \mathcal{I}_p(m) \mathcal{I}_q(m) \mathcal{F}_{ij}(m, x, x'). \quad (4.1)$$

In the above, $\mathcal{I}_{p,q}$ correspond to the four moments integrals incorporating the y and y' dependence, and defined in (3.47)-(3.50). These expressions are computed for each mode m and for each strip, but do not depend on the propagation constant k_z . The current distribution on all strips is described by the same number of basis functions N_b . Hence, the four integrals are calculated in an external subroutine and stored in an $M \times N_c \times N_b \times 4$ matrix where M is the maximum modal index number, N_b is the number of subsections and N_c is the number of strips. Once these integrals have been computed they need not be re-calculated unless the strip geometry or the width of the waveguide is changed. The moments integrals for the entire domain functions involve the computation of Bessel functions of real arguments and of integer and fractional orders which result from the expansion and testing functions, respectively (see Appendix C). An available subroutine is used to compute the Bessel functions of integer order based on recursive relations [57]. The Bessel functions of fractional order (spherical Bessel functions of the first kind) j_n are calculated in a straightforward manner using their trigonometric representation [58].

The terms $\mathcal{F}_{ij}(m, x, x')$ in equation (4.1) are functions of k_z and need to be re-computed for each value of the variable parameter k_z . By inspection of these terms in (3.43)-(3.46), we recognize that the expressions $\mathcal{X}_{a,f}(x, x')$ are common to all four impedance elements and are given by

$$\mathcal{F}_{yy}(m, x_i, x'_j) = j \frac{\delta_m}{b} \frac{1}{k_y^2 + k_z^2} \left[k_y^2 (\eta_c)_a^s \mathcal{X}_a(m, x_i, x'_j) + k_z^2 (\eta_c)_f^s \mathcal{X}_f(m, x_i, x'_j) \right] \quad (4.2)$$

$$\mathcal{F}_{yz}(m, x_i, x'_j) = \frac{\delta_m}{b} \frac{k_y k_z}{(k_y^2 + k_z^2)} \left[-(\eta_c)_a^s \mathcal{X}_a(m, x_i, x'_j) + (\eta_c)_f^s \mathcal{X}_f(m, x_i, x'_j) \right] \quad (4.3)$$

$$\mathcal{F}_{zy}(m, x_i, x'_j) = \frac{\delta_m}{b} \frac{k_y k_z}{(k_y^2 + k_z^2)} \left[(\eta_c)_a^s \mathcal{X}_a(m, x_i, x'_j) - (\eta_c)_f^s \mathcal{X}_f(m, x_i, x'_j) \right] \quad (4.4)$$

$$\mathcal{F}_{zz}(m, x_i, x'_j) = j \frac{\delta_m}{b} \frac{1}{k_y^2 + k_z^2} \left[k_z^2 (\eta_c)_a^s \mathcal{X}_a(m, x_i, x'_j) + k_y^2 (\eta_c)_f^s \mathcal{X}_f(m, x_i, x'_j) \right] \quad (4.5)$$

The function $\mathcal{X}_{a,f}(m, x, x')$ involves trigonometric functions with complex arguments, and care has to be taken in the analytical formulation to avoid floating point overflow as the index m increases. This problem is overcome by replacing the complex sine and cosine functions by tangent functions which asymptotically tend to 1 for large arguments,

$$\mathcal{X}_a(m, x_i, x'_j) = \begin{cases} \frac{\left\{ \frac{\tan k_x(x-h) + j\tilde{\eta}_u^{a,f}}{\tan k_x h (1 - \tilde{\eta}_u^{a,f} \tilde{\eta}_l^{a,f}) + j(\tilde{\eta}_l^{a,f} - \tilde{\eta}_u^{a,f})} \right\} \left\{ \frac{\tan k_x x' + j\tilde{\eta}_u^{a,f}}{\tan k_x(x'-h) + j\tilde{\eta}_l^{a,f}} \right\} \frac{\cos k_x x' \cos k_x(x-h)}{\cos k_x h}}{\left\{ \frac{\tan k_x x + j\tilde{\eta}_l^{a,f}}{\tan k_x h (1 - \tilde{\eta}_u^{a,f} \tilde{\eta}_l^{a,f}) + j(\tilde{\eta}_l^{a,f} - \tilde{\eta}_u^{a,f})} \right\} \left\{ \frac{\tan k_x(x'-h) + j\tilde{\eta}_l^{a,f}}{\tan k_x(x'-h) + j\tilde{\eta}_l^{a,f}} \right\} \frac{\cos k_x(x'-h) \cos k_x x}{\cos k_x h}} & \text{for } x > x' \\ \frac{\left\{ \frac{\tan k_x(x-h) + j\tilde{\eta}_u^{a,f}}{\tan k_x h (1 - \tilde{\eta}_u^{a,f} \tilde{\eta}_l^{a,f}) + j(\tilde{\eta}_l^{a,f} - \tilde{\eta}_u^{a,f})} \right\} \left\{ \frac{\tan k_x(x'-h) + j\tilde{\eta}_l^{a,f}}{\tan k_x(x'-h) + j\tilde{\eta}_l^{a,f}} \right\} \frac{\cos k_x(x'-h) \cos k_x x}{\cos k_x h}}{\left\{ \frac{\tan k_x x + j\tilde{\eta}_l^{a,f}}{\tan k_x h (1 - \tilde{\eta}_u^{a,f} \tilde{\eta}_l^{a,f}) + j(\tilde{\eta}_l^{a,f} - \tilde{\eta}_u^{a,f})} \right\} \left\{ \frac{\tan k_x(x'-h) + j\tilde{\eta}_l^{a,f}}{\tan k_x(x'-h) + j\tilde{\eta}_l^{a,f}} \right\} \frac{\cos k_x(x'-h) \cos k_x x}{\cos k_x h}} & \text{for } x < x' \end{cases} \quad (4.6)$$

The right-most fraction can be re-written in the following form

$$\frac{\cos k_x(x-h) \cos k_x x'}{\cos k_x h} = \frac{1}{2} \frac{[\cos k_x(x'+x-h) + \cos k_x(x'-x+h)]}{\cos k_x h} \quad \text{for } x > x'$$

$$\frac{\cos k_x(x'-h) \cos k_x x}{\cos k_x h} = \frac{1}{2} \frac{[\cos k_x(x'+x-h) + \cos k_x(x'-x-h)]}{\cos k_x h} \quad \text{for } x < x'$$

In the “large argument” limit, this ratio tends asymptotically to

$$\frac{\cos k_x(x-h) \cos k_x x'}{\cos k_x h} \rightarrow \frac{1}{2} \left[e^{-jk_x(x'+x-2h)} + e^{-jk_x(x'-x)} \right] \quad \text{for } x > x'$$

$$\frac{\cos k_x(x'-h) \cos k_x x}{\cos k_x h} \rightarrow \frac{1}{2} \left[e^{-jk_x(x'+x)} + e^{-jk_x(x'-x)} \right] \quad \text{for } x < x'$$

The main factor in the change of sign of the determinant is the zz component of the impedance matrix as shown in Figure 4.3 for the case where entire domain basis functions are used. Note that the elements \mathcal{Z}_{yy} , \mathcal{Z}_{yz} are almost constant over the phase constant range.

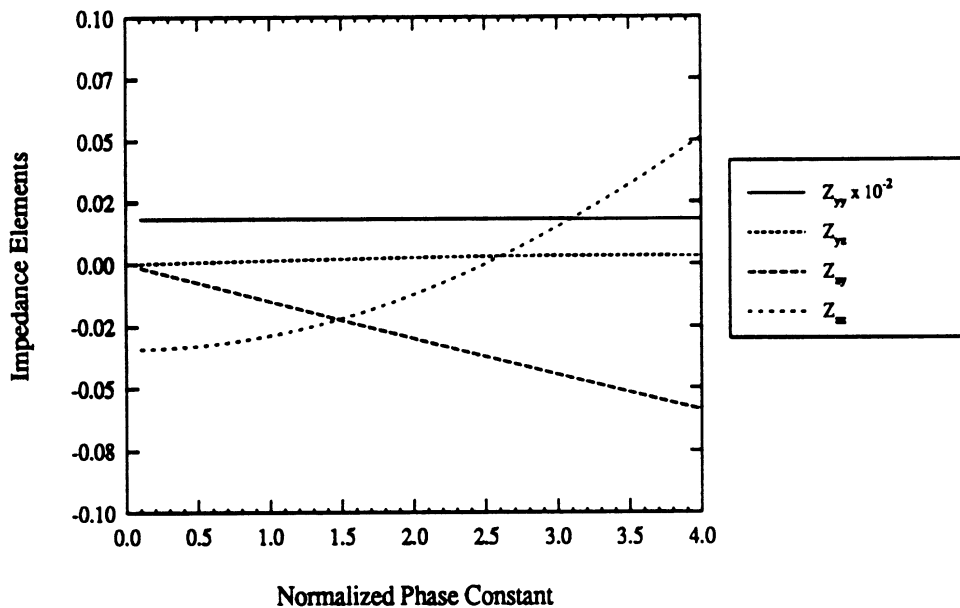


Figure 4.3: Impedance elements as a function of β ($a = b = 12.7$ mm, $w = h = 1.27$ mm, $\epsilon_r = 8.875$, $f = 5$ GHz)

4.1.3 Convergence considerations

The present method requires a certain amount of preprocessing in order to achieve good computational efficiency. As mentioned above, substantial CPU time is needed for the evaluation of the matrix elements which involves an infinite summation over the modal index m . However, the order of the final system can be kept very small provided an appropriate set of expansion functions is chosen. Convergence with respect to both the modal summation and the number of basis functions is discussed in the following sections.

Modal summation

Figure 4.4 shows the convergence behavior of the impedance elements as a function of the modal index m . The convergence of the calculated values of $\frac{\beta}{\beta_0}$, α and the

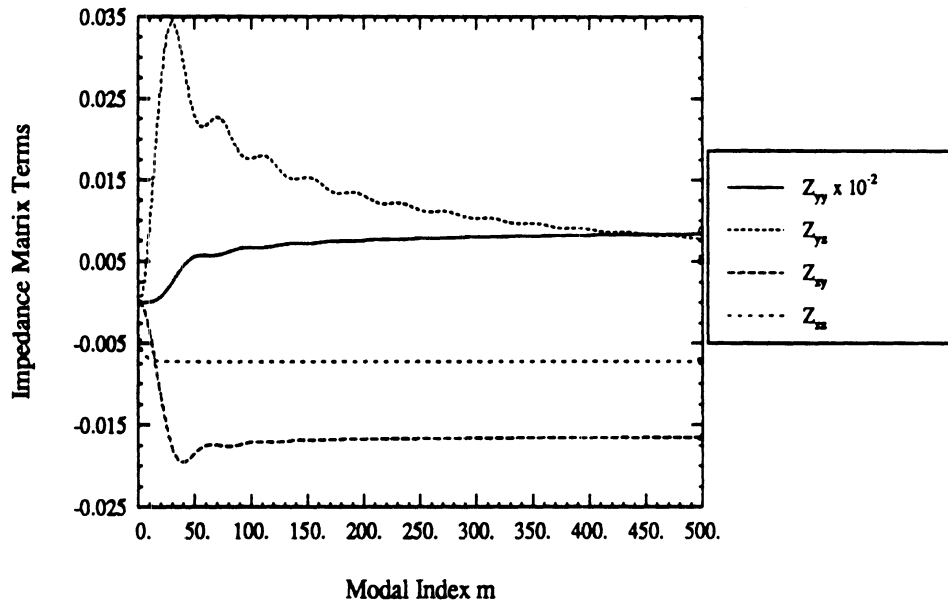


Figure 4.4: Convergence of the impedance elements with respect to the modal index m ($a = b = 12.7$ mm, $w = 0.635$ mm, $h = 1.27$ mm, $\epsilon_r = 8.875$, $f = 10$ GHz)

characteristic impedance Z_c with respect to the summation index m is illustrated in Figure 4.5 for the dominant microstrip mode where it is seen that the phase constant converges faster than the characteristic impedance.

To improve the overall convergence of the modal summation, auxiliary series transformations of the impedance matrix elements may be used. Such a formulation has been derived for pulse basis functions in the study of dielectric lines, as described in Chapter 7. In the case of Chebychev polynomials, however, these analytical transformations would require much algebraic effort and was not undertaken here.

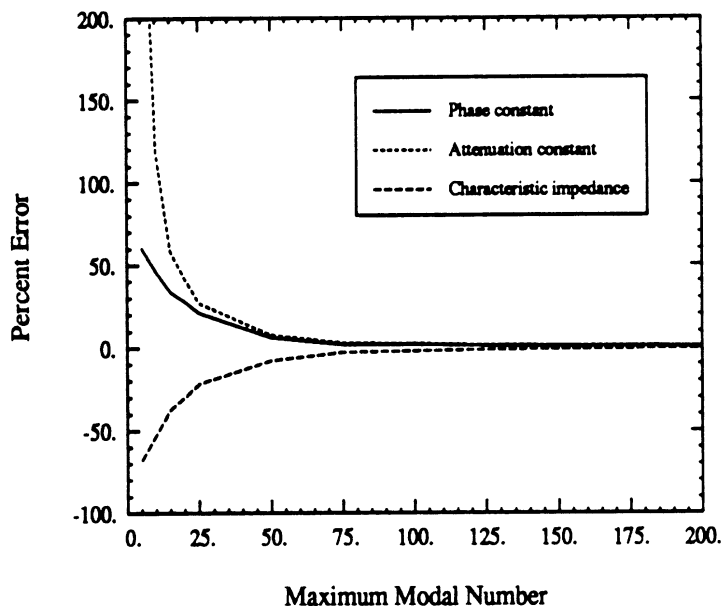


Figure 4.5: Convergence of the propagation characteristics with respect to the truncation modal number M ($a = 2.1$ mm, $b = 2$ mm, $w = 73$ μm , $d = 100$ μm , $\epsilon_r = 12.9$, $\sigma = 2 \times 10^7$ S/m, $t = 1$ μm , $f = 10$ GHz)

Number of basis functions

The order of the final system can be held very small by an appropriate choice of expansion or basis functions which satisfy the edge conditions, i.e. the right singularity at the edges of the strip. In this work, entire domain basis functions are chosen using Chebychev polynomials since the zeroth order function T_0 alone can represent the current Maxwellian distribution very closely, and therefore the true value of β is obtained with a very small number of expansion terms. In the case of pulse basis functions, the sampling rate needs to be at least 30 samples per wavelength to represent accurately the current distribution on the strip and therefore, convergence of the resulting impedance matrix will be slower than for entire domain basis functions. This is illustrated in Figure 4.6 where a convergence comparison between subsectional (pulse) and entire domain (Chebychev) basis functions is shown.

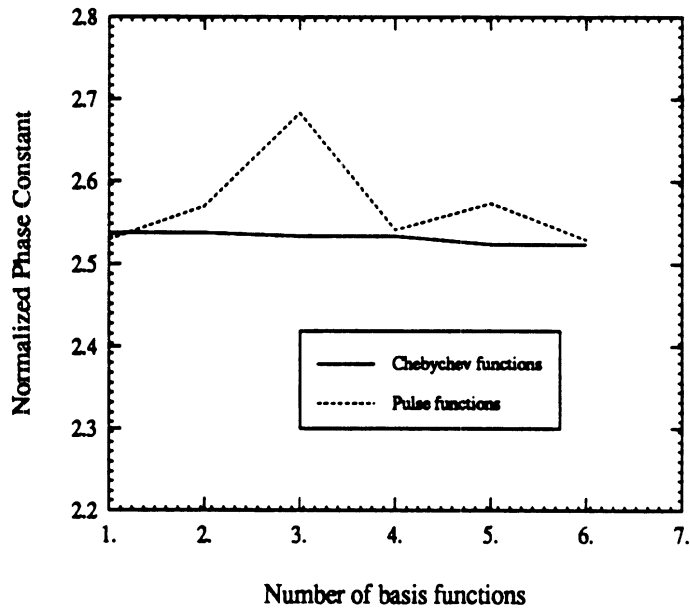


Figure 4.6: Convergence with respect to the number of basis functions ($a = 10$ mm, $b = 20$ mm, $d = 1$ mm, $\epsilon_r = 10$, $f = 1$ GHz)

For narrow lines, the longitudinal component of current I_z is much greater in magnitude than the transverse component, and can be represented with sufficient accuracy by T_0 . As the strip width increases, the contribution of the transverse component becomes more pronounced, and therefore the current distribution on the lines needs to be represented by two unknown components I_z and I_y which are incorporated in the present formulation and numerical implementation. In all the examples considered in the text, the propagation constant of single strips is only slightly influenced by the current distribution which is therefore approximated by the zeroth order Chebychev polynomials, unless otherwise specified.

4.2 Dispersion analysis

Microstrip lines are inherently dispersive due to the inhomogeneous nature of the dielectric medium. As a result, shielded microstrip lines propagate hybrid modes,

which can be represented as a superposition of TE and TM waves to the direction perpendicular to the interfaces. As the width of the line approaches a guided wavelength, the longitudinal components on the line cause the effective permittivity and the characteristic impedance to become dispersive.

In this section, dispersion is discussed for lossless structures to better understand and compare to the additional degradation due to losses. Much work has been published on dispersion, therefore the following results for single and multiple lines are only intended to validate the present full-wave analysis. Emphasis is placed on the frequency dependence of these lines and, in the case of coupled lines, also on the separation between lines as well. Some of the examples shown here are used again for the analysis of losses in the following sections.

4.2.1 Single microstrip line

As it has been discussed by many authors, shielded microstrip interconnects can propagate a dominant mode with zero cut-off frequency and higher order modes which are in one-to-one correspondence with the modes of the inhomogeneously filled waveguide surrounding them. All these modes are hybrid in nature and exhibit strong dependence on the electrical and geometrical characteristics of the microstrip interconnects and the shielding structure.

In Figure 4.7, the dispersion characteristics of a single microstrip are compared to the work of Yamashita where a nonuniform discretization of the electric field integral equation [59] was used. Examination of the results shows that only the dominant quasi-TEM mode propagates at low frequencies, and the normalized phase constant of the dominant TEM mode tends to a constant value $\sqrt{\epsilon_r}$ ($= 2.979$ in this case) as the frequency increases. This indicates that, in the high-frequency limit, the field

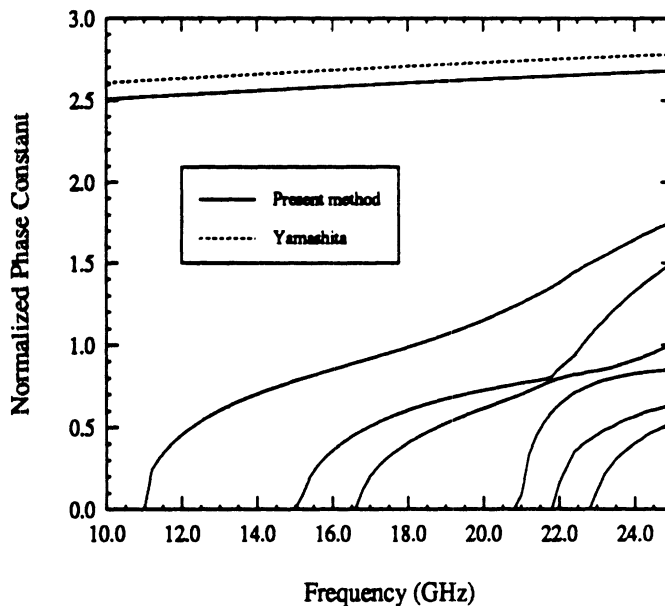


Figure 4.7: Dispersion curves for the even modes propagating along a single shielded microstrip ($a = b = 12.7$ mm, $w = 0.635$ mm, $h = 1.27$ mm, $\epsilon_r = 8.875$)

concentrates primarily in the dielectric region. A 4% discrepancy between the two methods is noted for the case of the dominant mode, and is in agreement with the findings of the study performed in [11]. When the frequency increases, the strip propagates higher order modes with cut-off frequencies very close to the roots of the corresponding LSE and LSM modes excited in the inhomogeneously-filled waveguide with no strip present. The partially-filled waveguides modes are calculated by solving the appropriate LSE and LSM transcendental equations [20] and are plotted for comparison to the corresponding microstrip structure in Figure 4.8.

The phase constant is also dependent on the geometrical parameters of the strip, namely the width of the strip W , the distance between the strip and ground plane h and the permittivity of the substrate. These effects are accounted for accurately by the present method, but are not included here for sake of brevity.

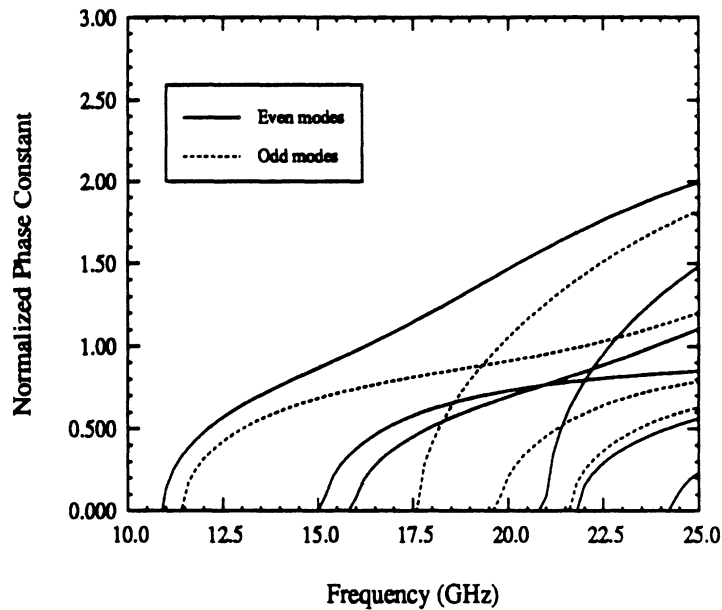


Figure 4.8: Dispersion curves for the LSE and LSM modes in an inhomogeneously-filled waveguide ($a = b = 12.7$ mm, $h = 1.27$ mm, $\epsilon_r = 8.875$)

4.2.2 Multiple microstrip lines

Today's MMIC technology involves the fabrication of multilevel metallized interconnects on multilayered substrates, with stringent requirements on the spacing between elements [60]. This, in turn, requires an accurate modelling of coupling effects, whether they are desirable as in the case of directional couplers, or undesirable (parasitic couplings). A shielded guiding structure which consists of N lines can support N dominant modes, and therefore the dispersion characteristics of these additional quasi-TEM modes must be determined. For some applications, e.g. directional couplers, the phase velocities of the modes should be nearly equal. This condition can be achieved by optimizing the geometry and location of the strips or by an overlay configuration with a high dielectric constant compared to the substrate, which slows the odd mode relative to the even mode [61]. Such effects can be read-

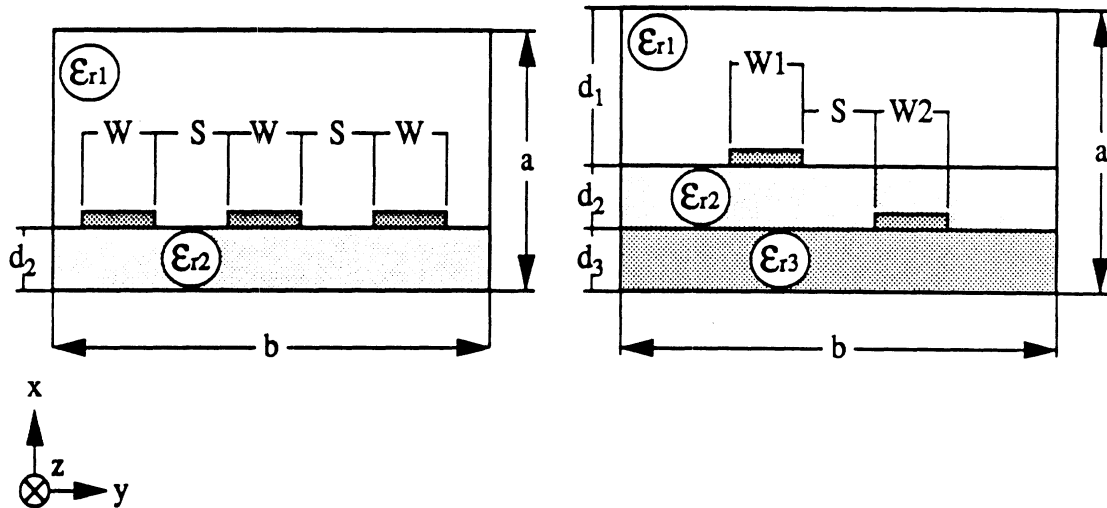


Figure 4.9: Geometry of coplanar and non-coplanar coupled strips

ily analyzed by the present generalized integral equation method without imposing limitations on the number of substrates and superstrates.

When weak coupling is desired, edge-coupled lines on a substrate are widely used whereas stronger coupling can be achieved by a broadside-coupled configuration. The generalized formulation derived in this work can be applied to coplanar strips as well as multilevel planar strips (Figure 4.9), and both types of structures are examined in the following sections.

Coplanar strips

Applications of such edge-coupled lines are illustrated in Figure 4.10. A symmetric two edge-coupled line system can propagate two orthogonal modes, namely the even and odd modes which correspond to an even and odd symmetry about a plane (electric or magnetic wall). Therefore the mode is called even when E_z is an even function of y (H_z odd) and the mode is called odd when E_z is an odd function of y (H_z even). For asymmetric lines, c and π modes are defined as the in-phase and anti-phase waves which reduce to even and odd modes in the case of symmetrical

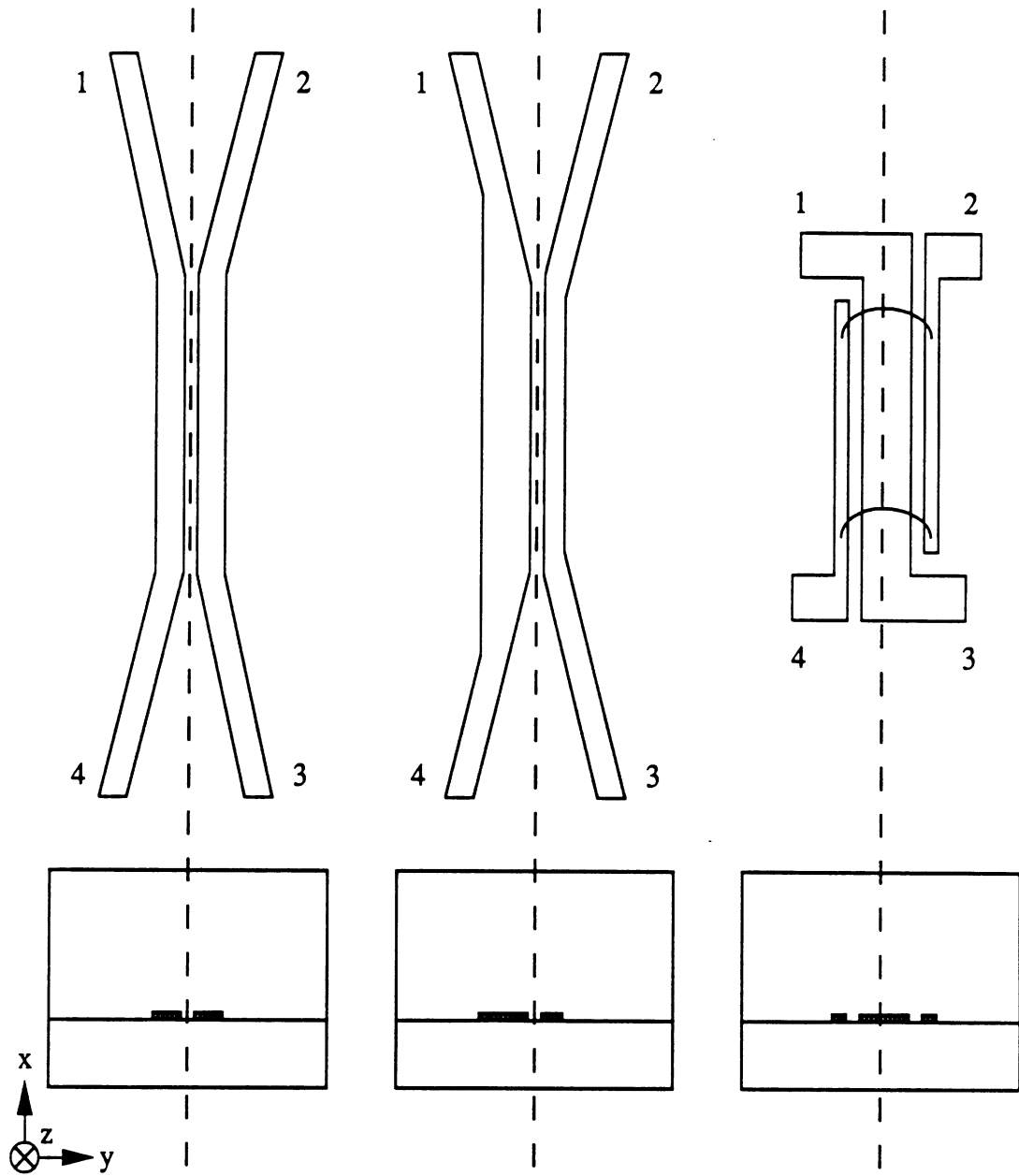


Figure 4.10: Example of applications for edge-coupled strips : symmetrical and asymmetrical 3-dB microstrip couplers, 3-line microstrip directional coupler

lines. The knowledge of the field configuration (Figure 4.11) provides an insight into the loss mechanisms described in the following sections.

Figure 4.12 shows the dispersion characteristics of two symmetric edge-coupled lines as a function of frequency for the geometry used in [59]. The parameters used were $w_1 = w_2 = 1.27$ mm, separation between the strips $s = 1.27$ mm, $\epsilon_r = 8.875$, substrate thickness $h = 1.27$ mm. The even and odd dominant (quasi-TEM) modes propagate in the structure with no cut-off frequency, whereas higher order microstrip even and odd modes are only excited above 11 GHz.

Non-coplanar strips

As mentioned above, two broadside-coupled strips on different levels propagate c and π modes with generic electric field distribution shown in Figure 4.13. To validate the accuracy of the present integral equation method, asymmetric broadside-coupled lines are studied here through two examples found in the literature.

First, the effect of horizontal strip separation s on the phase constant and characteristic impedance is plotted in Figure 4.14 where very good agreement is shown with the work of Diaz [62]. For large separation between the strips, the effective dielectric constants for the two modes come closer to each other since coupling is decreased. The same trend is shown for the even and odd characteristic impedances (Figure 4.14b), where both lines have the same modal impedance $Z_1^o = Z_2^o$ (odd mode) and $Z_1^e = Z_2^e$ (even mode) because of the symmetry of the structure.

Next, the frequency dependence of symmetric lossless coupled lines printed on different interfaces is compared to the spectral domain study performed by Carin et al. [63]. No symmetry applies in this case, and therefore all four modal impedances are plotted where Z_{ij} represents the impedance of line i for mode j (Figure 4.15).

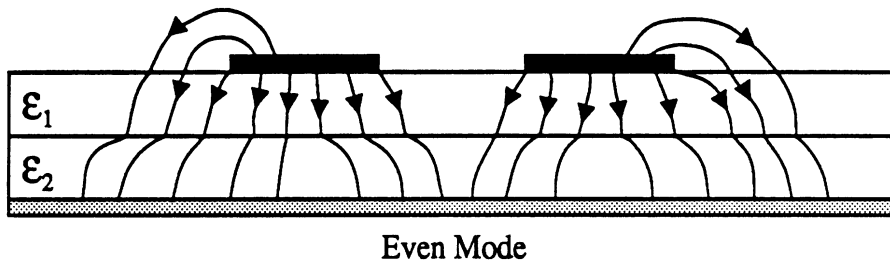
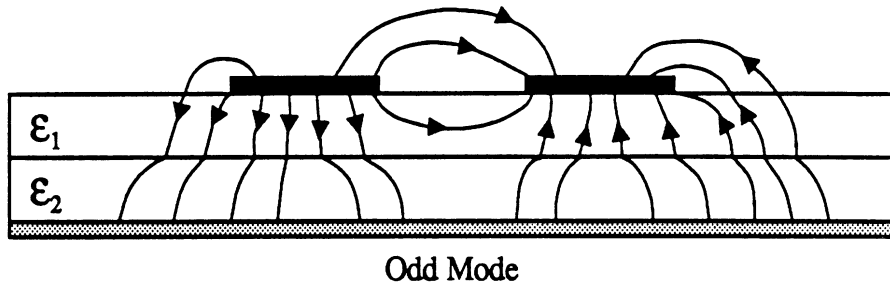


Figure 4.11: Field distribution for the even and odd modes of symmetric edge-coupled strips

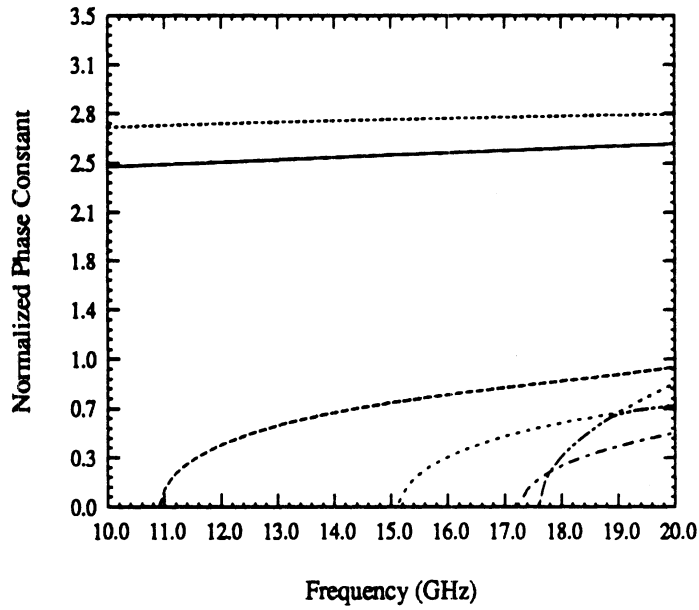


Figure 4.12: Propagation characteristics of two-coupled lines versus frequency ($a = b = 12.7$ mm, $w_1 = w_2 = h = 1.27$ mm, $s = 1.27$ mm, $\epsilon_r = 8.875$)

4.3 Substrate loss analysis

Several methods have been reported in the literature to account for dielectric losses in microstrip structures, such as the quasi-TEM approximation [64], the method of moments [65], and the perturbation method [30]. The quasi-TEM formu-

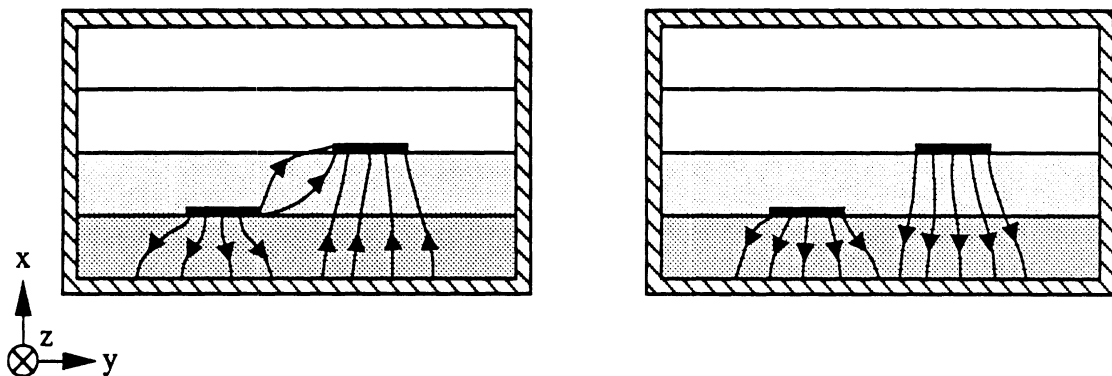
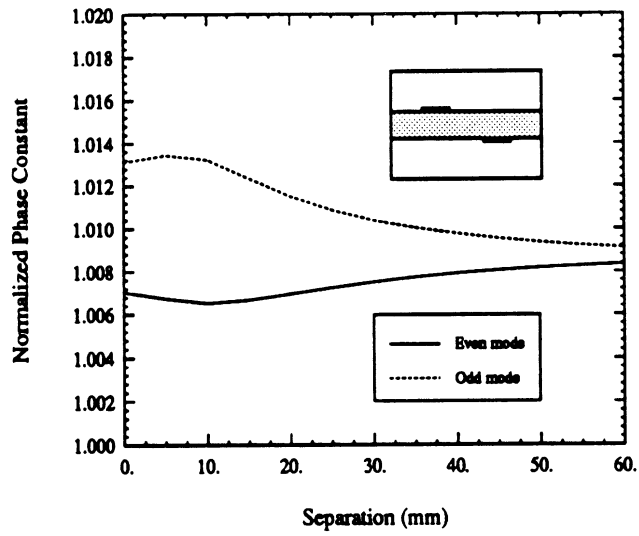
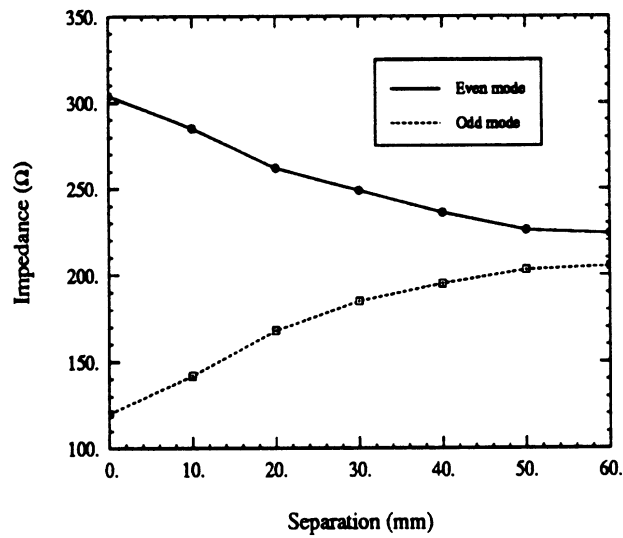


Figure 4.13: Field distribution for the even and odd modes of broadside coupled strips

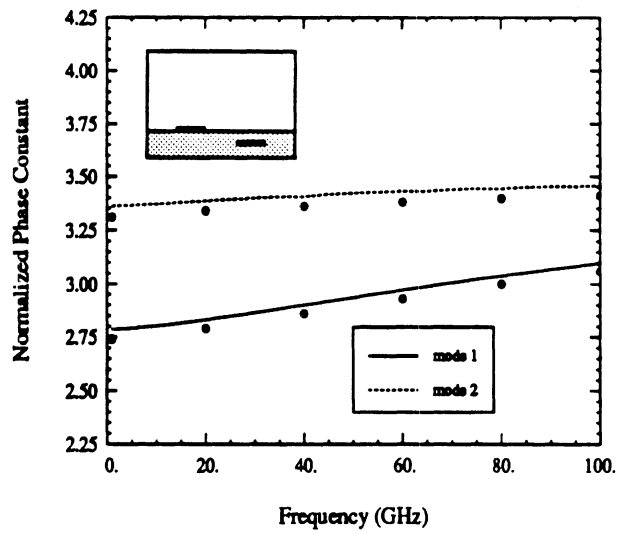


a. Phase constant

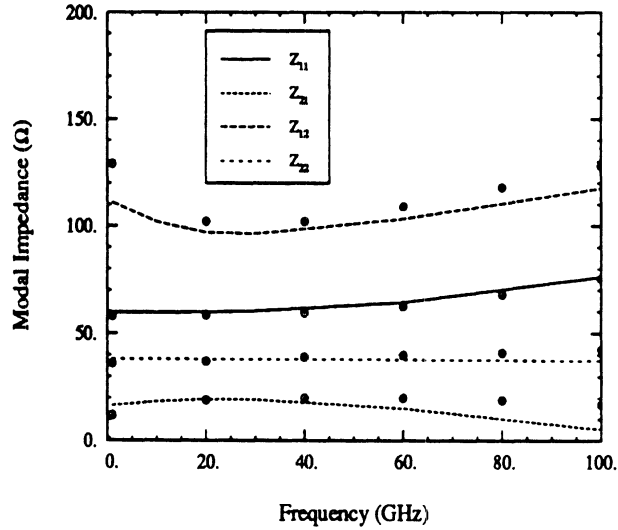


b. Characteristic impedance

Figure 4.14: Propagation characteristics of broadside-coupled lines as a function of horizontal separation ($b = 400$ mm, $\epsilon_{r1} = \epsilon_{r2} = \epsilon_{r3} = 1$, $\sigma = 3.33 \times 10^7$ S/m, $t = 3\mu\text{m}$, $d_1 = d_3 = 31$ mm, $d_2 = 10$ mm, $w_1 = w_2 = 5$ mm, $f = 1$ GHz)



a. Phase constant



b. Characteristic impedance

Figure 4.15: Propagation characteristics of broadside-coupled lines as a function of frequency : present method (lines), Carin (points) ($a = b = 2.54$ cm, $\epsilon_{r1} = 1$, $\epsilon_{r2} = \epsilon_{r3} = 12$, $d_2 = d_3 = 127 \mu\text{m}$, $s = 381 \mu\text{m}$)

lation uses the simplified design equation shown below

$$\alpha_d = \frac{20\pi}{\ln 10} \frac{q \tan \delta}{\lambda_g} \text{ dB / unit length} \quad (4.7)$$

where λ_g is the microstrip wavelength and q is the filling factor [64]. The most widely used method to quantify dielectric losses, however, has been the perturbation approach, where the loss tangent is assumed to be sufficiently small so that the perturbed fields can be approximated by the electromagnetic fields in the lossless case. According to this method, the attenuation constant due to dielectric losses may be written as

$$\alpha_d = \frac{P_d}{2P_o} \quad (4.8)$$

where P_d is the time-averaged power dissipated in the dielectrics given by

$$P_d = \omega \epsilon \tan \delta \int_{S_{diel}} |E_o|^2 dS. \quad (4.9)$$

P_o is the time-averaged power flow along the line

$$P_o = \Re \int_S \vec{E}_o \times \vec{H}_o^* \cdot \hat{z} dS, \quad (4.10)$$

with S_{diel} the area covered by the dielectric and S the complete cross-section.

In this work, an exact and simple formulation is adopted where dielectric losses are considered by assuming a complex permittivity for each dielectric layer i as

$$\epsilon_i = \epsilon_{r_i}(1 - j \tan \delta_i) \quad (4.11)$$

which in turn introduces a complex propagation constant. In this manner, for a given $\tan \delta$, attenuation due to dielectric losses is very accurately determined and is not subject to limiting assumptions applied on the substrate loss tangent δ .

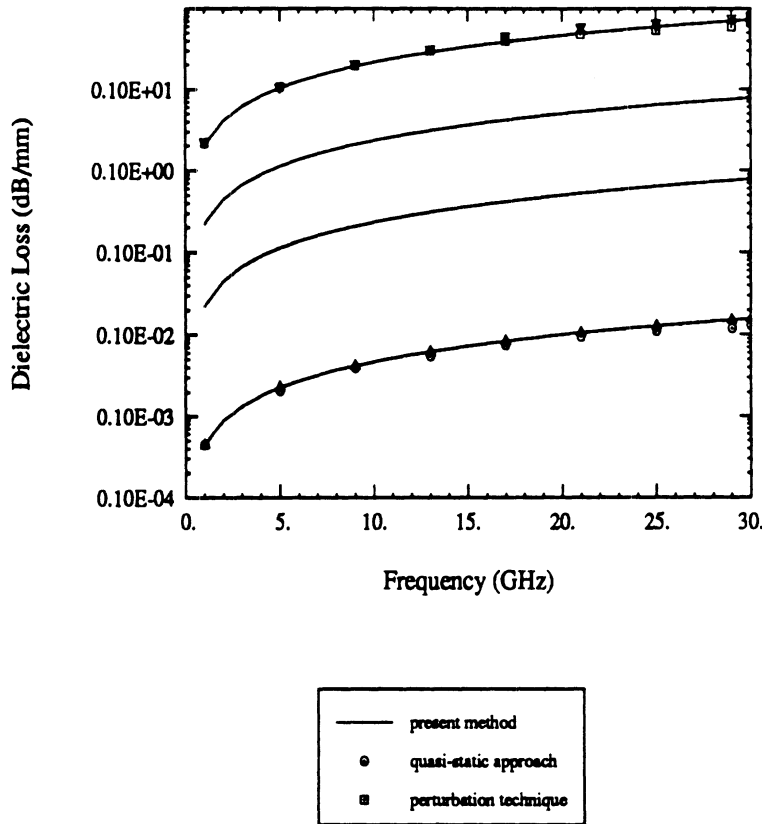


Figure 4.16: Dielectric loss of the dominant mode of a single microstrip versus frequency ($a = b = 20$ mm, $w = h = 0.5$ mm, $\epsilon_r = 10$, $\mu_r = 1$)

Among the parameters which affect the characteristics of the propagating modes, the operating frequency and the strip width-to-substrate thickness ratio (aspect ratio) are the most important ones. The curves in Figure 4.16, representing dielectric losses for a single strip on a lossy substrate, are displayed as a function of the operating frequency. Comparison is made between the present formulation, a perturbational method [30], a quasi-TEM approximation [64], and a full-wave spectral domain method [66]. Good agreement is shown for small values of $\tan \delta$, but the quasi-TEM and perturbation technique portray increasing differences from the full-wave techniques as the loss becomes larger than 0.1 .

Substrate loss is displayed for a single microstrip as a function of strip width

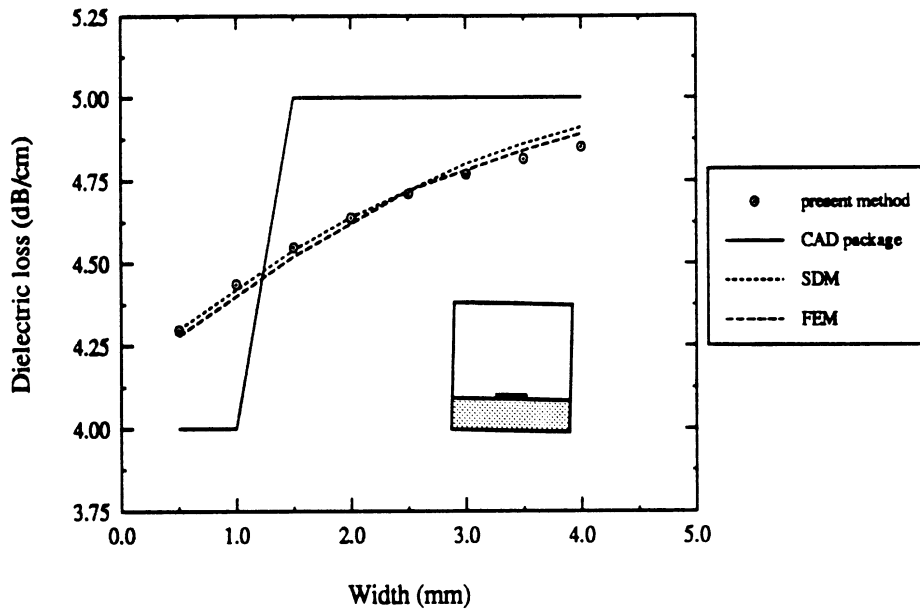


Figure 4.17: Dielectric losses of a single strip versus strip width ($a = 10$ mm, $b = 20$ mm, $d = 1$ mm, $\epsilon_r = 10$, $\tan\delta = 2 \times 10^{-4}$, $f = 1$ GHz)

W in Figure 4.17. The attenuation constant of the dominant mode is shown to increase monotonically with W and compares well to a perturbation technique used in the spectral-domain approach of Mirshekar-Syakhali [30] and in the finite-element method of Pantic [29]. Data from the commercially available CAD program *LineCalc* (available from EESOF) plotted on the same graph show a discretized behaviour caused by a round-off problem, but bounds the full-wave results in a conservative manner.

Figure 4.18 shows the dielectric attenuation constant for two edge-coupled strips as a function of the separation between the lines. Due to the higher field concentration in the substrate for the even mode (see Figure 4.11), the attenuation constant resulting from dielectric losses is more pronounced for this mode as shown in Figure 4.18. As the strip separation increases, coupling effects decrease and, in the case of wide spacing, the attenuation tends to the single strip value.

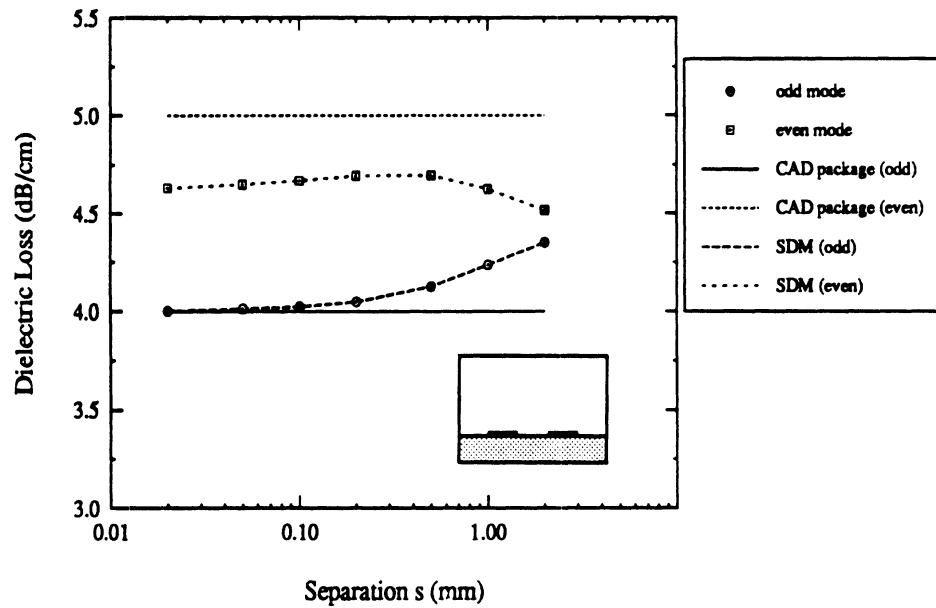


Figure 4.18: Dielectric losses of coupled strips versus line separation s/d ($a = 10$ mm, $b = 20$ mm, $W = d = 1$ mm, $\epsilon_r = 10$, $\tan\delta = 2 \times 10^{-4}$, $f = 1$ GHz)

Although dielectric losses are usually important when the substrate is made of semiconductor material, conductor losses should also be considered in the overall loss determination. For the new generation of MMIC's at microwave frequencies, dielectric losses are of much lesser magnitude than conductor losses (excluding superconductors) as discussed in the next section.

4.4 Conductor loss analysis

Today's MMIC technology involves the fabrication of interconnects with metalization thickness of the order of $10\mu\text{m}$ and less. At microwave and millimeter-wave frequencies, the cross-sectional dimensions of the strips are of the order of the skin depth (about $3\mu\text{m}$ at $f = 1$ GHz) which causes conductor loss to become a predominant effect on the propagation characteristics of shielded lines. It is therefore

important to include its influence in the overall design of MMIC's.

Up to the time when this work was performed, all the existing full-wave analysis models had evaluated conductor losses by assuming a zero-strip thickness and using a perturbation method where the attenuation constant is given by

$$\alpha_c = \frac{P_c}{2P_o} = \frac{R_s \int_{C_w} |\vec{H}_o|^2_{\tan} dl}{2\Re \int_S \vec{E}_o \times \vec{H}_o^* \cdot \hat{z} dS}. \quad (4.12)$$

P_c is the time-averaged power dissipated in the conductors, \vec{E}_o , \vec{H}_o are the electromagnetic fields for the lossless case and the surface resistivity R_s is given by the *incremental inductance rule* [24], or by

$$R_s = \left(\frac{\omega\mu}{2\sigma_c} \right)^{\frac{1}{2}}. \quad (4.13)$$

However these definitions of R_s assume that the strip dimensions are much larger than the skin depth and, as a result, these methods cannot predict losses for conducting strips with thickness of the order of a skin depth. Therefore, to validate the approach presented herein, a comparison with previous work was only possible for the thick strip limit (e.g. $t = 10 \mu\text{m} \simeq 3.5\delta$ at $f = 1\text{GHz}$). Figure 4.19 presents conductor losses derived with the present technique as a function of the aspect ratio. The results are compared with the finite element method (FEM) [29], the spectral domain method (SDM) [30], [66] and an analytic differentiation of Wheeler's *incremental inductance rule* [25]. This analytic differentiation implemented through the CAD package *LineCalc* is shown to overestimate the conductor losses by about 30%.

4.4.1 Skin effect

At high frequencies, each conductor surface has a layer of skin depth δ defined as the depth in which the wave has been attenuated to $1/e$ of its original value, or

$$\delta = \left(\frac{2}{\omega\mu\sigma_c} \right)^{\frac{1}{2}} \quad (4.14)$$

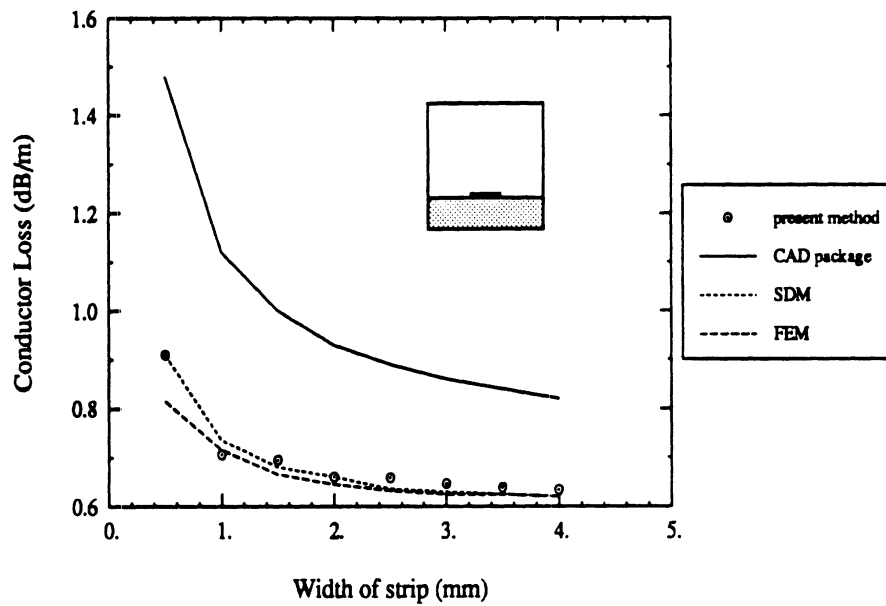


Figure 4.19: Conductor losses of a single strip versus strip width ($a = 10$ mm, $b = 20$ mm, $d = 1$ mm, $\epsilon_r = 10$, $\sigma = 3.33 \times 10^7$ S/m, $\tan\delta = 2 \times 10^{-4}$, $f = 1$ GHz, $t = 10$ μm)

where σ_c is defined as the conductivity of the line conductor. The strips considered here are made of material of conductivity $\sigma = 3.33 \times 10^7$ S/m. The curves in Figure 4.20 illustrate the influence of strip thickness on the attenuation constant where conductor losses versus strip width are plotted for the case of $t = 0.5\delta$ which appears substantially higher from the case of $t = 2, 3$ and 4δ (= electrically thick strips). Our results correctly predict that as the thickness of the strip increases to values large compared to the skin depth, the loss decreases significantly to the thick strip limit and does not change much thereafter. These results confirm the rule used in hybrid circuits of using a thickness $t \geq 3\delta$ at the highest frequency of interest to achieve low ohmic attenuation [68]. As the thickness of the strip decreases, the line exhibits higher attenuation because the current is forced to flow through a smaller area. Also, it can be seen from Figure 4.20 that the attenuation exhibits a more

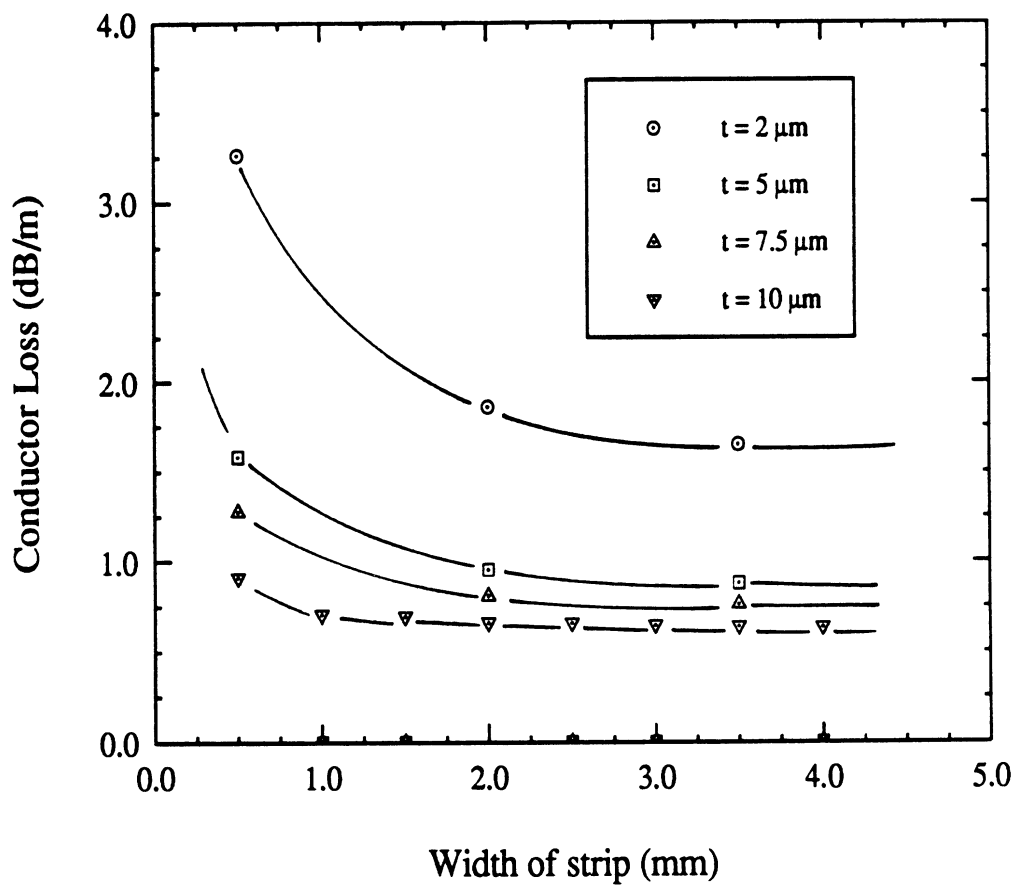


Figure 4.20: Effect of thickness on the ohmic attenuation constant ($a = 10 \text{ mm}$, $b = 20 \text{ mm}$, $d = 1 \text{ mm}$, $\epsilon_r = 10$, $\sigma = 3.33 \times 10^7 \text{ S/m}$, $f = 1 \text{ GHz}$)

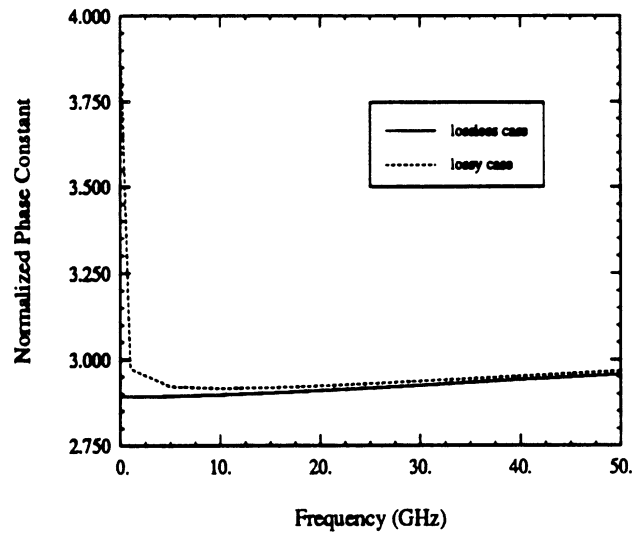
pronounced sensitivity to the thickness t for small strip widths.

The skin-effect problem may also be described as a function of frequency. Figures 4.21-4.22 present results corresponding to a microstrip line on a GaAs substrate with a total width of $73\mu\text{m}$ and a characteristic impedance of about $50\ \Omega$. As the operating frequency is increased, the per unit length inductance stays approximately constant, whereas the per unit length resistance increases rapidly because the current tends to concentrate at the surface of the strip and therefore is forced through a reduced cross-section. This behaviour of the equivalent surface impedance is reflected in the resulting attenuation constant which increases monotonically with frequency. From Figure 4.21, it is interesting to note that the phase constant is affected by conductor losses. In addition to dispersion, which can be seen over the frequency range studied, a drastic increase in β is noticed for low frequencies due to an increase in the internal inductance. Figure 4.22 shows the frequency dependence of the characteristic modal impedance where the impedance is now complex, with a negative imaginary part which is rather significant at lower frequencies. This behavior of the characteristic impedance agrees with the result obtained from the quasi-TEM definition of the characteristic impedance for a line with ohmic losses and negligible dielectric losses. Indeed, assuming $R \ll \omega L$, one finds

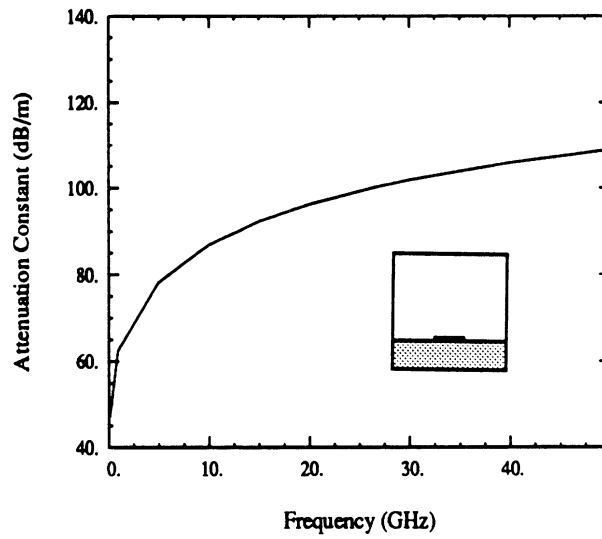
$$Z_0 = \sqrt{\frac{R + j\omega L}{j\omega C}} \sim \sqrt{\frac{L}{C}} - j\frac{R}{2\omega\sqrt{LC}}, \quad (4.15)$$

where R, L, C are the per-unit-length resistance, inductance, and capacitance of the line, respectively.

Finally, a comparison between conductor and dielectric losses is plotted in Figure 4.23 for frequencies up to 20 GHz which shows that dielectric losses are much less significant than conductor losses, i.e. about one tenth in this particular case.

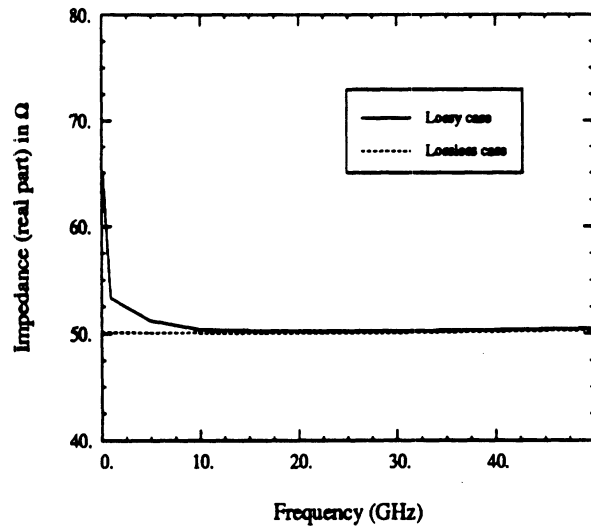


a. Phase constant

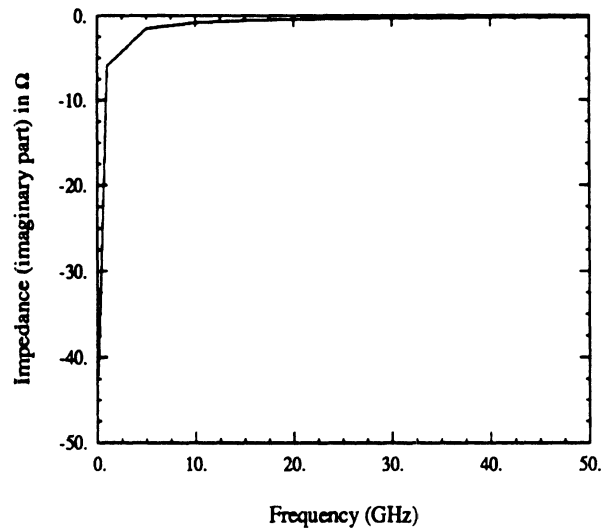


b. Attenuation constant

Figure 4.21: Propagation constant of a single lossy strip as a function of frequency ($a = 2.1$ mm, $b = 2$ mm, $W = 73$ μm , $d = 100$ μm , $\epsilon_r = 12.9$, $\sigma = 2 \times 10^7$ S/m, $t = 1$ μm)



a. Real part



b. Imaginary part

Figure 4.22: Characteristic impedance of a single lossy strip as a function of frequency ($a = 2.1$ mm, $b = 2$ mm, $W = 73$ μm , $d = 100$ μm , $\epsilon_r = 12.9$, $\sigma = 2 \times 10^7$ S/m, $t = 1$ μm)

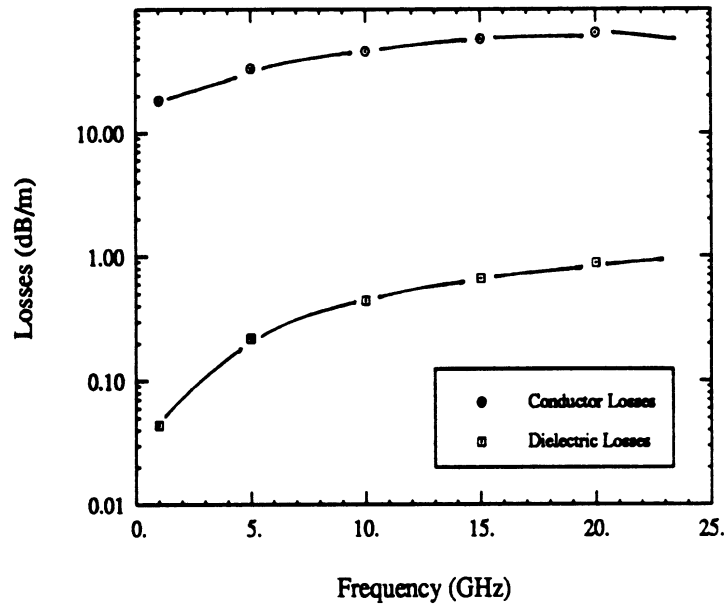


Figure 4.23: Comparison between dielectric and conductor losses as a function of frequency ($a = b = 500 \mu\text{m}$, $W = d = 50 \mu\text{m}$, $\epsilon_r = 10$, $\sigma = 3.33 \times 10^7 \text{ S/m}$, $t = 5 \mu\text{m}$)

4.4.2 Multiple metallization and roughness

The formulation used in this study for the surface impedance of conductors is amenable to a variety of conductor configurations, such as multiple metallizations. For certain types of microstrip circuit elements and transmission lines, a composite conductor is used, such as nickel, which serves as an intermediate bonding metal between gold and ceramic dielectrics (see Figure 4.24). The nickel layer is usually very thin compared to the strip conductor (200 \AA thick layer). In the present formulation, a non-uniform discretization is used to calculate the current distribution in the conductors, leading to a solution of the electromagnetic fields in both conductors, with no assumption on the thickness. Therefore propagation on lines made of several metallic layers can be modeled.

The present method can also account accurately for roughness on the surface

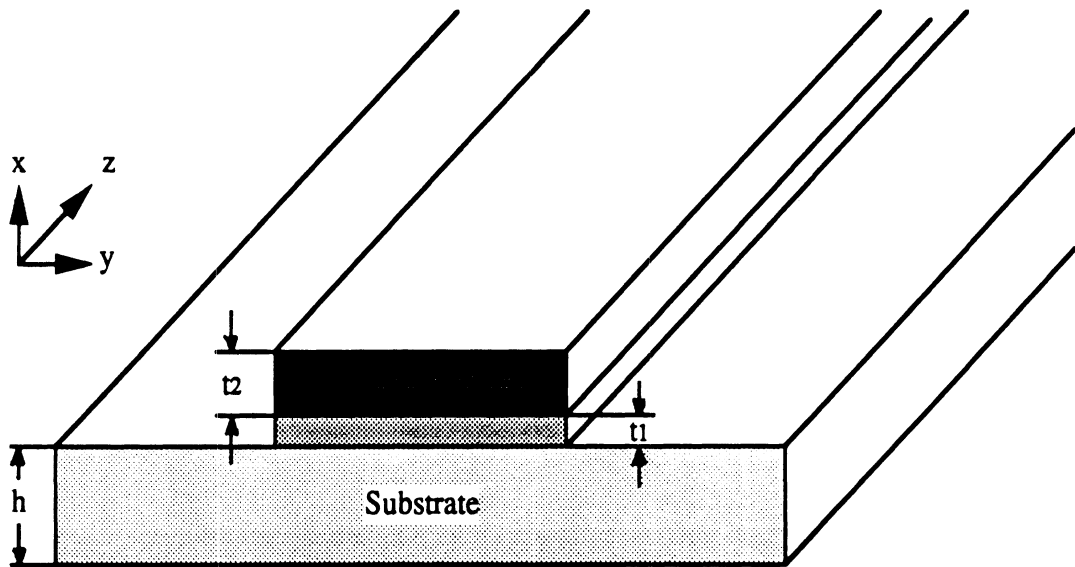


Figure 4.24: Geometry for a microstrip made of multiple metallization

of the strip conductors. If we assume that the surface of the conductor of a single microstrip line has a periodic variation such as the one shown in Figure 4.25 with a peak-to-peak value (r) of $1.5 \mu\text{m}$ and a period of $70 \mu\text{m}$ then the effect of this roughness on the surface resistivity and subsequently on conductor losses is plotted on the same figure as a function of frequency. The roughness has an important effect when the size of the discontinuity r is of the order of the skin depth.

4.4.3 Ground plane contribution

Conductor losses in the ground plane are incorporated in the formulation of the Green's function where a load impedance may be included on the lower and upper walls of the shielding waveguide (see section 2.3.3). The ground plane resistance is represented by the surface resistivity of an infinite thick plane as $R_s = 1/\sigma \delta$. This is a good assumption since the waveguide walls are made of electrically thick metal for mechanical strength. Figure 4.26 shows the effect of the lossy ground on conductor losses (Figure 4.26). The increase in attenuation is about 50% and therefore losses

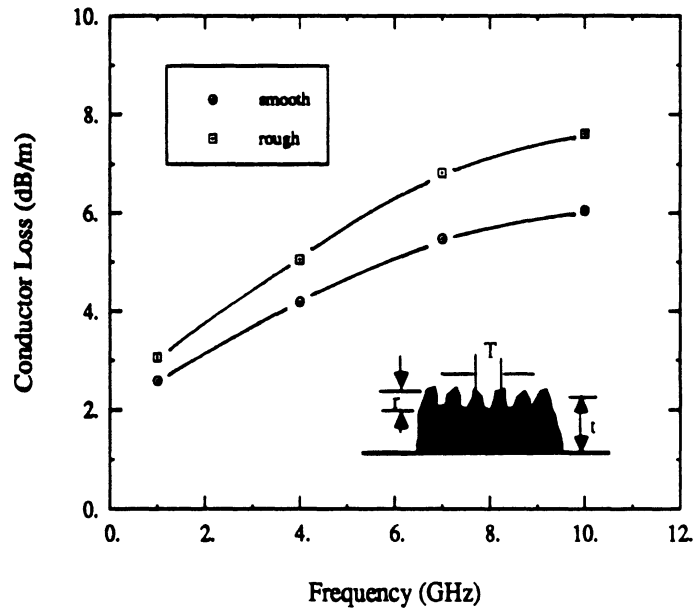


Figure 4.25: Effect of roughness on the ohmic attenuation constant as a function of frequency ($a = 10$ mm, $b = 20$ mm, $W = d = 280$ μm , $T = 70$ μm , $r = 1.5$ μm , $\epsilon_r = 10$, $\sigma = 4 \times 10^7$ S/m, $t = 6$ μm)

due to the ground plane cannot be neglected. When the strip is located closer to the ground plane, the overall attenuation constant increases due to a higher field concentration below the strip.

Figure 4.27 shows a comparison between the equivalent surface resistance of a single strip (3.28), calculated using the method described in Chapter 3, and the surface resistivity $R_s = 1/\sigma \delta$ of an infinite thick plane. As the operating frequency gets into the microwave region, the thick strip approximation increasingly overestimates the resistance and therefore the conductor losses. This behaviour is further verified experimentally in the next section.

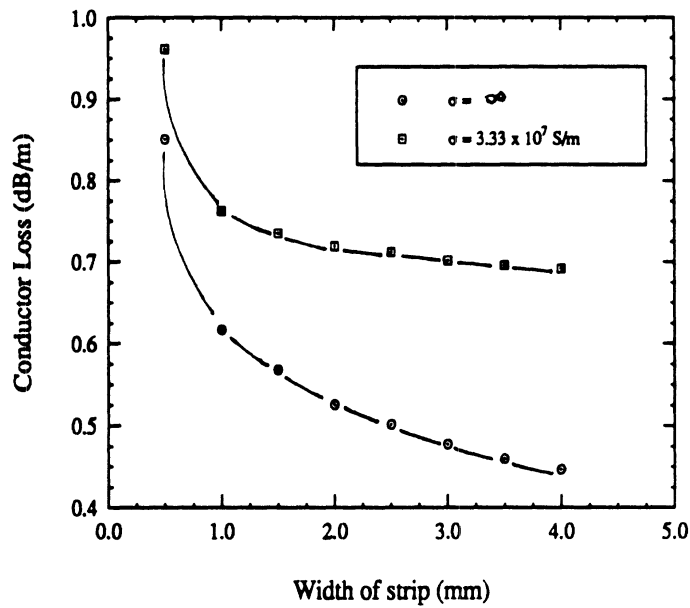


Figure 4.26: Effect of ground plane resistivity on the ohmic attenuation constant ($a = 10 \text{ mm}$, $b = 20 \text{ mm}$, $d = 1 \text{ mm}$, $\epsilon_r = 10$, $\sigma = 3.33 \times 10^7 \text{ S/m}$, $f = 1 \text{ GHz}$)

4.4.4 Experimental verification

Several experimental methods have been proposed in the literature for the characterization of dispersion on microstrip lines, but fewer deal with attenuation measurements. The attenuation due to conductor losses is not easy to measure ad hoc, but rather has to be de-embedded from an overall measurement of the total attenuation of the line which includes coupling phenomena, reflections, mismatches, end effects and surface roughness.

The present theoretical method for the study of losses on the propagation characteristics is validated by a comparison with measurements performed at Ball Aerospace, Boulder, CO [67] on a single microstrip transmission line measured over a range of frequencies extending up to 20 GHz. The strip is $73 \mu\text{m}$ wide and $2 \mu\text{m}$ thick, with conductivity $\sigma = 3.33 \times 10^7 \text{ S/m}$. The width of the metallic enclosure is 20mm and

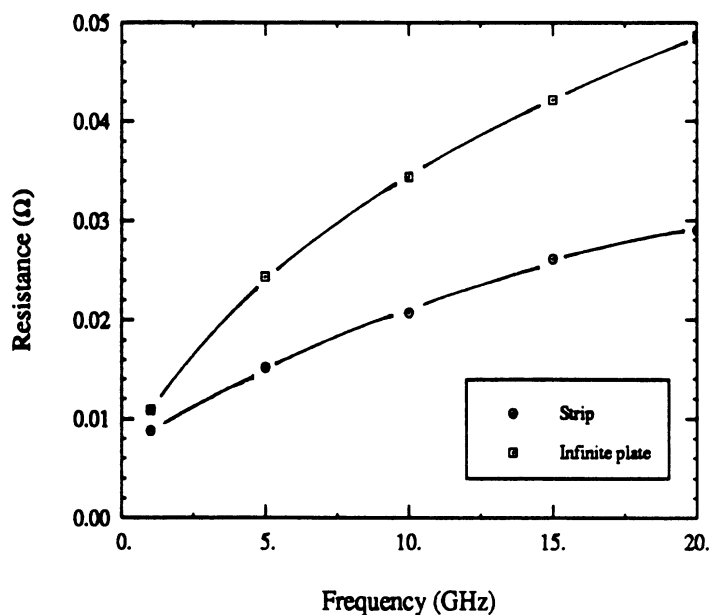
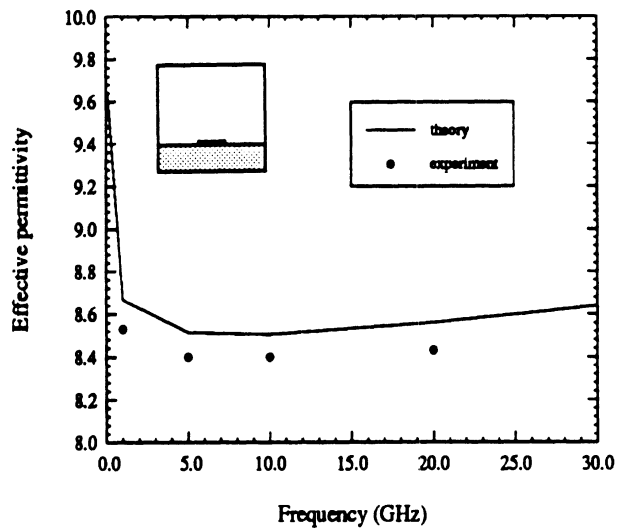


Figure 4.27: Equivalent surface resistivity R_l and ground resistivity R_s versus frequency ($a = b = 500 \mu\text{m}$, $W = d = 50 \mu\text{m}$, $\epsilon_r = 10$, $\sigma = 3.33 \times 10^7 \text{ S/m}$, $t = 5 \mu\text{m}$)

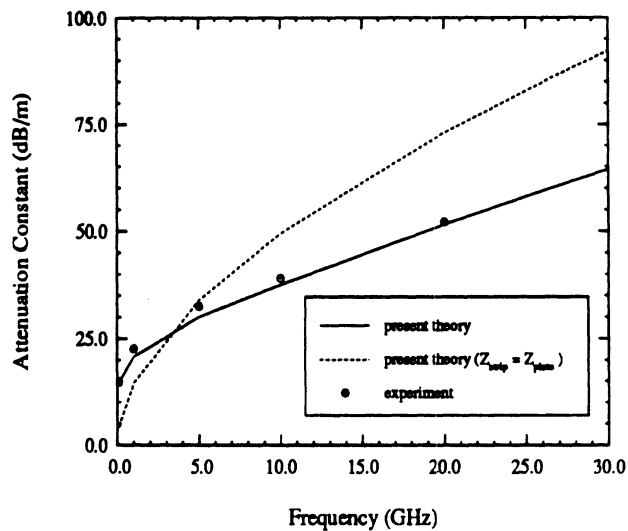
its height 10 mm. The substrate is $100 \mu\text{m}$ thick and its relative dielectric constant $\epsilon_r = 12.9$ with loss tangent estimated to be $\tan \delta = 16 \times 10^{-4}$. Both dielectric and conductor losses are included in the theoretical model. Agreement better than 4% is shown for the attenuation constant and 1.6% for the effective permittivity, as shown in Figure 4.28. These results are compared to the modeling of strip losses using the resistance of an infinite plate.

4.4.5 Multiple coupled strips

In order to design directional couplers and filters for high frequency applications, conductor losses should be accurately included in the computer-aided design models. During the past few years, a number of papers have been published for the characterization of multilevel planar transmission lines. However earlier attempts only



a. Effective permittivity



b. Attenuation constant

Figure 4.28: Comparison between theory and experiment for a single microstrip on a GaAs substrate ($a = 2.1$ mm, $b = 2$ mm, $W = 73$ μm , $d = 100$ μm , $\epsilon_r = 12.9$, $\sigma = 3.33 \times 10^7$ S/m, $\tan\delta = 16 \times 10^{-4}$, $t = 2$ μm)

included the effect of conductor loss degradation on the propagation properties of edge-coupled lines on a single planar level [68], [69] using a quasi-static method. In this work, the technique is applied to evaluate the effect of losses on the performance of directional couplers involving lines on the same planar level (edge-coupled lines) as well as in a multilevel configuration (broadside-coupled lines).

Edge-coupled strips

A comparison to earlier work on electrically thick strips is shown in Figure 4.29. Conductor losses are included in the analysis of the even and odd excitation modes for the case of two edge-coupled strips. The derived results are plotted as a function of the separation between the two strips and compare very well to results derived with the spectral domain method [30], [66]. The attenuation constant is larger for the odd mode than the even mode because of the high concentration of fields around the gap in the odd configuration $(\alpha_c)_{odd} > (\alpha_c)_{even}$ (see Figure 4.11). This also explains why the odd mode is more sensitive to the separation between strips, as the field distribution is changed more drastically in this case. As mentioned earlier, dielectric losses exhibit the opposite behaviour with $(\alpha_d)_{even} > (\alpha_d)_{odd}$.

The following example of two symmetric coupled lines will be used again in the next section to study the effect of coupling on pulse propagation. Figure 4.30 shows the frequency dependence of the even and odd mode propagation constants in the lossless and lossy case over a range of frequencies extending up to 10 GHz. The overall behavior of the complex modal impedances is illustrated in Figure 4.31 and agrees well with results derived for the case of a single line (see Figure 4.22). Because of the symmetry of the structure, both lines have the same modal impedance Z_{ij} for mode j , thus $Z_{11} = Z_{21}$ (odd mode) and $Z_{12} = Z_{22}$ (even mode).

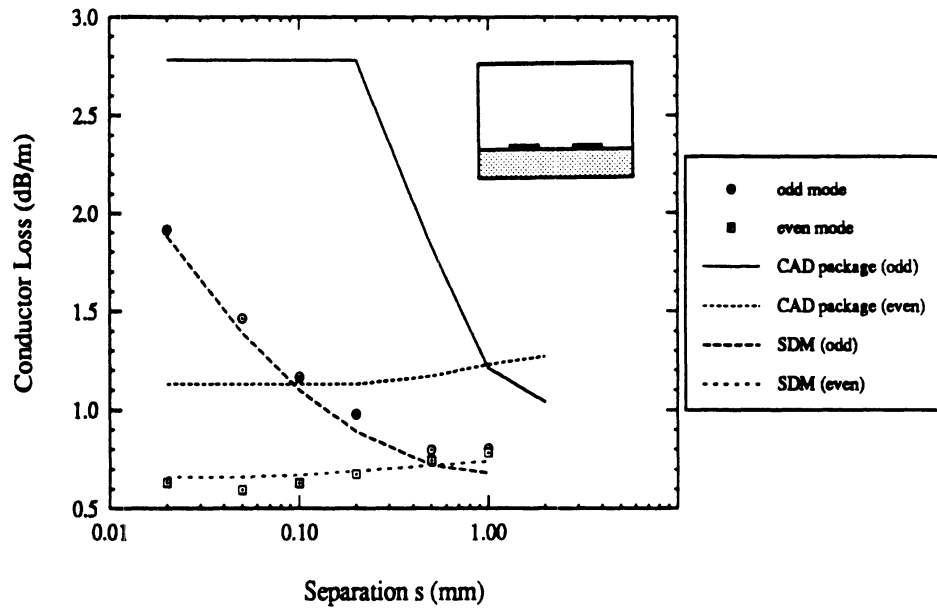
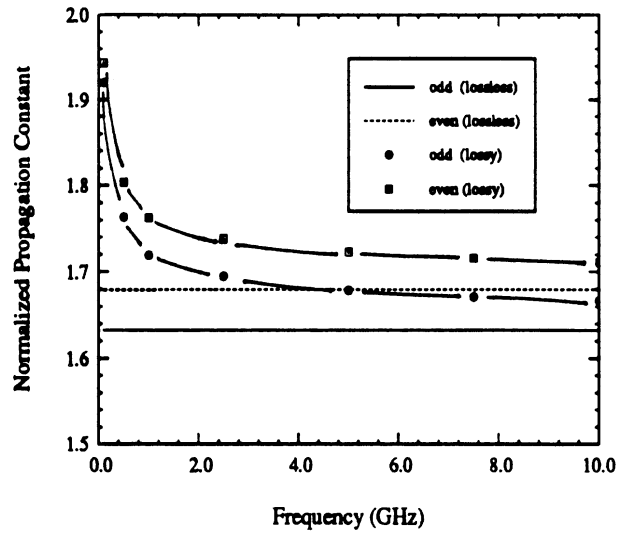


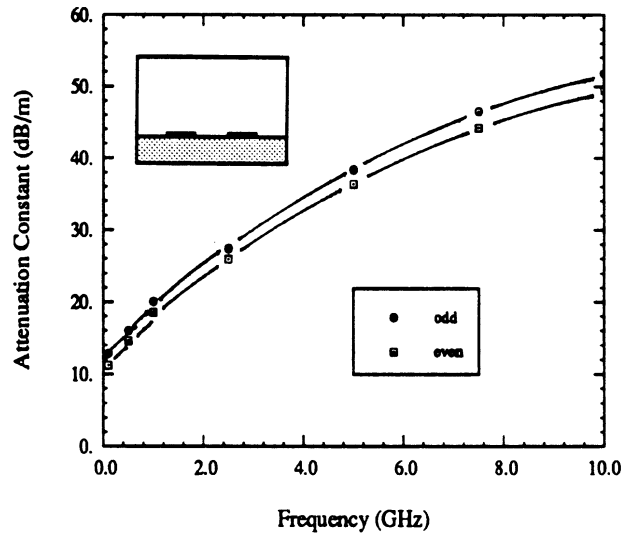
Figure 4.29: Conductor losses of coupled strips versus line separation ($a = 10$ mm, $b = 20$ mm, $W = d = 1$ mm, $\epsilon_r = 10$, $\sigma = 3.33 \times 10^7$ S/m, $\tan\delta = 2 \times 10^{-4}$, $f = 1$ GHz, $t = 0.01$ mm)

Broadside-coupled strips

The effect of losses on the propagation characteristics are illustrated here through the example of a two-level microstrip structure as a function of both horizontal (s) and vertical (d_2) spacing. In Figure 4.32, the equivalent *surface impedance* of the lines is described in terms of its resistance for the even and odd modes. The surface reactance has the same value for even and odd mode and therefore is not displayed here. The resistance for the even mode decreases monotonically as s and d_2 increase. For the odd mode, the surface resistance has a pronounced peak for $s = 100 \mu\text{m}$ and small vertical distances d_2 . This is due to the fact that the intensity of the magnetic field generated by the two lines add up near the inner edge and the current is concentrated at that point. This reduces the area where the current flows thus increasing the surface resistance.

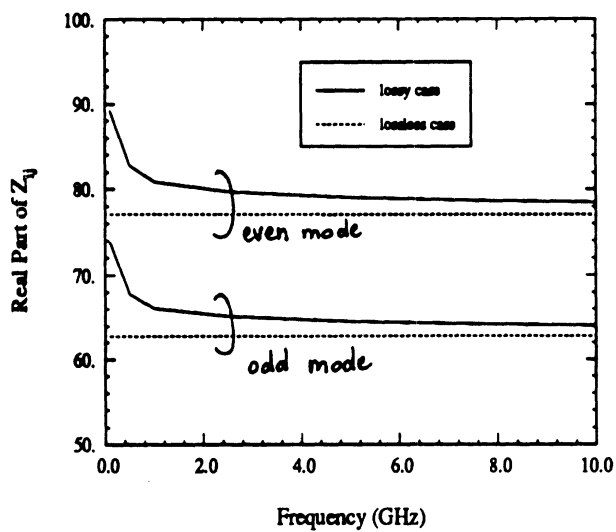


a. Phase constant

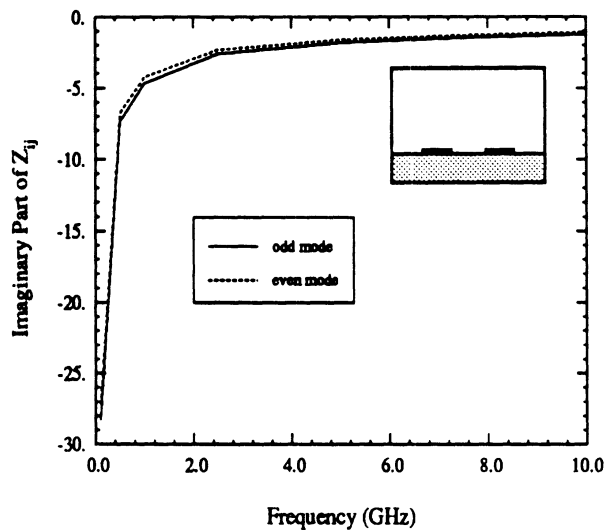


b. Attenuation constant

Figure 4.30: Two edge-coupled lines ($\epsilon_{r1} = 1$, $\epsilon_{r2} = \epsilon_{r3} = 4$, $\sigma = 4.8 \times 10^7$ S/m, $t = 4\mu\text{m}$, $d_1 = 40\mu\text{m}$, $d_2 = 20\mu\text{m}$, $w_1 = w_2 = 20\mu\text{m}$, $s = 40\mu\text{m}$)

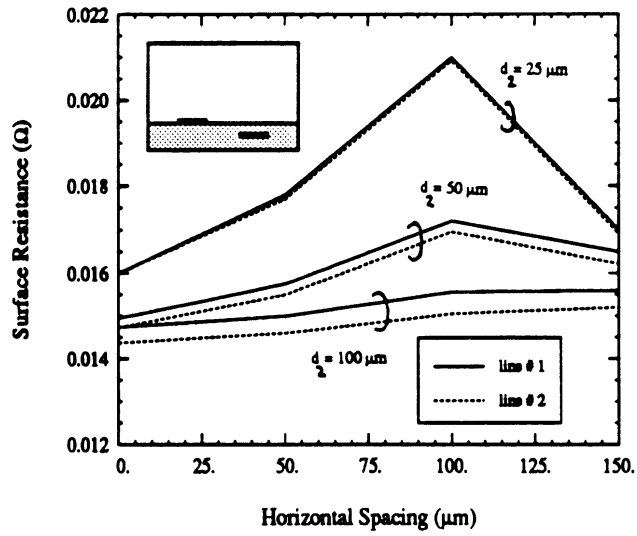


a. Real part of the characteristic impedance for the lossy and lossless case

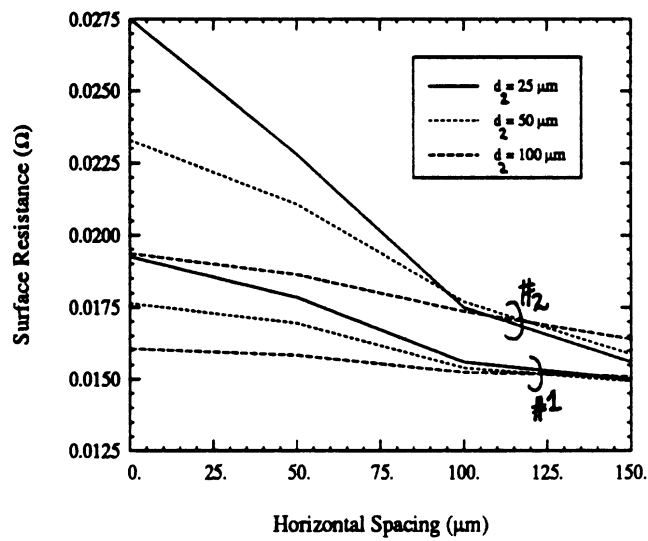


b. Imaginary part of the characteristic impedance (lossy case)

Figure 4.31: Frequency dependence of the characteristic modal impedances Z_{ij}



a. Surface resistance for odd mode



b. Surface resistance for even mode

Figure 4.32: Effect of strip spacing on the surface resistance for even and odd modes ($a = 1 \text{ mm}$, $b = 2 \text{ mm}$, $d_1 = 0.1 \text{ mm}$, $\epsilon_{r1} = 1$, $\epsilon_{r2} = \epsilon_{r3} = 4$, $\sigma = 3.33 \times 10^7 \text{ S/m}$, $t = 4 \mu\text{m}$, $d_3 = 100 \mu\text{m}$, $w_1 = w_2 = 100 \mu\text{m}$, $f = 5 \text{ GHz}$)

Figure 4.33 shows the behavior of the phase and attenuation constants for the odd and even modes as a function of horizontal (s) and vertical (d_2) separations. The phase constant follows the same overall behavior as in the lossless case. The attenuation due to conductor losses has the same trend as for edge-coupled lines [30]. As the vertical spacing is increased, the current is less affected by the other line and therefore the attenuation decreases, approaching the single strip value for both even and odd modes.

Coupling coefficient

The present study also involves the calculation of the coupling coefficient. In the case of two symmetric coupled lines, the coupling coefficient is defined according to classical transmission-line theory [70]

$$k = \left| \frac{j \sin \theta \left(\sqrt{\frac{Z_{oe}}{Z_{oo}}} - \sqrt{\frac{Z_{oo}}{Z_{oe}}} \right)}{2 \cos \theta + j \sin \theta \left(\sqrt{\frac{Z_{oe}}{Z_{oo}}} + \sqrt{\frac{Z_{oo}}{Z_{oe}}} \right)} \right| \quad (4.16)$$

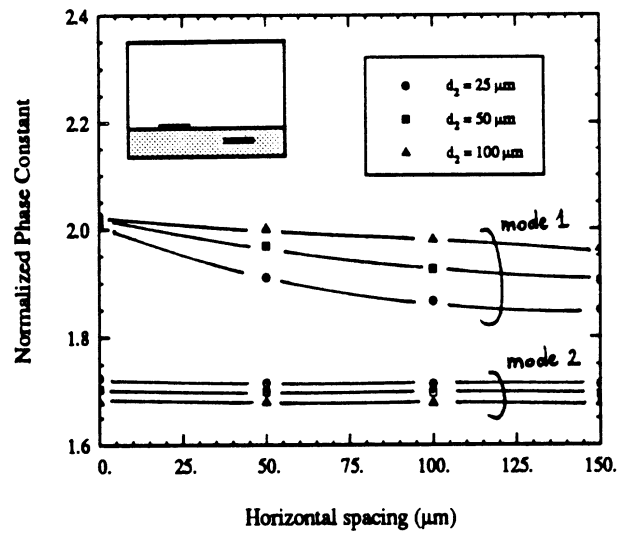
where Z_{oe} and Z_{oo} are the characteristic impedance of the even and odd modes respectively. The angle θ is the electrical length of the coupled lines. For maximum coupling, the coupler should be designed approximately $\frac{\lambda}{4}$ in length ($\lambda = \frac{\lambda_e + \lambda_o}{2}$) or

$$l = \frac{\pi}{\beta_o + \beta_e} \quad (4.17)$$

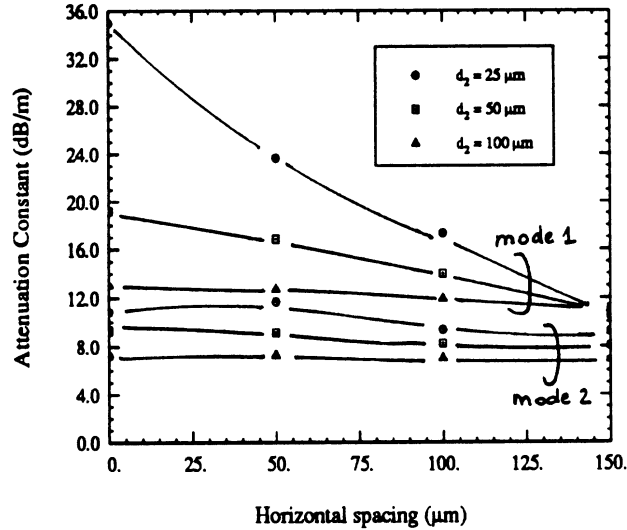
where β_o and β_e are the phase constants of the odd and even mode.

Coupling coefficient for the lossless and lossy case are presented in Table 1 as a function of separation s where k_o represents the coupling in the lossless case, and k_l is the calculated value for lossy strips.

Case A describes a broadsided-lines geometry where $b = 400$ mm, $\epsilon_{r1} = \epsilon_{r2} = \epsilon_{r3} = 1$, $\sigma = 3.33 \times 10^7$ S/m, $t = 3 \mu\text{m}$, $d_1 = d_3 = 31$ mm, $d_2 = 10$ mm, $w_1 = w_2 = 5$ mm, $f = 1$ GHz. Results are also shown for edge-coupled lines (Case B) with $\epsilon_{r1} = 1$,



a. Phase constant



b. Attenuation constant

Figure 4.33: Effect of strip spacing on the propagation constant of the dominant microstrip mode ($a = 1 \text{ mm}$, $b = 2 \text{ mm}$, $d_1 = 0.1 \text{ mm}$, $\epsilon_{r1} = 1$, $\epsilon_{r2} = \epsilon_{r3} = 4$, $\sigma = 3.33 \times 10^7 \text{ S/m}$, $t = 4 \mu\text{m}$, $d_3 = 100 \mu\text{m}$, $w_1 = w_2 = 100 \mu\text{m}$, $f = 5 \text{ GHz}$)

	s/d_2	$k_0(\text{dB})$	$k_1(\text{dB})$
CASE A	0	-7.556004	-7.568321
	2	-13.15119	-13.16493
	4	-20.70458	-20.70458
	6	-28.03051	-28.03051
CASE B	0.02	-7.9248	-8.0724
	0.1	-10.0147	-10.0997
	0.5	-17.9334	-18.0203
	1.0	-25.5180	-25.6149

Table 4.1: Coupling Coefficient for edge-coupled and broadside-coupled lines

$\epsilon_{r2} = \epsilon_{r3} = 10$, $\sigma = 3.33 \times 10^7 \text{ S/m}$, $t = 4\mu\text{m}$, $d_2 = d_3 = 50\mu\text{m}$, $w_1 = w_2 = 100\mu\text{m}$, $f = 1 \text{ GHz}$. Because of the particular geometry and the fact that wide lines were chosen, the effect of ohmic losses is relatively small. However, for narrow lines used in digital and high frequency applications, the effect of conductor losses will be much more pronounced.

4.5 Time domain analysis

In order to study the dispersive effects of both the dielectric inhomogeneity and the ohmic losses on pulse propagation and cross-talk, a one-inch section of transmission line was analyzed. The two strips are identical, $20 \mu\text{m}$ wide and $5 \mu\text{m}$ thick, with conductivity $\sigma = 4.8 \times 10^7 \text{ S/m}$, and positioned at a distance of $20\mu\text{m}$ from one another. The width of the metallic enclosure is $500\mu\text{m}$ and its height $60 \mu\text{m}$. The substrate is $20\mu\text{m}$ thick and its relative dielectric constant $\epsilon_r = 4$. The active line is driven by a source generating a trapezoidal-shape pulse train of amplitude 1 V and period 10 ns corresponding to a clock frequency of 100 MHz . The duration of each pulse in the train is 1 ns , with rise and fall times of 100 ps . The input impedance at the source and the terminating impedance for the active line is taken to be 74

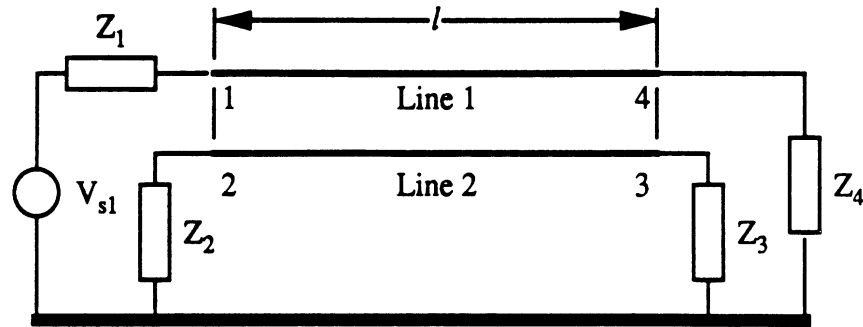
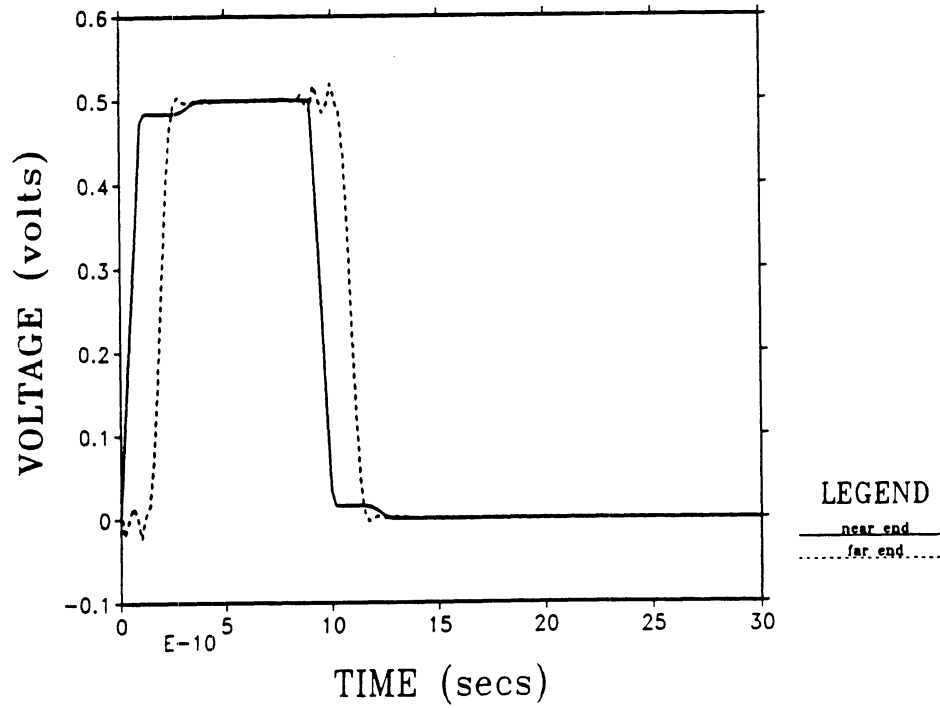


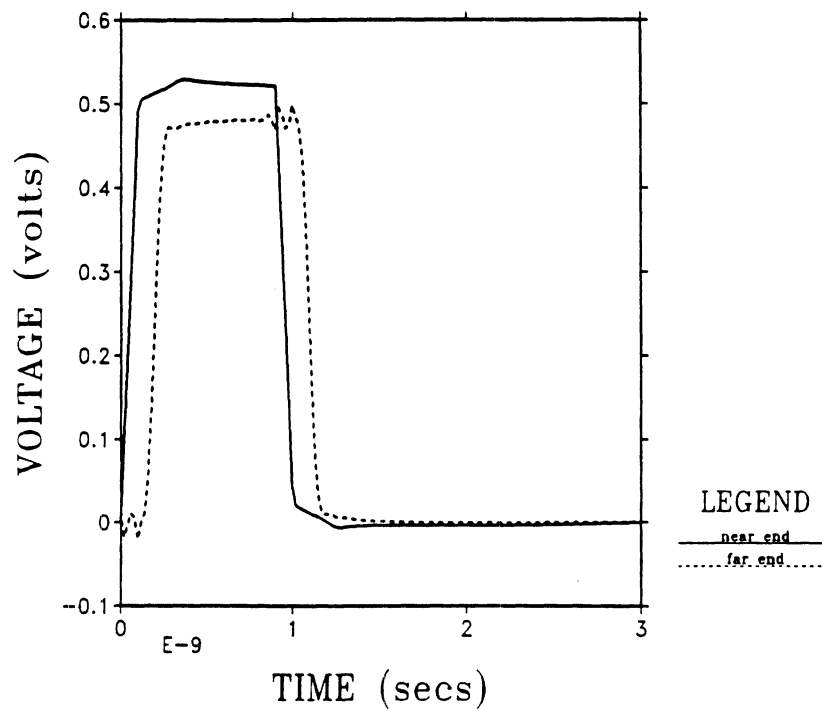
Figure 4.34: Equivalent circuit for the active and sense lines

ohms, a value close to the characteristic impedance for a single microstrip with strip dimensions, substrate thickness and dielectric constant same as those for the coupled line under consideration. Similarly, 74 ohm resistors are used to terminate both ends of the sense line.

In the previous section, the frequency dependence of the even- and odd-mode phase and attenuation constant, was plotted over a range of frequencies extending up to 10 GHz. This upper frequency limit was adequate for the excitation signal under consideration. The voltages at the near-end and the far-end points for the active line with and without ohmic losses are shown in Figure 4.35 a) and 4.35 b), respectively. The plots depict only one of the pulses in the pulse train. Notice that the lack of attenuation for the lossless case results in a transmitted signal at the far end of amplitude equal to that at the near end. For the lossy case, shown in Figure 4.35 b), the attenuation caused by the losses becomes apparent. In addition, the mismatch at the source, caused by the frequency-dependence of the modal impedances of the lines, results in an incident pulse of amplitude somewhat higher than the 0.5 V obtained for the lossless case. Figure 4.36 a) and 4.36 b) show the near-end and far-end cross-talk voltages on the sense line for the lossless and lossy case, respectively. Notice that, as expected, far-end cross-talk levels are lower for the lossy case. In addition, some of

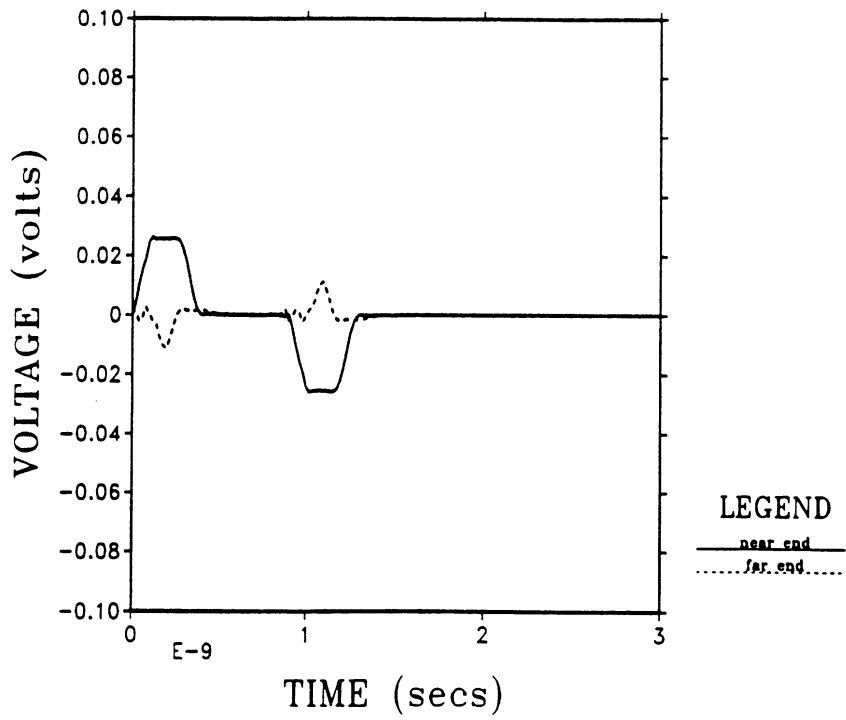


a. Lossless case

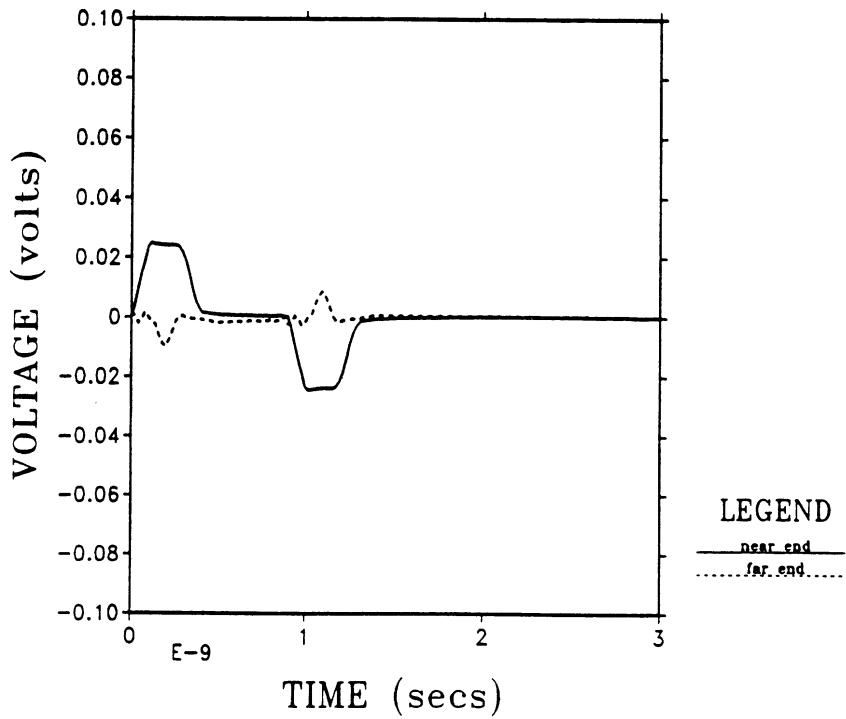


b. Lossy case

Figure 4.35: Voltages at the near-end and far-end points for the active line



a. Lossless case



b. Lossy case

Figure 4.36: Voltages at the near-end and far-end points for the sense line

the sharpness of the cross-talk signals observed in the lossless case is lost when losses are taken into account. This is due to the larger values of the attenuation constant at higher frequencies. Such effects are expected to become more profound as clock frequencies approach the gigahertz range.

CHAPTER V

LOSSES IN HIGH TEMPERATURE SUPERCONDUCTING THIN-FILM LINES

In this chapter, an integral equation approach is applied to calculate the propagation characteristics of high temperature thin-film superconducting lines at high frequencies. To evaluate losses in these lines, the superconducting strips are replaced by frequency-dependent surface impedance boundaries. The values of these surface impedances are measured experimentally by a TE_{01} cavity technique. Using this method, a parametric study is performed where phase and attenuation constants as well as characteristic impedance are evaluated as functions of frequency, temperature, permittivity and geometry of the structure.

5.1 Motivation and approach

Low temperature superconductors have been known since 1911, but their use was limited by the extremely low temperatures of early materials (4° to 23° K) requiring liquid helium as coolant. New high-temperature superconductors were introduced in the 1980's and operate in the 77° to 120° K temperature range, where liquid nitrogen can be used for cooling purposes. Superconductivity is characterized by two effects, namely zero resistance to electrical current, and diamagnetism, i.e. the expulsion of magnetic fields below a critical temperature T_c , a critical magnetic field and a critical

electrical current density. For high frequency applications, the major advantage of high temperature (T_c) superconductors is the reduced surface resistance of the lines as compared to normally conducting metal strips. This, in turn, significantly decreases conductor loss in microwave and millimeter-wave circuits where ohmic losses can be an important limitation, as discussed in the previous chapters. Also, the use of superconducting transmission lines in VLSI circuits may lead to higher switching speed, higher data bandwidth, lower cross-talk, higher density and reduced resistive heating. The lines currently developed are made of thin films which have a thickness large compared to λ , the penetration depth of the magnetic field into the superconductor. Several groups have reported theoretical evaluation of the surface resistance and propagation constant of high T_c films and strips [71]-[100]. One common characteristic in all these attempts has been the observed discrepancy between theoretical and experimental results which, in the case of attenuation constant, may be of a few orders of magnitude. This disagreement is mainly due to the inadequacy of the implemented theoretical models, such as the London or BCS theory, to characterize the electromagnetic behavior of the high T_c superconducting materials as they are presently made.

To avoid the shortcomings of existing theoretical treatments, the presented method does not attempt to solve for the electromagnetic fields inside the superconducting thin films. Only the electric/magnetic field relation on the surface of the strips is utilized to create an equivalent surface impedance boundary which will replace the superconducting strips. Due to the fact that superconducting strips made today have a large width-to-thickness ratio, the electric/magnetic field ratio on the strip surface is almost identical to the surface impedance of a thin superconducting plane. As a result, measured values of this surface impedance can simulate the superconducting

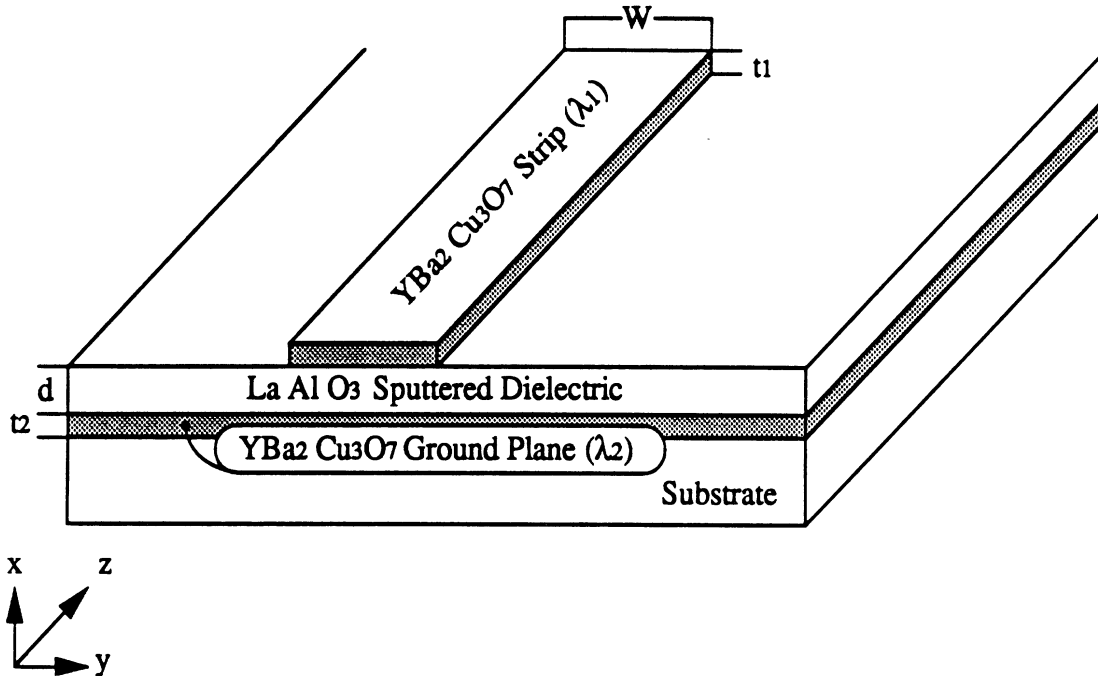


Figure 5.1: Superconducting microstrip line configuration

strip very accurately. Having defined an equivalent surface impedance, an integral equation method is developed to study the behavior of high T_c superconducting thin film strips at high frequencies [36]. However this simulation does not hold for very narrow lines where the edge conditions affect the current distribution considerably.

5.2 Theory

A shielded planar high T_c superconducting microstrip line of $\text{YBa}_2\text{Cu}_3\text{O}_7$ film (YBCO) deposited on lanthanum aluminate substrates (LaAlO_3) is considered as shown in Figure 5.2. The LaAlO_3 is well-suited for high-frequency passive component

applications because of its low losses in the microwave and millimeter-wave range. Also its dielectric constant is relatively low as compared to other materials (e.g. SrTiO₃) used in superconducting circuits. An important attribute of LaAlO₃ is that it is a good host for YBCO unlike MgO which has a more reasonable permittivity ($\epsilon_r \sim 10$) for microwave circuit design but is not lattice matched and can grow only under certain conditions. The permittivity of *LaAlO*₃ is weakly dependent on temperature with a nominal value around 22 at 20 GHz. Because different values have been reported in the literature [75],[76], a parametric study of the effect of the dielectric constant on the propagation characteristics is presented in the next section. Dielectric losses in the substrate material are accounted for by assuming a complex permittivity given by:

$$\epsilon = \epsilon_r (1 - j \tan \delta). \quad (5.1)$$

The imaginary part of the permittivity of this material varies with temperature from 0.2 at 20K to 1.1 at 150K [76]. However, up to this point, values of loss tangent are not precise and few experiments have given consistent values for $\tan \delta$ as a function of temperature and frequency. This discrepancy in the measured loss tangent reflects the fact that quality control of available films is poor and variations are hard to measure. Both the permittivity and loss tangent are independent of frequency in the range of interest.

The superconducting strip and ground plane which are of thickness t are replaced by equivalent surface impedance boundaries with values equal to the experimentally measured surface impedance of an infinite superconducting thin film of the same thickness. To confirm the validity of using the surface impedance of a thin film rather than a strip, calculation of the per-unit length impedance of a superconducting strip was performed for different widths, under the assumptions of weak magnetic fields

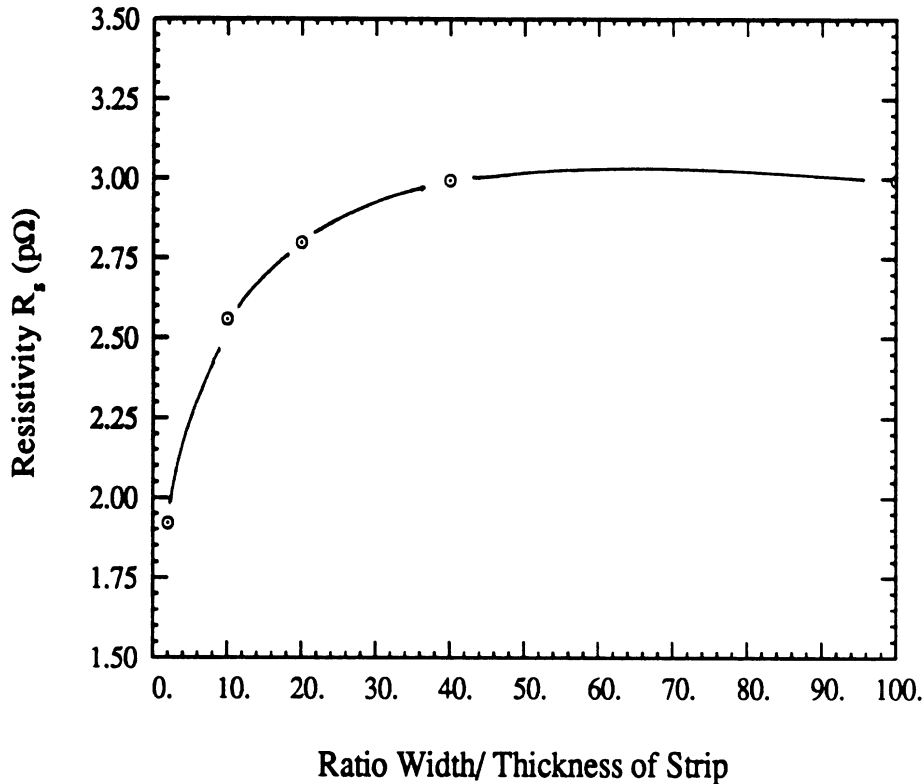


Figure 5.2: Surface resistance of a $YBa_2Cu_3F_xO_y$ microstrip line on a $LaAlO_3$ substrate as a function of the strip width to substrate thickness ratio ($\epsilon_r = 22$, $h = 0.5$ mm, $t = 0.5$ μ m, $a = b = 2.5$ mm, $T = 4$ K, $f = 5$ GHz)

and temperatures T well below the critical temperature T_c as presented in [72]. The results indicate that, when the width-to-thickness ratio of the strip becomes larger than 50, the surface impedance of the strip is approximately equal to the surface impedance of an infinite film of the same thickness (Figure 5.2). The present study assumes that the penetration depth λ is smaller than the film thickness. In high T_c superconductors and for the materials specified above, the width-to-thickness ratio is 500 and the penetration depth is smaller than one third of the film thickness. Under these conditions, the surface impedance of the superconducting strips can be effectively approximated by the measured surface impedance of the corresponding

infinite thin film. The same surface impedance replaces the superconducting ground plane. With these equivalent surface impedances in place, an integral equation for the unknown superconducting current is then formulated and solved by the method of moments.

5.2.1 Fabrication

Thin films of $YBa_2Cu_3O_x$ (YBCO) were deposited by simultaneous magnetron co-sputtering using Y , Cu and BaF_2 targets onto $LaAlO_3$ (100) 1.5 inch substrates. The depositions were carried out with the substrate at ambient temperature on both sides of the $LaAlO_3$ substrates. After dicing the substrate into 1 by 0.5 inch pieces for the RF devices, they were annealed at 850°C for 1 hour in a wet O_2 environment. The variation in thickness and composition uniformity was about 2% across a 1.5 inch substrate as determined by RBS and resistivity measurements. Each film ranged in thickness from 4000\AA to 6000\AA . Using resistivity and a.c. magnetic susceptibility measurements, the superconducting transition onset was around 90K with a transition width of 2K. Analysis of the films using X-ray diffraction and cross-section transmission electron microscopy showed highly oriented structures with the a and c axes perpendicular to the substrate. The films were patterned using standard photolithography followed by exposure to dilute phosphoric acid. Ohmic contacts were made using sequential depositions of 2000\AA Ag and 2000\AA Au which were annealed in O_2 at 550°C .

5.2.2 Measurement of the surface impedance

The surface impedance used in the theoretical derivation is directly related to the measured surface impedance. The *surface resistance* of the films described above was

measured by two different methods, namely the TE_{01} cavity technique [77] and the stripline resonator technique [78]. The TE_{01} cavity measurements were performed at three different frequencies (22, 86 and 146 GHz) as a function of temperature. The measurement procedure has been presented in [79] and will not be repeated here. The film was also measured at 4.2 K using a stripline resonator technique and good agreement with the cavity method was obtained. In both studies, the ω^2 dependence was verified and is consistent with the BCS theory and with experimental measurements on conventional low T_c superconductors. The surface resistivity varies from approximately $1m\Omega$ at 4.2K to $10m\Omega$ at 70K for a frequency of 22GHz. In situ grown films of YBCO of approximately the same thickness have been found to have significantly lower resistance, as low as $0.1m\Omega$ at 4.2 K at a frequency of 1GHz [79].

The *surface reactance* behaves as purely inductive and varies linearly with frequency as has been reported by several authors [80]-[82]. The value of the inductance of the superconducting strips considered here has been measured experimentally by A.T. Fiory using a two-coil mutual-inductance measurement technique [81].

In view of the above, the surface impedance used in our theoretical derivations is given by:

$$Z_{sc}(f, T) = R(f, T) + jX(f, T) \quad (5.2)$$

where $R(f, T)$ represents the resistive losses and $X(f, T)$ represents the inductive energy stored within the superconductors. In Equation (5.2), R and X are given by

$$R(f, T) = \omega^2 A(T) \quad (5.3)$$

$$X(f, T) = \omega L_{sc}(T). \quad (5.4)$$

For YBCO films at 77K, the value of $A(77)$ is $2.066 \text{ m } \Omega \cdot \text{sec}^2$ and L_{sc} is about 2 pH.

5.2.3 Calculation of the superconducting current

The influence of superconductor losses on the propagation constant is evaluated using an integral equation method. In this mathematical formulation, the superconducting strip is replaced by an infinitesimally thin surface impedance which serves as a boundary condition for the electromagnetic field excited in the volume surrounding the strip. The impedance of this surface boundary is given by (5.2) and describes the effect of the frequency dependent field penetration in the superconductor and the presence of grain boundaries. The fields in the dielectric region, which consists of an arbitrary number of layers, are computed by a method of moments solution of Pocklington's integral equation subject to the new introduced boundary condition as discussed in Chapter 3.

The resulting surface integral equation is given by:

$$\int_{C_w} \bar{\bar{G}}(x/x') \cdot \bar{J} dy' - Z_{sc} \bar{J} |_{k_z=k_z^{MS}} = 0 \quad (5.5)$$

where C_w is a path along the width of the conductor, $\bar{\bar{G}}$ is the dyadic green's function for the boundary value problem defined in Chapter 2 and \bar{J} is the superconducting current flowing in the impedance sheet Z_{sc} . The integral equation in (5.5) is solved numerically to give the complex propagation constant k_z^{MS} . The characteristic impedance of the superconducting lines is then evaluated from the conventional power-current relation shown below:

$$Z_o = \frac{P_{sc}}{2 |\bar{J}|^2} \quad (5.6)$$

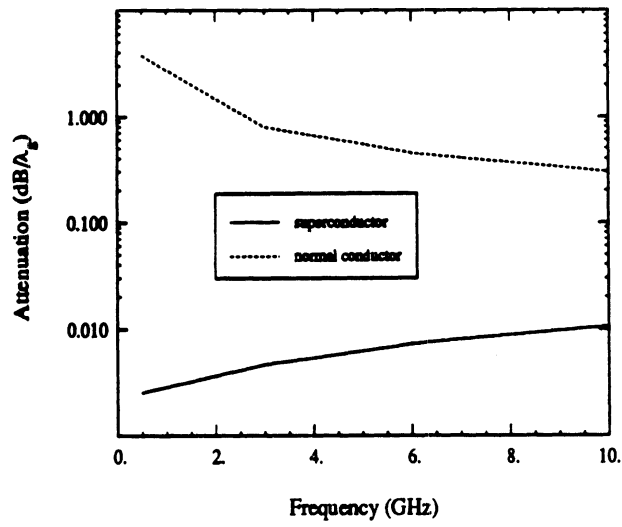
where P_{sc} is the power propagating in the superconducting structure and \bar{J} is the supercurrent.

One of the main advantage of superconducting materials is their low surface resistance. However, zero resistance at DC is somewhat misleading because the surface

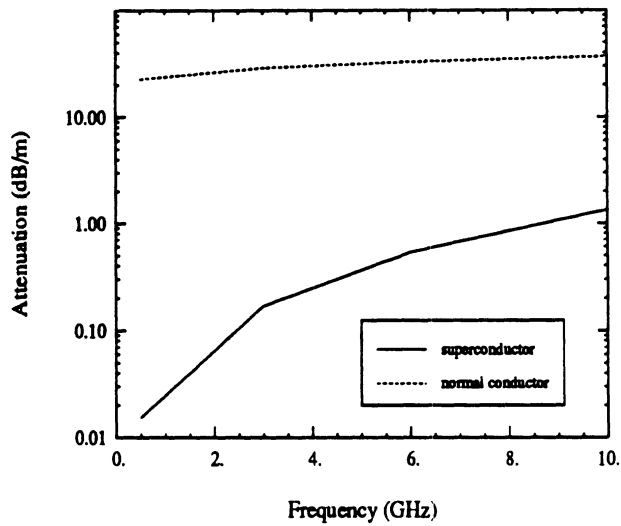
resistance of superconductors varies as the square of frequency, whereas the loss is much slower for a normal conductor. Since superconductor loss starts many orders of magnitude lower than copper, a good superconducting film will be comparatively more advantageous up to several hundred GHz. For comparison purposes, conductor loss is evaluated for superconductors and normal conductors in an identical configuration. In the case of normal conductors, the equivalent frequency-dependent impedance surface derived in Chapter 3 was used rather than applying the conventional skin-effect approximation which is not valid at low frequencies where the fields do not merely follow a square-root f dependence. Results show that for normal conductors, the conductor losses decrease with frequency when expressed in dB/ λ_g . In contrast, the ohmic losses in superconductors increase because of the ω^2 dependence of the surface resistivity of the thin film material. These trends are shown in Figure 5.3. As mentioned previously, normal conductors have a skin-depth which varies inversely with the frequency. On the other hand, due to the Meissner effect, waves do not propagate much in the superconductor and therefore the penetration depth of a superconductor is a function of the material rather than frequency. High frequency skin effects in normal and superconductors are sketched in Figure 5.4 where $\lambda \simeq 200$ nm for a good thin-film, and δ is about $2 \mu\text{m}$ for gold at 1 GHz.

5.3 Results

Using the approach described in the previous section a computer program was developed to calculate the complex propagation characteristics of superconducting lines. Throughout this section, unless otherwise noted, it is assumed that the structure has the geometry shown in Figure 5.2 with $\epsilon_r = 22$, $\mu_r = 1$, $h = 500\mu\text{m}$, $t = 0.5\mu\text{m}$ and $w = 250\mu\text{m}$. The operating temperature is taken to be below the



a. Attenuation constant in dB/λ_g



b. Attenuation constant in dB/m

Figure 5.3: Attenuation constant vs. frequency for (a) normal strips ($\sigma = 3.33 \times 10^7$ S/m, $T = 300$ K) and (b) superconducting strips ($T = 70$ K)

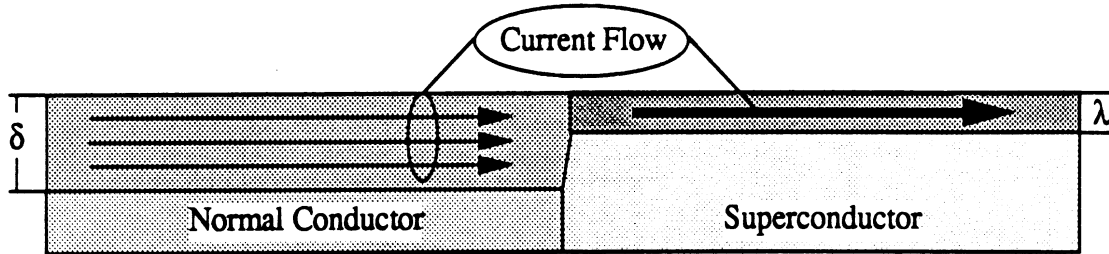


Figure 5.4: Current flow in normal and superconductors

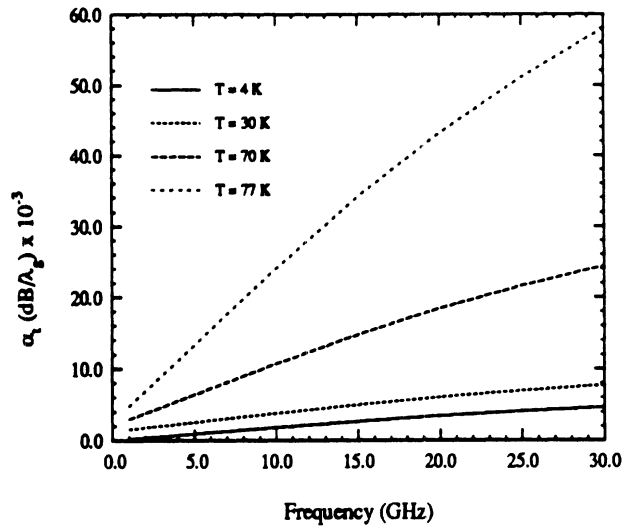
critical temperature T_c of the superconducting thin film.

The main goal of this study is to give a qualitative understanding of the effect of temperature, frequency, substrate permittivity, line width and substrate thickness on the attenuation associated with thin-film lines printed on $LaAlO_3$ substrates.

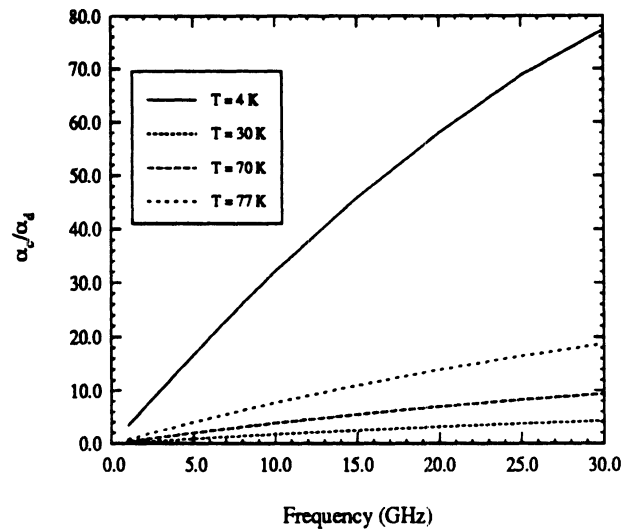
5.3.1 Temperature variation

As it has been discussed earlier, when the temperature varies from 4.2K to 77K, both R and $\tan \delta$ vary while ϵ_r remains unaffected. Figure 5.5a shows the effect of temperature and frequency variation on the attenuation constant α for a 250 μm wide post-annealed superconducting line. As expected, both dielectric and conductor losses increase with increasing temperature. The attenuation constant is usually given in Np/m or dB/m. However, when comparing losses over a large range of frequencies and different geometries, it is more informative to express α in dB/ λ_g where λ_g is the microstrip wavelength.

The ratio of conductor to dielectric losses (Figure 5.5b) gives an indication as to



a. Attenuation constant vs. frequency for $T = 4, 30, 70, 77$ K



b. Ratio conductor/dielectric losses vs. frequency for $T = 4, 30, 70, 77$ K

Figure 5.5: Effect of temperature on the attenuation constant of the dominant microstrip mode as a function of frequency ($\epsilon_r = 22$, $w = 250 \mu\text{m}$, $h = 0.5$ mm, $t = 0.5 \mu\text{m}$, $a = b = 2.5$ mm)

the limiting mechanism which affects propagation characteristics in superconducting lines printed on $LaAlO_3$ substrates. It is observed that, for low frequencies, losses due to the nonzero resistivity of the superconducting strips are overshadowed by dielectric losses in the dielectric substrate. However, depending on the temperature and frequency of operation, conductor losses may become comparable and even larger than dielectric losses as shown in the case of $T = 4$ K in Figure 5.5b. The theoretical method used in this paper was developed for a shielded microstrip geometry. The cut-off frequency of the shielding waveguide depends on its dimensions and on the substrate layer. For the $LaAlO_3$ substrates ($\epsilon_r \sim 22$), the waveguide cut-off frequency is about 30 GHz. To study the propagation characteristics over a larger frequency range, a waveguide of smaller dimensions was considered. Both geometries exhibit the same dependence of the attenuation constant on temperature and frequency with a predominant contribution of conductor losses in the smaller structure.

Several approaches are used to grow superconducting thin films. Besides the post-annealing process described above which requires high temperature annealing (about 900°C), in-situ thin film epitaxial growth up to 5000\AA is performed at lower temperature ($650\text{-}700^\circ\text{C}$) and has a surface resistance smaller by a factor of 5 [79],[83]. The results show that the in-situ technique yields a lower attenuation than the post-annealed technique (Figure 5.6). However a limitation of the in-situ technique is that it only allows for single side coating. In the case of post-annealed technology thin film coverage on both sides of the substrate is possible, thus both ground plane and circuitry are made of superconducting YBCO films. Another advantage of post-annealing technology is the large area uniformity for YBCO films deposited by co-sputtering ($\sim 5\text{ cm}^2$) as compared to $\sim 1\text{ cm}^2$ for in-situ grown films.

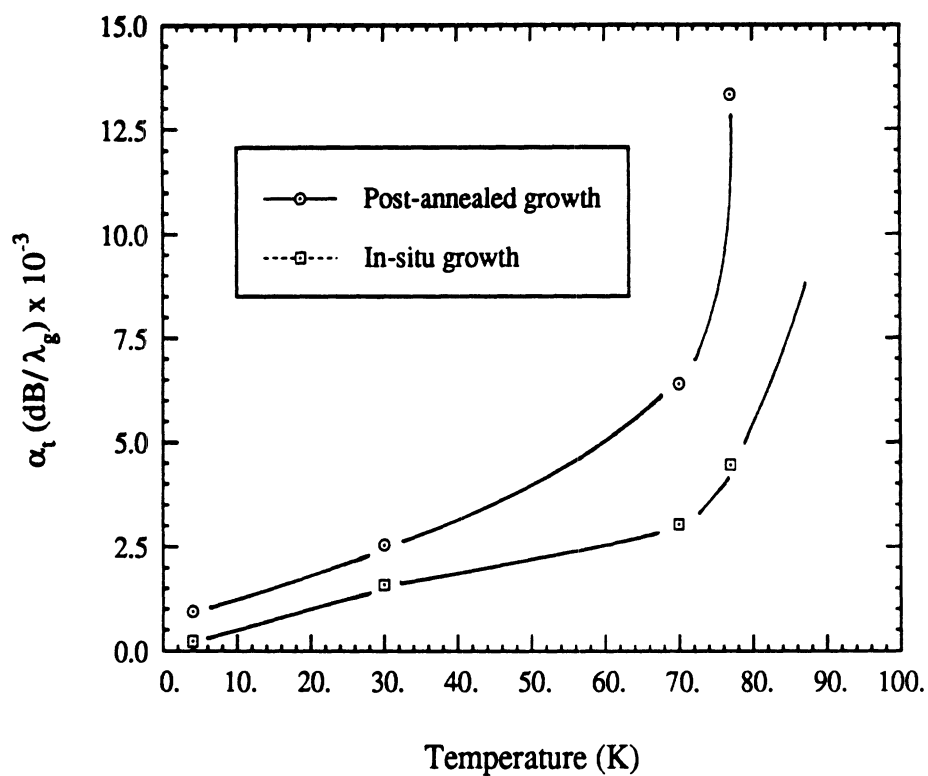


Figure 5.6: Comparison of attenuation constant for post-annealed and in-situ thin film lines ($\epsilon_r = 22$, $w = 250 \mu\text{m}$, $h = 0.5 \text{ mm}$, $t = 0.5 \mu\text{m}$, $a = b = 2.5 \text{ mm}$, $f = 5 \text{ GHz}$)

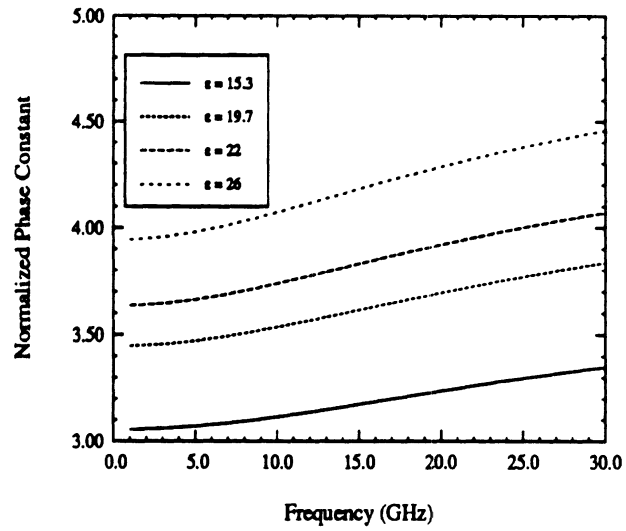
5.3.2 Permittivity variation

Because of discrepancies in the real part of the permittivity reported in the literature, it was found of interest to calculate the propagation constant for different values of ϵ_r of the substrate $LaAlO_3$. The values of ϵ_r chosen for this study span the range of available published data with $\epsilon_r = 15.3$ [84], $\epsilon_r = 19.7$ [76], $\epsilon_r = 22$ (nominal value) and $\epsilon_r = 26$ [75]. These data have been measured for several $LaAlO_3$ substrates and in different experimental set-ups. The results reflect the essential trends of β and α with varying ϵ_r (Figure 5.7). It is shown that α in dB/ λ_g is independent of the choice of ϵ_r for frequencies lower than 20 GHz.

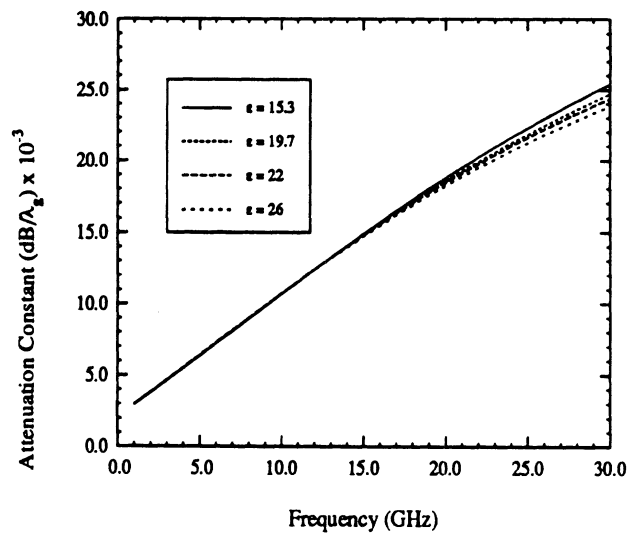
5.3.3 Line width and substrate thickness variation

The propagation characteristics of post-annealed superconducting lines are also studied as a function of the height of the substrate and line width. The phase constant (Figure 5.8) strongly depends on both parameters and dispersion occurs as the width of the strip and substrate thickness are increased. As expected, in the case of thin substrates, dispersion happens at much higher frequencies, which is of interest when designing circuits with very short pulses or delay lines. The attenuation constant (Figure 5.9) varies inversely to the height of the substrate and width of the line. The characteristic impedance (Figure 5.10) follows the same trend as in the case of lossless lines and shows very little dispersion over the frequency range studied here.

The validity of this program has been verified in the case of lossy normal conducting strips in Chapter 4. For further validation, attenuation derived by the present method was compared with calculated results using the phenomenological loss equivalence method (PEM) [100]. The PEM method was based on London's equations which ignore the presence of grain boundaries and assume perfect superconductors.

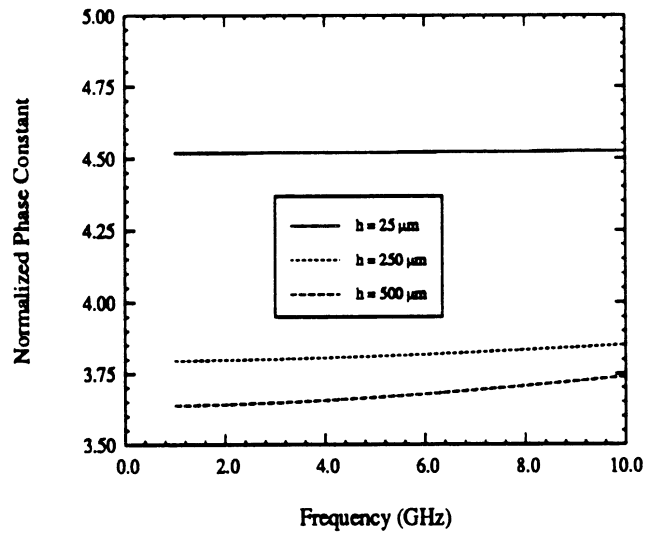


a. Phase constant

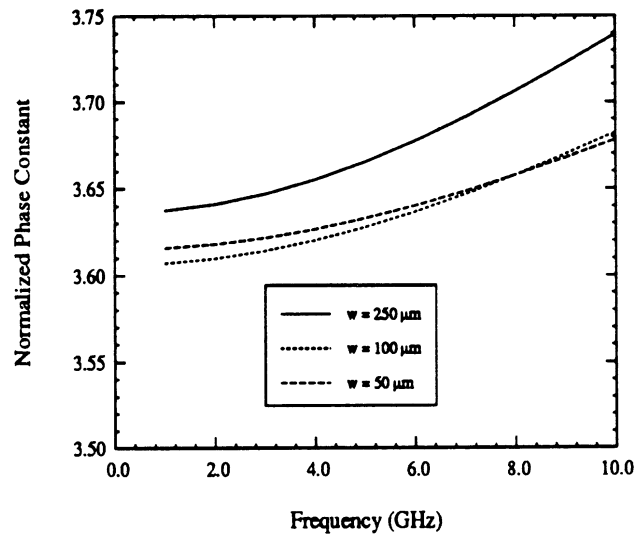


b. Attenuation constant

Figure 5.7: Attenuation constant vs. frequency as a function of permittivity ($w = 250 \mu\text{m}$, $h = 0.5 \text{ mm}$, $t = 0.5 \mu\text{m}$, $a = b = 2.5 \text{ mm}$)

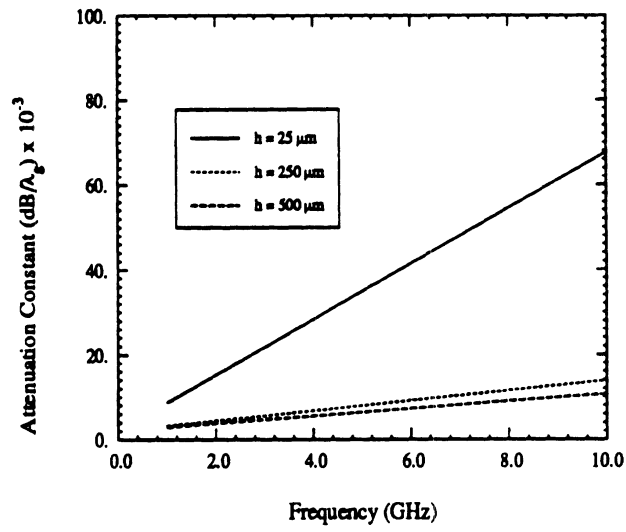


a. Effect of height variation ($w = 250 \mu\text{m}$)

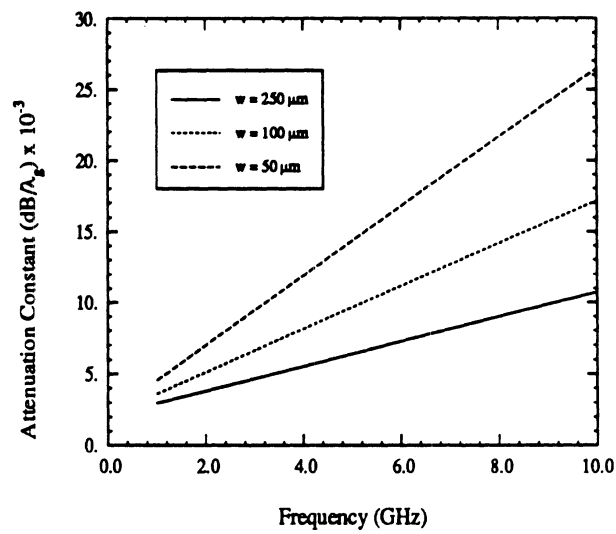


b. Effect of width variation ($h = 0.5 \text{ mm}$)

Figure 5.8: Phase constant of the dominant microstrip mode ($\epsilon_r = 22$, $\tan\delta = 5 \times 10^{-5}$, $t = 0.5 \mu\text{m}$, $R_s = 1 \text{ m}\Omega$)

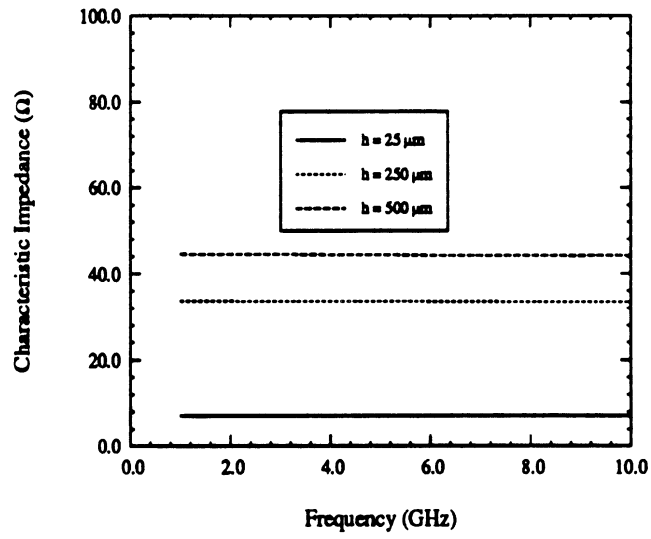


a. Effect of height variation ($w = 250 \mu\text{m}$)

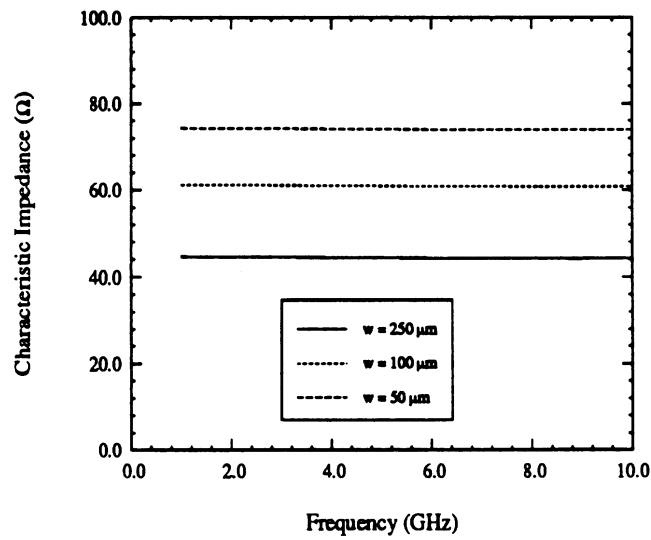


b. Effect of width variation ($h = 0.5 \text{ mm}$)

Figure 5.9: Attenuation constant of the dominant microstrip mode ($\epsilon_r = 22$, $\tan\delta = 5 \times 10^{-5}$, $t = 0.5 \mu\text{m}$, $R_s = 1 \text{ m}\Omega$)



a. Effect of height variation ($w = 250 \mu\text{m}$)



b. Effect of width variation ($h = 0.5 \text{ mm}$)

Figure 5.10: Characteristic Impedance of the dominant microstrip mode ($\epsilon_r = 22$, $\tan\delta = 5 \times 10^{-5}$, $t = 0.5 \mu\text{m}$, $R_s = 1 \text{ m}\Omega$)

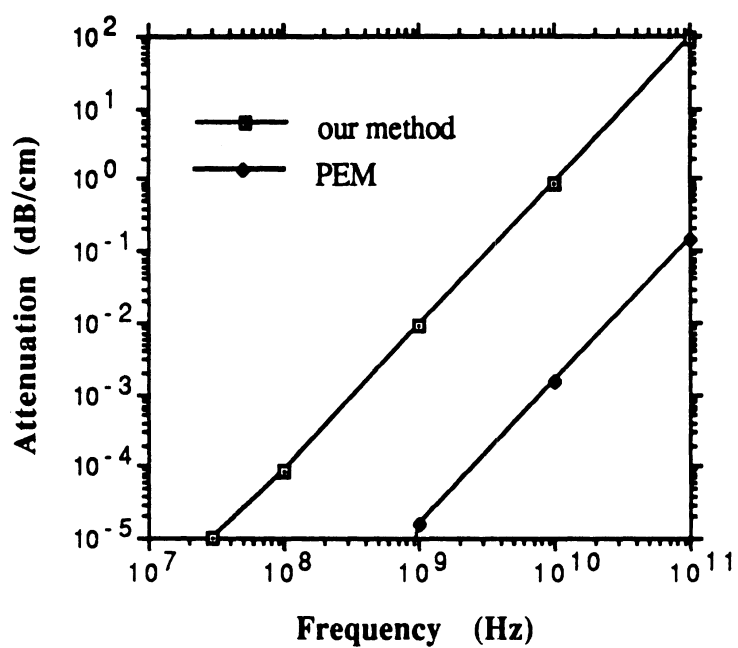


Figure 5.11: Attenuation constant vs. frequency using the present method and the PEM method ($\epsilon_r = 3.9$, $\tan\delta = 10^{-4}$, $w = 2 \mu\text{m}$, $h = 1 \mu\text{m}$, $a = b = 50 \mu\text{m}$, $T = 77 \text{ K}$)

Microscopic loss mechanisms such as the loss in granular films due to flux penetration in the weak links is included in the present method by using the actual measured values of the film surface impedance. As a result, the attenuation predicted by the PEM method is lower than the one predicted by this work (Figure 5.11).

CHAPTER VI

DIELECTRIC LINES: THE GENERALIZED INTEGRAL EQUATION METHOD

6.1 Motivation and background

At the present time, almost all monolithic circuits are made of thin strip conductors which provide simplicity in the fabrication and desired guiding properties for frequencies up to the millimeter-wave region. However, this technology introduces radiation and ohmic losses which become unacceptably high as the frequency approaches the terahertz region. In order to avoid these limitations, novel dielectric guiding structures and circuit elements operating in the terahertz regime have been recently proposed that use epitaxial semiconducting materials or heterostructures on GaAs or InP substrates [85], [1]. These low-loss ridged and semi-embedded lines are appropriate for high frequency monolithic applications, as they exhibit several advantages over more conventional conducting lines and can be designed for optimum confinement by stacking layers and ridges of different permittivities (Figure 6.1). They provide low dielectric losses compared to conductor losses of metallic interconnects at sub-millimeter frequencies. Lines of thickness and width measuring a fraction of a guided wavelength make for feasible fabrication by etching a layered wafer, and allow for easy construction of passive circuit elements as well as simple

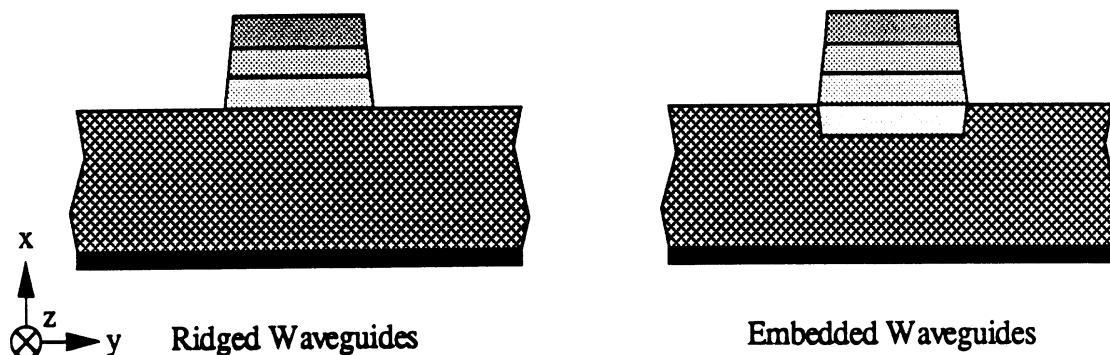


Figure 6.1: General configuration of low-loss ridged waveguides using heterostructures

integration of active devices. Types of dielectric lines can be classified based on their geometry and their permittivity relative to the substrate as shown in Figure 6.2.

The theoretical characterization of this new type of dielectric structure plays an important role in the design of low-loss circuits operating in the sub-millimeter wave region, such as power dividers, impedance transformers and filters. To design these circuit elements, a rigorous theoretical characterization is needed. Theoretical studies on geometrically simple optical and microwave dielectric waveguides have been presented in the past decade using approximate and numerical methods. The approximate methods are represented by an analytical approximation introduced by Marcatili [86] and by the effective index method [87], [88]. The numerical methods are divided into variational methods [89], mode-matching methods, finite-element methods [90] and integral equation methods using polarization currents [91]. These methods have been exclusively applied to two-dimensional problems where they perform a fine discretization of the cross-section introducing many unknowns and strong

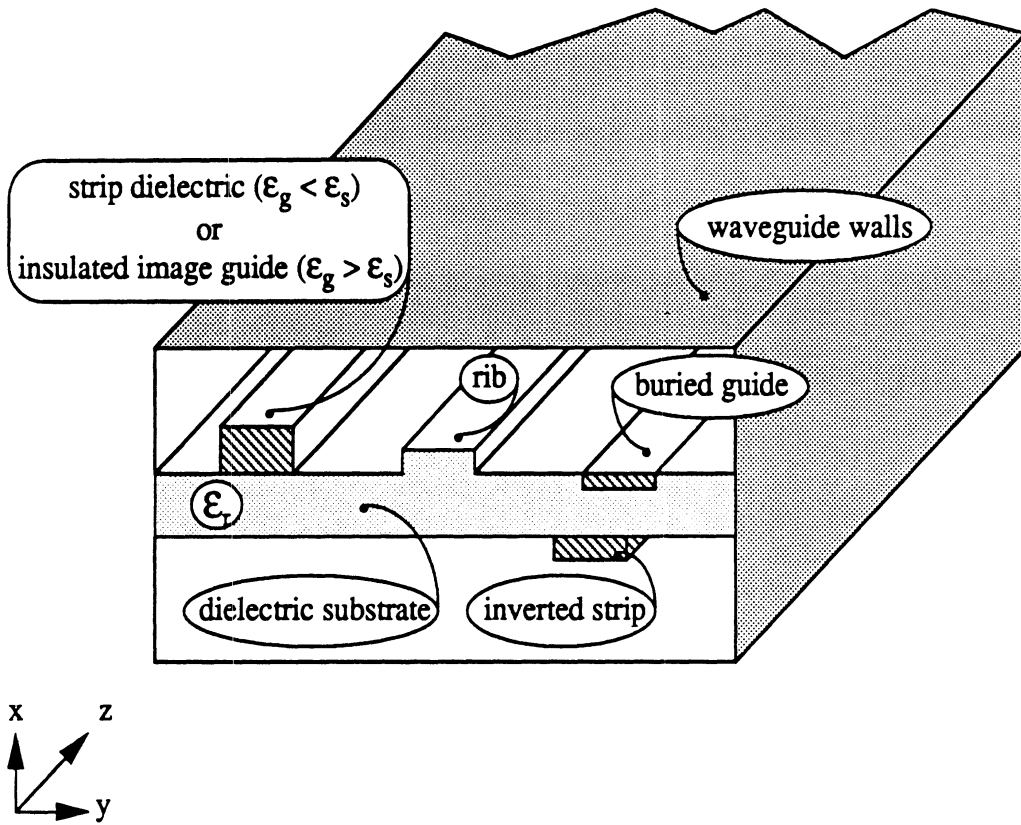


Figure 6.2: General configuration of dielectric waveguides

numerical instabilities. Consequently, an extension of these methods to three dimensional problems introduces many limitations and requires special care [92].

In this chapter, a novel two-dimensional theoretical method is presented which is appropriate for the analysis of multiple thin dielectric lines on multilayered substrates in a manner that allows for easy and accurate characterization of their propagation parameters. This approach is unique in terms of combined accuracy and simplicity and has demonstrated good performance when applied to basic dielectric structures. The major advantage of this technique is that it can easily be extended to three dimensional problems without increasing the complexity of the solution. The technique presented in this chapter is then applied to study different geometries of low-loss dielectric ridge lines in Chapter 7, where results are presented along with a detailed description of the numerical implementation of the method.

6.2 Approach

This section introduces the generalized integral equation (GIE) method which has been developed to characterize complex geometries at submillimeter-wave and terahertz frequencies. In this mathematical scheme, the formulation of the electric field in terms of equivalent electric and magnetic polarization currents is shown to lead to a modified integral equation eigenproblem as summarized in the flowchart of Figure 6.3 and outlined below.

First, a conventional formulation utilizing volume electric polarization currents inside the strips is used. Then, an equivalent problem is defined with respect to the fields outside of the dielectric strips to facilitate the computation of the propagation characteristics of such strips. Equivalent planar polarization dipole moments are introduced to simulate the lines, reducing in effect the dimension of the unknown

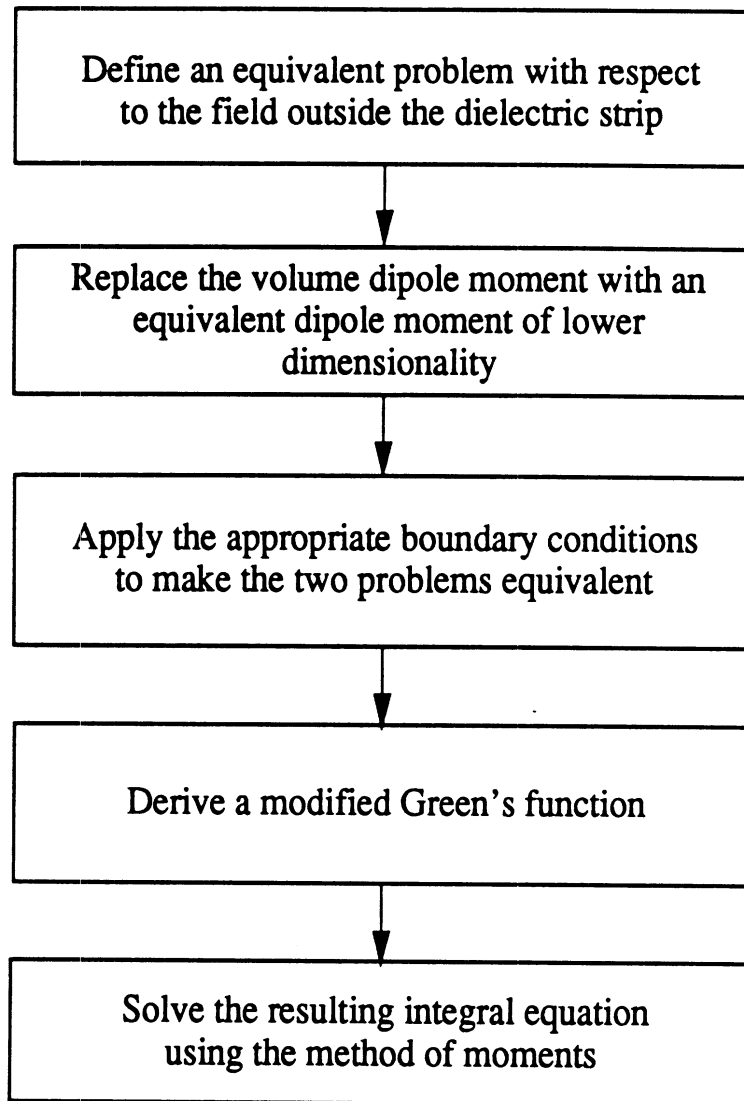


Figure 6.3: Approach used in the derivation of the GIE method

by one, as discussed in section 6.3. To make the two above problems equivalent, the concept of generalized boundary conditions is applied to the electric field at the surfaces of the strips via a Taylor's series expansion method (section 6.4).

Introduced in the 1960's [93], generalized impedance boundary conditions (GIBC) have been used for both analytical and numerical treatment of scattering problems [94]. Earlier on, effective models were developed to simulate very thin and high contrast materials, such as the standard impedance boundary condition [95] which involves a zero or first order derivative of the field components. An accurate simulation of thicker layers requires to include higher order derivatives of the field, usually referred to as generalized impedance boundary conditions (GIBC) which can be written in terms of normal derivatives of the field components. The order of the condition refers to that of the highest derivative used in the definition.

With the replacement of the dielectric strips by equivalent currents of lower dimensionality, the original problem is simplified and an eigenvalue equation for the propagation constant k_z is derived through the use of a modified planar integral equation (section 6.5). This integral equation can then be treated as any other two-dimensional problem with unknown planar current densities as described in Chapters 2 and 3. Applying Galerkin's method, the current densities are represented by a set of pulse basis functions (section 6.7).

The GIE method is derived in a general context and can be applied equally well to open, shielded or covered dielectric waveguide problems with the presumption that the boundary conditions away from the dielectric strip surfaces are satisfied by the appropriate Green's functions. Herein, the formulation is applied to structures with multiple dielectric strips printed on different levels within a multilayered substrate environment, and the electric Green's function $\bar{\bar{G}}^e$ described in Chapter 2 is used to

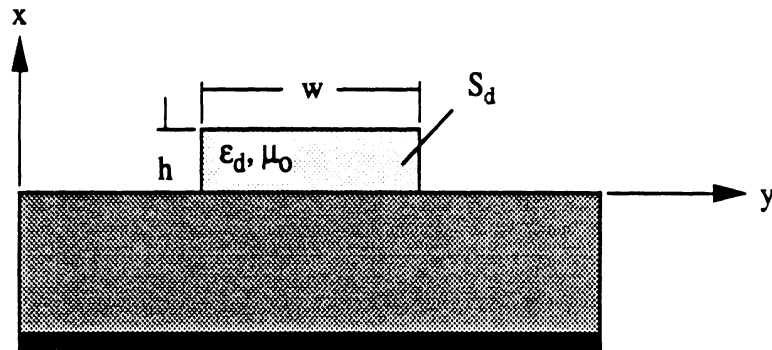


Figure 6.4: Geometry of the analyzed structure

derive a modified Green's function \bar{G}_{mod} (section 6.6). The technique accounts for an accurate modelling of dispersion at high frequencies, including the effect of the actual coupling between multiple strips. Throughout this derivation, conductor losses in the ground plane and shielding waveguide may be accounted for in the Green's function as described in Chapter 3. Also lossy strips can be handled by considering materials with complex permittivities.

6.3 Description of the problem

The generalized integral equation (GIE) model developed in this section is two-fold. First, we substitute the original problem with an equivalent polarization current, and second, we replace it by an equivalent planar current. The technique is general and can be applied to a multilevel structure comprising several dielectric strips ($i = 1, 2, \dots, N$). These rectangular shaped strips are made of nonmagnetic materials with permittivity ϵ_i . Their thickness h_i equals a fraction of the wavelength in the dielectric and is small compared to the strip width w_i (Figure 6.4). The strips

rest in a multilayered environment which is intended to represent a typical integrated dielectric waveguide made of substrates, film and possible superstrates.

6.3.1 Polarization formulation

For the sake of simplicity in the presentation of the technique, we shall focus now on the cross-section of a single dielectric strip line of thickness h centered on the plane $x = x_p$ and resting on the surface of a grounded dielectric slab of permittivity ϵ_d . We denote S_d to be the cross sectional area of the dielectric strip (Figure 6.5a). Under these assumptions, Maxwell's equations take the following form:

$$\vec{\nabla} \times \vec{E} = -j\omega\mu_o\vec{H} \quad (6.1)$$

$$\vec{\nabla} \times \vec{H} = j\omega\epsilon\vec{E} + j\omega\vec{P} \ , \quad (6.2)$$

where ϵ indicates the permittivity in the slab and half-space above it.

The excitation of the electromagnetic field is provided by an impressed electric field \vec{E}^i which gives rise to a displacement current $\vec{J}_p = j\omega\vec{P}$ or equivalently to an electric dipole moment per unit volume \vec{P} (Figure 6.5b). This dipole moment \vec{P} , also known as the *polarization vector*, stems from the discontinuity in permittivity between the background region ϵ_b and the dielectric strip ϵ_d as discussed in [20], and is given by

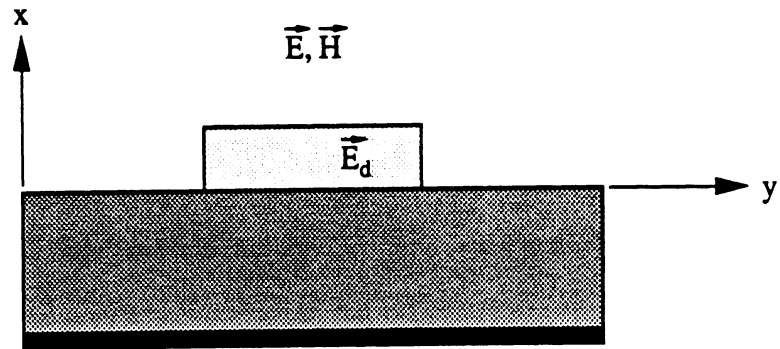
$$\vec{P} = \begin{cases} (\epsilon_d - \epsilon_b) \vec{E}_d & , \text{ in } S_d \\ 0 & , \text{ elsewhere.} \end{cases} \quad (6.3)$$

Using Maxwell-Ampere's law (2.19) in the strip region

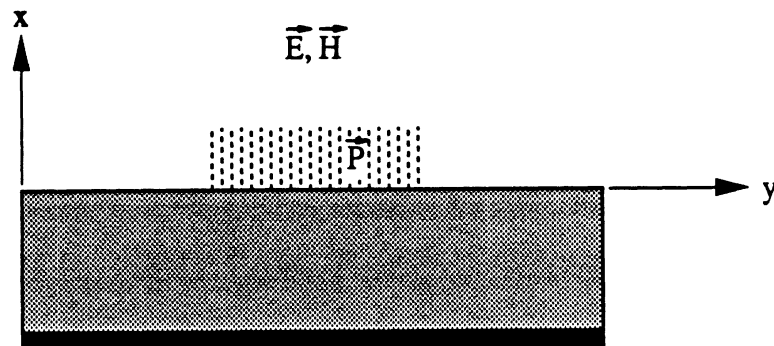
$$\vec{\nabla} \times \vec{H} = \vec{J}^i + j\omega\epsilon_d\vec{E}_d, \quad (6.4)$$

we can define the equivalent polarization vector \vec{P} by mere addition and subtraction of the background medium as

$$\vec{\nabla} \times \vec{H} = \vec{J}^i + j\omega(\epsilon_d - \epsilon_b)\vec{E}_d + j\omega\epsilon_b\vec{E}_d \quad (6.5)$$



a. Initial problem



b. Polarization current

Figure 6.5: Equivalent polarization current

$$= \vec{J}^i + j\omega\vec{P} + j\omega\epsilon_b\vec{E}_d \quad (6.6)$$

where \vec{J}^i is the impressed current and \vec{E}_d is the total field in the dielectric region with complex permittivity ϵ_d

$$\epsilon_d = \left(\epsilon_{r_d} - j \frac{\sigma}{\omega\epsilon_o} \right) \epsilon_o. \quad (6.7)$$

As discussed in Chapter 2, the current \vec{J}_p or polarization vector \vec{P} will result in a total field \vec{E} given by equation (2.2) or

$$\vec{E}(\vec{r}) = j\omega \int \int \int_V \vec{G}^e(\vec{r}/\vec{r}') \cdot \vec{P}(\vec{r}') dv'. \quad (6.8)$$

In the two-dimensional problem, the Pocklington's integral equation reduces to a surface integral formulation as discussed in section 2.2.1.

$$\vec{E} = j\omega \int \int_{S_d} \vec{G}^e(x, y/x', y') \cdot \vec{P}(y') dx' dy' |_{k_z=k'_z}. \quad (6.9)$$

This integral is carried out over the cross-section of the dielectric region, which can be divided into rectangular segments across which the current is assumed constant. A method of moments is implemented using two-dimensional basis functions along the x and y axes, leading to a matrix equation which is solved for the unknown polarization current distribution. This formulation has been used extensively in scattering problems [91], [96]-[97] but has a major disadvantage in that it requires subsectioning with a grid sufficiently fine with respect to the wavelength. Thus it becomes numerically intensive as the frequency gets large or in the case of three-dimensional problems. It is therefore of interest to modify the formulation by lowering the degree of dimensionality as discussed below.

6.3.2 Equivalent planar problem

At this point, we define a problem which is equivalent to the original one with respect to the field outside the dielectric strip where we seek to simulate the radiated

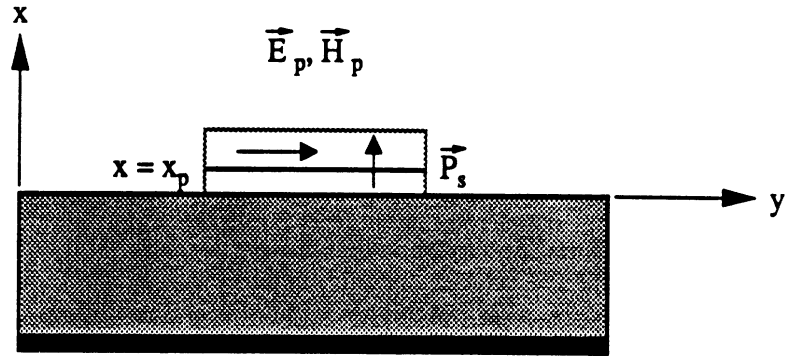


Figure 6.6: Equivalent dipole moment per unit surface

field using an infinitesimally thin sheet. First, the dielectric strip is replaced by a planar-strip *polarization surface* extending over the width of the strip as shown in Figure 6.6. This fictitious surface rests on the plane x_p and is characterized by a *dipole moment per unit surface* \vec{P}_s , given by:

$$\vec{P}_s(x, y) = \int_0^h \vec{P}(x', y) dx'. \quad (6.10)$$

The electric field \vec{E}_d throughout the dielectric region can be written in terms of the electric field on the upper and lower interface of the surrounding surface S_d by using a Taylor's expansion as

$$\vec{E}_d(x, y) = \sum_{n=0}^{\infty} \frac{1}{\Gamma(n+1)} \left[\frac{\partial^n \vec{E}_d(x, y)}{\partial x^n} \right]_{x=0, h} \begin{cases} (x-h)^n & \text{if } x_p \leq x \leq h \\ x^n & \text{if } 0 \leq x \leq x_p \end{cases} \quad (6.11)$$

where \vec{E}_d is the electric field in the dielectric strip. In view of (6.11), equation (6.10) takes the form

$$\vec{P}_s(x, y) = \vec{P}_s^+(x, y) + \vec{P}_s^-(x, y) \quad (6.12)$$

where we can express the dipole moment per unit surface \vec{P}_s in terms of the higher

order derivatives of this electric field as shown below:

$$\vec{P}_s^+(x, y) = (\epsilon_d - \epsilon_b) \sum_{n=0}^{\infty} \frac{(x_p - h)^{n+1}}{\Gamma(n+2)} \frac{\partial^n}{\partial x^n} \vec{E}_d(x, y) \Big|_{x=h} \quad (6.13)$$

$$\vec{P}_s^-(x, y) = (\epsilon_d - \epsilon_b) \sum_{n=0}^{\infty} \frac{(x_p)^{n+1}}{\Gamma(n+2)} \frac{\partial^n}{\partial x^n} \vec{E}_d(x, y) \Big|_{x=0}. \quad (6.14)$$

In the presence of the planar polarization surface, the electromagnetic field satisfies Maxwell's equations in the following form:

$$\vec{\nabla} \times \vec{E}_p = -j\omega\mu_o\vec{H}_p \quad (6.15)$$

$$\vec{\nabla} \times \vec{H}_p = j\omega\epsilon\vec{E}_p + j\omega\vec{P}_s. \quad (6.16)$$

Based on equations (6.15)-(6.16) and with the use of a polarization potential [15], the electric field \vec{E}_p due to the equivalent planar dipole moment at $x' = x_p$ is given by a line integral as :

$$\vec{E}_p(x, y) = j\omega \int_{L_p} \left[\vec{\bar{G}}(x, y/x_p, y') \right] \cdot \vec{P}_s(x_p, y') dy' \quad (6.17)$$

where $\vec{\bar{G}}$ is the dyadic Green's function for the problem. If the dielectric ridge is inside a rectangular waveguide section, this function can be found analytically as a superposition of all the propagating and attenuating modes in the inhomogeneously filled waveguide. For free space problems, the Green's function is written in terms of single Sommerfeld integrals.

6.4 Application of the boundary conditions

In order to make the above two problems equivalent in the volume outside the dielectric strip, appropriate boundary conditions have to be enforced outside the strip as well as at its interfaces.

6.4.1 Outside the strip

In the regions outside of the dielectric strips, the field \vec{E}_p has to be identical to the original \vec{E} field on the surface of the dielectric waveguide indicated by the path C_s on the cross-sectional plane. As a result, these fields must satisfy the following equations:

$$\frac{\partial^n \vec{E}_p}{\partial x^n} = \frac{\partial^n \vec{E}}{\partial x^n} \quad \forall n = 0, 1, \dots \quad \text{on } C_s \quad (6.18)$$

6.4.2 At the strip interfaces

Recalling the assumption of the strip width to thickness ratio to be large, the boundary conditions on the sides are incorporated in a general manner in the Green's function kernel. In addition, we need to enforce the appropriate boundary conditions of continuity of the tangential E and H fields at the interfaces $x = h$ and $x = 0$,

$$\hat{n} \times \left(\vec{E}^\mp \Big|_{x=0,h} - \vec{E}_d \Big|_{x=0,h} \right) = 0 \quad (6.19)$$

$$\hat{n} \times \left(\vec{H}^\mp \Big|_{x=0,h} - \vec{H}_d \Big|_{x=0,h} \right) = 0 \quad (6.20)$$

and discontinuity of the normal components of those fields

$$\hat{n} \cdot \left(\epsilon_b \vec{E}^\mp \Big|_{x=0,h} - \epsilon_d \vec{E}_d \Big|_{x=0,h} \right) = 0 \quad (6.21)$$

$$\hat{n} \cdot \left(\mu_b \vec{H}^\mp \Big|_{x=0,h} - \mu_d \vec{H}_d \Big|_{x=0,h} \right) = 0. \quad (6.22)$$

where the plus and minus signs represent the exterior fields on the upper and lower surfaces of the strip. In the following, equations (6.19)-(6.22) will be referred to as the *initial conditions*. Recalling (6.12), we can write

$$\begin{aligned} \vec{P}_s(x, y) &= (\epsilon_d - \epsilon_b) \sum_{n=0}^{\infty} \frac{1}{\Gamma(n+2)} \\ &\left\{ (x_p - h)^{n+1} \frac{\partial^n}{\partial x^n} \vec{E}^d(x, y) \Big|_{x=h} + (x_p)^{n+1} \frac{\partial^n}{\partial x^n} \vec{E}^d(x, y) \Big|_{x=0} \right\} \end{aligned} \quad (6.23)$$

To a first approximation, i.e. for $n = 0$, the dipole moment per unit surface can be obtained by enforcing the *initial conditions* as

$$P_{x_s} = \frac{(\epsilon_d - \epsilon_b)}{\epsilon_d} \left\{ (x_p - h) E_{x_s}^+ \Big|_{x=h} + x_p E_{x_s}^- \Big|_{x=0} \right\} \quad (6.24)$$

$$P_{y_s} = (\epsilon_d - \epsilon_b) \left\{ (x_p - h) E_{y_s}^+ \Big|_{x=h} + x_p E_{y_s}^- \Big|_{x=0} \right\} \quad (6.25)$$

$$P_{z_s} = (\epsilon_d - \epsilon_b) \left\{ (x_p - h) E_{z_s}^+ \Big|_{x=h} + x_p E_{z_s}^- \Big|_{x=0} \right\}. \quad (6.26)$$

The above equations are only accurate for very thin dielectric layers. The problem can be improved by including higher order derivatives of the field components in the boundary conditions [94], in which case relations between the higher order derivatives of the electric field on each side of the interface with respect to the normal component x have to be used. A detailed derivation of the generalized boundary conditions used at the interface between two homogeneous, isotropic media is given in Appendix E and summarized below.

Using Maxwell's equations together with (6.20), we can evaluate the boundary conditions of the first-order derivative of the tangential components of the electric field at the upper and lower interfaces as

$$\frac{\partial}{\partial x} E_y \Big|_{x=0,h} - \frac{\partial}{\partial x} E_y^d \Big|_{x=0,h} = \left(\frac{\epsilon_d}{\epsilon_b} - 1 \right) \frac{\partial}{\partial y} E_x^d \Big|_{x=0,h} \quad (6.27)$$

$$\frac{\partial}{\partial x} E_z \Big|_{x=0,h} - \frac{\partial}{\partial x} E_z^d \Big|_{x=0,h} = \gamma_z \left(1 - \frac{\epsilon_d}{\epsilon_b} \right) E_x^d \Big|_{x=0,h} \quad (6.28)$$

where the \pm signs are omitted. The derivatives of the x -component of the electric field are derived from Gauss's law in source-free regions to yield

$$\frac{\partial E_x}{\partial x} \Big|_{x=0,h} = \frac{\partial E_x^d}{\partial x} \Big|_{x=0,h}. \quad (6.29)$$

Making use of the wave equation and the *initial conditions*, the boundary condition of the second-order derivative of the electric field can be found as

$$\frac{\partial^2 E_\xi}{\partial x^2} \Big|_{x=0,h} - \frac{\partial^2 E_\xi^d}{\partial x^2} \Big|_{x=0,h} = (k_d^2 - k_b^2) E_\xi \Big|_{x=0,h} \quad (6.30)$$

where ξ denotes all three components of the electric field. If we take the n th-order derivative of the above equation, a recurrence relation can be derived where the normal derivatives of the outside electric field \vec{E} on the surfaces at $x = 0$ and $x = h$ are related to the normal derivatives of the electric field \vec{E}_d excited inside the dielectric strip by

$$\left. \frac{\partial^n \vec{E}_d}{\partial x^n} \right|_{x=0,h} = \bar{\bar{\mathcal{K}}}_n \cdot \vec{E} \Big|_{x=0,h}. \quad (6.31)$$

In equation (6.31), $\bar{\bar{\mathcal{K}}}_n$ is a tensor operator defined as

$$\bar{\bar{\mathcal{K}}}_n = \begin{pmatrix} \mathcal{K}_{xx}\hat{x}\hat{x} + \mathcal{K}_{xy}\hat{x}\hat{y} + \mathcal{K}_{xz}\hat{x}\hat{z} \\ \mathcal{K}_{yx}\hat{y}\hat{x} + \mathcal{K}_{yy}\hat{y}\hat{y} + \mathcal{K}_{yz}\hat{y}\hat{z} \\ \mathcal{K}_{zx}\hat{z}\hat{x} + \mathcal{K}_{zy}\hat{z}\hat{y} + \mathcal{K}_{zz}\hat{z}\hat{z} \end{pmatrix} \quad (6.32)$$

with individual components

$$\mathcal{K}_{xx} = \frac{\epsilon_b}{\epsilon_d} \left\{ \frac{\partial^n}{\partial x^n} + \Delta \sum_{\nu=1}^{\lfloor \frac{n}{2} \rfloor} (-F)^{\nu-1} \frac{\partial^{n-2\nu}}{\partial x^{n-2\nu}} + (-F)^{\lfloor \frac{n}{2} \rfloor} \left(\frac{\epsilon_d}{\epsilon_b} - 1 \right) \kappa_n \frac{\partial}{\partial x} \right\} \quad (6.33)$$

$$\mathcal{K}_{xy} = 0 \quad (6.34)$$

$$\mathcal{K}_{xz} = 0 \quad (6.35)$$

$$\mathcal{K}_{yx} = (-F)^{\lfloor \frac{n}{2} \rfloor} \left(\frac{\epsilon_b}{\epsilon_d} - 1 \right) \kappa_n \frac{\partial}{\partial y} \quad (6.36)$$

$$\mathcal{K}_{yy} = \frac{\partial^n}{\partial x^n} + \Delta \sum_{\nu=1}^{\lfloor \frac{n}{2} \rfloor} (-F)^{\nu-1} \frac{\partial^{n-2\nu}}{\partial x^{n-2\nu}} \quad (6.37)$$

$$\mathcal{K}_{yz} = 0 \quad (6.38)$$

$$\mathcal{K}_{zx} = (-F)^{\lfloor \frac{n}{2} \rfloor} \left(\frac{\epsilon_b}{\epsilon_d} - 1 \right) \kappa_n \frac{\partial}{\partial z} \quad (6.39)$$

$$\mathcal{K}_{zy} = 0 \quad (6.40)$$

$$\mathcal{K}_{zz} = \frac{\partial^n}{\partial x^n} + \Delta \sum_{\nu=1}^{\lfloor \frac{n}{2} \rfloor} (-F)^{\nu-1} \frac{\partial^{n-2\nu}}{\partial x^{n-2\nu}} \quad (6.41)$$

where

$$\kappa_n = \begin{cases} 1, & n \text{ odd} \\ 0, & n \text{ even} \end{cases} \quad (6.42)$$

and

$$\Delta = k_0^2(\epsilon_b - \epsilon_d) \quad (6.43)$$

$$F = \frac{\partial^2}{\partial y^2} + k_d^2 - k_z^2. \quad (6.44)$$

The tensor operator $\bar{\bar{\mathcal{K}}}_n$ can be written as

$$\bar{\bar{\mathcal{K}}}_n = \begin{pmatrix} \frac{\epsilon_b}{\epsilon_d} \left(A_n + B_n + C_n \frac{\partial}{\partial x} \right) & 0 & 0 \\ C_n \frac{\partial}{\partial y} & A_n + B_n & 0 \\ C_n \frac{\partial}{\partial z} & 0 & A_n + B_n \end{pmatrix} \quad (6.45)$$

where A_n, B_n are n th order linear differential operators and

$$A_n = \frac{\partial^n}{\partial x^n} \quad (6.46)$$

$$B_n = \Delta \sum_{\nu=1}^{\lfloor \frac{n}{2} \rfloor} (-F)^{\nu-1} \frac{\partial^{n-2\nu}}{\partial x^{n-2\nu}} \quad (6.47)$$

$$C_n = (-F)^{\lfloor \frac{n}{2} \rfloor} \left(\frac{\epsilon_b}{\epsilon_d} - 1 \right) \kappa_n. \quad (6.48)$$

In summary, the derivatives of the electric fields with respect to the direction perpendicular to the interface between two media are related at the boundary and can be expressed through fundamental recurrence relations. The formulation of these generalized boundary conditions is further verified in Appendix F, for the case of a dielectric slab illuminated by a plane wave. It is shown that the relations given in (6.31) are equivalent to the relations of continuity of tangential electric and magnetic fields at the interface. Indeed, the combination of the initial and higher-order boundary conditions of the electric field at an interface reproduces the known reflection coefficient for a dielectric layer of infinite extent.

6.5 Formulation of the modified integral equation

To derive the modified integral equation for the determination of propagation characteristics, we start with (6.18) and make use of the generalized boundary con-

ditions (6.31) to obtain

$$\left. \frac{\partial^n \vec{E}_d}{\partial x^n} \right|_{x=0,h} = \bar{\mathcal{K}}_n \cdot \vec{E}_p \Big|_{x=0,h}. \quad (6.49)$$

This equation, when combined with (6.17), leads to

$$\left. \frac{\partial^n \vec{E}_d}{\partial x^n} \right|_{x=0,h} = \bar{\mathcal{K}}_n \cdot \left[j\omega \int_{L_p} [\bar{G}(x, y/x_p, y')] \cdot \vec{P}_s(x_p, y') dy' \right]_{x=0,h} \quad (6.50)$$

$$= j\omega \int_{L_p} [\bar{\mathcal{K}}_n \cdot \bar{G}(x, y/x_p, y')]_{x=0,h} \cdot \vec{P}_s(x_p, y') dy' \quad (6.51)$$

By substituting (6.51) into (6.23), the equivalent strip dipole moment per unit surface can be expressed in terms of the outside electric fields at the upper and lower strip surfaces as

$$\begin{aligned} \vec{P}_s &= j\omega (\epsilon_d - \epsilon_b) \sum_{n=0}^{\infty} \frac{1}{\Gamma(n+2)} \\ &\quad \left\{ (x_p - h)^{n+1} \int_{L_p} [\bar{\mathcal{K}}_n \cdot \bar{G}(x, y/x_p, y')]_{x=h} \cdot \vec{P}_s(x_p, y') dy' \right. \\ &\quad \left. + (x_p)^{n+1} \int_{L_p} [\bar{\mathcal{K}}_n \cdot \bar{G}(x, y/x_p, y')]_{x=0} \cdot \vec{P}_s(x_p, y') dy' \right\} \quad (6.52) \end{aligned}$$

or

$$\begin{aligned} \vec{P}_s &= j\omega (\epsilon_d - \epsilon_b) \int_{L_p} \sum_{n=0}^{\infty} \frac{1}{\Gamma(n+2)} \\ &\quad \left\{ (x_p - h)^{n+1} [\bar{\mathcal{K}}_n \cdot \bar{G}]_{x=h} + (x_p)^{n+1} [\bar{\mathcal{K}}_n \cdot \bar{G}]_{x=0} \right\} \cdot \vec{P}_s dy' \quad (6.53) \end{aligned}$$

The above equation can be cast as a homogeneous *Fredholm Integral Equation of the second kind*:

$$\vec{P}_s = j\omega (\epsilon_d - \epsilon_b) \int_{L_p} \bar{G}_{mod} \cdot \vec{P}_s dy' \quad (6.54)$$

where the modified dyadic Green's function \bar{G}_{mod} forms the kernel of the equation, and is given by

$$\bar{G}_{mod} = \sum_{n=0}^{\infty} \frac{1}{\Gamma(n+2)} \left\{ (x_p - h)^{n+1} [\bar{\mathcal{K}}_n \cdot \bar{G}]_{x=h} + (x_p)^{n+1} [\bar{\mathcal{K}}_n \cdot \bar{G}]_{x=0} \right\}. \quad (6.55)$$

For the case of multiple lines, the integral equation is generalized to

$$\vec{P}_s^i = j\omega(\epsilon_{di} - \epsilon_b) \sum_{j=1}^N \int_{L_p} \bar{G}_{mod}^{ij} \cdot \vec{P}_s^j dy' , \quad (6.56)$$

which may be solved to determine the unknown equivalent planar currents. In the above, \bar{G}_{mod}^{ij} is the Green's function at the i th dielectric strip due to an equivalent dipole moment on the j th strip. Knowledge of the propagation constant can provide accurate and complete information about ohmic losses, leakage and radiation effects. The procedure as described up to this point can be applied to **open** or **shielded** dielectric waveguide problems with the presumption that the boundary conditions away from the dielectric strip surfaces are satisfied appropriately by the Green's functions \bar{G}_{mod}^{ij} . In both cases the application of the generalized boundary conditions result in infinite summations which can be evaluated analytically leading to simplified kernels as will be discussed next.

6.6 Modified Green's function for the shielded case

In this section, the modified dyadic Green's function is presented for the case of a multilayered dielectric structure within a shielded metallic waveguide. The notation and geometry are the same as that used in the derivation of the Green's function of an electric point source in a multilayered structure described in Chapter 2. The geometry used in the derivation of the modified Green's function corresponds to Figure A.4 where the source layer s is taken to have the height of the dielectric strip and is surrounded by the background medium of permittivity ϵ_b . The dielectric substrates and superstrates are taken into account in the formulation of the original Green's function \bar{G} . In the following, the equivalent planar dipole moment \vec{P}_s is set

at the center of the strip, i.e. $x' = x_p = h/2$, which reduces (6.55) to

$$\bar{G}_{mod} = \sum_{n=0}^{\infty} \frac{\left(\frac{h}{2}\right)^{n+1}}{\Gamma(n+2)} \left[(-1)^n \bar{\mathcal{K}}_n \cdot \bar{G}\Big|_{x=h} + \bar{\mathcal{K}}_n \cdot \bar{G}\Big|_{x=0} \right] \quad (6.57)$$

Making use of (6.45), we can write

$$\bar{G}_{mod} = \begin{pmatrix} \frac{\epsilon_h}{\epsilon_d} \left(\mathcal{A} + \mathcal{B} + \mathcal{C} \frac{\partial}{\partial x} \right) & 0 & 0 \\ \mathcal{C} \frac{\partial}{\partial y} & \mathcal{A} + \mathcal{B} & 0 \\ \mathcal{C} \frac{\partial}{\partial z} & 0 & \mathcal{A} + \mathcal{B} \end{pmatrix} \cdot \begin{pmatrix} G_{xx} \hat{x} \hat{x} & G_{xy} \hat{x} \hat{y} & G_{xz} \hat{x} \hat{z} \\ G_{yx} \hat{y} \hat{x} & G_{yy} \hat{y} \hat{y} & G_{yz} \hat{y} \hat{z} \\ G_{zx} \hat{z} \hat{x} & G_{zy} \hat{z} \hat{y} & G_{zz} \hat{z} \hat{z} \end{pmatrix} \quad (6.58)$$

where

$$\mathcal{A} = \sum_{n=0}^{\infty} \frac{\left(\frac{h}{2}\right)^{n+1}}{\Gamma(n+2)} A_n \quad (6.59)$$

$$\mathcal{B} = \sum_{n=2}^{\infty} \frac{\left(\frac{h}{2}\right)^{n+1}}{\Gamma(n+2)} B_n \quad (6.60)$$

$$\mathcal{C} = \sum_{n=1,3,5}^{\infty} \frac{\left(\frac{h}{2}\right)^{n+1}}{\Gamma(n+2)} C_n. \quad (6.61)$$

From (6.46)-(6.47), it is clear that the operators \mathcal{A} and \mathcal{B} affect only the x -dependence of \bar{G} . The Green's function formulation involves trigonometric expansions which allows for an analytical evaluation of the infinite summations over the index n in terms of closed-form expressions given in Appendix G. This further enhances the versatility of the GIBC's by reducing the infinite order derivatives to simple expressions, thus avoiding the summation over n . In scattering problems, finite-order approximations have to be considered leading to truncated Taylor's series expansions.

The components of the modified Green's function \bar{G}_{mod} are of the following form

$$(G_{mod})_{xx} = \frac{j}{\omega \epsilon_b^*} \sum_{m=0}^{\infty} \frac{\delta_m}{b} \frac{(k_y^2 + k_z^2)}{k_{xd}^2} \left[\Upsilon_a^+ v_a^+(x_p) + \Upsilon_a^- v_a^-(x_p) \right] \sin k_y y \sin k_y y'$$

$$(G_{mod})_{xy} = -\frac{j}{\omega \epsilon_b^*} \sum_{m=0}^{\infty} \frac{\delta_m}{b} \frac{k_y k_x}{k_{xd}^2} \left[\Upsilon_a^+ \varphi_a^+(x_p) + \Upsilon_a^- \varphi_a^-(x_p) \right] \sin k_y y \cos k_y y'$$

$$\begin{aligned}
(G_{mod})_{xz} &= \frac{1}{\omega \epsilon_b^*} \sum_{m=0}^{\infty} \frac{\delta_m k_z k_x}{b k_{xd}^2} \left[\Upsilon_a^+ \varphi_a^+(x_p) + \Upsilon_a^- \varphi_a^-(x_p) \right] \sin k_y y \sin k_y y' \\
(G_{mod})_{yx} &= -\frac{j}{\omega \epsilon_b^*} \sum_{m=0}^{\infty} \frac{\delta_m k_y}{b k_{xd}} \left[\Psi_a^+ v_a^+(x_p) + \Psi_a^- v_a^-(x_p) \right] \cos k_y y \sin k_y y' \\
(G_{mod})_{yy} &= j \sum_{m=0}^{\infty} \frac{\delta_m}{b} \frac{1}{k_y^2 + k_z^2} \frac{1}{k_{xd}} \cos k_y y \cos k_y y' \\
&\quad \left[k_y^2 (\eta_c)_a^b \left(\Psi_a^+ \varphi_a^+(x_p) + \Psi_a^- \varphi_a^-(x_p) \right) \right. \\
&\quad \left. + k_z^2 (\eta_c)_f^b \left(\Psi_f^+ \varphi_f^+(x_p) + \Psi_f^- \varphi_f^-(x_p) \right) \right] \\
(G_{mod})_{yz} &= \sum_{m=0}^{\infty} \frac{\delta_m}{b} \frac{k_y k_z}{(k_y^2 + k_z^2)} \frac{1}{k_{xd}} \cos k_y y \sin k_y y' \\
&\quad \left[-(\eta_c)_a^b \left(\Psi_a^+ \varphi_a^+(x_p) + \Psi_a^- \varphi_a^-(x_p) \right) \right. \\
&\quad \left. + (\eta_c)_f^b \left(\Psi_f^+ \varphi_f^+(x_p) + \Psi_f^- \varphi_f^-(x_p) \right) \right] \\
(G_{mod})_{zx} &= -\frac{1}{\omega \epsilon_b^*} \sum_{m=0}^{\infty} \frac{\delta_m k_z}{b k_{xd}} \left[\Psi_a^+ v_a^+(x_p) + \Psi_a^- v_a^-(x_p) \right] \sin k_y y \sin k_y y' \\
(G_{mod})_{zy} &= \sum_{m=0}^{\infty} \frac{\delta_m}{b} \frac{k_y k_z}{(k_y^2 + k_z^2)} \frac{1}{k_{xd}} \sin k_y y \cos k_y y' \\
&\quad \left[(\eta_c)_a^b \left(\Psi_a^+ \varphi_a^+(x_p) + \Psi_a^- \varphi_a^-(x_p) \right) \right. \\
&\quad \left. - (\eta_c)_f^b \left(\Psi_f^+ \varphi_f^+(x_p) + \Psi_f^- \varphi_f^-(x_p) \right) \right] \\
(G_{mod})_{zz} &= j \sum_{m=0}^{\infty} \frac{\delta_m}{b} \frac{1}{k_y^2 + k_z^2} \frac{1}{k_{xd}} \sin k_y y \sin k_y y' \\
&\quad \left[k_z^2 (\eta_c)_a^b \left(\Psi_a^+ \varphi_a^+(x_p) + \Psi_a^- \varphi_a^-(x_p) \right) \right. \\
&\quad \left. + k_y^2 (\eta_c)_f^b \left(\Psi_f^+ \varphi_f^+(x_p) + \Psi_f^- \varphi_f^-(x_p) \right) \right] \tag{6.62}
\end{aligned}$$

where

$$k_i = \omega \sqrt{\epsilon_i^* \mu_0} \tag{6.63}$$

$$k_y = \frac{m\pi}{b} \tag{6.64}$$

$$k_{x_i} = \sqrt{(k_i)^2 - k_y^2 - k_z^2}. \tag{6.65}$$

The x dependence has been modified to give at the interfaces $x = 0$ and $x = h$

$$\Upsilon_{a,f}^{\pm} = \begin{cases} \frac{(\eta_c)_{a,f}^d}{(\eta_c)_{a,f}^b} \sin k_{xd} \frac{h}{2} - j\tilde{\eta}_u^{a,f} (\cos k_{xd} \frac{h}{2} - 1) & , x = h \\ \frac{(\eta_c)_{a,f}^d}{(\eta_c)_{a,f}^b} \sin k_{xd} \frac{h}{2} + j\tilde{\eta}_l^{a,f} (\cos k_{xd} \frac{h}{2} - 1) & , x = 0 \end{cases} \quad (6.66)$$

$$\Psi_{a,f}^{\pm} = \begin{cases} \frac{(\eta_c)_{a,f}^d}{(\eta_c)_{a,f}^b} (\cos k_{xd} \frac{h}{2} - 1) + j\tilde{\eta}_u^{a,f} \sin k_{xd} \frac{h}{2} & , x = h \\ -\frac{(\eta_c)_{a,f}^d}{(\eta_c)_{a,f}^b} (\cos k_{xd} \frac{h}{2} - 1) + j\tilde{\eta}_l^{a,f} \sin k_{xd} \frac{h}{2} & , x = 0 \end{cases} \quad (6.67)$$

Also, the x' dependence is given by

$$\varphi_{a,f}^{\pm}(x') = \frac{1}{\mathcal{D}_{a,f}} \begin{cases} \sin k_x x' + j\tilde{\eta}_l^{a,f} \cos k_x x' & , x = h \\ \sin k_x (x' - h) + j\tilde{\eta}_u^{a,f} \cos k_x (x' - h) & , x = 0 \end{cases} \quad (6.68)$$

$$v_{a,f}^{\pm}(x') = \frac{1}{\mathcal{D}_{a,f}} \begin{cases} \cos k_x x' - j\tilde{\eta}_l^{a,f} \sin k_x x' & , x = h \\ \cos k_x (x' - h) - j\tilde{\eta}_u^{a,f} \sin k_x (x' - h) & , x = 0 \end{cases} \quad (6.69)$$

where the denominator $\mathcal{D}_{a,f}$ may be written as

$$\mathcal{D}_{a,f} = \sin k_x h (1 - \tilde{\eta}_u^{a,f} \tilde{\eta}_l^{a,f}) + j(\tilde{\eta}_l^{a,f} - \tilde{\eta}_u^{a,f}) \cos k_x h. \quad (6.70)$$

The impedances $\tilde{\eta}_l$, $\tilde{\eta}_u$ and η_c are defined as in Appendix A.

CHAPTER VII

DIELECTRIC LINES: NUMERICAL CONSIDERATIONS AND RESULTS

This chapter is divided into two parts. First, the numerical implementation of the GIE method is discussed: an algorithm for the study of propagation in dielectric lines is presented and consideration is given to the convergence of the different summations involved in the formulation. Second, we apply the generalized integral equation method to determine the propagation characteristics of different types of dielectric strip waveguides; the strip dielectric guide, the insulated image guide and the optical rib waveguide. Numerical results for single and coupled strips are presented and compared to those of other formulations.

7.1 Method of moments solution

The method of moments is applied to the dipole moments \vec{P}_s^i to solve (6.56) and Galerkin's method is used to transform the integral equation into a matrix equation as described below. Subsectional pulse basis functions are chosen as expansion functions for the transverse dependence of the dipole moments.

7.1.1 Matrix formulation

Let N_b be the number of subsections used to discretize the surface of the equivalent dipole moment of width w into linear elements (subsectional bases). The total number of elements, N_T , is given by $N_T = \sum_{i=1}^{N_s} N_b = N_s \times N_b$, where N_s is the number of dielectric strips. Although the equivalent dipole moment \vec{P}_s lies in a planar configuration, it is a three-dimensional vector quantity with components given by

$$\begin{aligned} P_{s_x}^i(y') &= \sum_{p=1}^{N_b} p_{xp}^i b_{xp}^i(y') \\ P_{s_y}^i(y') &= \sum_{p=1}^{N_b} p_{yp}^i b_{yp}^i(y') \\ P_{s_z}^i(y') &= \sum_{p=1}^{N_b} p_{zp}^i b_{zp}^i(y') \end{aligned} \quad (7.1)$$

where p_{xp}^i , p_{yp}^i and p_{zp}^i are unknown coefficients. Following a procedure similar to the case of microstrip lines (section 3.5), weighted averages are applied and reduce the integral equation to a matrix equation of the form

$$[\mathcal{Z}_{mod}][I] = [0] \quad (7.2)$$

where \mathcal{Z}_{mod} contains 9 submatrices

$$[\mathcal{Z}_{mod}] = \begin{bmatrix} [\mathcal{Z}_{xx}]_{mod} & [\mathcal{Z}_{xy}]_{mod} & [\mathcal{Z}_{xz}]_{mod} \\ [\mathcal{Z}_{yx}]_{mod} & [\mathcal{Z}_{yy}]_{mod} & [\mathcal{Z}_{yz}]_{mod} \\ [\mathcal{Z}_{zx}]_{mod} & [\mathcal{Z}_{zy}]_{mod} & [\mathcal{Z}_{zz}]_{mod} \end{bmatrix}. \quad (7.3)$$

For the general case of N_s strips in a multilayered configuration, the impedance matrix $[\mathcal{Z}_{mod}]$ is represented by a $[3N_b N_s \times 3N_b N_s]$ matrix.

7.1.2 Expansion and testing functions

In the case of microstrip lines, the unknown current distribution was expanded in terms of a set of entire domain basis functions with special properties, such as

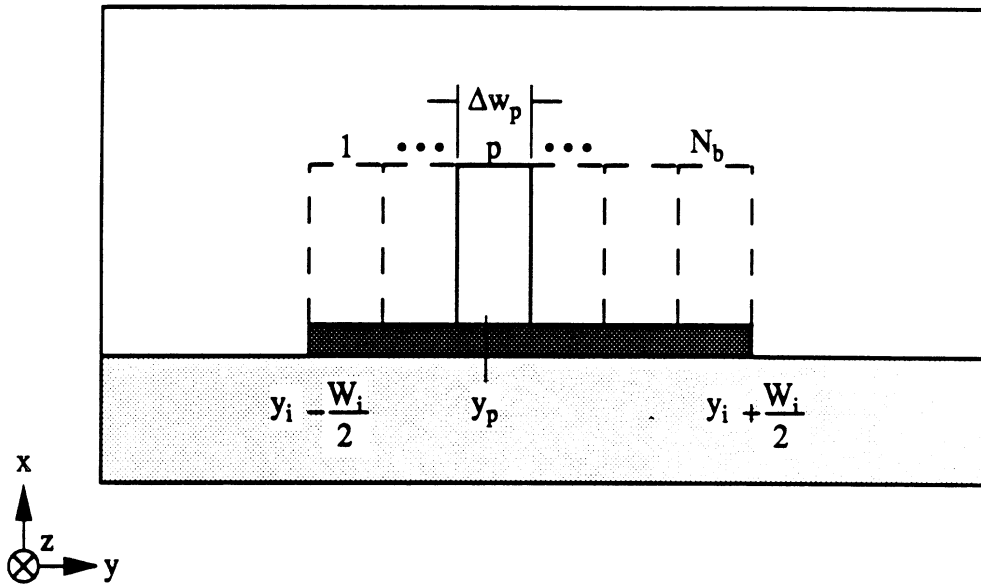


Figure 7.1: Geometry for subsectional basis functions

the built-in edge condition for the charge distributions. When a large number of expansion functions is required to approximate the unknown function or when the solution is difficult to predict, it is advantageous to use functions that make the inner products easy to compute. Since the choice of entire domain basis functions is not readily evident for the type of lines discussed here, subdomain basis functions are chosen to be unit pulse functions over the p th element and of magnitude zero over all other elements

$$P_y = \begin{cases} 1 & , |y| < \frac{1}{2N} \\ 0 & , |y| > \frac{1}{2N} \end{cases} \quad (7.4)$$

providing the ability to generate simple asymptotic formulas for increased convergence and computer efficiency. Let the strip be divided in N_b subsections and y_p be the coordinates of the center of the element $\Delta W_p = \frac{W}{N_b}$ as shown in Figure 7.1. Forcing (7.3) to be satisfied at all the y_p points provides a set of $3N_b N_s$ equations for the unknowns p_{xp}^i , p_{yp}^i and p_{zp}^i .

For this choice of basis functions, Galerkin's method may be implemented in which pulses are used for both testing and expansion functions, as $\vec{w}_p(y') = \vec{b}_p(y')$. This implies that the resulting sub-matrices in (7.3) are symmetrical, with moments integrals of the form

$$\begin{aligned} \mathcal{I}_p^{(1)} &= \mathcal{I}_p^{(3)} = \int_{w_j} \sin k_y y \, dy \\ &= \frac{W_i}{N_b} \text{Sinc} \left(k_y \frac{W_i}{2N_b} \right) \sin k_y \left(y_i - \frac{W_i}{2} + \left(p - \frac{1}{2} \right) \frac{W_i}{N_b} \right) \end{aligned} \quad (7.5)$$

and

$$\begin{aligned} \mathcal{I}_p^{(2)} &= \mathcal{I}_p^{(4)} = \int_{w_j} \cos k_y y \, dy \\ &= \frac{W_i}{N_b} \text{Sinc} \left(k_y \frac{W_i}{2N_b} \right) \cos k_y \left(y_i - \frac{W_i}{2} + \left(p - \frac{1}{2} \right) \frac{W_i}{N_b} \right) \end{aligned} \quad (7.6)$$

$$\begin{aligned} \mathcal{I}_{pq}^{(5)} &= \mathcal{I}_{pq}^{(6)} = \int_{w_j} dy b_{yp}^j(y) w_{yq}^j(y) \\ &= \begin{cases} 1 & , p = q \\ 0 & , p \neq q. \end{cases} \end{aligned} \quad (7.7)$$

The derivation of these integrals may be found in Appendix D. The method of moments solution for the equivalent dipole moment distribution discussed above was implemented in a FORTRAN 77 program using double-precision. The various computation steps used in the algorithm are outlined in the following section.

7.2 Algorithm

The search for the roots of the matrix equation is similar to the one described in Chapter 4. First, a data file is set up that includes all geometrical parameters of the structure under consideration and the operating frequencies. After the strip geometry is defined, the moments integrals (7.2) are computed. These integrals are independent of the propagation constant and the operating frequency, and once they have been calculated they need not be re-computed unless the waveguide width or the

strip geometry has changed. For each frequency, a numerical search is performed to find the values of k_{zg} which satisfy (7.2) and thus correspond to strip guided modes. This is done by computing the modified impedance matrix (7.3) for increasing values of k_z and searching for the zeros of the determinant of the matrix. To gain insight in the nature of these matrices, plots of a typical impedance matrix and a typical determinant are shown next.

Typical impedance matrix elements: Figure 7.2 shows the self-terms Z_{xx}^{mod} , Z_{yy}^{mod} , Z_{zz}^{mod} of a typical modified impedance matrix. The cross terms are not shown because their small amplitude does not vary much over the k_z range. For this example where the waveguide height is larger than its width ($a > b$), it is seen that the yy term has the greatest amplitude and changes sign twice in the k_z interval. In the case where $a < b$, the xx term plays the predominant role.

Typical determinant: Figure 7.3 shows the variation of the determinant with increasing propagation constant, where the determinant exhibits the same overall behavior as the yy term in Figure 7.2. The roots of the problem are found by searching for a change of sign in the determinant, however care has to be taken to differentiate between poles and zeroes. In this particular example, the determinant exhibits a pole corresponding to the partially-filled waveguide mode at $k_z = 0.4425$ and a root corresponding to the strip mode at $k_z = 0.672$.

In the development of the GIE method described in Chapter 6, the dielectric strips and substrates were assumed lossy in general. Although the program accounts for complex permittivities, only lossless structures are considered in this chapter and, therefore, the roots $k_{zg} = \beta_g$ are real. The propagation constant is varied within

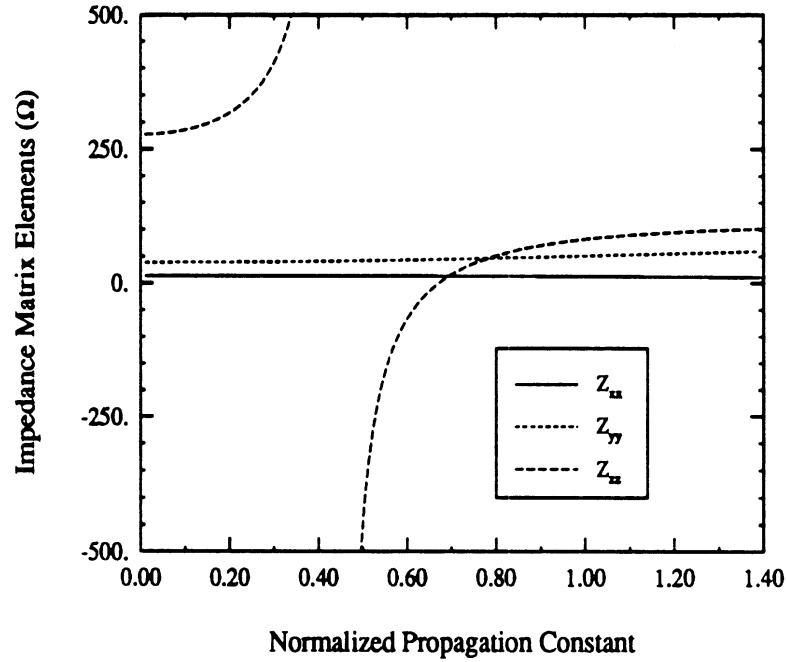


Figure 7.2: Modified impedance matrix elements as a function of k_z for a single strip ($a = 5$ cm, $b = 2$ cm, $h_1 = 2.625$ cm, $h_2 = 0.5$ cm, $h_3 = 1.875$ cm, $w = 1$ cm, $\epsilon_{strip} = 12$, $\epsilon_{substrate} = 2$, $f = 3$ GHz)

an interval (k_{z0}, k_{z1}) and the lower and upper bounds of the k_z range are determined using the transverse resonance method as discussed next.

Upper and lower bounds

Consider a dielectric strip within a waveguide consisting of N_d dielectric layers. In the limiting cases where the width of the dielectric strip either spans the whole width of the waveguide ($W = b$) or vanishes ($W \rightarrow 0$), the structure corresponds to a partially-filled waveguide made up of $N_d + 1$ or N_d layers, respectively. The modes propagating in such a waveguide are determined through the solution of transcendental equations for the LSE and LSM waveguide modes, as shown for the case of two layers by Harrington [20]. These transcendental equations are derived in this section

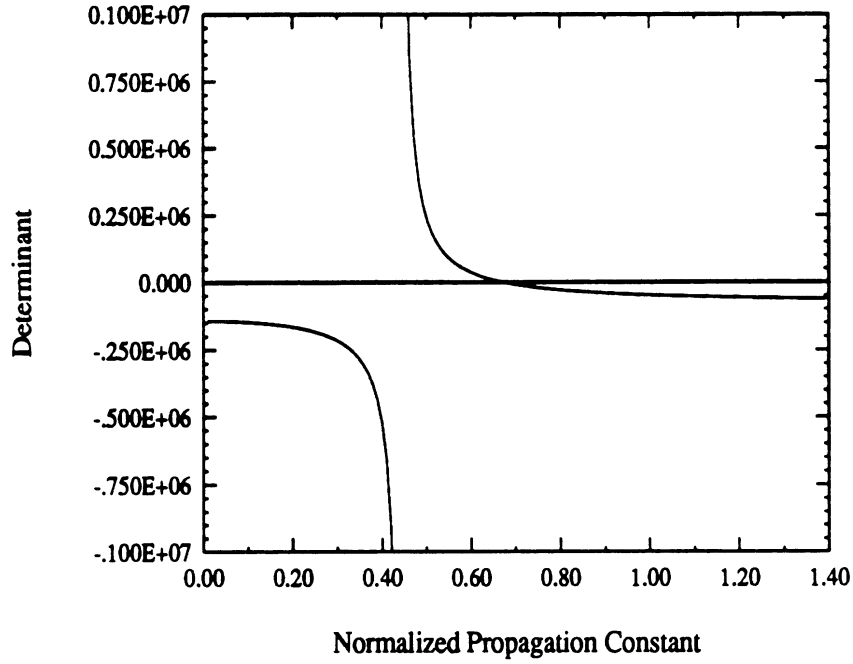


Figure 7.3: Variation of the determinant versus the propagation constant for a single strip ($a = 5$ cm, $b = 2$ cm, $h_1 = 2.625$ cm, $h_2 = 0.5$ cm, $h_3 = 1.875$ cm, $w = 1$ cm, $\epsilon_{strip} = 12$, $\epsilon_{substrate} = 2$, $f = 3$ GHz)

for a general multilayered waveguide, and their roots are used as lower and upper limiting bounds for the range of allowable propagation constants for a dielectric strip.

To be consistent with the derivation of the Green's function, we use an A_x , F_x formulation as described in (A.52)-(A.55)

$$\tilde{A}_x^{(I)} = \sum_{m=0}^{\infty} A_m^{(I)} [\cos k_x(x-h) - j\tilde{\eta}_u^a \sin k_x(x-h)] \sin k_y y \quad (7.8)$$

$$\tilde{A}_x^{(II)} = \sum_{m=0}^{\infty} A_m^{(II)} [\cos k_x x - j\tilde{\eta}_l^a \sin k_x x] \sin k_y y \quad (7.9)$$

$$\tilde{F}_x^{(I)} = \sum_{m=0}^{\infty} D_m^{(I)} [\sin k_x(x-h) + j\tilde{\eta}_u^f \cos k_x(x-h)] \cos k_y y \quad (7.10)$$

$$\tilde{F}_x^{(II)} = \sum_{m=0}^{\infty} D_m^{(II)} [\sin k_x x + j\tilde{\eta}_l^f \cos k_x x] \cos k_y y. \quad (7.11)$$

The geometry is shown in Figure 7.4 with no source present, and where impedance

boundary conditions are used on the upper interface of layer (*I*) and lower interface (*II*). Continuity of the tangential electric field at the interface $x = x'$ provides two equations which can be solved for the unknowns $A_m^{(II)}$, $D_m^{(II)}$ leading to the following expressions

$$A_m^{II} = A_m^I \frac{\sin k_x(x' - h) + j\tilde{\eta}_u^a \cos k_x(x' - h)}{\sin k_x x' + j\tilde{\eta}_l^a \cos k_x x'} \quad (7.12)$$

$$D_m^{II} = D_m^I \frac{\sin k_x(x' - h) + j\tilde{\eta}_u^f \cos k_x(x' - h)}{\sin k_x x' + j\tilde{\eta}_l^f \cos k_x x'}. \quad (7.13)$$

In addition, continuity of the tangential magnetic fields is enforced resulting in the following transcendental equations

$$\frac{k_{x1}}{\mu_1} \frac{\cos k_x(x' - h) - j\tilde{\eta}_u^f \sin k_x(x' - h)}{\sin k_x(x' - h) + j\tilde{\eta}_u^f \cos k_x(x' - h)} = \frac{k_{x2}}{\mu_2} \frac{\cos k_x x' - j\tilde{\eta}_l^f \sin k_x x'}{\sin k_x x' + j\tilde{\eta}_l^f \cos k_x x'} \quad (7.14)$$

for the LSE modes, and

$$\frac{\epsilon_1}{k_{x1}} \frac{\cos k_x(x' - h) - j\tilde{\eta}_u^a \sin k_x(x' - h)}{\sin k_x(x' - h) + j\tilde{\eta}_u^a \cos k_x(x' - h)} = \frac{\epsilon_2}{k_{x2}} \frac{\cos k_x x' - j\tilde{\eta}_l^a \sin k_x x'}{\sin k_x x' + j\tilde{\eta}_l^a \cos k_x x'} \quad (7.15)$$

for the LSM modes.

For verification purposes, let the upper and lower layers be metallic walls, i.e. $\tilde{\eta}_l = \tilde{\eta}_u = 0$. In this case, the problem simplifies to a two-layer waveguide and equations (7.14) and (7.15) reduce to

$$\frac{k_{x1}}{\mu_1} \cot k_{x1}(x' - h) = \frac{k_{x2}}{\mu_2} \cot k_{x2}x' \quad (7.16)$$

$$\frac{k_{x1}}{\epsilon_1} \tan k_{x1}(x' - h) = \frac{k_{x2}}{\epsilon_2} \tan k_{x2}x' \quad (7.17)$$

which are identical to (4.45), (4.47) in [20].

A subroutine was written to compute the complex propagation constant of the hybrid modes propagating in an inhomogeneously-filled waveguide with any number of lossy substrates and non-perfectly conducting walls [98]. These hybrid modes are denoted LSE_{mn} and LSM_{mn} . The transcendental equations have an infinite number

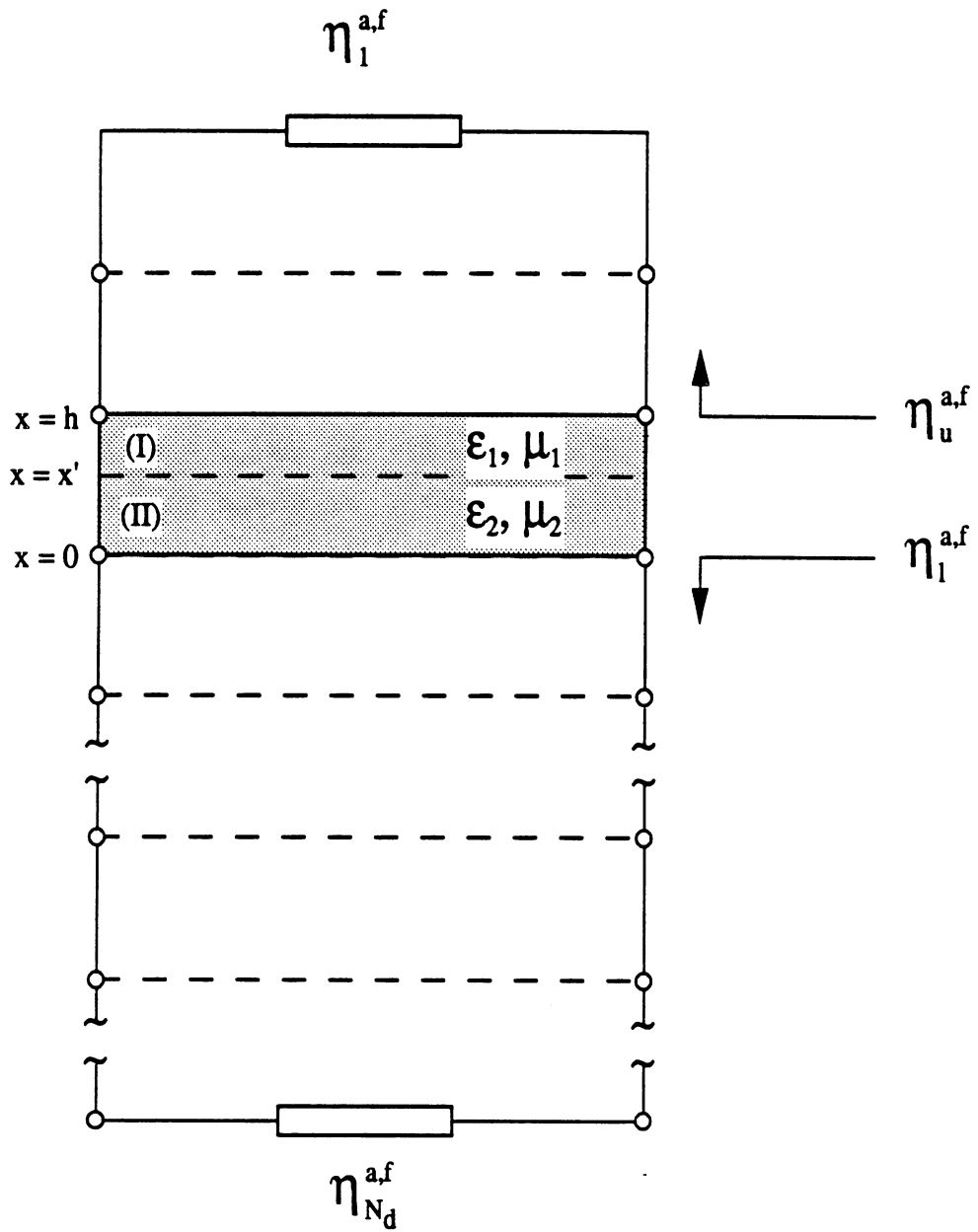


Figure 7.4: Geometry and notation of a partially-filled waveguide

of discrete solutions m for each given mode number n . The numbering is chosen to be consistent with that of the empty waveguide [20]. In the case of perfectly conducting walls, the end transmission-lines are shortcircuited as shown in Figure 7.4. However finite conductivity of the metal housing has been implemented where the top and bottom walls can have a conductivity σ , which in turns can be described by a load at the end of the transmission line. The program also accounts for substrate losses and can calculate the cut-off frequency of the modes by choosing a frequency increment small enough around $k_z = 0$.

7.3 Convergence considerations

The GIE technique described in Chapter 6 involves several infinite summations which have to be truncated during numerical implementation. Consideration of the convergence of these summations is therefore an important process in establishing reliable results, requiring a thorough investigation of the acceptable range of upper limits for the different summations. Improvement in program efficiency is realized through the use of series transformations and asymptotic expressions.

7.3.1 Number of basis functions

As mentioned in section 7.1, Galerkin's method is applied using subsectional pulse basis functions to describe the equivalent dipole moment \vec{P}_s on the dielectric strip. The number of expansion functions depends on the geometrical parameters and the operating frequency. The dipole moment \vec{P} is proportional to the electric field in the strip, and therefore does not show abrupt discontinuities, unlike the case of microstrips where the current distribution displays singularities at the edges. As the width or the frequency increases, more subsections are needed to accurately model

the equivalent dipole moment since higher order modes may be triggered requiring a larger number of subsections to describe the resulting field distribution.

7.3.2 Modal summations

The modified Green's function involves an infinite modal summation in the y direction for each of its components (see equation 6.62). When the strip width W spans the width of the waveguide ($W = b$), only one mode should be necessary to describe the dominant LSE or LSM waveguide mode. As the width of the strip decreases, more modes are needed to represent the perturbation caused by the strip in the waveguide, thus the summation over m needs to incorporate more terms. Therefore the numerical evaluation of the infinite summation over m depends on the strip width and may result in large CPU time. This problem is overcome by the use of some mathematical identities and series transformations which greatly improve the program efficiency and insure fast convergence and accurate results.

The elements of the modified matrix Z_{mod} can be written in terms of an infinite summation as follows

$$Z_{ij}^{mod} = \sum_{m=0}^{\infty} \Xi_{ij}(k_x) \Pi_{ij}(k_y) \quad (7.18)$$

where Ξ and Π reflect the x and y dependence of the matrix elements. As the modal index m increases, the terms $\Xi_{ij}(k_x)$ converge asymptotically to analytical expressions indicated by Ξ_{ij}^{conv} . The matrix elements can then be written as

$$Z_{ij}^{mod} = \sum_{m=0}^{m_{conv}} \Xi_{ij}(k_x) \Pi_{ij}(k_y) + \Xi_{ij}^{conv} \sum_{m_{conv}}^{\infty} \Pi_{ij}(k_y) \quad (7.19)$$

$$= \sum_{m=0}^{m_{conv}} (\Xi_{ij}(k_x) - \Xi_{ij}^{conv}) \Pi_{ij}(k_y) + \Xi_{ij}^{conv} \sum_{m=0}^{\infty} \Pi_{ij}(k_y) \quad (7.20)$$

where the upper limit of convergence m_{conv} is found numerically for a given geometry according to the desired accuracy. The infinite summation (7.18) is therefore trans-

formed into two terms: a rapidly converging finite sum and an infinite series which often may be expressed in closed form. The following sections describe the derivation of the asymptotic expressions Ξ_{ij}^{conv} and the evaluation of the k_y summations $\sum_{m=0}^{\infty} \Pi_{ij}(k_y)$.

Evaluation of the asymptotic expressions Ξ_{ij}^{conv}

According to the notation defined in Chapter 6, the terms $\Xi_{ij}(k_x)$ are given by

$$\begin{aligned}
\Xi_{xx} &= \frac{j}{\omega \epsilon_b^*} \frac{\delta_m}{b} \frac{(k_y^2 + k_z^2)}{k_{xd}^2} \left[\Upsilon_a^+ v_a^+(x_p) + \Upsilon_a^- v_a^-(x_p) \right] \\
\Xi_{xy} &= -\frac{j}{\omega \epsilon_b^*} \frac{\delta_m}{b} \frac{k_y k_x}{k_{xd}^2} \left[\Upsilon_a^+ \varphi_a^+(x_p) + \Upsilon_a^- \varphi_a^-(x_p) \right] \\
\Xi_{xz} &= \frac{1}{\omega \epsilon_b^*} \frac{\delta_m}{b} \frac{k_z k_x}{k_{xd}^2} \left[\Upsilon_a^+ \varphi_a^+(x_p) + \Upsilon_a^- \varphi_a^-(x_p) \right] \\
\Xi_{yx} &= -\frac{j}{\omega \epsilon_b^*} \frac{\delta_m}{b} \frac{k_y}{k_{xd}} \left[\Psi_a^+ v_a^+(x_p) + \Psi_a^- v_a^-(x_p) \right] \\
\Xi_{yy} &= j \frac{\delta_m}{b} \frac{1}{k_y^2 + k_z^2} \frac{1}{k_{xd}} \\
&\quad \left[k_y^2 (\eta_c)_a^b \left(\Psi_a^+ \varphi_a^+(x_p) + \Psi_a^- \varphi_a^-(x_p) \right) + k_z^2 (\eta_c)_f^b \left(\Psi_f^+ \varphi_f^+(x_p) + \Psi_f^- \varphi_f^-(x_p) \right) \right] \\
\Xi_{yz} &= \frac{\delta_m}{b} \frac{k_y k_z}{(k_y^2 + k_z^2)} \frac{1}{k_{xd}} \\
&\quad \left[-(\eta_c)_a^b \left(\Psi_a^+ \varphi_a^+(x_p) + \Psi_a^- \varphi_a^-(x_p) \right) + (\eta_c)_f^b \left(\Psi_f^+ \varphi_f^+(x_p) + \Psi_f^- \varphi_f^-(x_p) \right) \right] \\
\Xi_{zx} &= -\frac{1}{\omega \epsilon_b^*} \frac{\delta_m}{b} \frac{k_z}{k_{xd}} \left[\Psi_a^+ v_a^+(x_p) + \Psi_a^- v_a^-(x_p) \right] \\
\Xi_{zy} &= \frac{\delta_m}{b} \frac{k_y k_z}{(k_y^2 + k_z^2)} \frac{1}{k_{xd}} \\
&\quad \left[(\eta_c)_a^b \left(\Psi_a^+ \varphi_a^+(x_p) + \Psi_a^- \varphi_a^-(x_p) \right) - (\eta_c)_f^b \left(\Psi_f^+ \varphi_f^+(x_p) + \Psi_f^- \varphi_f^-(x_p) \right) \right] \\
\Xi_{zz} &= j \frac{\delta_m}{b} \frac{1}{k_y^2 + k_z^2} \frac{1}{k_{xd}} \\
&\quad \left[k_z^2 (\eta_c)_a^b \left(\Psi_a^+ \varphi_a^+(x_p) + \Psi_a^- \varphi_a^-(x_p) \right) + k_y^2 (\eta_c)_f^b \left(\Psi_f^+ \varphi_f^+(x_p) + \Psi_f^- \varphi_f^-(x_p) \right) \right]
\end{aligned} \tag{7.21}$$

where

$$k_y = m \frac{\pi}{b} \quad (7.22)$$

$$k_x = \sqrt{k^2 - k_y^2 - k_z^2} = -j \sqrt{k_z^2 + k_y^2 - k^2} \quad (7.23)$$

$$k_z = \text{constant} \quad (7.24)$$

As the modal index m increases to large values, the mode number k_y increases linearly, and $k_x \rightarrow -jk_y$, while k_z and k are independent of m . Also the impedances η_u and η_l degenerate to a constant ratio given by

$$\eta_u^a \rightarrow \frac{\epsilon_b}{\epsilon_{s-1}} \equiv \eta_u^{as} \quad (7.25)$$

$$\eta_l^a \rightarrow \frac{\epsilon_b}{\epsilon_{s+1}} \equiv \eta_l^{as} \quad (7.26)$$

Therefore the multilayered case does not require special treatment since, as $m \rightarrow \infty$, the impedances only involve the permittivities of the background and of the layer just adjacent to the source region. The elements Ξ simplify to

$$\begin{aligned} \Xi_{xx}^{conv} &= -\frac{j}{\omega \epsilon_b^*} \frac{1}{b} \left[2 \frac{\epsilon_b}{\epsilon_d} + \left(1 - \frac{\epsilon_b}{\epsilon_d} \right) \left(\frac{\eta_u^{as}}{1 + \eta_u^{as}} - \frac{\eta_l^{as}}{1 - \eta_l^{as}} \right) \right] \\ \Xi_{xy}^{conv} &= -\frac{j}{\omega \epsilon_b^*} \frac{1}{b} \left[\left(1 - \frac{\epsilon_b}{\epsilon_d} \right) \left(\frac{\eta_u^{as}}{1 + \eta_u^{as}} + \frac{\eta_l^{as}}{1 - \eta_l^{as}} \right) \right] \\ \Xi_{xz}^{conv} &= 0 \\ \Xi_{yx}^{conv} &= -\frac{j}{\omega \epsilon_b^*} \frac{1}{b} \left[\left(1 - \frac{\epsilon_b}{\epsilon_d} \right) \left(\frac{1}{1 + \eta_u^{as}} - \frac{1}{1 - \eta_l^{as}} \right) \right] \\ \Xi_{yy}^{conv} &= \frac{j}{\omega \epsilon_b^*} \frac{1}{b} \left[2 - \left(1 - \frac{\epsilon_b}{\epsilon_d} \right) \left(\frac{1}{1 + \eta_u^{as}} + \frac{1}{1 - \eta_l^{as}} \right) \right] \\ \Xi_{yz}^{conv} &= \frac{1}{\omega \epsilon_b^*} \frac{1}{b} \left[2 - \left(1 - \frac{\epsilon_b}{\epsilon_d} \right) \left(\frac{1}{1 + \eta_u^{as}} + \frac{1}{1 - \eta_l^{as}} \right) \right] \\ \Xi_{zx}^{conv} &= 0 \\ \Xi_{zy}^{conv} &= -\Xi_{yz}^{conv} \\ \Xi_{zz}^{conv} &= \frac{j}{\omega \epsilon_b^*} \frac{1}{b} \left[2 (k_z^2 - k_o^2) - k_z^2 \left(1 - \frac{\epsilon_b}{\epsilon_d} \right) \left(\frac{1}{1 + \eta_u^{as}} + \frac{1}{1 - \eta_l^{as}} \right) \right] \quad (7.27) \end{aligned}$$

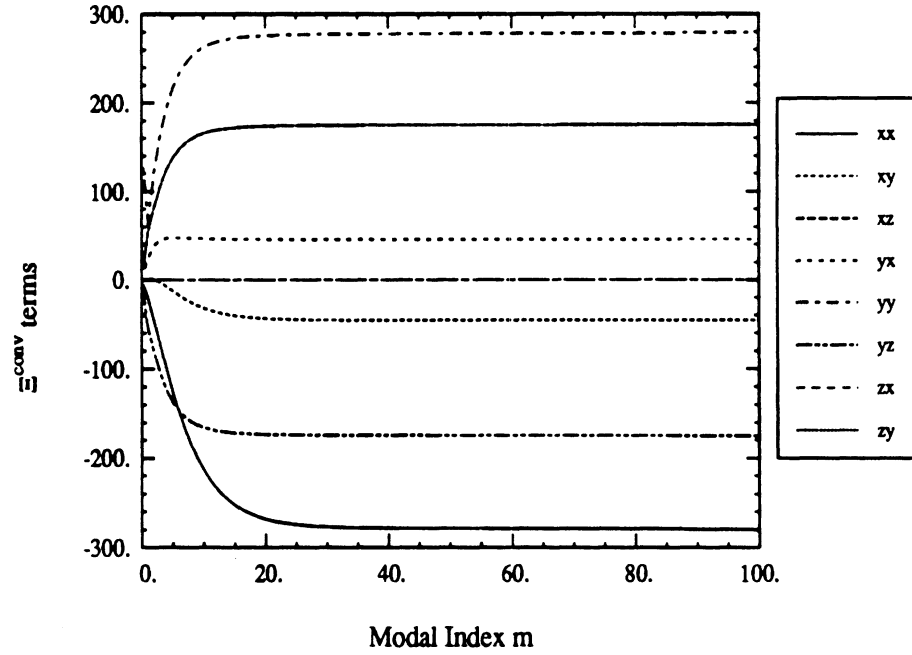


Figure 7.5: Convergence of the Ξ_{ij} terms as a function of the modal index m ($a = 5$ cm, $b = 2$ cm, $h_1 = 2.625$ cm, $h_2 = 0.5$ cm, $h_3 = 1.875$ cm, $w = 1$ cm, $\epsilon_{strip} = 12$, $\epsilon_{substrate} = 2$, $f = 3$ GHz)

where the k_y dependence of Ξ_{yz} , Ξ_{zy} , Ξ_{zz} is lumped with the expressions Π_{yz} , Π_{zy} and Π_{zz} . Because the behavior of these functions increases monotonically, a 'percent change' criterion is used to establish the upper limit of convergence, m_{conv} , with no source of error. In the example shown in Figure 7.5, the terms are seen to converge to within 0.1% after only 88 modes.

Evaluation of the infinite k_y summations

The terms of the infinite summations in equation (7.20) can be written as

$$\Pi_{xx}(k_y) = \Pi_{xz}(k_y) = \Pi_{zx}(k_y) = \mathcal{I}_p^{(2)} \mathcal{I}_q^{(2)}$$

$$\Pi_{xy}(k_y) = \mathcal{I}_p^{(1)} \mathcal{I}_q^{(2)}$$

$$\Pi_{yx}(k_y) = \mathcal{I}_p^{(2)} \mathcal{I}_q^{(1)}$$

$$\begin{aligned}
\Pi_{yy}(k_y) &= \mathcal{I}_p^{(1)} \mathcal{I}_q^{(1)} \\
\Pi_{yz}(k_y) &= \mathcal{I}_p^{(2)} \mathcal{I}_q^{(1)} \frac{1}{k_y} \\
\Pi_{zy}(k_y) &= \mathcal{I}_p^{(1)} \mathcal{I}_q^{(2)} \frac{1}{k_y} \\
\Pi_{zz}(k_y) &= \mathcal{I}_p^{(2)} \mathcal{I}_q^{(2)} \frac{1}{k_y^2}
\end{aligned} \tag{7.28}$$

where the \mathcal{I}_p terms represent the moments integrals resulting from the application of the method of moments. Out of the nine infinite summations over $\Pi_{ij}(k_y)$, only the series involving Π_{xy} and Π_{yx} cannot be cast in terms of closed-form expressions. The derivation of these expressions is illustrated through the series $\Pi_{xx}(k_y)$ where the infinite k_y summation defined in (7.19) becomes

$$\sum_{m=1}^{\infty} \text{Sinc}^2 \left(k_y \frac{W}{2Q} \right) \sin \left(y_o - \frac{W}{2} + (q - \frac{1}{2}) \frac{W}{Q} \right) \sin \left(y_o - \frac{W}{2} + (p - \frac{1}{2}) \frac{W}{Q} \right) \tag{7.29}$$

which may be written in terms of cosines as

$$\begin{aligned}
& \frac{1}{\left(k_y \frac{W}{Q} \right)^2} \left[\cos \left(k_y (q - p) \frac{W}{Q} \right) \right. \\
& - \frac{1}{2} \left\{ \cos \left(k_y (q - p + 1) \frac{W}{Q} \right) + \cos \left(k_y (q - p - 1) \frac{W}{Q} \right) \right\} \\
& + \frac{1}{2} \left\{ \cos \left(k_y \left(2 \left(y_o - \frac{W}{2} \right) + (q + p) \frac{W}{Q} \right) \right) \right. \\
& \left. + \cos \left(k_y \left(2 \left(y_o - \frac{W}{2} \right) + (q + p - 2) \frac{W}{Q} \right) \right) \right\} \\
& \left. - \cos \left(k_y \left(2 \left(y_o - \frac{W}{2} \right) + (q + p - 1) \frac{W}{Q} \right) \right) \right].
\end{aligned} \tag{7.30}$$

Using the trigonometric series transformation [111],

$$\sum_{m=1}^{\infty} \frac{\cos kx}{k^2} = \frac{\pi^2}{6} - \frac{\pi|x|}{2} + \frac{|x|^2}{4}, \quad 0 \leq |x| \leq 2\pi \tag{7.31}$$

and after some algebraic manipulation, the series (7.29) may be cast in the following form

$$\sum_{m=1}^{\infty} \text{Sinc}^2 \left(k_y \frac{W}{2Q} \right) \sin \left(y_o - \frac{W}{2} + (q - \frac{1}{2}) \frac{W}{Q} \right) \sin \left(y_o - \frac{W}{2} + (p - \frac{1}{2}) \frac{W}{Q} \right)$$

$$= \begin{cases} \frac{b}{2} \frac{Q}{W} & , p = q \\ 0 & , p \neq q \end{cases} \quad (7.32)$$

The other summations are derived in a similar fashion where the following Fourier series are used

$$\sum_{m=1}^{\infty} \frac{\sin kx}{k^3} = \text{signum}(x) \left[\frac{\pi^2|x|}{6} - \frac{\pi|x|^2}{4} + \frac{|x|^3}{12} \right], \quad 0 \leq |x| \leq 2\pi \quad (7.33)$$

$$\sum_{m=1}^{\infty} \frac{\cos kx}{k^4} = \frac{\pi^4}{90} - \frac{\pi^2|x|^2}{12} + \frac{\pi|x|^3}{12} - \frac{|x|^4}{48}, \quad 0 \leq |x| \leq 2\pi \quad (7.34)$$

In summary, the four k_y summations are given by

$$\sum_{m=1}^{\infty} \text{Sinc}^2 \left(m \frac{\pi W}{2 b Q} \right) \sin(m\phi_q) \sin(m\phi_p) = \frac{b}{2} \frac{Q}{W} \delta(q-p) \quad (7.35)$$

$$\sum_{m=1}^{\infty} \text{Sinc}^2 \left(m \frac{\pi W}{2 b Q} \right) \cos(m\phi_q) \cos(m\phi_p) = \frac{1}{2} + \frac{b}{2} \frac{Q}{W} \delta(q-p) \quad (7.36)$$

$$\sum_{m=1}^{\infty} \text{Sinc}^2 \left(m \frac{\pi W}{2 b Q} \right) \sin(m\phi_q) \cos(m\phi_p) \frac{b}{m\pi} = \frac{b}{2} \epsilon_{q,p} - \frac{1}{4} \left\{ 2\left(y_o - \frac{W}{2}\right) + \frac{W}{Q}(2q-1) \right\} \quad (7.37)$$

$$\sum_{m=1}^{\infty} \text{Sinc}^2 \left(m \frac{\pi W}{2 b Q} \right) \sin(m\phi_q) \sin(m\phi_p) \left(\frac{b}{m\pi} \right)^2 = \frac{b}{4} \left\{ 2\left(y_o - \frac{W}{2}\right) + \frac{W}{Q} \xi_{q,p} \right\} - \frac{1}{8} \left\{ \left(2\left(y_o - \frac{W}{2}\right) + (q+p+1) \right)^2 - \left(\frac{W}{Q} \right)^2 (q-p)^2 \right\} \quad (7.38)$$

where

$$\phi_q = \frac{\pi}{b} \left(y_o - \frac{W}{2} + (q - \frac{1}{2}) \frac{W}{Q} \right) \quad (7.39)$$

$$\epsilon_{q,p} = \begin{cases} \frac{1}{2} & , p = q \\ 1 & , p < q \\ 0 & , p > q \end{cases} \quad (7.40)$$

and

$$\xi_{q,p} = \begin{cases} 2q - \frac{4}{3} & , p = q \\ 2p - 1 & , p < q \\ 2q - 1 & , p > q \end{cases} \quad (7.41)$$

These closed-form expressions are independent of m and need to be computed only once for each (p,q) pair, significantly improving the convergence of the computer program.

7.4 Validation and limitations of the method

In this section, the Generalized Integral Equation method is validated through comparison to other well-established methods for the solution of the propagation characteristics in dielectric strips where both parallel and perpendicular polarizations are studied. A discussion of the limitation of the method for the case of perpendicular polarization ($a < b$) is presented.

7.4.1 Parallel polarization

Comparison to the mode matching technique

As a demonstration of the validity of the presented technique, theoretical results using the present method are compared to results derived from the classical 2-D modal analysis [1]. Good agreement is shown for the phase constant of the dominant mode as a function of frequency (Figure 7.6). In this mode, the electric field component which is parallel to the dielectric interface (E_y) is a few orders of magnitude larger than the other two components. As can be seen in Figure 7.6, the technique applies very efficiently even for electrically thick ridges ($w = 0.25 \lambda_g$ at 120 GHz).

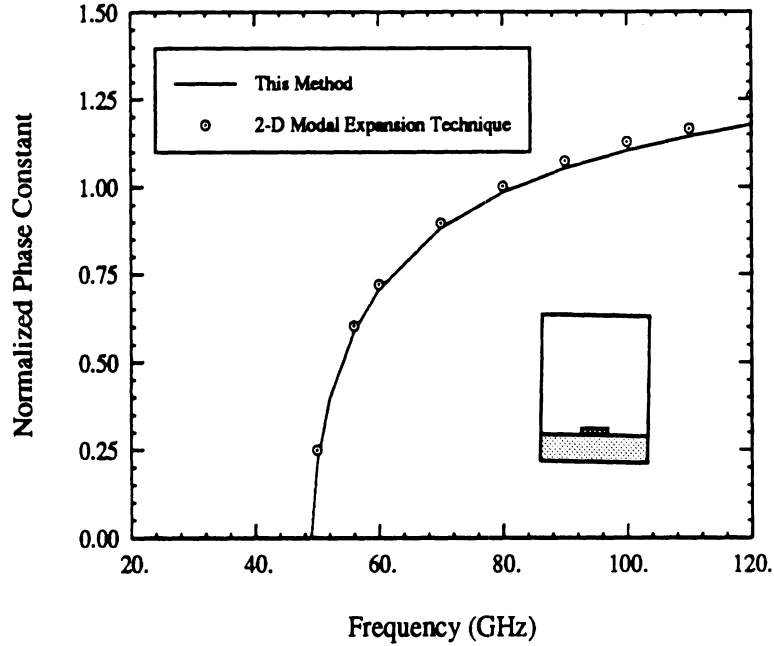


Figure 7.6: Comparison between the GIE method and the modal expansion method ($w = 0.5$ mm, $h = 62.5$ μ m, $s = 250$ μ m, $\epsilon_{strip} = 2$, $\epsilon_{substrate} = 12$)

Comparison to volume polarization current formulation

The Generalized Integral Equation method is also validated by comparison to the classical polarization current formulation. In this case, the electric field in the dielectric strip is represented in terms of a polarization current \vec{J}_p present only over the cross-section of the strip, as

$$\vec{E}_d = j\omega \int_0^h dx' \int_{y_0 - \frac{w}{2}}^{y_0 + \frac{w}{2}} dy' \tilde{\tilde{G}}^e(x, y/x', y') \cdot \vec{P}(x', y'). \quad (7.42)$$

Recalling (6.3), we can write the above integral equation in terms of a Fredholm integral equation of the second kind as

$$\frac{\vec{P}(x, y)}{(\epsilon_d - \epsilon_b)} = j\omega \int_0^h dx' \int_{y_0 - \frac{w}{2}}^{y_0 + \frac{w}{2}} dy' \tilde{\tilde{G}}^e(x, y/x', y') \cdot \vec{P}(x', y') \quad (7.43)$$

$$= j\omega \int_{y_0 - \frac{w}{2}}^{y_0 + \frac{w}{2}} dy' \left[\int_0^x dx' \tilde{\tilde{G}}^{(I)} + \int_x^h dx' \tilde{\tilde{G}}^{(II)} \right] \cdot \vec{P} \quad (7.44)$$

$$= j\omega \int_{y_0 - \frac{W}{2}}^{y_0 + \frac{W}{2}} dy' \Gamma(x, y) \cdot \vec{P}(x', y') \quad (7.45)$$

where $\Gamma(x, y)$ is given by

$$\Gamma(x, y) = \int_0^x dx' \vec{G}^{(I)}(x, y/x', y') + \int_x^h dx' \vec{G}^{(II)}(x, y/x', y'). \quad (7.46)$$

and (I) and (II) represent the regions $x > x'$ and $x < x'$, respectively. In the above, it is assumed that the strip thickness is small with respect to the guided wavelength λ_g and therefore, in the following, a single pulse is used to represent the vertical x dependence of the polarization current. A set of subsectional pulse expansion functions is used for the transverse y direction to represent $\vec{P}(x', y')$, yielding

$$\int_0^h dx \int_{y_0 - \frac{W}{2}}^{y_0 + \frac{W}{2}} dy \frac{\vec{P}(x, y)}{(\epsilon_r - 1)\epsilon_0} = j\omega \int_0^h dx \int_{y_0 - \frac{W}{2}}^{y_0 + \frac{W}{2}} dy \int_{y_0 - \frac{W}{2}}^{y_0 + \frac{W}{2}} dy' \Gamma(x, y) \cdot \vec{P}(x', y') \quad (7.47)$$

In Figure 7.7, results using the GIE method are compared to the polarization current formulation where very good agreement is shown for the dominant mode. The propagation constant of the dominant mode has been computed as a function of the width of the dielectric strip. As predicted for the extreme cases $W = 0$ and $W = b$, the structure simplifies to a partially-filled waveguide with homogeneous dielectric layers, for which the propagation constants are simply found by solving the appropriate characteristic equations [22].

7.4.2 Perpendicular polarization

In this section, the GIE method is applied to the case of a single strip in a waveguide structure with $a < b$. Figure 7.8 shows numerical results for the propagation constant as a function of the strip width using the GIE method and the mode matching method. For the case where $W = b$, the structure becomes a partially-filled waveguide for which this method agrees within 0.1% to the transcendental

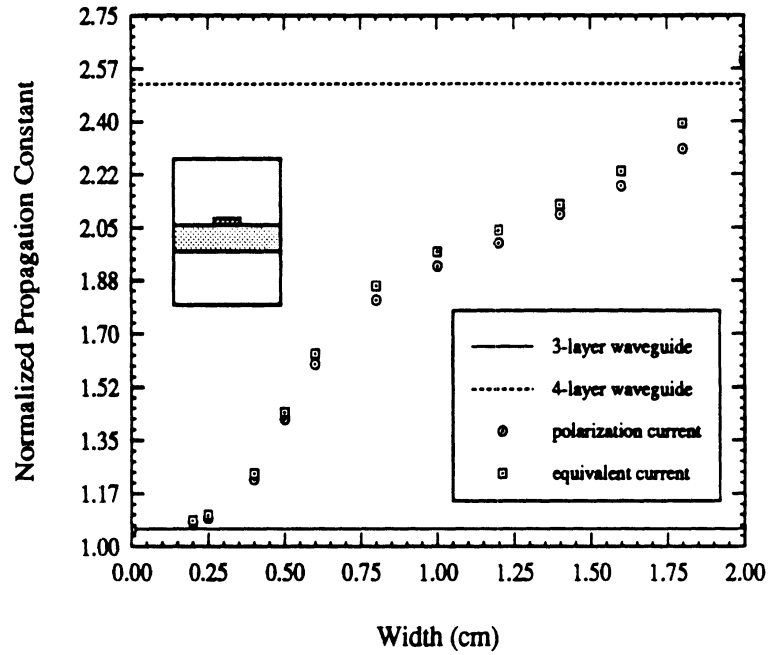


Figure 7.7: Comparison between the GIE method and the polarization current formulation ($a = 5$ cm, $b = 2$ cm, $h_1 = 2.5$ cm, $y_o = 0.75$ cm, $h_2 = 0.2$ cm, $h_3 = 2.3$ cm, $\epsilon_{strip} = 12$, $\epsilon_{substrate} = 2$, $f = 15$ GHz)

equations (7.14)-(7.15) as illustrated in Figure 7.8. For the case of very small strip width, the present method should provide a root close to the pole corresponding to the two-layer waveguide. However, deviation from the expected behaviour is noticed as the strip width to thickness ratio (aspect ratio) decreases (Figure 7.8). Similar problems have been encountered in scattering where it was noticed that GIBC's are invalid near abrupt discontinuities [99].

From the performed study, indications have been found which point out to the following interesting observations:

1. The method fails when the thickness to width ratio approaches or exceeds 0.3.
2. As the frequency of operation increases, the numerical solution of the derived planar Fredholm integral equation of the second kind provides spurious modes

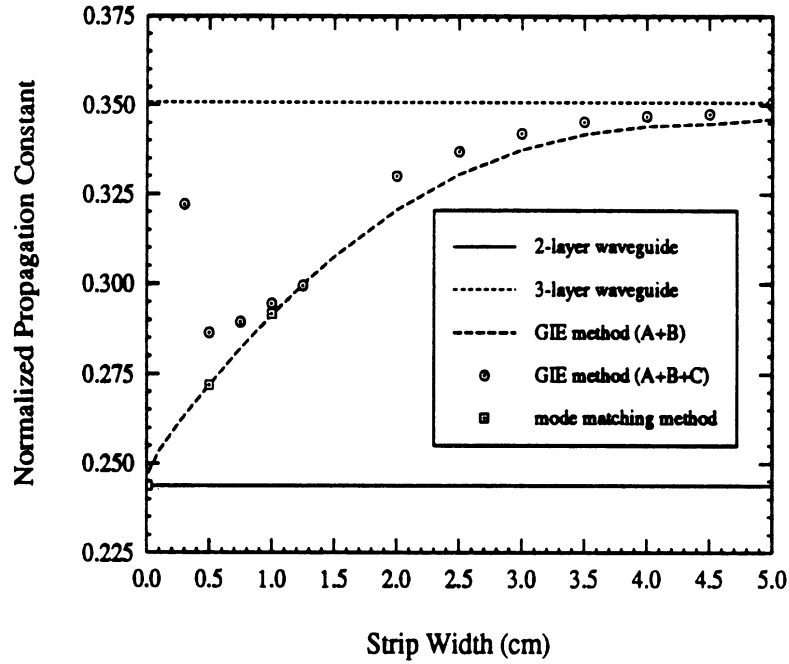


Figure 7.8: Comparison between the GIE method and the modal expansion method ($a = 2$ cm, $b = 5$ cm, $h_1 = 1.8$ cm, $h_2 = 0.2$ cm, $t = 0.1$ cm, $\epsilon_{strip} = 12$, $\epsilon_{substrate} = 2$, $f = 3$ GHz)

around the physically existing ones.

3. The presence and intensity of the problem described in the above are dominated by the definition of the planar polarization current. Preliminary results have indicated the possibility of eliminating this problem by using an appropriate weighting function in the definition of the planar current in terms of the polarization current in (6.10).

This is an important problem for future study.

7.5 Numerical results

A computer program was implemented to calculate the propagation constant of single and multiple lines using the approach described above. The results presented

in this section are derived for the case of two-dimensional dielectric strips within a shielding waveguide. The presence of the waveguide does not affect the guiding properties of the lines when the walls are far enough. The electric field of the fundamental mode on the line is excited by feeding the structure with a TE_{01} rectangular waveguide mode. Two types of modes may then propagate in the dielectric structure, namely waveguide modes (known as surface wave modes in open configuration) which are related to the supporting structure, and strip modes which are confined to the dielectric waveguides. The first modes will always propagate above the cut-off of the waveguide. On the other hand, the strip mode will not exist unless the guiding layer is above a critical thickness and width. In this analysis, the width-to-thickness ratio of the strips is moderately large. The strips rest in a multilayered environment which is intended to represent a typical integrated dielectric waveguide made of substrates, film and possible superstrates.

7.5.1 Single strip

The structure of Figure 7.9 has been analyzed using the Generalized Integral Equation method where the propagation constant of the dominant mode has been computed as a function of the width of the dielectric strip. As predicted for the extreme cases $W = 0$ and $W = b$, the structure simplifies to a partially-filled waveguide with three and four homogeneous dielectric regions, for which the propagation constants are simply found by solving the appropriate characteristic equations as mentioned above [20], [98].

In the present formulation, it is assumed that the thickness of the strip equals a fraction of the wavelength in the dielectric and is small compared to the strip width w_s . To test the range of validity of the GIE method with respect to the strip thickness,

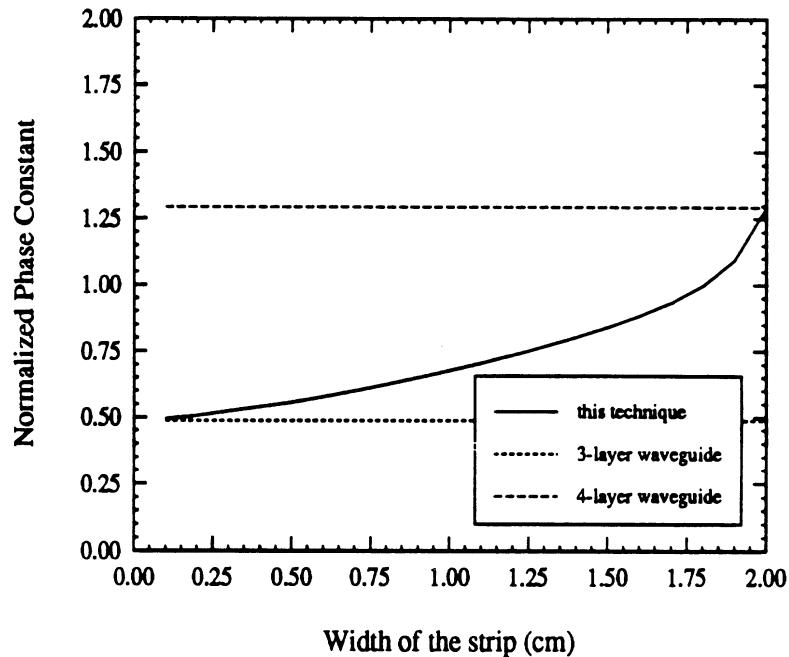
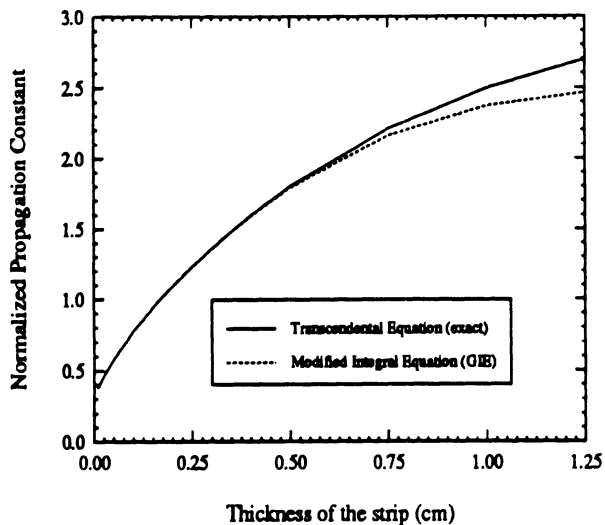


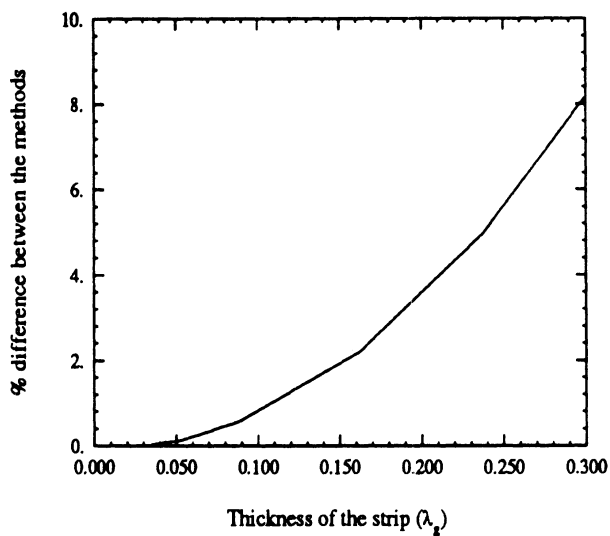
Figure 7.9: Phase constant as a function of strip width compared to a partially-filled waveguide structure ($f = 3$ GHz)

comparison is made between the present technique and the exact formulation which uses the transcendental equations (7.14)-(7.15) derived for the case where the strip width spans the width of the waveguide. In Figure 7.10, the propagation constant of the strip is shown as a function of the strip thickness where it is seen that, as the thickness of the strip is increased, the GIE method starts to deviate from the exact solution. However, this method is derived to analyze thin strips up to 0.1 guided wavelength, and displays an accuracy better than 1% in that range as seen in Figure 7.10b.

In Figure 7.11, the dispersion characteristics of a single strip have been computed as a function of frequency for the dominant mode and first higher order mode. Results are plotted for several strip width values, and are well confined between the cases $W = 0$ and $W = b$.



a. Propagation constant for a single strip as a function of the strip thickness



b. Percent difference between the GIE method and the exact formulation

Figure 7.10: Effect of strip thickness on the propagation characteristics ($a = 5$ cm, $b = 2$ cm, $h_1 = 2.3$ cm, $h_2 = 0.2$ cm, $h_3 = 2.3$ cm, $w = 2$ cm, $\epsilon_{strip} = 12$, $\epsilon_{substrate} = 2.2$, $f = 3$ GHz)

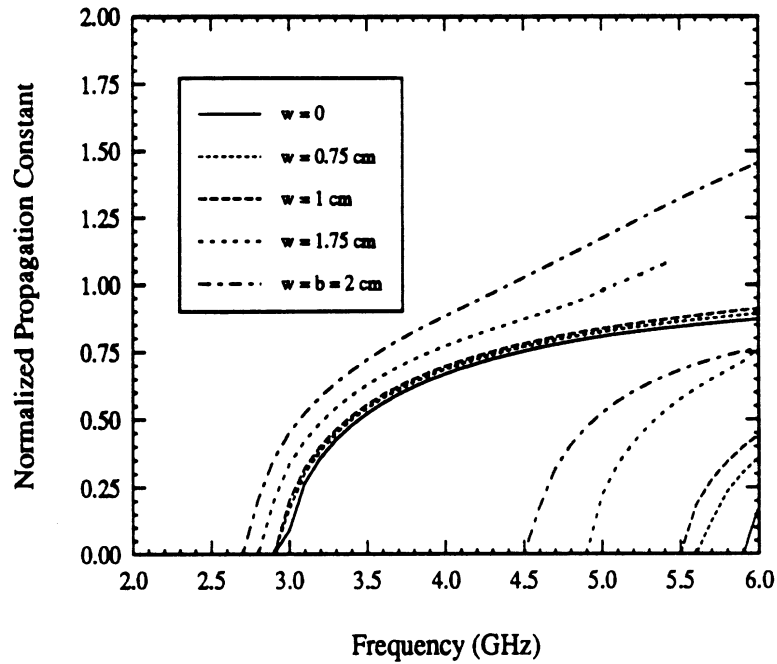


Figure 7.11: Frequency dependence of a single strip for different widths ($a = 5$ cm, $b = 2$ cm, $h_1 = 4.5$ cm, $h_2 = 0.5$ cm, $t = 0.2$ cm, $\epsilon_{strip} = 12$, $\epsilon_{substrate} = 2.2$)

7.5.2 Multiple strips

The fabrication of geometrically complex circuits on multilayered substrates faces stringent requirements on the spacing between elements. This in turn requires a good understanding of various coupling mechanisms. During the past few years, a number of papers have been published on the characterization of edge-coupled dielectric lines at millimeter-wave frequencies using the effective dielectric constant (EDC) method [100], [101], the mode-matching technique [102], variational methods [103] and integral equation formulations [104], [105].

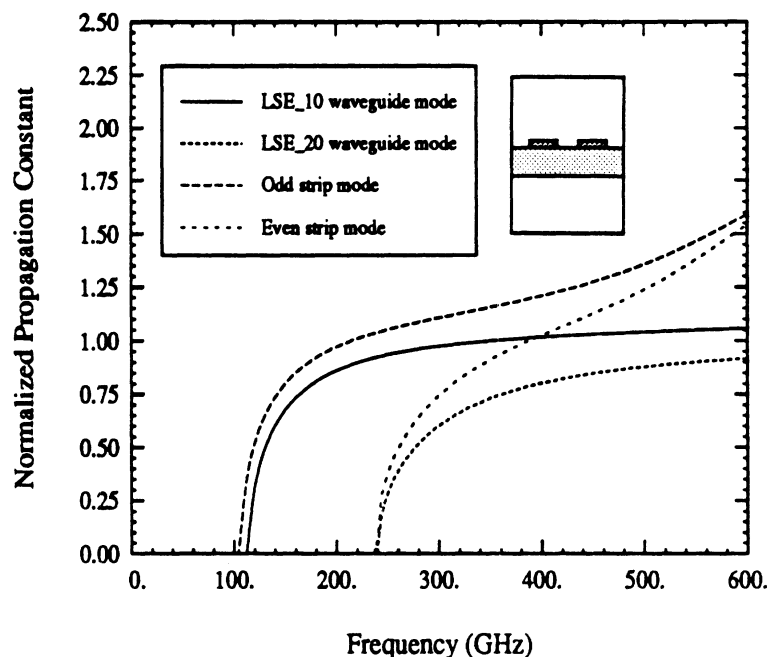


Figure 7.12: Normalized phase constant of the propagating modes as a function of frequency ($a = 1.25\text{mm}$, $b = 500\mu\text{m}$, $w_1 = w_2 = 125\mu\text{m}$, $h = h_1 = h_2 = 50\mu\text{m}$, $t = 50\mu\text{m}$, $s = 125\mu\text{m}$, $\epsilon_l = 12$, $\epsilon_{sub} = 2.2$)

Frequency dependence

The computer program was implemented to calculate the propagation constant and coupling coefficient of multilevel lines using the approach described above [108]. Figure 7.12 shows the dispersion characteristics of coupled dielectric lines in a horizontal (E_y) field configuration. The dotted lines correspond to the first two waveguide modes of the partially-filled structure (LSE_{10} and LSE_{20} , in this example) and the solid lines to the modes of the structure with the strips present. For high frequencies, the odd mode is actually higher than the even mode because of the waveguide polarization in this particular example. As the operating frequency decreases, the strips become electrically small and the fields are no more confined to the strips. The corresponding modes then degenerate to a perturbation of the partially-filled waveguide

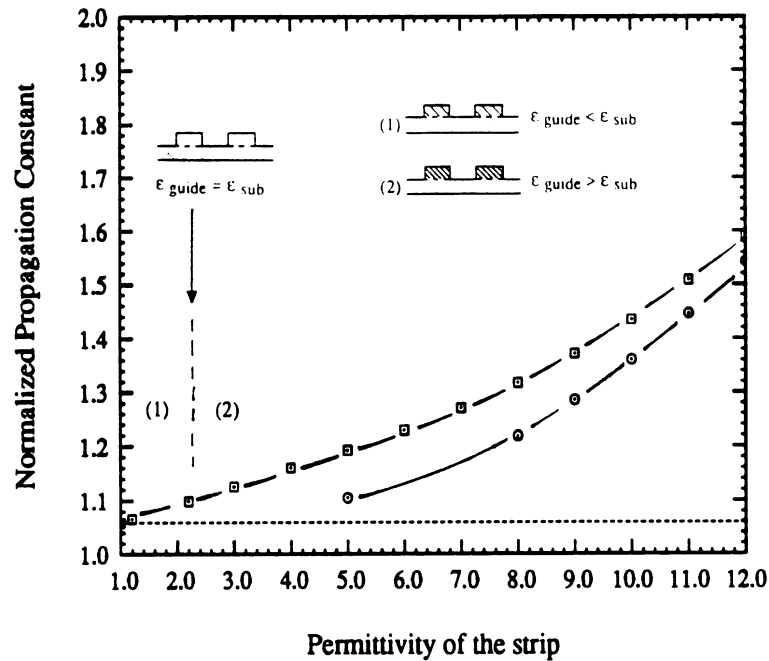


Figure 7.13: Propagation constant as a function of permittivity of the line ($a = 5\text{cm}$, $b = 2\text{cm}$, $w_1 = w_2 = 5\text{mm}$, $h_1 = h_2 = 2\text{mm}$, $s = 5\text{mm}$, $\epsilon_{\text{sub}} = 2.2$, $f = 15\text{GHz}$)

modes. A number of non-physical modes without low-frequency cut-off were found. The pattern of these spurious modes was easily recognizable and was disregarded on Figure 7.12 for sake of clarity (as were the many higher-order modes propagating above 250 GHz). This type of problem is not uncommon in the numerical solution of electromagnetics problems, as in the case of the finite-element method [109].

Effect of strip permittivity

In Figure 7.13, the phase constant of the odd and even modes are investigated for three different types of guides : the rib ($\epsilon_{\text{guide}} = \epsilon_{\text{substrate}}$), the strip dielectric ($\epsilon_{\text{guide}} < \epsilon_{\text{substrate}}$) in region 1 and the insulated image guide ($\epsilon_{\text{guide}} > \epsilon_{\text{substrate}}$) in region 2. Note that for $\epsilon_{\text{guide}} = 1$, no strip is actually present, and the phase constant

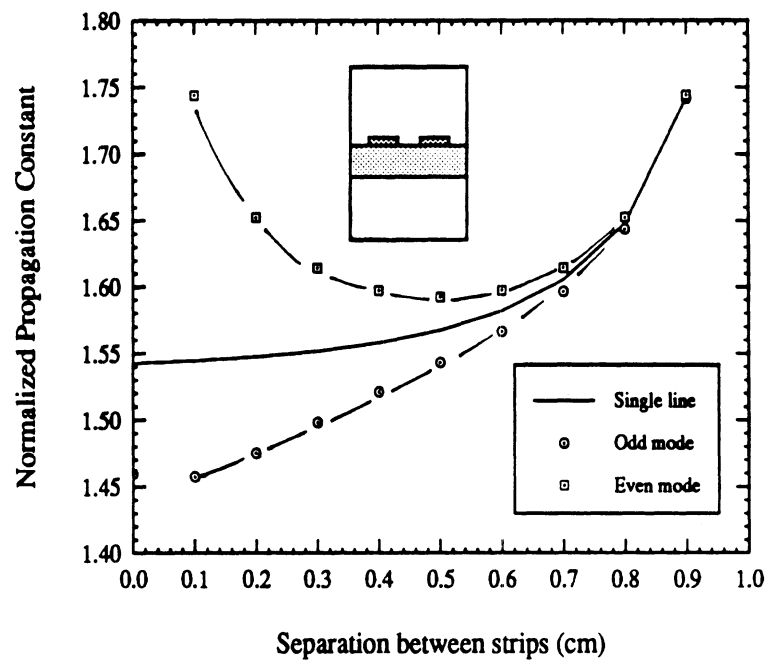


Figure 7.14: The normalized phase constant as a function of strip separation ($a = 5\text{cm}$, $b = 2\text{cm}$, $w_1 = w_2 = 5\text{mm}$, $h_1 = h_2 = 2\text{mm}$, $\epsilon_l = 12$, $\epsilon_{sub} = 2.2$, $f = 15\text{GHz}$)

reduces to the waveguide mode of the partially-filled structure. The permittivity of the substrate was chosen to be 2.2 in this example. However, in actual fabrication, III-V materials must be selected for the substrate and lines due to their adhesion properties.

Coupling effects

The phase constant is shown (Figure 7.14) for two identical strip dielectric guides as a function of separation s and compared to a single line at the location of strip #1. The normalized propagation constant of the odd and even modes tends to degenerate to the single line case as the separation increases, showing a decrease in the coupling between the lines. This is due to the fact that at higher frequencies the fields tend

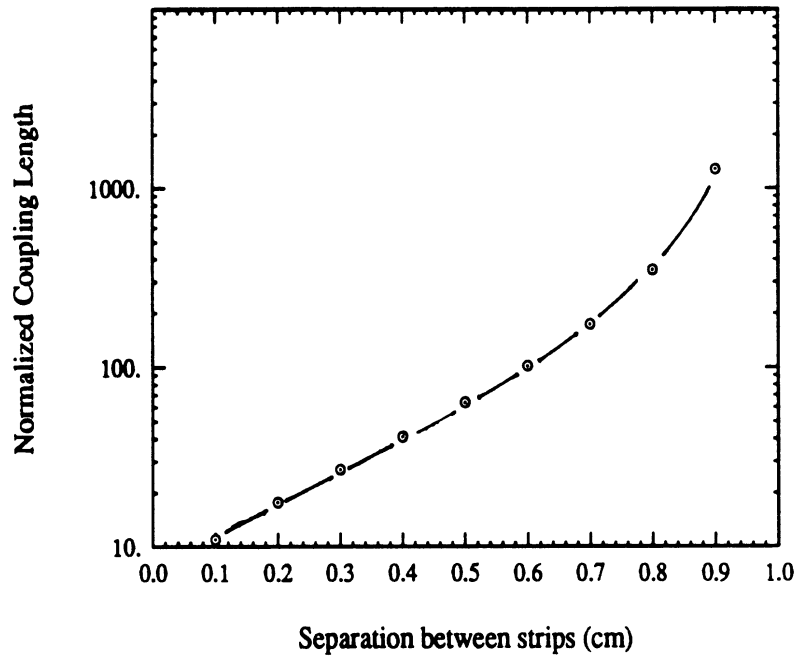


Figure 7.15: The normalized coupling length for total power transfer versus strip separation

to concentrate in the strip regions.

The present study also involves the calculation of the coupling coefficient. In the case of two symmetric coupled lines, the coupling coefficient is defined according to classical coupled mode theory [107]. For maximum coupling, the coupler should be designed with a length of

$$L = \frac{\pi}{\beta_e - \beta_o} \quad (7.48)$$

where β_e and β_o are the phase constants of the even and odd mode, respectively. The normalized coupling length L/h is plotted in Figure 7.15, where h is the height of the dielectric guide. The higher the normalized wavenumber of the waveguide, the higher is the coupling length.

CHAPTER VIII

CONCLUSIONS AND RECOMMENDATIONS

The basic structures treated in this thesis involve two-dimensional metallic and dielectric lines which can be used as building block for interconnects. Both types of structures are analyzed using integral equation techniques to provide the transmission line propagation characteristics. The integral equation approach is based on a full-wave formulation and contains a Green's function derived for shielded waveguiding structures involving multilayered substrates and superstrates. The dielectric layers are incorporated in the dyadic Green's function through the use of impedance boundary conditions derived from transmission line analysis. The formulation accounts for multilevel lines without limitation on the width, the location or the number of strips.

The approach involves Fredholm integral equations of the second kind that are solved by the method of moments using entire domain and subsectional basis functions for the expansion of the unknown currents. The analytical and numerical techniques derived in this thesis have been implemented in powerful computer programs capable of characterizing multiple microstrip lines and dielectric strip guides. Extensive numerical results illustrate important aspects regarding losses and dispersion in high frequency metallic interconnects and the propagation characteristics of

dielectric lines. In the following sections a summary of achievements is presented and extensions of the present work are proposed.

8.1 Summary of achievements

8.1.1 Microstrip lines

The present work calculated the effect of dispersion and losses in microstrip lines with thicknesses of the order of a skin depth. To that end, an integral equation formulation using dyadic Green's functions was used to solve for the dispersion relations and frequency-dependent circuit parameters of single and coupled metallic microstrip interconnects.

In this mathematical formulation, the fields were computed inside the conductors and were utilized to define an equivalent impedance on the surface of the strips. This surface impedance was used as a boundary condition for the solution of the electromagnetic problem outside the conductors. The novelty of this method resides in the application of the boundary condition on the strip with the tangential electric field related to the finite current on the strip by the surface impedance described above. The resulting general integral equation that accounts for both dielectric and conductor losses was solved numerically by the method of moments.

The total attenuation of the wave is due to losses in the conducting strips as well as in the dielectric materials. However, for microwave circuits of practical interest, dielectric losses were seen to be much smaller than conductor losses. For microstrip lines with thickness of the order of a skin depth, it was observed that the skin effect has a large influence on the phase constant, the attenuation and the characteristic impedance of the dominant propagating mode. Therefore, conductor loss has to be accounted for as a first order effect in the modeling and design of today's MMIC's

circuits with thin metallizations.

Another contribution is the accurate modeling of the effect of conductor losses on pulse dispersion and on cross-talk between lines on different levels in VLSI circuits. Conductor losses were shown to reduce the pulse amplitude and smooth the sharpness of the pulses and were increasingly important as the rise and fall times of the pulses became less than 100 ps.

The method was validated by measurements and by comparison with other methods in the literature. The formulation is general and therefore applicable to the evaluation and design of different types of MMIC structures, such as multilevel structures with broadside-coupled conductors, as well as coplanar lines, striplines and finlines.

8.1.2 Superconducting lines

The generalized integral equation derived to study losses in normal conductors was applied to calculate the propagation characteristics of high temperature thin-film superconducting lines at high frequencies. To evaluate the losses in these lines, the superconducting strips were replaced by frequency-dependent surface impedance boundaries. The novelty of the approach was the use of a measured surface impedance of the high temperature superconducting YBCO films to simulate an equivalent boundary condition on the strip. The values of the surface impedances were measured experimentally versus frequency and temperature by a stripline resonator technique. Using this method, phase and attenuation constants as well as characteristic impedance were evaluated and presented as functions of frequency and temperature for various geometries. As expected, it was noticed that ohmic losses are negligible and that dispersion is virtually nonexistent up to several GHz. Also, dissipative losses in the strips are mainly due to the dielectric substrates rather than to the high

T_c films.

8.1.3 Dielectric lines

A modified planar integral equation approach was developed for the analysis of monolithic structures using equivalent polarization currents. This method employed an integral equation formulation and used a dyadic Green's function together with higher-order generalized boundary conditions to study the influence of frequency, material constants and geometrical dimensions on the propagation constants of single and coupled dielectric strip waveguides. Propagation characteristics were presented for dielectric ridges on layered substrates and compared very closely to other well-established numerical methods for the polarization parallel to the dielectric interface.

8.2 Recommendation for future work

During the last couple of years, the developments made in analysis techniques for the study of microstrip dispersion and losses have made it possible to analyze microwave interconnects with arbitrary metallizations. Because of these essential improvements, the design of planar microwave passive components and interconnects is now a mature area where no further extension of this work is anticipated. However, the methodology described in this thesis can be applied to analyze high speed digital integrated circuits and multichip modules used in VLSI technology.

8.2.1 VLSI interconnects

The VLSI chips and modules are currently being designed and built with clock rates exceeding 60 MHz and up to 200 MHz. The 60-200 MHz clock rates require rise and fall times of the order of 100 ps which have a frequency content up to 10 GHz.

The thin metallic and dielectric layers used in multichip modules result in significant dispersion and delay, and large conductor losses due to the high series resistance and capacitance to ground present in multilayered lines. The study of interconnects for high-speed/high-density applications has not kept pace with the rapid technological progress. The design methods used today follow rules derived from elementary transmission line equations. Basically, high speed circuits use appropriate resistive terminations but neglect coupling, cross-talk, shielding and packaging effects, as well as losses at high frequencies and dispersion in the lines. These effects impose major limitations on many aspects of digital circuits, such as rise and fall times, spectral content of pulses, high error rates and low dynamic range due to unacceptable level of cross-talk and interference. It is therefore important to study these effects in order to build accurate models for the design and characterization of high-speed digital circuits and multichip modules. This will eliminate several design cycles and greatly reduce the manufacturing cost of high-speed digital integrated circuits.

8.2.2 Dielectric interconnects

The Generalized Integral Equation (GIE) technique introduced in this thesis is a novel method which can be implemented to study different geometries of low-loss dielectric ridge lines. However, additional theoretical and experimental research is needed to establish the accuracy of this method in the case of the characterization of strips with small width for perpendicular polarization. As discussed in Chapter 7, a thorough theoretical analysis needs to be performed to accurately predict the electrical characteristics of dielectric interconnects with arbitrary width to thickness ratio and the derived theoretical results should be validated by extensive experiments. Several areas should be further investigated which form the basis for extensions to

this work and are presented below.

A rather simple extension of the present work will be the study of the effect of dielectric losses in the substrates and in the guiding strips on the performance of thin dielectric lines at high frequencies. The proposed method can also be extended to layered structures by appropriately modifying the Taylor's expansion to account for the existence of the layers and the appropriate boundary conditions on the interfaces between them. Then, the solution can proceed exactly as has been previously described. As another application, this technique can be used to study the propagation characteristics and field distributions of optical waveguides and interconnects constructed from polyamide strips on GaAs substrates.

The effect of the shielding on the strip propagation behavior can be significant, and requires accurate modelling at high frequencies. In the present context, dielectric lines were analyzed within a shielded environment. However, for applications of dielectric lines in millimeter-wave and terahertz antennas, it is important to study the propagation characteristics in an open environment.

The planar integral equation technique can be further applied to study three-dimensional passive circuit elements such as power dividers, impedance transformers, bends and stubs. Such an extension is rather simple. With the replacement of the volume polarization current with an equivalent current of lower dimensionality, the original problem is simplified and can be treated as any other three-dimensional problem with unknown planar current densities [8]. The development of this technique allows the design of novel monolithic circuits which can provide high performance at frequencies up to the terahertz region.

APPENDICES

APPENDIX A

DERIVATION OF THE GENERALIZED GREEN'S FUNCTIONS OF A MULTILAYERED WAVEGUIDE

The goal of this work is to study the fundamental properties of two-dimensional circuit elements, and in particular, the propagation constants and characteristic impedances of transmission line interconnects. These parameters are directly related to the solution of the fields in the structure, which in turn requires the evaluation of the appropriate Green's functions. In this appendix, the electric and magnetic dyadic Green's functions, $\bar{\bar{G}}^e$ and $\bar{\bar{G}}^h$, respectively, are derived for an infinitesimal electric current placed in an inhomogeneously-filled rectangular waveguide uniform in the z direction (Figure A.1).

The calculation of the propagation constant can be determined from the knowledge of the fields in the source region alone. Thus, the first part of this appendix deals with the formulation of the Green's functions in the source region using potential theory where impedance boundary conditions are used to simulate the surrounding layers.

In order to calculate the characteristic impedance, the electric and magnetic fields have to be known over the whole cross-section of the waveguide. To that end, the next section provides a generalized formulation of the Green's functions in each dielectric

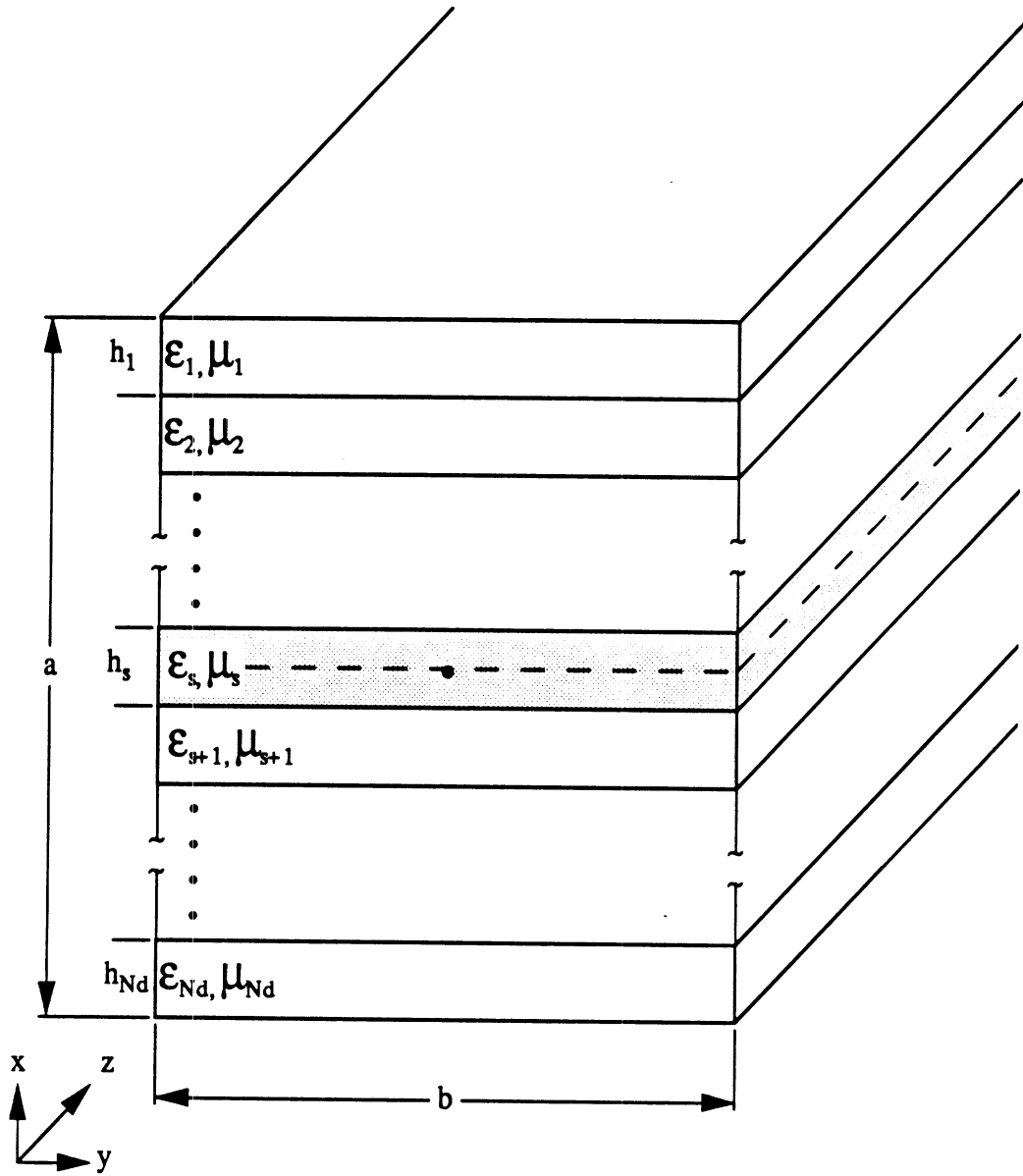


Figure A.1: Green's function geometry

layer within the shielded environment.

The dyadic Green's function is the solution of the fields due to a point source and can be represented, in rectangular coordinates, by

$$\bar{\bar{G}} = \begin{pmatrix} G_{xx}\hat{x}\hat{x} + G_{xy}\hat{x}\hat{y} + G_{xz}\hat{x}\hat{z} \\ G_{yx}\hat{y}\hat{x} + G_{yy}\hat{y}\hat{y} + G_{yz}\hat{y}\hat{z} \\ G_{zx}\hat{z}\hat{x} + G_{zy}\hat{z}\hat{y} + G_{zz}\hat{z}\hat{z} \end{pmatrix} \quad (\text{A.1})$$

where G_{ij} is the i th component of the field due to a unit j -directed current source $\delta(\vec{r} - \vec{r}')\hat{j}$.

A hybrid mode formulation involving LSM and LSE modes is used to derive the Green's function, where the following magnetic vector potential \vec{A} and electric vector potential \vec{F} are chosen to be

$$\vec{A} = \hat{x}A_x, \quad \vec{F} = \hat{x}F_x \quad (\text{A.2})$$

as discussed in Chapter 2. Using Maxwell's equations

$$\vec{\nabla} \times \vec{E} = -j\omega\mu\vec{H} \quad (\text{A.3})$$

$$\vec{\nabla} \times \vec{H} = \vec{J} + j\omega\epsilon\vec{E} \quad (\text{A.4})$$

together with

$$\vec{H} = \frac{1}{\mu}\vec{\nabla} \times \vec{A} \quad (\text{A.5})$$

$$\vec{E} = -\frac{1}{\epsilon}\vec{\nabla} \times \vec{F}, \quad (\text{A.6})$$

we can relate the electric and magnetic fields to the vector potentials \vec{A} and \vec{F} by

$$\vec{E} = -\frac{1}{\epsilon}\nabla \times \vec{F} - j\omega\vec{A} + \frac{1}{j\omega\epsilon\mu}\nabla\nabla \cdot \vec{A} \quad (\text{A.7})$$

$$\vec{H} = \frac{1}{\mu}\nabla \times \vec{A} - j\omega\vec{F} + \frac{1}{j\omega\epsilon\mu}\nabla\nabla \cdot \vec{F}. \quad (\text{A.8})$$

The individual components can be decomposed into their LSE contribution

$$E_x = 0 \quad (\text{A.9})$$

$$E_y = -\frac{1}{\epsilon} \frac{\partial}{\partial z} F_x \quad (\text{A.10})$$

$$E_z = \frac{1}{\epsilon} \frac{\partial}{\partial y} F_x \quad (\text{A.11})$$

$$H_x = -j\omega F_x + \frac{1}{j\omega\epsilon\mu} \frac{\partial^2}{\partial x^2} F_x \quad (\text{A.12})$$

$$H_y = \frac{1}{j\omega\epsilon\mu} \frac{\partial^2}{\partial x\partial y} F_x \quad (\text{A.13})$$

$$H_z = \frac{1}{j\omega\epsilon\mu} \frac{\partial^2}{\partial x\partial z} F_x \quad (\text{A.14})$$

and LSM contribution as

$$E_x = -j\omega A_x + \frac{1}{j\omega\epsilon\mu} \frac{\partial^2}{\partial x^2} A_x \quad (\text{A.15})$$

$$E_y = \frac{1}{j\omega\epsilon\mu} \frac{\partial^2}{\partial x\partial y} A_x \quad (\text{A.16})$$

$$E_z = \frac{1}{j\omega\epsilon\mu} \frac{\partial^2}{\partial x\partial z} A_x \quad (\text{A.17})$$

$$H_x = 0 \quad (\text{A.18})$$

$$H_y = \frac{1}{\mu} \frac{\partial}{\partial z} A_x \quad (\text{A.19})$$

$$H_z = -\frac{1}{\mu} \frac{\partial}{\partial y} A_x. \quad (\text{A.20})$$

Away from the source, the vector potentials satisfy the homogeneous vector Helmholtz equations

$$\nabla^2 \vec{A} + k^2 \vec{A} = 0 \quad (\text{A.21})$$

$$\nabla^2 \vec{F} + k^2 \vec{F} = 0 \quad (\text{A.22})$$

where $k = \omega\sqrt{\epsilon\mu}$. Equations (A.21)-(A.22) are solved for \vec{A} and \vec{F} using the method of separation of variables by applying the appropriate boundary conditions of the problem. Once the vector potentials are known, the electric and magnetic Green's functions may be derived through the use of (A.7) and (A.8).

A.1 Green's functions in the source layer

We will first restrict our attention to a point source within a homogeneous layer to simplify the notation without loss of generality. The problem is solved with the current source placed a distance x' above the reference plane to study the more general type of configuration shown in Figure A.1. After solving the general problem, the current can be set on one of the interfaces. The electric and magnetic fields due to the point source are derived in the source layer (s layer) which is divided in two regions, above (I) and below (II) the point source respectively (Figure A.2). Using the concept of wave impedances, the surrounding layers are replaced by impedance boundaries which are calculated by applying the transmission line theory. The application of the boundary conditions of the problem is twofold. First, the appropriate boundary conditions of the equivalent waveguide are applied. Then, the components of the Green's function are found by considering three subproblems corresponding to each direction of current (Figure A.3).

A.1.1 Application of the boundary conditions of the waveguide structure

Boundary conditions on the waveguide walls

The waveguide side walls are assumed to be perfectly conducting, and thus the tangential electric field must vanish at $y = 0$ and b , as

$$E_x^i(y = 0, b) = 0 \quad (\text{A.23})$$

$$E_z^i(y = 0, b) = 0 \quad (\text{A.24})$$

where i represents regions (I) and (II), above and below the current source.

Applying the method of separation of variables to solve (A.21) and (A.22), the potentials are obtained in terms of a series expansion, where the single summation

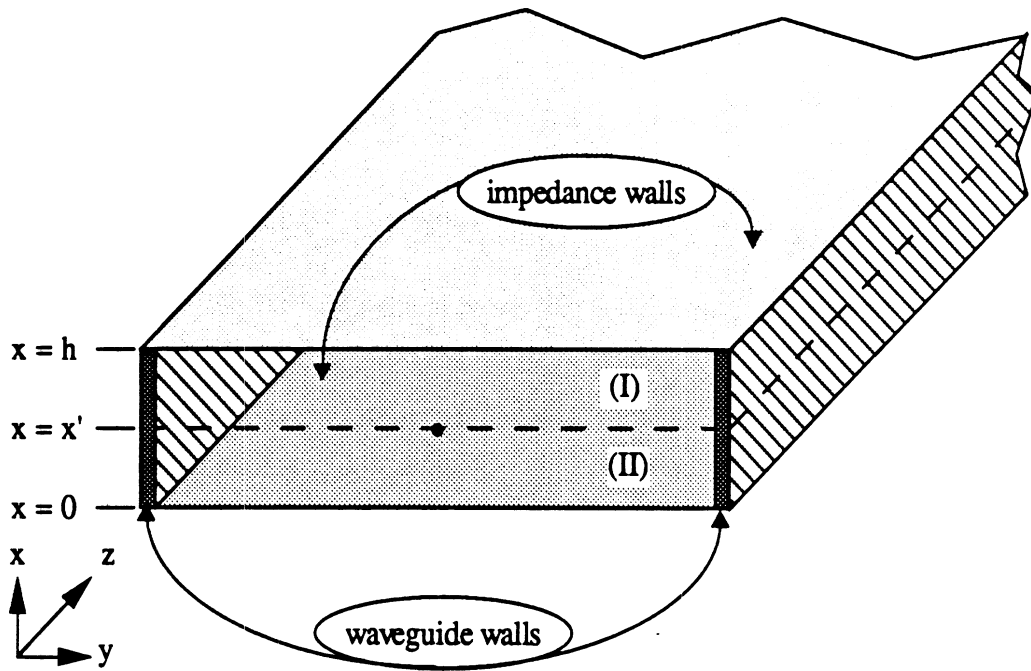


Figure A.2: Geometry of the source layer

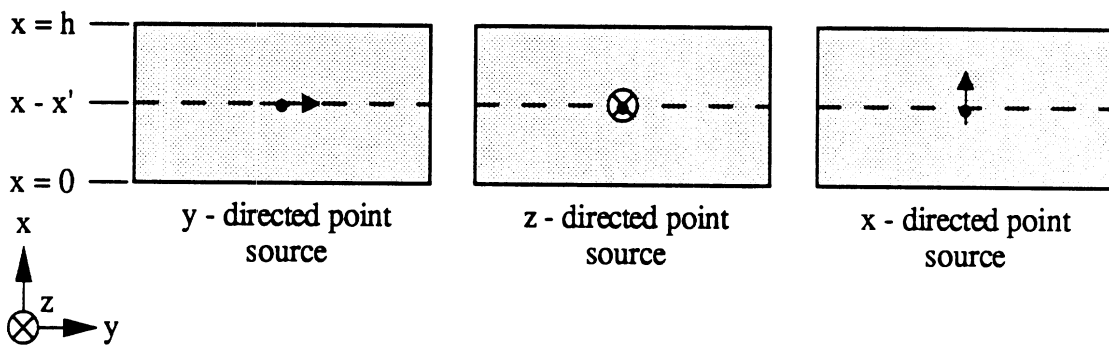


Figure A.3: Current point sources

is taken over all possible modes as

$$A_x^I = \sum_{m=0}^{\infty} \left[A_m^I \cos k_x(x-h) + B_m^I \sin k_x(x-h) \right] \sin k_y y e^{-jk_z z} \quad (\text{A.25})$$

$$A_x^{II} = \sum_{m=0}^{\infty} \left[A_m^{II} \cos k_x x + B_m^{II} \sin k_x x \right] \sin k_y y e^{-jk_z z} \quad (\text{A.26})$$

$$F_x^I = \sum_{m=0}^{\infty} \left[C_m^I \cos k_x(x-h) + D_m^I \sin k_x(x-h) \right] \cos k_y y e^{-jk_z z} \quad (\text{A.27})$$

$$F_x^{II} = \sum_{m=0}^{\infty} \left[C_m^{II} \cos k_x x + D_m^{II} \sin k_x x \right] \cos k_y y e^{-jk_z z} \quad (\text{A.28})$$

with

$$k_i = \omega \sqrt{\epsilon_i \mu_i} \quad (\text{A.29})$$

$$k_y = \frac{m\pi}{b}, \quad m=0,1,2,\dots \quad (\text{A.30})$$

$$k_x^2 = k_i^2 - k_y^2 - k_z^2. \quad (\text{A.31})$$

Since the waveguide and the current source are infinite along the z -direction, the wavenumber k_z is a continuously distributed eigenvalue. To simplify the notation and avoid carrying out the z -dependence that is common to all components, the vector potential components may be written in terms of their Fourier transform representation as

$$A_x = \frac{1}{2\pi} \int_{-\infty}^{\infty} dk_z \tilde{A}_x e^{-jk_z z} \quad (\text{A.32})$$

$$F_x = \frac{1}{2\pi} \int_{-\infty}^{\infty} dk_z \tilde{F}_x e^{-jk_z z} \quad (\text{A.33})$$

where

$$\tilde{A}_x = \int_{-\infty}^{\infty} dz A_x e^{jk_z z} \quad (\text{A.34})$$

$$\tilde{F}_x = \int_{-\infty}^{\infty} dz F_x e^{jk_z z}. \quad (\text{A.35})$$

Using this notation, the fields become, in the transform k_z domain

$$\tilde{E}_x = \frac{1}{j\omega\epsilon\mu} \left(k^2 + \frac{\partial^2}{\partial x^2} \right) \tilde{A}_x \quad (\text{A.36})$$

$$\tilde{E}_y = j \frac{k_z}{\epsilon} \tilde{F}_x + \frac{1}{j\omega\epsilon\mu} \frac{\partial^2}{\partial x \partial y} \tilde{A}_x \quad (\text{A.37})$$

$$\tilde{E}_z = \frac{1}{\epsilon} \frac{\partial}{\partial y} \tilde{F}_x - \frac{k_z}{\omega\epsilon\mu} \frac{\partial}{\partial x} \tilde{A}_x \quad (\text{A.38})$$

$$\tilde{H}_x = \frac{1}{j\omega\epsilon\mu} \left(k^2 + \frac{\partial^2}{\partial x^2} \right) \tilde{F}_x \quad (\text{A.39})$$

$$\tilde{H}_y = \frac{1}{j\omega\epsilon\mu} \frac{\partial^2}{\partial x \partial y} \tilde{F}_x - j \frac{k_z}{\mu} \tilde{A}_x \quad (\text{A.40})$$

$$\tilde{H}_z = -\frac{k_z}{\omega\epsilon\mu} \frac{\partial}{\partial x} \tilde{F}_x - \frac{1}{\mu} \frac{\partial}{\partial y} \tilde{A}_x \quad (\text{A.41})$$

where differentiation with respect to z in (A.9)-(A.20) is replaced by multiplication by jk_z in the Fourier-transformed domain. Since the Fourier transform chosen for the two-dimensional problem affects only the z coordinate, all boundary conditions specified for the spatial electromagnetic field can be directly transferred in the spectral domain, unless otherwise specified.

Boundary conditions at the upper and lower interfaces

The eight unknown coefficients in (A.25)-(A.28) are determined by the application of the appropriate boundary conditions. As defined in (2.46)-(2.47) we can define the following relations on the lower and upper guide walls

$$\eta_l^a = \left(\frac{\tilde{E}_y}{\tilde{H}_z} \right)^{LSM}, @ x = 0 \quad (\text{A.42})$$

$$\eta_l^f = \left(\frac{\tilde{E}_y}{\tilde{H}_z} \right)^{LSE}, @ x = 0 \quad (\text{A.43})$$

and

$$\eta_u^a = \left(\frac{\tilde{E}_y}{\tilde{H}_z} \right)^{LSM}, @ x = h \quad (\text{A.44})$$

$$\eta_u^f = \left(\frac{\tilde{E}_y}{\tilde{H}_z} \right)^{LSE}, @ x = h \quad (\text{A.45})$$

where η_u and η_l represent the impedances at the upper and lower interfaces, respectively. These are computed by applying transmission line theory to the other layers

as described in Chapter 2. From (A.36)-(A.41) and (A.42)-(A.45), one obtains

$$B_m^I = -j \left(\frac{\omega \epsilon}{k_x} \right) \eta_u^a A_m^I = -j \tilde{\eta}_u^a A_m^I \quad (\text{A.46})$$

$$C_m^I = j \left(\frac{k_x}{\omega \mu} \right) \eta_u^f D_m^I = j \tilde{\eta}_u^f D_m^I \quad (\text{A.47})$$

$$B_m^{II} = -j \left(\frac{\omega \epsilon}{k_x} \right) \eta_l^a A_m^{II} = -j \tilde{\eta}_l^a A_m^{II} \quad (\text{A.48})$$

$$C_m^{II} = j \left(\frac{k_x}{\omega \mu} \right) \eta_l^f D_m^{II} = j \tilde{\eta}_l^f D_m^{II} \quad (\text{A.49})$$

where $\tilde{\eta}_u$ and $\tilde{\eta}_l$ are introduced to simplify the notation and represent the normalized impedance boundary conditions with respect to the modal impedance of the dielectric layer as

$$\tilde{\eta}_{u,l}^f = \eta_{u,l}^f \left(\frac{k_x}{\omega \mu} \right) \quad (\text{A.50})$$

$$\tilde{\eta}_{u,l}^a = \eta_{u,l}^a \left(\frac{\omega \epsilon}{k_x} \right). \quad (\text{A.51})$$

Substituting (A.47)-(A.48) into the transform of (A.25)-(A.28), we get

$$\tilde{A}_x^{(I)} = \sum_{m=0}^{\infty} A_m^{(I)} [\cos k_x(x-h) - j\tilde{\eta}_u^a \sin k_x(x-h)] \sin k_y y \quad (\text{A.52})$$

$$\tilde{A}_x^{(II)} = \sum_{m=0}^{\infty} A_m^{(II)} [\cos k_x x - j\tilde{\eta}_l^a \sin k_x x] \sin k_y y \quad (\text{A.53})$$

$$\tilde{F}_x^{(I)} = \sum_{m=0}^{\infty} D_m^{(I)} [\sin k_x(x-h) + j\tilde{\eta}_u^f \cos k_x(x-h)] \cos k_y y \quad (\text{A.54})$$

$$\tilde{F}_x^{(II)} = \sum_{m=0}^{\infty} D_m^{(II)} [\sin k_x x + j\tilde{\eta}_l^f \cos k_x x] \cos k_y y. \quad (\text{A.55})$$

At this point we have reduced the problem to four unknowns complex coefficients $A_m^{(I)}$, $A_m^{(II)}$, $D_m^{(I)}$ and $D_m^{(II)}$. In the next section, boundary conditions at the source will be employed to solve for these unknowns.

A.1.2 Application of the boundary conditions at the source

The three subproblems shown in Figure A.3 are solved in this section. First a horizontal excitation parallel to the layers is assumed (y and z direction). Next, a

vertically oriented dipole is considered.

Electric and magnetic Green's functions for a y-directed current

The electric current is of the form

$$\vec{J} = \hat{y} \delta(x - x') \delta(y - y') \delta(z - z'). \quad (\text{A.56})$$

The complex coefficients for the potentials in region (II) are related to those in region (I) by applying continuity of the electric field tangential to the plane $x = x'$

$$\tilde{E}_y^I = \tilde{E}_y^{II} \quad , \quad x = x' \quad (\text{A.57})$$

$$\tilde{E}_z^I = \tilde{E}_z^{II} \quad , \quad x = x'. \quad (\text{A.58})$$

Combining (A.37)-(A.38) and (A.57)-(A.58), it follows that

$$A_m^{II} = A_m^I \frac{\sin k_x(x' - h) + j\tilde{\eta}_u^a \cos k_x(x' - h)}{\sin k_x x' + j\tilde{\eta}_l^a \cos k_x x'} \quad (\text{A.59})$$

$$D_m^{II} = D_m^I \frac{\sin k_x(x' - h) + j\tilde{\eta}_u^f \cos k_x(x' - h)}{\sin k_x x' + j\tilde{\eta}_l^f \cos k_x x'}. \quad (\text{A.60})$$

Recognizing the boundary condition for the magnetic field as

$$\hat{n} \times \vec{H} = \vec{J} \quad (\text{A.61})$$

the following boundary conditions at $x = x'$ are used to solve for the remaining two unknowns of the problem

$$H_y^I - H_y^{II} = 0 \quad (\text{A.62})$$

$$H_z^I - H_z^{II} = -J_y = -\delta(x - x')\delta(y - y')\delta(z - z'). \quad (\text{A.63})$$

Equation (A.63) represents the discontinuity of the z-component of the magnetic field at the interface $x = x'$ due to a y-directed current source. Only this boundary

condition will be different in the transform domain. Taking the Fourier transform defined as $\frac{1}{2\pi} \int_{-\infty}^{\infty} dk_z e^{-jk_z(z-z')} = \delta(z-z')$, (A.63) becomes

$$\widetilde{H}_z^I - \widetilde{H}_z^{II} = -\delta(y-y') e^{jk_z z'} \quad , x = x'. \quad (\text{A.64})$$

Multiplying the above equation by $\cos \frac{n\pi}{b}y$ and integrating both sides of the resulting equations over the cross-section of the waveguide, we get

$$\int_0^b (\widetilde{H}_z^I - \widetilde{H}_z^{II}) \cos \frac{n\pi}{b}y dy = - \int_0^b \delta(y-y') e^{jk_z z'} \cos \frac{n\pi}{b}y dy. \quad (\text{A.65})$$

Using the orthogonal properties of the cosine trigonometric function

$$\int_0^b \cos \frac{m\pi}{b}y \cos \frac{n\pi}{b}y dy = \begin{cases} b & , \text{ for } m = n = 0 \\ \frac{b}{2} & , \text{ for } m = n \neq 0 \\ 0 & , \text{ for } m \neq n \end{cases} \quad (\text{A.66})$$

yields, after simplification

$$A_m^I = \frac{\delta_m}{b} \mu k_y \cos k_y y' \frac{1}{k_y^2 + k_z^2} e^{jk_z z'} \frac{\sin k_x x' + j\tilde{\eta}_l^a \cos k_x x'}{\sin k_x h (1 - \tilde{\eta}_u^a \tilde{\eta}_l^a) + j(\tilde{\eta}_l^a - \tilde{\eta}_u^a) \cos k_x h} \quad (\text{A.67})$$

$$D_m^I = \frac{\delta_m}{b} \mu k_z \cos k_y y' \left(\frac{\omega \epsilon}{k_x} \right) \frac{1}{k_y^2 + k_z^2} e^{jk_z z'} \frac{\sin k_x x' + j\tilde{\eta}_l^f \cos k_x x'}{\sin k_x h (1 - \tilde{\eta}_u^f \tilde{\eta}_l^f) + j(\tilde{\eta}_l^f - \tilde{\eta}_u^f) \cos k_x h} \quad (\text{A.68})$$

where δ_m is the Neumann delta, given by

$$\delta_m = \begin{cases} 1 & , \text{ for } m = 0 \\ 2 & , \text{ for } m \neq 0. \end{cases} \quad (\text{A.69})$$

Using (A.52)-(A.55), we can finally write the \vec{A} and \vec{F} vector potentials in region (I) as

$$\vec{A}_x^{(I)} = \sum_{m=0}^{\infty} \frac{\delta_m}{b} \mu \frac{k_y}{k_y^2 + k_z^2} \frac{1}{\mathcal{D}_a} \sin k_y y \cos k_y y' e^{jk_z z'}$$

$$[\cos k_x(x-h) - j\tilde{\eta}_u^a \sin k_x(x-h)] [\sin k_x x' + j\tilde{\eta}_l^a \cos k_x x'] \quad (\text{A.70})$$

$$\begin{aligned} \tilde{F}_x^{(I)} = & \sum_{m=0}^{\infty} \frac{\delta_m}{b} \mu \frac{k_z}{k_y^2 + k_z^2} \frac{1}{\mathcal{D}_f} \cos k_y y \cos k_y y' e^{jk_x z'} \left(\frac{\omega \epsilon}{k_x} \right) \\ & [\sin k_x(x-h) + j\tilde{\eta}_u^f \cos k_x(x-h)] [\sin k_x x' + j\tilde{\eta}_l^f \cos k_x x'] \quad (\text{A.71}) \end{aligned}$$

where the denominator $\mathcal{D}_{a,f}$ is given by

$$\mathcal{D}_{a,f} = \sin k_x h (1 - \tilde{\eta}_u^{a,f} \tilde{\eta}_l^{a,f}) + j(\tilde{\eta}_l^{a,f} - \tilde{\eta}_u^{a,f}) \cos k_x h. \quad (\text{A.72})$$

After appropriate substitutions in (A.36)-(A.41), the components of the Green's function in region (I) due to a y directed current are obtained as

$$\begin{aligned} (\tilde{G}_{xy}^e)^I = & -\frac{j}{\omega \epsilon} \sum_{m=0}^{\infty} \frac{\delta_m}{b} k_y \frac{1}{\mathcal{D}_a} \sin k_y y \cos k_y y' e^{jk_x z'} \\ & \{ \cos k_x(x-h) - j\tilde{\eta}_u^a \sin k_x(x-h) \} \\ & \{ \sin k_x x' + j\tilde{\eta}_l^a \cos k_x x' \} \quad (\text{A.73}) \end{aligned}$$

$$\begin{aligned} (\tilde{G}_{yy}^e)^I = & j \sum_{m=0}^{\infty} \frac{\delta_m}{b} \frac{1}{k_y^2 + k_z^2} \cos k_y y \cos k_y y' e^{jk_x z'} \\ & \left[k_y^2 \left(\frac{k_x}{\omega \epsilon} \right) \frac{1}{\mathcal{D}_a} \{ \sin k_x x' + j\tilde{\eta}_l^a \cos k_x x' \} \right. \\ & \left. \{ \sin k_x(x-h) + j\tilde{\eta}_u^a \cos k_x(x-h) \} \right. \\ & \left. + k_z^2 \left(\frac{\omega \mu}{k_x} \right) \frac{1}{\mathcal{D}_f} \{ \sin k_x x' + j\tilde{\eta}_l^f \cos k_x x' \} \right. \\ & \left. \{ \sin k_x(x-h) + j\tilde{\eta}_u^f \cos k_x(x-h) \} \right] \quad (\text{A.74}) \end{aligned}$$

$$\begin{aligned} (\tilde{G}_{zy}^e)^I = & \sum_{m=0}^{\infty} \frac{\delta_m}{b} \frac{k_y k_z}{k_y^2 + k_z^2} \sin k_y y \cos k_y y' e^{jk_x z'} \\ & \left[\left(\frac{k_x}{\omega \epsilon} \right) \frac{1}{\mathcal{D}_a} \{ \sin k_x x' + j\tilde{\eta}_l^a \cos k_x x' \} \right. \\ & \left. \{ \sin k_x(x-h) + j\tilde{\eta}_u^a \cos k_x(x-h) \} \right. \\ & \left. - \left(\frac{\omega \mu}{k_x} \right) \frac{1}{\mathcal{D}_f} \{ \sin k_x x' + j\tilde{\eta}_l^f \cos k_x x' \} \right. \\ & \left. \{ \sin k_x(x-h) + j\tilde{\eta}_u^f \cos k_x(x-h) \} \right] \quad (\text{A.75}) \end{aligned}$$

$$\begin{aligned}
(\tilde{G}_{xy}^h)^I &= -j \sum_{m=0}^{\infty} \frac{\delta_m}{b} \frac{k_z}{k_x} \frac{1}{\mathcal{D}_f} \cos k_y y \cos k_y y' e^{jk_z z'} \\
&\quad \left\{ \sin k_x(x-h) + j\tilde{\eta}_u^f \cos k_x(x-h) \right\} \\
&\quad \left\{ \sin k_x x' + j\tilde{\eta}_l^f \cos k_x x' \right\}
\end{aligned} \tag{A.76}$$

$$\begin{aligned}
(\tilde{G}_{yy}^h)^I &= j \sum_{m=0}^{\infty} \frac{\delta_m}{b} \frac{k_y k_z}{k_y^2 + k_z^2} \sin k_y y \cos k_y y' e^{jk_z z'} \\
&\quad \left[-\frac{1}{\mathcal{D}_a} \left\{ \sin k_x x' + j\tilde{\eta}_l^a \cos k_x x' \right\} \right. \\
&\quad \left. \left\{ \cos k_x(x-h) - j\tilde{\eta}_u^a \sin k_x(x-h) \right\} \right. \\
&\quad \left. + \frac{1}{\mathcal{D}_f} \left\{ \sin k_x x' + j\tilde{\eta}_l^f \cos k_x x' \right\} \right. \\
&\quad \left. \left\{ \cos k_x(x-h) - j\tilde{\eta}_u^f \sin k_x(x-h) \right\} \right]
\end{aligned} \tag{A.77}$$

$$\begin{aligned}
(\tilde{G}_{zy}^h)^I &= - \sum_{m=0}^{\infty} \frac{\delta_m}{b} \frac{1}{k_y^2 + k_z^2} \cos k_y y \cos k_y y' e^{jk_z z'} \\
&\quad \left[k_y^2 \frac{1}{\mathcal{D}_a} \left\{ \sin k_x x' + j\tilde{\eta}_l^a \cos k_x x' \right\} \right. \\
&\quad \left. \left\{ \cos k_x(x-h) - j\tilde{\eta}_u^a \sin k_x(x-h) \right\} \right. \\
&\quad \left. + k_z^2 \frac{1}{\mathcal{D}_f} \left\{ \sin k_x x' + j\tilde{\eta}_l^f \cos k_x x' \right\} \right. \\
&\quad \left. \left\{ \cos k_x(x-h) - j\tilde{\eta}_u^f \sin k_x(x-h) \right\} \right].
\end{aligned} \tag{A.78}$$

In region (II), substitution of (A.67)-(A.68) in (A.59) and (A.60) yields

$$\begin{aligned}
A_m^{II} &= \frac{\delta_m}{b} \mu k_y \cos k_y y' \frac{1}{\mathcal{D}_a} \frac{1}{k_y^2 + k_z^2} e^{jk_z z'} \\
&\quad \left\{ \sin k_x(x'-h) + j\tilde{\eta}_u^a \cos k_x(x'-h) \right\}
\end{aligned} \tag{A.79}$$

$$\begin{aligned}
D_m^{II} &= \frac{\delta_m}{b} \mu k_z \cos k_y y' \frac{1}{\mathcal{D}_f} \left(\frac{\omega \epsilon}{k_x} \right) \frac{1}{k_y^2 + k_z^2} e^{jk_z z'} \\
&\quad \left\{ \sin k_x(x'-h) + j\tilde{\eta}_l^f \cos k_x(x'-h) \right\}
\end{aligned} \tag{A.80}$$

from which we obtain

$$\tilde{A}_x^{(II)} = \sum_{m=0}^{\infty} \frac{\delta_m}{b} \mu \frac{k_y}{k_y^2 + k_z^2} \frac{1}{\mathcal{D}_a} \sin k_y y \cos k_y y' e^{jk_z z'}$$

$$[\cos k_x x - j\tilde{\eta}_i^a \sin k_x x] [\sin k_x(x' - h) + j\tilde{\eta}_u^a \cos k_x(x' - h)] \quad (\text{A.81})$$

$$\begin{aligned} \tilde{F}_z^{(II)} = & \sum_{m=0}^{\infty} \frac{\delta_m}{b} \mu \frac{k_z}{k_y^2 + k_z^2} \frac{1}{\mathcal{D}_f} \cos k_y y \cos k_y y' e^{jk_z z'} \left(\frac{\omega \epsilon}{k_x} \right) \\ & [\sin k_x x + j\tilde{\eta}_i^f \cos k_x x] [\sin k_x(x' - h) + j\tilde{\eta}_u^f \cos k_x(x' - h)]. \quad (\text{A.82}) \end{aligned}$$

Note the duality between the relations in region (I) and (II) where the following transformations may be made to derive the Green's function components

$$\text{Region (I)} \longrightarrow \text{Region (II)}$$

$$x - h \longrightarrow x \quad (\text{A.83})$$

$$x' \longrightarrow x' - h \quad (\text{A.84})$$

$$\tilde{\eta}_u^f \longleftrightarrow \tilde{\eta}_i^f \quad (\text{A.85})$$

$$\tilde{\eta}_u^a \longleftrightarrow \tilde{\eta}_i^a. \quad (\text{A.86})$$

Electric and magnetic Green's functions for a z-directed current

The same steps as above are applied for the case of a z-directed electric dipole at (x', y', z') . The formulation only differs in the application of the boundary conditions at the source which are now represented by a discontinuity in the y-component of the magnetic field

$$H_y^I - H_y^{II} = J_z = \delta(x - x') \delta(y - y') \delta(z - z') \quad (\text{A.87})$$

$$H_z^I - H_z^{II} = 0. \quad (\text{A.88})$$

Orthogonality is applied to the transform of (A.87) where the following property of the sine trigonometric function is used

$$\int_0^b \sin \frac{m\pi}{b} y \sin \frac{n\pi}{b} y dy = \begin{cases} \frac{b}{2} & , \text{ for } m = n \neq 0 \\ 0 & , \text{ for } m \neq n \end{cases} \quad (\text{A.89})$$

to yield

$$A_m^I = j \frac{\delta_m}{b} \sin k_y y' \frac{\mu}{\mathcal{D}_a} \frac{k_z}{k_y^2 + k_z^2} e^{jk_z z'} \{ \sin k_x x' + j \tilde{\eta}_l^a \cos k_x x' \} \quad (\text{A.90})$$

$$D_m^I = -j \frac{\delta_m}{b} \sin k_y y' \frac{\mu}{\mathcal{D}_f} \left(\frac{\omega \epsilon}{k_x} \right) \frac{k_y}{k_y^2 + k_z^2} e^{jk_z z'} \{ \sin k_x x' + j \tilde{\eta}_l^f \cos k_x x' \} \quad (\text{A.91})$$

Hence, the components of the electric and magnetic Green's functions due to a z directed point source are given by

$$\begin{aligned} (\tilde{G}_{xx}^e)^I &= \frac{1}{\omega \epsilon} \sum_{m=0}^{\infty} \frac{\delta_m}{b} k_x \frac{1}{\mathcal{D}_a} \sin k_y y \sin k_y y' e^{jk_z z'} \\ &\quad \{ \cos k_x(x-h) - j \tilde{\eta}_u^a \sin k_x(x-h) \} \\ &\quad \{ \sin k_x x' + j \tilde{\eta}_l^a \cos k_x x' \} \end{aligned} \quad (\text{A.92})$$

$$\begin{aligned} (\tilde{G}_{yz}^e)^I &= \sum_{m=0}^{\infty} \frac{\delta_m}{b} \frac{k_y k_z}{k_y^2 + k_z^2} \cos k_y y \sin k_y y' e^{jk_z z'} \\ &\quad \left[- \left(\frac{k_x}{\omega \epsilon} \right) \frac{1}{\mathcal{D}_a} \{ \sin k_x x' + j \tilde{\eta}_l^a \cos k_x x' \} \right. \\ &\quad \quad \{ \sin k_x(x-h) + j \tilde{\eta}_u^a \cos k_x(x-h) \} \\ &\quad \quad \left. + \left(\frac{\omega \mu}{k_x} \right) \frac{1}{\mathcal{D}_f} \{ \sin k_x x' + j \tilde{\eta}_l^f \cos k_x x' \} \right. \\ &\quad \quad \left. \{ \sin k_x(x-h) + j \tilde{\eta}_u^f \cos k_x(x-h) \} \right] \end{aligned} \quad (\text{A.93})$$

$$\begin{aligned} (\tilde{G}_{zz}^e)^I &= j \sum_{m=0}^{\infty} \frac{\delta_m}{b} \frac{1}{k_y^2 + k_z^2} \sin k_y y \sin k_y y' e^{jk_z z'} \\ &\quad \left[k_z^2 \left(\frac{k_x}{\omega \epsilon} \right) \frac{1}{\mathcal{D}_a} \{ \sin k_x x' + j \tilde{\eta}_l^a \cos k_x x' \} \right. \\ &\quad \quad \{ \sin k_x(x-h) + j \tilde{\eta}_u^a \cos k_x(x-h) \} \\ &\quad \quad \left. + k_y^2 \left(\frac{\omega \mu}{k_x} \right) \frac{1}{\mathcal{D}_f} \{ \sin k_x x' + j \tilde{\eta}_l^f \cos k_x x' \} \right. \\ &\quad \quad \left. \{ \sin k_x(x-h) + j \tilde{\eta}_u^f \cos k_x(x-h) \} \right] \end{aligned} \quad (\text{A.94})$$

$$\begin{aligned} (\tilde{G}_{xz}^h)^I &= - \sum_{m=0}^{\infty} \frac{\delta_m}{b} \frac{k_y}{k_x} \frac{1}{\mathcal{D}_f} \cos k_y y \sin k_y y' e^{jk_z z'} \\ &\quad \{ \sin k_x(x-h) + j \tilde{\eta}_u^f \cos k_x(x-h) \} \\ &\quad \{ \sin k_x x' + j \tilde{\eta}_l^f \cos k_x x' \} \end{aligned} \quad (\text{A.95})$$

$$\begin{aligned}
(\tilde{G}_{yz}^h)^I &= \sum_{m=0}^{\infty} \frac{\delta_m}{b} \frac{1}{k_y^2 + k_z^2} \sin k_y y \sin k_y y' e^{jk_z z'} \\
&\quad \left[k_z^2 \frac{1}{\mathcal{D}_a} \{ \sin k_x x' + j\tilde{\eta}_l^a \cos k_x x' \} \right. \\
&\quad \quad \left. \{ \cos k_x(x-h) - j\tilde{\eta}_u^a \sin k_x(x-h) \} \right. \\
&\quad \quad \left. + k_y^2 \frac{1}{\mathcal{D}_f} \{ \sin k_x x' + j\tilde{\eta}_l^f \cos k_x x' \} \right. \\
&\quad \quad \left. \{ \cos k_x(x-h) - j\tilde{\eta}_u^f \sin k_x(x-h) \} \right] \quad (A.96)
\end{aligned}$$

$$\begin{aligned}
(\tilde{G}_{zz}^h)^I &= j \sum_{m=0}^{\infty} \frac{\delta_m}{b} \frac{k_y k_z}{k_y^2 + k_z^2} \cos k_y y \sin k_y y' e^{jk_z z'} \\
&\quad \left[-\frac{1}{\mathcal{D}_a} \{ \sin k_x x' + j\tilde{\eta}_l^a \cos k_x x' \} \right. \\
&\quad \quad \left. \{ \cos k_x(x-h) - j\tilde{\eta}_u^a \sin k_x(x-h) \} \right. \\
&\quad \quad \left. + \frac{1}{\mathcal{D}_f} \{ \sin k_x x' + j\tilde{\eta}_l^f \cos k_x x' \} \right. \\
&\quad \quad \left. \{ \cos k_x(x-h) - j\tilde{\eta}_u^f \sin k_x(x-h) \} \right]. \quad (A.97)
\end{aligned}$$

Similar expressions for the Green's functions in region (II) are derived using the transformations stated above (A.83) through (A.86).

Electric and magnetic Green's functions for a x-directed current

In the case of a current dipole perpendicular to the interface, only the magnetic vector potential $\vec{A} = A_x \hat{x}$ is needed to represent the fields [110]. The following boundary conditions are employed to solve for the two unknowns complex coefficients

$$E_z^I = E_z^{II} \quad (A.98)$$

$$\nabla^2 \vec{A} + k^2 \vec{A} = -\mu \delta(\vec{r} - \vec{r}') \hat{x}. \quad (A.99)$$

We start with (A.38) and use (A.98) to obtain

$$A_m^{II} = A_m^I \frac{\cos k_x(x' - h) - j\tilde{\eta}_u^a \sin k_x(x' - h)}{\cos k_x x' - j\tilde{\eta}_l^a \sin k_x x'} \quad (A.100)$$

The other boundary condition to apply is equation (A.99) which reduces from a vector wave equation to a scalar wave equation since the vector potential \vec{A} has only a component in the x direction

$$\nabla^2 A_x + k^2 A_x = -\mu \delta(\vec{r} - \vec{r}') \quad , x = x' \quad (\text{A.101})$$

and implies in rectangular coordinates

$$\left(\frac{\partial^2}{\partial x^2} - k_y^2 - k_z^2 \right) A_x + k^2 A_x = -\mu \delta(\vec{r} - \vec{r}'). \quad (\text{A.102})$$

Substitution of (A.31) in (A.102) yields

$$\left(\frac{\partial^2}{\partial x^2} + k_x^2 \right) A_x = -\mu \delta(x - x') \delta(y - y') \delta(z - z') \quad (\text{A.103})$$

which becomes in the transform k_z domain,

$$\left(\frac{\partial^2}{\partial x^2} + k_x^2 \right) \tilde{A}_x = -\mu \delta(x - x') \delta(y - y') e^{jk_z z'}. \quad (\text{A.104})$$

Multiplying both sides of Equation (A.104) by $\sin \frac{n\pi}{b} y$, and integrating the differential equation across the boundary at $x = x'$, we get

$$\left(\frac{\partial^2}{\partial x^2} + k_x^2 \right) \tilde{A}_x(x) = -\mu \delta(x - x') \frac{\delta_m}{b} \sin k_y y' e^{jk_z z'} \quad (\text{A.105})$$

where \tilde{A}_x is now only a function of x . We then integrate both sides of this equation (A.105) over a small interval passing through the source point \vec{r}' and take the limit as the interval vanishes

$$\lim_{\epsilon \rightarrow 0} \int_{x' - \epsilon}^{x' + \epsilon} \left(\frac{\partial^2}{\partial x^2} + k_x^2 \right) \tilde{A}_x(x) dx = -\mu \frac{\delta_m}{b} \sin k_y y' e^{jk_z z'}. \quad (\text{A.106})$$

If we make use of (A.52) and (A.53), we can show that the second term of the integrand vanishes as follows

$$\begin{aligned} \lim_{\epsilon \rightarrow 0} \int_{x' - \epsilon}^{x' + \epsilon} k_x^2 \tilde{A}_x(x) dx &= \lim_{\epsilon \rightarrow 0} \sum_{m=0}^{\infty} -k_x A_m^{(I)} [\sin k_x(x - h) + j\tilde{\eta}_u^a \cos k_x(x - h)] \Big|_{x=x'}^{x=x'+\epsilon} \\ &+ \lim_{\epsilon \rightarrow 0} \sum_{m=0}^{\infty} -k_x A_m^{(II)} [\sin k_x x + j\tilde{\eta}_l^a \cos k_x x] \Big|_{x=x'-\epsilon}^{x=x'} \end{aligned} \quad (\text{A.107})$$

since each limit vanishes individually. Therefore (A.106) can be reduced to

$$\left. \frac{d\tilde{A}_x(x)}{dx} \right|_{x'-\epsilon}^{x'+\epsilon} = -\mu \frac{\delta_m}{b} \sin k_y y' e^{jk_z z'} \quad (\text{A.108})$$

from which we obtain

$$A_m^I = -\frac{\delta_m}{b} \mu \sin k_y y' e^{jk_z z'} \frac{1}{k_x} \frac{1}{\mathcal{D}_a} \{ \cos k_x x' - j\tilde{\eta}_l^a \sin k_x x' \}. \quad (\text{A.109})$$

The xx component of the electric Green's function is found by applying (A.15)

as

$$G_{xx}^e = -j\omega A_x + \frac{1}{j\omega\epsilon\mu} \frac{\partial^2}{\partial x^2} A_x \quad (\text{A.110})$$

$$= \frac{1}{j\omega\epsilon\mu} \left(k^2 + \frac{\partial^2}{\partial x^2} \right) A_x. \quad (\text{A.111})$$

From (A.101) or (A.102), we can write

$$\left(k^2 + \frac{\partial^2}{\partial x^2} \right) A_x = -\mu\delta(\vec{r} - \vec{r}') + (k_y^2 + k_z^2) A_x. \quad (\text{A.112})$$

This equation shows that the self term G_{xx} has a singularity at the source point

$$G_{xx}^e = \frac{1}{j\omega\epsilon\mu} \left[-\mu\delta(\vec{r} - \vec{r}') + (k_y^2 + k_z^2) A_x \right] \quad (\text{A.113})$$

which may be written in the k_z space as

$$\tilde{G}_{xx}^e = \frac{1}{j\omega\epsilon\mu} \left[-\mu\delta(x - x') \delta(y - y') e^{jk_z z'} + (k_y^2 + k_z^2) \tilde{A}_x \right]. \quad (\text{A.114})$$

After appropriate substitutions, the components of the electric and magnetic Green's functions can be expressed as

$$\begin{aligned} (\tilde{G}_{xx}^e)^I &= \frac{j}{\omega\epsilon} e^{jk_z z'} [\delta(x - x') \delta(y - y')] \\ &+ \sum_{m=0}^{\infty} \frac{\delta_m}{b} \frac{k_y^2 + k_z^2}{k_x} \frac{1}{\mathcal{D}_a} \sin k_y y \sin k_y y' \\ &\quad \{ \cos k_x(x - h) - j\tilde{\eta}_u^a \sin k_x(x - h) \} \end{aligned}$$

$$\{\cos k_x x' - j\tilde{\eta}_l^a \sin k_x x'\} \quad (\text{A.115})$$

$$\begin{aligned} (\tilde{G}_{yx}^e)^I &= -\frac{j}{\omega\epsilon} \sum_{m=0}^{\infty} \frac{\delta_m}{b} k_y \cos k_y y \sin k_y y' e^{jk_x z'} \\ &\quad \frac{1}{\mathcal{D}_a} \{\cos k_x x' - j\tilde{\eta}_l^a \sin k_x x'\} \\ &\quad \{\sin k_x(x-h) + j\tilde{\eta}_u^a \cos k_x(x-h)\} \end{aligned} \quad (\text{A.116})$$

$$\begin{aligned} (\tilde{G}_{zx}^e)^I &= -\frac{1}{\omega\epsilon} \sum_{m=0}^{\infty} \frac{\delta_m}{b} k_z \sin k_y y \sin k_y y' e^{jk_x z'} \\ &\quad \frac{1}{\mathcal{D}_a} \{\cos k_x x' - j\tilde{\eta}_l^a \sin k_x x'\} \\ &\quad \{\sin k_x(x-h) + j\tilde{\eta}_u^a \cos k_x(x-h)\} \end{aligned} \quad (\text{A.117})$$

$$(\tilde{G}_{xx}^h)^I = 0 \quad (\text{A.118})$$

$$\begin{aligned} (\tilde{G}_{yx}^h)^I &= \frac{j}{\omega\mu} \sum_{m=0}^{\infty} \frac{\delta_m}{b} k_z \sin k_y y \sin k_y y' e^{jk_x z'} \\ &\quad \left(\frac{\omega\mu}{k_x}\right) \frac{1}{\mathcal{D}_a} \{\cos k_x x' - j\tilde{\eta}_l^a \sin k_x x'\} \\ &\quad \{\cos k_x(x-h) - j\tilde{\eta}_u^a \sin k_x(x-h)\} \end{aligned} \quad (\text{A.119})$$

$$\begin{aligned} (\tilde{G}_{zx}^h)^I &= \frac{1}{\omega\mu} \sum_{m=0}^{\infty} \frac{\delta_m}{b} k_y \cos k_y y \sin k_y y' e^{jk_x z'} \\ &\quad \left(\frac{\omega\mu}{k_x}\right) \frac{1}{\mathcal{D}_a} \{\cos k_x x' - j\tilde{\eta}_l^a \sin k_x x'\} \\ &\quad \{\cos k_x(x-h) - j\tilde{\eta}_u^a \sin k_x(x-h)\}. \end{aligned} \quad (\text{A.120})$$

A.2 Green's functions in the surrounding layers

The vector potentials in the layer above the source layer may be cast in the following form

$$\begin{aligned} \tilde{A}_x^{(s-1)} &= \sum_{m=0}^{\infty} A_m^{(s-1)} \sin k_y y \\ &\quad \left[\cos k_{x_{s-1}}(x-h-h_{s-1}) - j\tilde{\eta}_{s-1}^a \sin k_{x_{s-1}}(x-h-h_{s-1}) \right] \end{aligned} \quad (\text{A.121})$$

$$\begin{aligned} \tilde{F}_x^{(s-1)} &= \sum_{m=0}^{\infty} D_m^{(s-1)} \cos k_y y \\ &\quad \left[\sin k_{x_{s-1}}(x-h-h_{s-1}) + j\tilde{\eta}_{s-1}^f \cos k_{x_{s-1}}(x-h-h_{s-1}) \right] \end{aligned} \quad (\text{A.122})$$

where the impedances are given by

$$\tilde{\eta}_{s-1}^f = \eta_{s-1}^f \frac{k_{x_{s-1}}}{\omega \mu_{s-1}} \quad (\text{A.123})$$

$$\tilde{\eta}_{s-1}^a = \eta_{s-1}^a \frac{\omega \epsilon_{s-1}}{k_{x_{s-1}}}. \quad (\text{A.124})$$

These are related to (A.42)-(A.44) by

$$\tilde{\eta}_u^a = \frac{\omega \mu_{s-1}}{k_{x_{s-1}}} \frac{\tilde{\eta}_{s-1}^a + j \tan k_{x_{s-1}} h_{s-1}}{1 + j \tilde{\eta}_{s-1}^a \tan k_{x_{s-1}} h_{s-1}} \quad (\text{A.125})$$

$$\tilde{\eta}_u^f = \frac{k_{x_{s-1}}}{\omega \epsilon_{s-1}} \frac{\tilde{\eta}_{s-1}^f + j \tan k_{x_{s-1}} h_{s-1}}{1 + j \tilde{\eta}_{s-1}^f \tan k_{x_{s-1}} h_{s-1}}. \quad (\text{A.126})$$

By matching tangential components on the boundary $x = h$,

$$\tilde{E}_y^I = \tilde{E}_y^{s-1} \quad (\text{A.127})$$

$$\tilde{E}_z^I = \tilde{E}_z^{s-1} \quad (\text{A.128})$$

one gets, for a z directed current

$$A_m^{s-1} = \frac{\delta_m}{b} \frac{\mu_{s-1}}{\mathcal{D}_a} \frac{k_z}{k_y^2 + k_z^2} \left(\frac{\omega \epsilon_{s-1}}{k_{x_{s-1}}} \right) \eta_u^a \sin k_y y' e^{jk_z z'} \frac{\sin k_x x' + j \tilde{\eta}_i^a \cos k_x x'}{\sin k_{x_{s-1}} h_{s-1} - j \tilde{\eta}_{s-1}^a \cos k_{x_{s-1}} h_{s-1}} \quad (\text{A.129})$$

$$D_m^{s-1} = \frac{\delta_m}{b} \frac{\epsilon_{s-1}}{\mathcal{D}_f} \eta_u^f \frac{k_y}{k_y^2 + k_z^2} \sin k_y y' e^{jk_z z'} \frac{\sin k_x x' + j \tilde{\eta}_i^f \cos k_x x'}{\sin k_{x_{s-1}} h_{s-1} - j \tilde{\eta}_{s-1}^f \cos k_{x_{s-1}} h_{s-1}}. \quad (\text{A.130})$$

Using (A.125)-(A.126), it can be shown that

$$\frac{\left(\frac{\omega \epsilon_{s-1}}{k_{x_{s-1}}} \right) \eta_u^a}{\tan k_{x_{s-1}} h_{s-1} - j \tilde{\eta}_{s-1}^a} = j \frac{1}{1 + j \tilde{\eta}_{s-1}^a \tan k_{x_{s-1}} h_{s-1}} \quad (\text{A.131})$$

$$\frac{\left(\frac{k_{x_{s-1}}}{\omega \mu_{s-1}} \right) \eta_u^f}{\tan k_{x_{s-1}} h_{s-1} - j \tilde{\eta}_{s-1}^f} = j \frac{1}{1 + j \tilde{\eta}_{s-1}^f \tan k_{x_{s-1}} h_{s-1}}. \quad (\text{A.132})$$

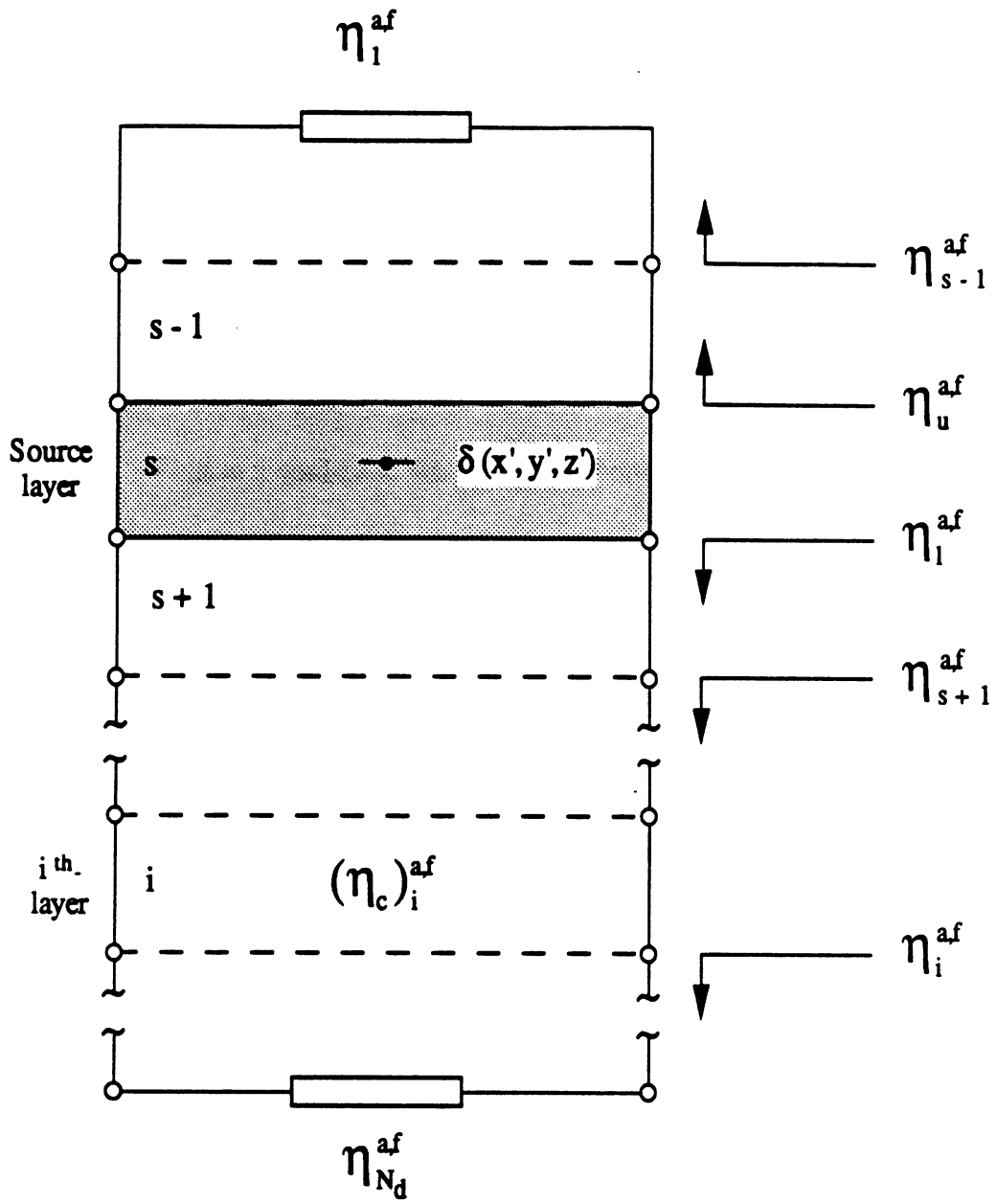


Figure A.4: Notation for multiple layers

In view of the above, it is interesting to compare these results to (A.90), (A.91)

$$A_m^{s-1} = -A_m^{(I)} \frac{\mu_{s-1}}{\mu} \frac{1}{\cos k_{x_{s-1}} h_{s-1} + j \tilde{\eta}_{s-1}^a \sin k_{x_{s-1}} h_{s-1}} \quad (\text{A.133})$$

$$D_m^{s-1} = -D_m^{(I)} \frac{\mu_{s-1}}{\mu} \frac{\epsilon_{s-1}}{\epsilon} \frac{k_x}{k_{x_{s-1}}} \frac{1}{\cos k_{x_{s-1}} h_{s-1} + j \tilde{\eta}_{s-1}^f \sin k_{x_{s-1}} h_{s-1}}. \quad (\text{A.134})$$

Substituting the above in (A.121)-(A.122) and using the relations derived between potentials and fields, we can write the generalized form of the electric and magnetic Green's functions for the i th layer in compact form. This notation is valid for all layers except the source layer

$$(G_{xx}^e)^i = \frac{j}{\omega \epsilon_i^*} \sum_{m=0}^{\infty} \frac{\delta_m}{b} \frac{(k_y^2 + k_z^2)}{k_x} \mathcal{R}_a^i \varsigma_a^i(x) v_a^i(x') \sin k_y y \sin k_y y' \quad (\text{A.135})$$

$$(G_{xy}^e)^i = -\frac{j}{\omega \epsilon_i^*} \sum_{m=0}^{\infty} \frac{\delta_m}{b} k_y \mathcal{R}_a^i \varsigma_a^i(x) \varphi_a^i(x') \sin k_y y \cos k_y y' \quad (\text{A.136})$$

$$(G_{xz}^e)^i = \frac{1}{\omega \epsilon_i^*} \sum_{m=0}^{\infty} \frac{\delta_m}{b} k_z \mathcal{R}_a^i \varsigma_a^i(x) \varphi_a^i(x') \sin k_y y \sin k_y y' \quad (\text{A.137})$$

$$(G_{yx}^e)^i = -\frac{j}{\omega \epsilon_i^*} \sum_{m=0}^{\infty} \frac{\delta_m}{b} k_y \mathcal{R}_a^i \psi_a^i(x) v_a^i(x') \cos k_y y \sin k_y y' \quad (\text{A.138})$$

$$(G_{yy}^e)^i = j \sum_{m=0}^{\infty} \frac{\delta_m}{b} \frac{1}{k_y^2 + k_z^2} \cos k_y y \cos k_y y' \\ \left[k_y^2 \mathcal{R}_a^i (\eta_c)_a^i \psi_a^i(x) \varphi_a^i(x') + k_z^2 \mathcal{R}_f^i (\eta_c)_f^i \psi_f^i(x) \varphi_f^i(x') \right] \quad (\text{A.139})$$

$$(G_{yz}^e)^i = \sum_{m=0}^{\infty} \frac{\delta_m}{b} \frac{k_y k_z}{(k_y^2 + k_z^2)} \cos k_y y \sin k_y y' \\ \left[-\mathcal{R}_a^i (\eta_c)_a^i \psi_a^i(x) \varphi_a^i(x') + \mathcal{R}_f^i (\eta_c)_f^i \psi_f^i(x) \varphi_f^i(x') \right] \quad (\text{A.140})$$

$$(G_{zx}^e)^i = -\frac{1}{\omega \epsilon_i^*} \sum_{m=0}^{\infty} \frac{\delta_m}{b} k_z \mathcal{R}_a^i \psi_a^i(x) v_a^i(x') \sin k_y y \sin k_y y' \quad (\text{A.141})$$

$$(G_{zy}^e)^i = \sum_{m=0}^{\infty} \frac{\delta_m}{b} \frac{k_y k_z}{(k_y^2 + k_z^2)} \sin k_y y \cos k_y y' \\ \left[\mathcal{R}_a^i (\eta_c)_a^i \psi_a^i(x) \varphi_a^i(x') - \mathcal{R}_f^i (\eta_c)_f^i \psi_f^i(x) \varphi_f^i(x') \right] \quad (\text{A.142})$$

$$(G_{zz}^e)^i = j \sum_{m=0}^{\infty} \frac{\delta_m}{b} \frac{1}{k_y^2 + k_z^2} \sin k_y y \sin k_y y' \\ \left[k_z^2 \mathcal{R}_a^i (\eta_c)_a^i \psi_a^i(x) \varphi_a^i(x') + k_y^2 \mathcal{R}_f^i (\eta_c)_f^i \psi_f^i(x) \varphi_f^i(x') \right] \quad (\text{A.143})$$

where

$$k_i = \omega \sqrt{\epsilon_i^* \mu_0} \quad (\text{A.144})$$

$$k_y = \frac{m\pi}{b} \quad (\text{A.145})$$

$$k_{x_i} = \sqrt{k_i^2 - k_y^2 - k_z^2}. \quad (\text{A.146})$$

Above the source $x > x'$

For the regions above the source $x > x'$, the x' dependence is given by

$$\varphi_m^{a,f}(x') = \sin k_x x' + j \tilde{\eta}_i^{a,f} \cos k_x x' \quad (\text{A.147})$$

$$v_m^{a,f}(x') = \cos k_x x' - j \tilde{\eta}_i^{a,f} \sin k_x x'. \quad (\text{A.148})$$

The x dependence may be written as

$$\zeta_m^{a,f}(x) = \cos k_{x_i} \left(x - h - \sum_{r=1}^i h_r \right) - j \tilde{\eta}_i^{a,f} \sin k_{x_i} \left(x - h - \sum_{r=1}^i h_r \right) \quad (\text{A.149})$$

$$\psi_m^{a,f}(x) = \sin k_{x_i} \left(x - h - \sum_{r=1}^i h_r \right) + j \tilde{\eta}_i^{a,f} \cos k_{x_i} \left(x - h - \sum_{r=1}^i h_r \right). \quad (\text{A.150})$$

The denominator $\mathcal{R}_{a,f}$ is given by

$$\mathcal{R}_{a,f}^i = \frac{1}{\mathcal{D}_{a,f} \prod_{r=1}^i \left\{ \cos k_{x_r} h_r + j \tilde{\eta}_r^{a,f} \sin k_{x_r} h_r \right\}}. \quad (\text{A.151})$$

Below the source $x < x'$

For the regions below the source $x < x'$, the x' dependence is given by

$$\varphi_m^{a,f}(x') = \sin k_x (x' - h) + j \tilde{\eta}_i^{a,f} \cos k_x (x' - h) \quad (\text{A.152})$$

$$v_m^{a,f}(x') = \cos k_x (x' - h) - j \tilde{\eta}_i^{a,f} \sin k_x (x' - h) \quad (\text{A.153})$$

and the x dependence is

$$\zeta_m^{a,f}(x) = \cos k_{xi} \left(x + \sum_{r=1}^i h_r \right) - j\tilde{\eta}_i^{a,f} \sin k_{xi} \left(x + \sum_{r=1}^i h_r \right) \quad (\text{A.154})$$

$$\psi_m^{a,f}(x) = \sin k_{xi} \left(x + \sum_{r=1}^i h_r \right) + j\tilde{\eta}_i^{a,f} \cos k_{xi} \left(x + \sum_{r=1}^i h_r \right) \quad (\text{A.155})$$

where, now,

$$\mathcal{R}_{a,f}^i = \frac{1}{\mathcal{D}_{a,f} \prod_{r=1}^i \left\{ \cos k_{xr} h_r - j\tilde{\eta}_r^{a,f} \sin k_{xr} h_r \right\}} \quad (\text{A.156})$$

and the impedances are given by

$$\tilde{\eta}_i^f = \eta_i^f \frac{k_{xi}}{\omega \mu_i} \quad (\text{A.157})$$

$$\tilde{\eta}_i^a = \eta_i^a \frac{\omega \epsilon_i}{k_{xi}}. \quad (\text{A.158})$$

The characteristic impedances η_c^a and η_c^f are taken to be the wave impedance of the TM_x and the TE_x modes, respectively, or

$$(\eta_c)_a^i = \frac{k_{xi}}{\omega \epsilon_i^*} \quad (\text{A.159})$$

$$(\eta_c)_f^i = \frac{\omega \mu_0}{k_{xi}}. \quad (\text{A.160})$$

In the above equations, the input impedances $\eta_i^{a,f}$ are given, according to the impedance-transfer equation, as

$$\tilde{\eta}_i^{a,f} = \frac{(\eta_c)_{a,f}^i}{(\eta_c)_{a,f}^{i-1}} \frac{\tilde{\eta}_{i-1}^{a,f} + j \tan k_{x_{i-1}} h_{i-1}}{1 + j\tilde{\eta}_{i-1}^{a,f} \tan k_{x_{i-1}} h_{i-1}}, \quad i < s \quad (\text{A.161})$$

$$\tilde{\eta}_i^{a,f} = \frac{(\eta_c)_{a,f}^i}{(\eta_c)_{a,f}^{i+1}} \frac{\tilde{\eta}_{i+1}^{a,f} - j \tan k_{x_{i+1}} h_{i+1}}{1 - j\tilde{\eta}_{i+1}^{a,f} \tan k_{x_{i+1}} h_{i+1}}, \quad i > s. \quad (\text{A.162})$$

APPENDIX B

EVALUATION OF POWER INTEGRALS

In this appendix, the derivation of the power expressions found in section 3.6.4. are detailed. In the evaluation of the modal characteristic impedances, integrals of complex functions are encountered which can be decomposed in the four types shown below

$$CC = \int_a^b \cos zx (\cos zx)^* dx \quad (\text{B.1})$$

$$SS = \int_a^b \sin zx (\sin zx)^* dx \quad (\text{B.2})$$

$$CS = \int_a^b \cos zx (\sin zx)^* dx \quad (\text{B.3})$$

$$SC = \int_a^b \sin zx (\cos zx)^* dx \quad (\text{B.4})$$

In the above expressions, z represents a complex number $z = r + ji$. Substituting the expanded form of z in the above equations and making use of well-known trigonometric and hyperbolic identities, we can write

$$\begin{aligned} CC &= \int_a^b (\cos^2 rx \cosh^2 ix + \sin^2 rx \sinh^2 ix) dx \\ &= \frac{1}{2} \int_a^b (\cosh 2ix + \cos 2rx) dx \\ &= \frac{1}{4} \left\{ \frac{\sinh 2ix}{i} \Big|_a^b + \frac{\sin 2rx}{r} \Big|_a^b \right\} \end{aligned} \quad (\text{B.5})$$

$$SS = \int_a^b (\sin^2 rx \cosh^2 ix + \cos^2 rx \sinh^2 ix) dx$$

$$\begin{aligned}
&= \frac{1}{2} \int_a^b (\cosh 2ix - \cos 2rx) dx \\
&= \frac{1}{4} \left\{ \frac{\sinh 2ix}{i} \Big|_a^b - \frac{\sin 2rx}{r} \Big|_a^b \right\} \tag{B.6}
\end{aligned}$$

$$\begin{aligned}
CS &= \int_a^b (\sin rx \cos rx - j \sinh ix \cosh ix) dx \\
&= \frac{1}{2} \int_a^b (\sin 2rx - j \sinh 2ix) dx \\
&= -\frac{1}{4} \left\{ j \frac{\cosh 2ix}{i} \Big|_a^b + \frac{\cos 2rx}{r} \Big|_a^b \right\} \tag{B.7}
\end{aligned}$$

$$\begin{aligned}
SC &= \int_a^b (\sin rx \cos rx + j \sinh ix \cosh ix) dx \\
&= \frac{1}{2} \int_a^b (\sin 2rx + j \sinh 2ix) dx \\
&= \frac{1}{4} \left\{ j \frac{\cosh 2ix}{i} \Big|_a^b - \frac{\cos 2rx}{r} \Big|_a^b \right\} \tag{B.8}
\end{aligned}$$

The following integrals need to be evaluated in each dielectric region as :

$$\begin{aligned}
&\int_a^b \{\cos zx - j\eta_i \sin zx\} \{\cos zx - j\eta_j \sin zx\}^* dx \\
&= \frac{1}{4} \left[\frac{\sinh 2ix}{i} \Big|_a^b (1 + \eta_i \eta_j^*) + \frac{\sin 2rx}{r} \Big|_a^b (1 - \eta_i \eta_j^*) \right. \\
&\quad \left. + j \frac{\cos 2rx}{r} \Big|_a^b (\eta_i - \eta_j^*) + \frac{\cosh 2ix}{i} \Big|_a^b (\eta_i + \eta_j^*) \right] \tag{B.9}
\end{aligned}$$

$$\begin{aligned}
&\int_a^b \{\sin zx + j\eta_i \cos zx\} \{\sin zx + j\eta_j \cos zx\}^* dx \\
&= \frac{1}{4} \left[\frac{\sinh 2ix}{i} \Big|_a^b (1 + \eta_i \eta_j^*) - \frac{\sin 2rx}{r} \Big|_a^b (1 - \eta_i \eta_j^*) \right. \\
&\quad \left. - j \frac{\cos 2rx}{r} \Big|_a^b (\eta_i - \eta_j^*) + \frac{\cosh 2ix}{i} \Big|_a^b (\eta_i + \eta_j^*) \right] \tag{B.10}
\end{aligned}$$

B.1 Around the source region

The x dependence and the limits of integration for regions around the source layer are given in Table B.1.

	x dependence	limits of integration	
above the source region	$x - h - \sum_l^r h_l$	$a = h + \sum_l^{r-1} h_l$	$b = h + \sum_l^r h_l$
below the source region	$x + \sum_l^r h_l$	$a = -\sum_l^r h_l$	$b = -\sum_l^{r-1} h_l$

Table B.1: Integration in the layers around the source region

In view of (B.9) and (B.10), the integrals may be re-written as

$$\begin{aligned}
& \int_a^b \{\cos zx - j\eta_i \sin zx\} \{\cos zx - j\eta_j \sin zx\}^* dx \\
&= \frac{1}{4} \left[\frac{\sinh 2ih_r}{i} (1 + \eta_i \eta_j^*) + \frac{\sin 2rh_r}{r} (1 - \eta_i \eta_j^*) \right. \\
& \quad \left. \pm j \frac{(1 - \cos 2rh_r)}{r} (\eta_i - \eta_j^*) \pm \frac{(1 - \cosh 2ih_r)}{i} (\eta_i + \eta_j^*) \right] \quad (B.11)
\end{aligned}$$

where the upper and lower signs (\pm) correspond to the layers above and below the source region, respectively. The other type of integrals encountered gives

$$\begin{aligned}
& \int_a^b \{\sin zx + j\eta_i \cos zx\} \{\sin zx + j\eta_j \cos zx\}^* dx \\
&= \frac{1}{4} \left[\frac{\sinh 2ih_r}{i} (1 + \eta_i \eta_j^*) - \frac{\sin 2rh_r}{r} (1 - \eta_i \eta_j^*) \right. \\
& \quad \left. \mp j \frac{(1 - \cos 2rh_r)}{r} (\eta_i - \eta_j^*) \pm \frac{(1 - \cosh 2ih_r)}{i} (\eta_i + \eta_j^*) \right] \quad (B.12)
\end{aligned}$$

B.2 In the source region

The source region can be divided into three sub-regions as shown in Table B.2.

	x dependence	limits of integration	
$x > x'_j > x'_i$	$(x - h)$	$a = x'_j$	$b = h$
$x'_j > x > x'_i$	$x, (x - h)$	$a = x'_i$	$b = x'_j$
$x'_j > x'_i > x$	x	$a = 0$	$b = x'_i$

Table B.2: Integration in the source region

In the process, an additional type of integrals has to be performed

$$\mathcal{C}\mathcal{C}_h = \int_a^b \cos zx (\cos z(x - h))^* dx = \mathcal{C}\mathcal{C} \cos^* zh + \mathcal{C}\mathcal{S} \sin^* zh \quad (B.13)$$

$$\mathcal{S}\mathcal{S}_h = \int_a^b \sin zx (\sin z(x-h))^* dx = \mathcal{S}\mathcal{S} \cos^* zh - \mathcal{S}\mathcal{C} \sin^* zh \quad (\text{B.14})$$

$$\mathcal{C}\mathcal{S}_h = \int_a^b \cos zx (\sin z(x-h))^* dx = \mathcal{C}\mathcal{S} \cos^* zh - \mathcal{C}\mathcal{C} \sin^* zh \quad (\text{B.15})$$

$$\mathcal{S}\mathcal{C}_h = \int_a^b \sin zx (\cos z(x-h))^* dx = \mathcal{S}\mathcal{C} \cos^* zh + \mathcal{S}\mathcal{S} \sin^* zh \quad (\text{B.16})$$

The x dependence is then written as

$$\begin{aligned} & \int_a^b \{\cos zx - j\eta_i \sin zx\} \{\cos z(x-h) - j\eta_j \sin z(x-h)\}^* dx \\ &= \frac{1}{4} [\mathcal{C}\mathcal{C} (\cos^* zh - j\eta_j^* \sin^* zh) + \mathcal{S}\mathcal{C} (\eta_i \eta_j^* \cos^* zh - j\eta_i \sin^* zh) \\ & \quad + \mathcal{S}\mathcal{C} (-\eta_i \eta_j^* \sin^* zh - j\eta_i \cos^* zh) + \mathcal{C}\mathcal{S} (\sin^* zh + j\eta_j^* \cos^* zh)] \\ &= \frac{1}{4} \left[\frac{\sinh 2ix}{i} \Big|_a^b \{\cos^* zh (1 + \eta_i \eta_j^*) - j (\eta_i + \eta_j^*) \sin^* zh\} \right. \\ & \quad + \frac{\cosh 2ix}{i} \Big|_a^b \{\cos^* zh (\eta_i + \eta_j^*) - j (1 + \eta_i \eta_j^*) \sin^* zh\} \\ & \quad + \frac{\sin 2rx}{r} \Big|_a^b \{\cos^* zh (1 - \eta_i \eta_j^*) + j (\eta_i - \eta_j^*) \sin^* zh\} \\ & \quad \left. + \frac{\cos 2rx}{r} \Big|_a^b \{-\sin^* zh (1 - \eta_i \eta_j^*) + j (\eta_i - \eta_j^*) \cos^* zh\} \right] \quad (\text{B.17}) \end{aligned}$$

and

$$\begin{aligned} & \int_a^b \{\sin zx + j\eta_i \cos zx\} \{\sin z(x-h) + j\eta_j \cos z(x-h)\}^* dx \\ &= \frac{1}{4} [\mathcal{S}\mathcal{S} (\cos^* zh - j\eta_j^* \sin^* zh) + \mathcal{C}\mathcal{C} (\eta_i \eta_j^* \cos^* zh - j\eta_i \sin^* zh) \\ & \quad + \mathcal{C}\mathcal{S} (\eta_i \eta_j^* \sin^* zh + j\eta_i \cos^* zh) - \mathcal{S}\mathcal{C} (\sin^* zh + j\eta_j^* \cos^* zh)] \\ &= \frac{1}{4} \left[\frac{\sinh 2ix}{i} \Big|_a^b \{\cos^* zh (1 + \eta_i \eta_j^*) - j (\eta_i + \eta_j^*) \sin^* zh\} \right. \\ & \quad + \frac{\cosh 2ix}{i} \Big|_a^b \{\cos^* zh (\eta_i + \eta_j^*) - j (1 + \eta_i \eta_j^*) \sin^* zh\} \\ & \quad - \frac{\sin 2rx}{r} \Big|_a^b \{\cos^* zh (1 - \eta_i \eta_j^*) + j (\eta_i - \eta_j^*) \sin^* zh\} \\ & \quad \left. - \frac{\cos 2rx}{r} \Big|_a^b \{\sin^* zh (1 - \eta_i \eta_j^*) - j (\eta_i - \eta_j^*) \cos^* zh\} \right] \quad (\text{B.18}) \end{aligned}$$

APPENDIX C

EVALUATION OF ENTIRE DOMAIN MOMENTS INTEGRALS

When applying the Method of Moments (MoM) to (3.36), the unknown current on the strips is expanded in terms of entire domain basis functions chosen to approximate as closely as possible its physical behavior for numerical efficiency. The Chebychev family of orthogonal polynomials has been selected and an overview of their properties is presented in this appendix. Also, in the formulation of the matrix resulting from the MoM, three sets of integrals have to be evaluated, corresponding to the basis functions expansion, to the application of weighted averages and to the conductor surface impedance term. The solution of these integrals is detailed below.

C.1 Chebychev polynomials

The Chebychev polynomials of the first kind are orthogonal over $[-1,1]$ with respect to the weighting factor $(1 - x^2)^{-\frac{1}{2}}$. For the family of Chebychev polynomials of the second kind, the weighting factor is $(1 - x^2)^{\frac{1}{2}}$.

The orthogonal relations give

$$\int_{-1}^1 \frac{T_n(x)T_m(x)}{\sqrt{1-x^2}} dx = \begin{cases} \pi & , \text{ for } m = n = 0 \\ \frac{\pi}{2} & , \text{ for } m = n \neq 0 \\ 0 & , \text{ for } m \neq n. \end{cases} \quad (\text{C.1})$$

and

$$\int_{-1}^1 U_n(x)U_m(x)\sqrt{1-x^2} dx = \begin{cases} \frac{\pi}{2} & , \text{ for } m = n \\ 0 & , \text{ for } m \neq n. \end{cases} \quad (\text{C.2})$$

The Chebychev polynomials are historically the oldest set of orthogonal polynomials. This is mainly because they are simply related to the trigonometric functions by the formula

$$T_n(\cos \theta) = \cos(n\theta) \quad (\text{C.3})$$

$$U_n(\cos \theta) = \frac{\sin(n+1)\theta}{\sin \theta} \quad (\text{C.4})$$

Thus, using some well-known trigonometric identities we can conclude that

$$\begin{aligned} T_0(x) &= 1 & U_0(x) &= 1 \\ T_1(x) &= x & U_1(x) &= 2x \\ T_2(x) &= 2x^2 - 1 & U_2(x) &= 4x^2 - 1. \end{aligned} \quad (\text{C.5})$$

It can be seen that the polynomials of even order are even functions of x and those of odd order are odd functions of x . The Chebychev polynomials of the first and second kind are shown in Figure C.1.

The remaining Chebychev polynomials may be tabulated quite simply with the aid of the recurrence formula

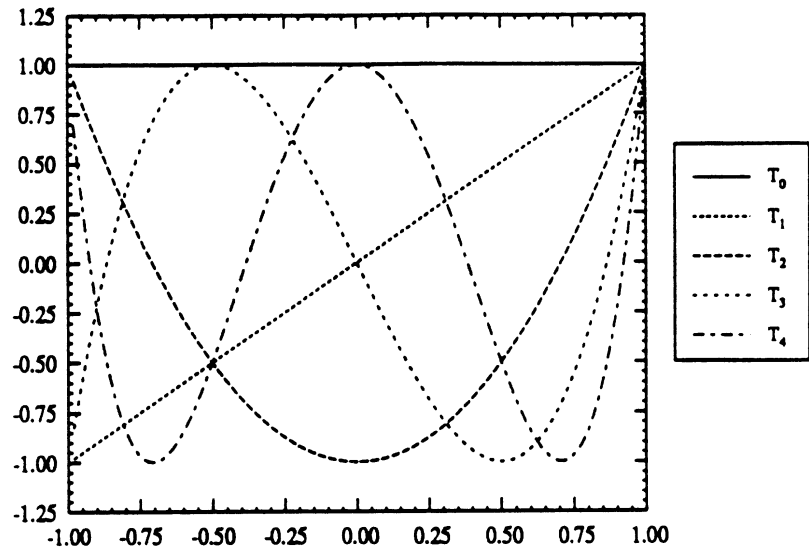
$$T_{n+1}(x) - 2x T_n(x) + T_{n-1}(x) = 0 \quad (\text{C.6})$$

$$U_{n+1}(x) - 2x U_n(x) + U_{n-1}(x) = 0 \quad (\text{C.7})$$

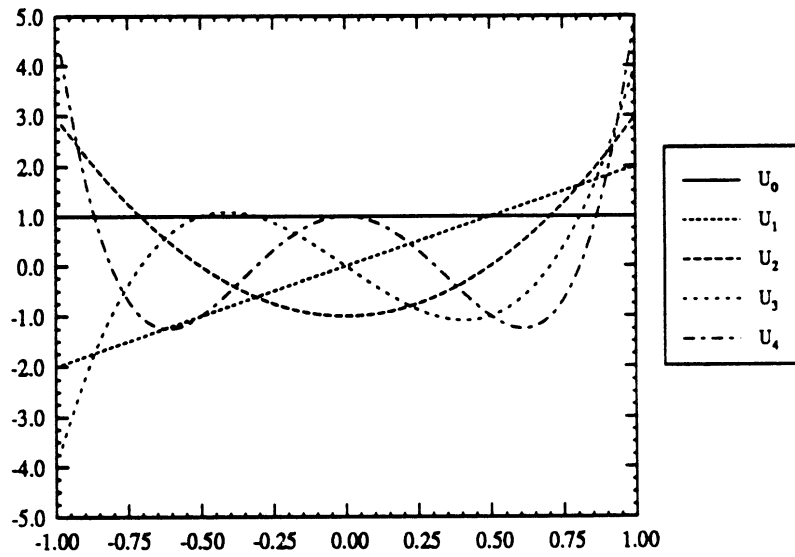
and

$$2 T_n(x) = U_n(x) - U_{n-2}(x). \quad (\text{C.8})$$

In a sense, the U_n 's are more fundamental than the T_n 's since the latter can always be expressed simply in terms of the former, but not conversely.



a. Chebyshev functions of the first kind, T_i



b. Chebyshev functions of the second kind, U_i

Figure C.1: Chebyshev family of orthogonal polynomials

C.2 Integration over the basis functions

The set of basis functions that approximates the behaviour of the unknown current has been chosen as the Chebychev polynomials of first and second kind multiplied by their respective weight factor, to satisfy the boundary conditions for the current at the edges of the strip.

The integrals over the basis functions that are encountered in the evaluation of the matrix system are of two types as shown below

$$\mathcal{I}_n^{(1)} = \int_{y_0 - \frac{W}{2}}^{y_0 + \frac{W}{2}} U_n\left(\frac{2}{W}(y - y_0)\right) \sqrt{1 - \left[\frac{2}{W}(y - y_0)\right]^2} \cos(k_y y) dy \quad (\text{C.9})$$

$$\mathcal{I}_n^{(2)} = \int_{y_0 - \frac{W}{2}}^{y_0 + \frac{W}{2}} \frac{T_n\left(\frac{2}{W}(y - y_0)\right)}{\sqrt{1 - \left[\frac{2}{W}(y - y_0)\right]^2}} \sin(k_y y) dy, \quad (\text{C.10})$$

where T_n is the Chebychev polynomial of the first kind of degree n , and U_n is the Chebychev polynomial of the second kind of degree n . Using the explicit trigonometric expressions for the Chebychev polynomials,

$$U_n(\cos \theta) = \frac{\sin(n+1)\theta}{\sin \theta} \quad (\text{C.11})$$

$$T_n(\cos \theta) = \cos n\theta \quad (\text{C.12})$$

and letting

$$\begin{aligned} \cos \theta &= \frac{2}{W}(y - y_0) \implies -\sin \theta d\theta = \frac{2}{W} dy \\ y &= \frac{W}{2} \cos \theta + y_0 \implies dy = -\frac{W}{2} \sin \theta d\theta \end{aligned} \quad (\text{C.13})$$

the above integrals become

$$\mathcal{I}_n^{(1)} = \int_0^\pi \frac{\sin(n+1)\theta}{\sin \theta} \sin \theta \cos k_y \left(\frac{W}{2} \cos \theta + y_0\right) \frac{W}{2} \sin \theta d\theta \quad (\text{C.14})$$

$$\mathcal{I}_n^{(2)} = \int_0^\pi \frac{\cos n\theta}{\sin \theta} \sin k_y \left(\frac{W}{2} \cos \theta + y_0\right) \frac{W}{2} \sin \theta d\theta. \quad (\text{C.15})$$

C.2.1 Evaluation of $\mathcal{I}_n^{(1)}$

We will first calculate the integral corresponding to the y -component of current.

Substituting the above trigonometric transformation in (C.9), we get

$$\mathcal{I}_n^{(1)} = \frac{W}{2} \int_0^\pi \sin(n+1)\theta \cos k_y \left(\frac{W}{2} \cos \theta + y_0 \right) \sin \theta d\theta. \quad (\text{C.16})$$

Using some trigonometric expansion formulas,

$$\begin{aligned} \mathcal{I}_n^{(1)} &= \frac{W}{2} \int_0^\pi \frac{1}{2} [\cos n\theta - \cos(n+2)\theta] \cos k_y \left(\frac{W}{2} \cos \theta + y_0 \right) d\theta \\ &= \frac{W}{4} \cos k_y y_0 \left\{ \int_0^\pi \cos n\theta \cos k_y \left(\frac{W}{2} \cos \theta \right) d\theta \right. \\ &\quad \left. - \int_0^\pi \cos(n+2)\theta \cos \left(k_y \left(\frac{W}{2} \cos \theta \right) \right) d\theta \right\} \\ &\quad - \frac{W}{4} \sin k_y y_0 \left\{ \int_0^\pi \cos n\theta \sin k_y \left(\frac{W}{2} \cos \theta \right) d\theta \right. \\ &\quad \left. - \int_0^\pi \cos(n+2)\theta \sin k_y \left(\frac{W}{2} \cos \theta \right) d\theta \right\}. \end{aligned} \quad (\text{C.17})$$

These definite integrals have a closed-form solution given in [111] of the type

$$\int_0^\pi \cos(z \cos x) \cos n x dx = \pi \cos \frac{n\pi}{2} J_n(z) \quad (\text{C.18})$$

$$\int_0^\pi \sin(z \cos x) \cos n x dx = \pi \sin \frac{n\pi}{2} J_n(z) \quad (\text{C.19})$$

where $J_n(z)$ is the Bessel function of the first kind of the n th order. Therefore, (C.17)

becomes

$$\begin{aligned} \mathcal{I}_n^{(1)} &= \frac{W}{4} \pi \cos k_y y_0 \left\{ \cos \left(n \frac{\pi}{2} \right) J_n \left(k_y \frac{W}{2} \right) - \cos(n+2) \frac{\pi}{2} J_{n+2} \left(k_y \frac{W}{2} \right) \right\} \\ &\quad - \frac{W}{4} \pi \sin k_y y_0 \left\{ \sin \left(n \frac{\pi}{2} \right) J_n \left(k_y \frac{W}{2} \right) - \sin(n+2) \frac{\pi}{2} J_{n+2} \left(k_y \frac{W}{2} \right) \right\} \\ &= \frac{W}{4} \pi \left[\cos \left(k_y y_0 + n \frac{\pi}{2} \right) J_n \left(k_y \frac{W}{2} \right) - \cos \left(k_y y_0 + (n+2) \frac{\pi}{2} \right) J_{n+2} \left(k_y \frac{W}{2} \right) \right] \end{aligned} \quad (\text{C.20})$$

which yields

$$\mathcal{I}_n^{(1)} = \frac{W}{4} \pi \cos \left(k_y y_0 + n \frac{\pi}{2} \right) \left[J_n \left(k_y \frac{W}{2} \right) + J_{n+2} \left(k_y \frac{W}{2} \right) \right]. \quad (\text{C.21})$$

Using the following recurrence relation,

$$J_{n+1}(z) = \frac{2n}{z} J_n(z) - J_{n-1}(z) \quad (\text{C.22})$$

it follows that

$$\mathcal{I}_n^{(1)} = \frac{\pi}{k_y} (n+1) \cos(k_y y_0 + n \frac{\pi}{2}) J_{n+1}(k_y \frac{W}{2}). \quad (\text{C.23})$$

C.2.2 Evaluation of $\mathcal{I}_n^{(2)}$

The second step is to calculate the integral corresponding to the z -component of current. Following the same procedure as above, we get

$$\mathcal{I}_n^{(2)} = \frac{W}{2} \int_0^\pi \cos n\theta \sin k_y (\frac{W}{2} \cos \theta + y_0) d\theta. \quad (\text{C.24})$$

Using some trigonometric expansion formulas,

$$\begin{aligned} \mathcal{I}_n^{(2)} &= \frac{W}{2} \int_0^\pi \cos n\theta [\cos k_y y_0 \sin k_y (\frac{W}{2} \cos \theta) + \sin k_y y_0 \cos k_y (\frac{W}{2} \cos \theta)] d\theta \\ &= \frac{W}{2} \cos k_y y_0 \int_0^\pi \cos n\theta \sin k_y (\frac{W}{2} \cos \theta) d\theta \\ &\quad + \frac{W}{2} \sin k_y y_0 \int_0^\pi \cos n\theta \cos k_y (\frac{W}{2} \cos \theta) d\theta. \end{aligned} \quad (\text{C.25})$$

These definite integrals have the form given in (C.18),(C.19). Therefore, (C.25) becomes

$$\begin{aligned} \mathcal{I}_n^{(2)} &= \frac{W}{2} \pi [\cos k_y y_0 \sin(n \frac{\pi}{2}) J_n(k_y \frac{W}{2}) + \sin k_y y_0 \cos(n \frac{\pi}{2}) J_n(k_y \frac{W}{2})] \\ &= \frac{W}{2} \pi J_n(k_y \frac{W}{2}) \sin(k_y y_0 + n \frac{\pi}{2}). \end{aligned} \quad (\text{C.26})$$

This completes the $\mathcal{I}_n^{(2)}$ integration.

C.3 Integration over the testing functions

From (3.70) and (3.71), the integrals resulting from the weighting averages are given by

$$\mathcal{I}_m^{(3)} = \int_{y_0 - \frac{W}{2}}^{y_0 + \frac{W}{2}} U_m\left(\frac{2}{W}(y - y_0)\right) \cos(k_y y) dy \quad (\text{C.27})$$

$$\mathcal{I}_m^{(4)} = \int_{y_0 - \frac{W}{2}}^{y_0 + \frac{W}{2}} T_m\left(\frac{2}{W}(y - y_0)\right) \sin(k_y y) dy. \quad (\text{C.28})$$

C.3.1 Evaluation of $\mathcal{I}_m^{(3)}$

With the substitutions defined in (C.13),

$$\mathcal{I}_m^{(3)} = \frac{W}{2} \int_0^\pi \sin(m+1)\theta \cos k_y \left(\frac{W}{2} \cos \theta + y_0\right) d\theta. \quad (\text{C.29})$$

After some trigonometric manipulations, this expression may be written as

$$\begin{aligned} \mathcal{I}_m^{(3)} &= \frac{W}{2} \cos k_y y_0 \int_0^\pi \sin(m+1)\theta \cos\left(k_y \frac{W}{2} \cos \theta\right) d\theta \\ &\quad - \frac{W}{2} \sin k_y y_0 \int_0^\pi \sin(m+1)\theta \sin\left(k_y \frac{W}{2} \cos \theta\right) d\theta. \end{aligned} \quad (\text{C.30})$$

No general recurrence formulation was found for the integrals above. However, by comparison with the spherical Bessel functions of the l th order given by [58]

$$j_l(z) = \frac{1}{2} (-i)^l \int_0^\pi e^{iz \cos \theta} P_l(\cos \theta) \sin \theta d\theta \quad (\text{C.31})$$

where P_l corresponds to the Legendre polynomials of order l , we can write

$$\int_0^\pi P_l(\cos \theta) \sin \theta \sin(z \cos \theta) d\theta = \mathcal{I}m\{2(i)^l j_l(z)\} \quad (\text{C.32})$$

$$\int_0^\pi P_l(\cos \theta) \sin \theta \cos(z \cos \theta) d\theta = \mathcal{R}e\{2(i)^l j_l(z)\}. \quad (\text{C.33})$$

Expanding $\sin m\theta$ in terms of a summation over these polynomials as

$$\sin m\theta = \sin \theta \sum_{l=0}^m A_{lm} P_l(\cos \theta) \quad (\text{C.34})$$

m	l = 0	l = 1	l = 2	l = 3	l = 4	l = 5	l = 6	l = 7
1	1							
2	0	2						
3	1/3	0	8/3					
4	0	4/5	0	16/5				
5	1/5	0	8/7	0	128/35			
6	0	18/35	0	64/45	0	256/63		
7	1/7	0	16/21	0	128/77	0	1024/231	
8	0	8/21	0	32/33	0	512/273	0	2048/429

Table C.1: Coefficients A_{lm} for the expansion of $\sin m\theta$ in terms of Legendre polynomials of order l , P_l

we may readily see that

$$\int_0^\pi \sin m\theta \sin(z \cos \theta) d\theta = \sum_{l=0}^m A_{lm} \operatorname{Im}\{2(-i)^{-l} j_l(z)\} \quad (\text{C.35})$$

$$\int_0^\pi \sin m\theta \cos(z \cos \theta) d\theta = \sum_{l=0}^m A_{lm} \operatorname{Re}\{2(-i)^{-l} j_l(z)\}. \quad (\text{C.36})$$

Therefore these integrals can be written as a weighted sum of spherical Bessel functions. Note from (C.32)-(C.33) that, for any given m , one of the above two integrals alternatively evaluates to zero.

The coefficients A_{lm} are readily calculated and given in Table C.1 for the first few orders. After appropriate substitutions and some algebra, (C.30) becomes

$$\begin{aligned} \mathcal{I}_0^{(3)} &= W \cos k_y y_0 j_0\left(k_y \frac{W}{2}\right) \\ \mathcal{I}_1^{(3)} &= -2W \sin k_y y_0 j_1\left(k_y \frac{W}{2}\right) \\ \mathcal{I}_2^{(3)} &= \frac{W}{3} \cos k_y y_0 \left\{ j_0\left(k_y \frac{W}{2}\right) - 8 j_2\left(k_y \frac{W}{2}\right) \right\} \\ \mathcal{I}_3^{(3)} &= -\frac{4W}{5} \sin k_y y_0 \left\{ j_1\left(k_y \frac{W}{2}\right) - 4 j_3\left(k_y \frac{W}{2}\right) \right\} \end{aligned}$$

$$\begin{aligned}
\mathcal{I}_4^{(3)} &= W \cos k_y y_0 \left\{ \frac{1}{5} j_0(k_y \frac{W}{2}) - \frac{8}{7} j_2(k_y \frac{W}{2}) + \frac{128}{35} j_4(k_y \frac{W}{2}) \right\} \\
\mathcal{I}_5^{(3)} &= -W \sin k_y y_0 \left\{ \frac{18}{35} j_1(k_y \frac{W}{2}) - \frac{64}{45} j_3(k_y \frac{W}{2}) + \frac{256}{63} j_5(k_y \frac{W}{2}) \right\} \\
\mathcal{I}_6^{(3)} &= W \cos k_y y_0 \\
&\quad \left\{ \frac{1}{7} j_0(k_y \frac{W}{2}) - \frac{16}{21} j_2(k_y \frac{W}{2}) + \frac{128}{77} j_4(k_y \frac{W}{2}) - \frac{1024}{231} j_6(k_y \frac{W}{2}) \right\} \\
\mathcal{I}_7^{(3)} &= -W \sin k_y y_0 \\
&\quad \left\{ \frac{8}{21} j_1(k_y \frac{W}{2}) - \frac{32}{33} j_3(k_y \frac{W}{2}) + \frac{512}{273} j_5(k_y \frac{W}{2}) - \frac{2048}{429} j_7(k_y \frac{W}{2}) \right\} \text{C.37}
\end{aligned}$$

Using Rayleigh's formula [58],

$$j_n(z) = z^n \left(-\frac{1}{z} \frac{d}{dz} \left(\frac{\sin z}{z} \right) \right)^n \frac{\sin z}{z}, \quad (\text{C.38})$$

the spherical Bessel functions can be written in terms of trigonometric functions, which yields for the first five orders

$$j_0(z) = \frac{\sin z}{z} \quad (\text{C.39})$$

$$j_1(z) = \frac{\sin z}{z^2} - \frac{\cos z}{z} \quad (\text{C.40})$$

$$j_2(z) = \sin z \left(\frac{3}{z^3} - \frac{1}{z} \right) - \frac{3}{z^2} \cos z \quad (\text{C.41})$$

$$j_3(z) = \sin z \left(\frac{15}{z^4} - \frac{6}{z^2} \right) + \cos z \left(-\frac{15}{z^3} + \frac{1}{z} \right) \quad (\text{C.42})$$

$$j_4(z) = \sin z \left(\frac{105}{z^5} - \frac{45}{z^3} + \frac{1}{z} \right) + \cos z \left(-\frac{105}{z^4} + \frac{10}{z^2} \right) \quad (\text{C.43})$$

$$j_5(z) = \sin z \left(\frac{945}{z^6} - \frac{420}{z^4} + \frac{15}{z^2} \right) + \cos z \left(-\frac{945}{z^5} + \frac{105}{z^3} - \frac{1}{z} \right) \quad (\text{C.44})$$

$$j_6(z) = \sin z \left(\frac{10395}{z^5} - \frac{4725}{z^5} + \frac{210}{z^3} - \frac{1}{z} \right) + \cos z \left(\frac{10395}{z^6} + \frac{1260}{z^4} - \frac{21}{z^2} \right) \quad (\text{C.45})$$

$$\begin{aligned}
j_7(z) &= \sin z \left(\frac{135135}{z^8} - \frac{62370}{z^6} + \frac{3150}{z^4} - \frac{28}{z^2} \right) \\
&\quad - \cos z \left(\frac{135135}{z^7} - \frac{17325}{z^5} + \frac{378}{z^3} - \frac{1}{z} \right). \quad (\text{C.46})
\end{aligned}$$

C.3.2 Evaluation of $\mathcal{I}_m^{(4)}$

A similar derivation can be done for the integral arising from the weighting average with Chebychev polynomial of the first kind (C.28) as

$$\begin{aligned}
\mathcal{I}_m^{(4)} &= \frac{W}{2} \int_0^\pi \cos m\theta \sin \theta \left\{ \cos k_y y_0 \sin\left(k_y \frac{W}{2} \cos \theta\right) + \right. \\
&\quad \left. \sin k_y y_0 \cos\left(k_y \frac{W}{2} \cos \theta\right) \right\} d\theta \\
&= \frac{W}{4} \cos k_y y_0 \int_0^\pi \left\{ \sin(m+1)\theta \sin\left(k_y \frac{W}{2} \cos \theta\right) - \sin(m-1)\theta \right. \\
&\quad \left. \cdot \sin\left(k_y \frac{W}{2} \cos \theta\right) \right\} d\theta + \frac{W}{4} \sin k_y y_0 \int_0^\pi \left\{ \sin(m+1)\theta \cos\left(k_y \frac{W}{2} \cos \theta\right) \right. \\
&\quad \left. - \sin(m-1)\theta \cos\left(k_y \frac{W}{2} \cos \theta\right) \right\} d\theta. \tag{C.47}
\end{aligned}$$

In view of (C.31) and (C.34), it follows that

$$\begin{aligned}
\mathcal{I}_0^{(4)} &= W \sin k_y y_0 j_0\left(k_y \frac{W}{2}\right) \\
\mathcal{I}_1^{(4)} &= W \cos k_y y_0 j_1\left(k_y \frac{W}{2}\right) \\
\mathcal{I}_2^{(4)} &= -\frac{W}{3} \sin k_y y_0 \left\{ j_0\left(k_y \frac{W}{2}\right) + 4j_2\left(k_y \frac{W}{2}\right) \right\} \\
\mathcal{I}_3^{(4)} &= -\frac{W}{5} \cos k_y y_0 \left\{ (3j_1\left(k_y \frac{W}{2}\right) + 8j_3\left(k_y \frac{W}{2}\right)) \right\} \\
\mathcal{I}_4^{(4)} &= W \sin k_y y_0 \left\{ \left(-\frac{1}{15}j_0\left(k_y \frac{W}{2}\right) + \frac{16}{21}j_2\left(k_y \frac{W}{2}\right) + \frac{64}{35}j_4\left(k_y \frac{W}{2}\right)\right) \right\} \\
\mathcal{I}_5^{(4)} &= W \cos k_y y_0 \left\{ \left(-5j_1\left(k_y \frac{W}{2}\right) + 8j_3\left(k_y \frac{W}{2}\right) + 128j_5\left(k_y \frac{W}{2}\right)\right) \right\} \\
\mathcal{I}_6^{(4)} &= W \sin k_y y_0 \\
&\quad \left\{ \left(-\frac{1}{35}j_0\left(k_y \frac{W}{2}\right) + \frac{4}{21}j_2\left(k_y \frac{W}{2}\right) - \frac{384}{385}j_4\left(k_y \frac{W}{2}\right) - \frac{512}{231}j_6\left(k_y \frac{W}{2}\right)\right) \right\} \\
\mathcal{I}_7^{(4)} &= W \cos k_y y_0 \\
&\quad \left\{ \left(-\frac{1}{15}j_1\left(k_y \frac{W}{2}\right) + \frac{112}{495}j_3\left(k_y \frac{W}{2}\right) - \frac{128}{117}j_5\left(k_y \frac{W}{2}\right) - \frac{1024}{429}j_7\left(k_y \frac{W}{2}\right)\right) \right\} \tag{C.48}
\end{aligned}$$

C.4 Integration over the conductor term

The second term on the left hand side of equation (3.36) takes into account the ohmic losses due to the finite conductivity of the strips. After applying the method

of moments, the resulting integrals may be written as

$$\mathcal{I}_{nm}^{(5)} = \int_{y_0 - \frac{W}{2}}^{y_0 + \frac{W}{2}} U_n\left(\frac{2}{W}(y - y_0)\right) \sqrt{1 - \left[\frac{2}{W}(y - y_0)\right]^2} U_m\left(\frac{2}{W}(y - y_0)\right) dy \quad (\text{C.49})$$

$$\mathcal{I}_{nm}^{(6)} = \int_{y_0 - \frac{W}{2}}^{y_0 + \frac{W}{2}} \frac{T_n\left(\frac{2}{W}(y - y_0)\right)}{\sqrt{1 - \left[\frac{2}{W}(y - y_0)\right]^2}} T_m\left(\frac{2}{W}(y - y_0)\right) dy. \quad (\text{C.50})$$

From (C.1) and (C.2), and using the orthogonal properties of the Chebychev functions, (C.49) and (C.50) become

$$\mathcal{I}^{(5)} = W \begin{cases} \frac{\pi}{4} & , \text{ for } m = n \\ 0 & , \text{ for } m \neq n. \end{cases} \quad (\text{C.51})$$

and

$$\mathcal{I}^{(6)} = W \begin{cases} \frac{\pi}{2} & , \text{ for } m = n = 0 \\ \frac{\pi}{4} & , \text{ for } m = n \neq 0 \\ 0 & , \text{ for } m \neq n \end{cases} \quad (\text{C.52})$$

APPENDIX D

EVALUATION OF SUBSECTIONAL MOMENTS INTEGRALS

When applying the method of moments (MoM) to (3.36), the unknown current on the strips is expanded in terms of subsectional basis functions. Galerkin's method is used here, where the testing functions are equal to the basis functions. Therefore only two sets of integrals have to be evaluated, corresponding to the basis functions expansion and to the conductor surface impedance term. The solution of these integrals is detailed below.

D.1 Pulse functions

Let us assume N equispaced points on the interval $y_0 - \frac{W}{2} \leq y \leq y_0 + \frac{W}{2}$ defined by the y_n

$$y_n = y_0 - \frac{W}{2} + (n - \frac{1}{2}) \Delta W, \quad n = 1, 2, \dots, N \quad (\text{D.1})$$

A subsection is defined to be of width ΔW centered on the y_n coordinate. The pulse function is defined over only one subsection as shown in Figure D.1

$$P(y) = \begin{cases} 1 & , |y| < \Delta W \\ 0 & , |y| > \Delta W \end{cases} \quad (\text{D.2})$$

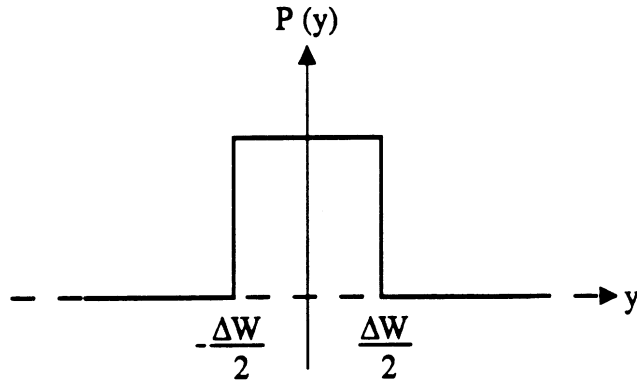


Figure D.1: Pulse function

D.2 Integration over the expansion functions

The integrals that are encountered in the evaluation of the matrix system are of two types as shown below

$$\mathcal{I}_n^{(1)} = \mathcal{I}_n^{(3)} = \int_{y_0 - \frac{W}{2}}^{y_0 + \frac{W}{2}} \sin(k_y y) P(y - y_n) dy \quad (\text{D.3})$$

$$\mathcal{I}_n^{(2)} = \mathcal{I}_n^{(4)} = \int_{y_0 - \frac{W}{2}}^{y_0 + \frac{W}{2}} \cos(k_y y) P(y - y_n) dy. \quad (\text{D.4})$$

For a y directed current on a strip of width W , $\mathcal{I}_n^{(1)}$ becomes

$$\mathcal{I}_n^{(1)} = \int_{y_0 - \frac{W}{2} + (n-1)\frac{W}{N}}^{y_0 - \frac{W}{2} + n\frac{W}{N}} \sin(k_y y) P(y - y_n) dy \quad (\text{D.5})$$

$$= \frac{1}{k_y} \left[\cos k_y \left(y_0 - \frac{W}{2} + (n-1)\frac{W}{N} \right) - \cos k_y \left(y_0 - \frac{W}{2} + n\frac{W}{N} \right) \right] \quad (\text{D.6})$$

or

$$\mathcal{I}_n^{(1)} = \begin{cases} \frac{2}{k_y} \sin k_y \left(y_0 - \frac{W}{2} + (n - \frac{1}{2})\frac{W}{N} \right) \sin k_y \left(\frac{W}{2N} \right) & , m \neq 0 \\ 0 & , m = 0. \end{cases} \quad (\text{D.7})$$

where $k_y = \frac{m\pi}{b}$ with $m = 0, 1, 2, \dots$

The second step is to calculate the integral corresponding to the z component of the current. Following the same procedure as above, we get

$$\mathcal{I}_n^{(2)} = \int_{y_0 - \frac{W}{2} + (n-1)\frac{W}{N}}^{y_0 - \frac{W}{2} + n\frac{W}{N}} \cos(k_y y) P(y - y_n) dy \quad (\text{D.8})$$

$$= \frac{1}{k_y} \left[\sin k_y \left(y_0 - \frac{W}{2} + n \frac{W}{N} \right) - \sin k_y \left(y_0 - \frac{W}{2} + (n-1) \frac{W}{N} \right) \right] \quad (\text{D.9})$$

or

$$\mathcal{I}_n^{(2)} = \begin{cases} \frac{2}{k_y} \cos k_y \left(y_0 - \frac{W}{2} + (n - \frac{1}{2}) \frac{W}{N} \right) \sin k_y \left(\frac{W}{2N} \right) & , m \neq 0 \\ \frac{W}{N} & , m = 0 \end{cases} \quad (\text{D.10})$$

D.3 Integration over the conductor term

The last term in (3.36) takes into account the ohmic losses due to the finite conductivity of the strips. After applying the method of moments, the resulting integrals are

$$\mathcal{I}_{nl} = \mathcal{I}_n^{(5)} = \mathcal{I}_n^{(6)} = \int_{y_0 - \frac{W}{2}}^{y_0 + \frac{W}{2}} P(y - y_n) P(y - y_l) dy \quad (\text{D.11})$$

$$\mathcal{I}_{nl} = \begin{cases} 1 & , l = n \\ 0 & , l \neq n. \end{cases} \quad (\text{D.12})$$

APPENDIX E

**GENERAL BOUNDARY CONDITIONS
BETWEEN TWO HOMOGENEOUS,
ISOTROPIC MEDIA**

Let us consider an interface between two media, as shown in Figure E.1, along which there are no charges or sources. These conditions are satisfied provided that neither of the two media is a perfect conductor or that sources are not placed there. Regions 1 and 2 are characterized, respectively, by the constitutive parameters $\epsilon_1, \mu_1, \sigma_1$ and $\epsilon_2, \mu_2, \sigma_2$. In this derivation, we will assume the media to be isotropic, homogeneous and non-magnetic ($\mu_1 = \mu_2 = \mu_0$).

The x, y, z coordinate system is chosen to represent the local geometry. For rectilinear propagation along the z direction, the fields can be written in terms of their transverse and longitudinal components as

$$\vec{E} = (\vec{e}_t + \vec{e}_z) \exp(-\gamma_z z) \quad (\text{E.1})$$

$$\vec{H} = (\vec{h}_t + \vec{h}_z) \exp(-\gamma_z z) \quad (\text{E.2})$$

In this appendix, generalized boundary conditions between two homogeneous, isotropic media are derived. The dependence of the field vectors on the electrical properties of the media along boundaries of discontinuity is referred to as the *initial boundary conditions*. Using these initial boundary conditions of the electromagnetic

fields, it is shown that the derivatives of the electric fields in the two media with respect to the direction perpendicular to the interface are related at the boundary and can be expressed through a general recurrence formula.

E.1 Initial boundary conditions

Maxwell's equations in integral form provide the most convenient formulation for derivation of the initial boundary conditions, and can be found in any elementary electromagnetic textbook (e.g. [112]). The boundary conditions for the electric field are

- the tangential components of the electric field across an interface between two media with no impressed magnetic current densities along the boundary of the interface are continuous

$$\hat{n} \times (\vec{E}^{(1)} - \vec{E}^{(2)}) = 0, \quad (\text{E.3})$$

- the normal components of the electric field intensity across an interface are discontinuous

$$\hat{n} \cdot (\epsilon_1 \vec{E}^{(1)} - \epsilon_2 \vec{E}^{(2)}) = 0 \quad (\text{E.4})$$

and for the magnetic field,

- the tangential components of the magnetic field across an interface between two media, neither of which is a perfect conductor, are continuous

$$\hat{n} \times (\vec{H}^{(1)} - \vec{H}^{(2)}) = 0, \quad (\text{E.5})$$

- the normal components of the magnetic field intensity across an interface are discontinuous

$$\hat{n} \cdot (\mu_1 \vec{H}^{(1)} - \mu_2 \vec{H}^{(2)}) = 0. \quad (\text{E.6})$$

In the x, y, z coordinate system defined in Figure 1 and at $x = x_0$, Equations (E.3), (E.4) take the form

$$\mathbf{e}_x^{(2)} = \frac{\epsilon_1}{\epsilon_2} \mathbf{e}_x^{(1)} \quad (\text{E.7})$$

$$\mathbf{e}_y^{(2)} = \mathbf{e}_y^{(1)} \quad (\text{E.8})$$

$$\mathbf{e}_z^{(2)} = \mathbf{e}_z^{(1)} \quad (\text{E.9})$$

while (E.5), (E.6) become

$$\mathbf{h}_x^{(2)} = \mathbf{h}_x^{(1)} \quad (\text{E.10})$$

$$\mathbf{h}_y^{(2)} = \mathbf{h}_y^{(1)} \quad (\text{E.11})$$

$$\mathbf{h}_z^{(2)} = \mathbf{h}_z^{(1)}. \quad (\text{E.12})$$

The **bold** notation is used for the field components evaluated at the interface $x = x_0$.

E.2 First-order boundary conditions

To evaluate the boundary condition of the first-order derivative of the electric field, we make use of Maxwell's equations. Since we are interested in the boundary conditions for the electric field only, Maxwell's equation from Faraday's law will be used

$$\vec{\nabla} \times \vec{E} = -j\omega\mu_0\vec{H} \quad (\text{E.13})$$

or in terms of longitudinal and transverse components

$$(\vec{\nabla}_t - \gamma_z \hat{z}) \times (\vec{e}_t + \vec{e}_z) = -j\omega\mu_0(\vec{h}_t + \vec{h}_z) \quad (\text{E.14})$$

which may be decomposed to lead

$$\vec{\nabla}_t \times \vec{e}_t = -j\omega\mu_0\vec{h}_z \quad (\text{E.15})$$

$$\hat{z} \times (\vec{\nabla}_t e_z + \gamma_z \vec{e}_t) = j\omega\mu_0\vec{h}_t. \quad (\text{E.16})$$

Making use of (E.15)

$$\left(\hat{x}\frac{\partial}{\partial x} + \hat{y}\frac{\partial}{\partial y}\right) \times (e_x\hat{x} + e_y\hat{y}) = -j\omega\mu_0 h_z \hat{z} \quad (\text{E.17})$$

we get

$$\frac{\partial e_x}{\partial y} - \frac{\partial e_y}{\partial x} = j\omega\mu_0 h_z. \quad (\text{E.18})$$

This relation holds at any point in space, therefore in region (1)

$$\frac{\partial e_x^{(1)}}{\partial y} - \frac{\partial e_y^{(1)}}{\partial x} = j\omega\mu_0 h_z^{(1)} \quad (\text{E.19})$$

and in region (2)

$$\frac{\partial e_x^{(2)}}{\partial y} - \frac{\partial e_y^{(2)}}{\partial x} = j\omega\mu_0 h_z^{(2)}. \quad (\text{E.20})$$

At $x = x_0$ and for any y along the boundary, we can write

$$\left(\frac{\partial e_x^{(2)}}{\partial y} - \frac{\partial e_x^{(1)}}{\partial y}\right) - \left(\frac{\partial e_y^{(2)}}{\partial x} - \frac{\partial e_y^{(1)}}{\partial x}\right) = j\omega\mu_0 (h_z^{(2)} - h_z^{(1)}). \quad (\text{E.21})$$

Recalling the continuity of the magnetic field intensity from (E.5),

$$h_z^{(2)} = h_z^{(1)} \quad (\text{E.22})$$

we obtain

$$\frac{\partial e_y^{(2)}}{\partial x} - \frac{\partial e_y^{(1)}}{\partial x} = \frac{\partial e_x^{(2)}}{\partial y} - \frac{\partial e_x^{(1)}}{\partial y}. \quad (\text{E.23})$$

The media exhibit discontinuity along the x-direction only. In the y- and z- directions the field quantities are single-valued, bounded, and possess (along with their derivatives) continuous distributions, thus

$$\frac{\partial^n e_\xi^{(1)}}{\partial y^n} = \frac{\partial^n e_\xi^{(2)}}{\partial y^n}, \quad \forall n \quad (\text{E.24})$$

$$\frac{\partial^n e_\xi^{(1)}}{\partial z^n} = \frac{\partial^n e_\xi^{(2)}}{\partial z^n}, \quad \forall n \quad (\text{E.25})$$

where ξ denotes the y or z coordinate. Similarly, upon using (E.7), we get

$$\frac{\partial^n \mathbf{e}_x^{(2)}}{\partial y^n} = \frac{\epsilon_1}{\epsilon_2} \frac{\partial^n \mathbf{e}_x^{(1)}}{\partial y^n}. \quad (\text{E.26})$$

Hence (E.23) yields

$$\boxed{\frac{\partial}{\partial x} \mathbf{e}_y^{(2)} - \frac{\partial}{\partial x} \mathbf{e}_y^{(1)} = \left(\frac{\epsilon_1}{\epsilon_2} - 1\right) \frac{\partial}{\partial y} \mathbf{e}_x^{(1)}}.$$

Proceeding in a similar fashion for the z component, from (E.16) we have

$$\hat{z} \times \left(\hat{x} \frac{\partial e_z}{\partial x} + \hat{y} \frac{\partial e_z}{\partial y} + \gamma_z \hat{x} e_x + \gamma_z \hat{y} e_y \right) = j\omega\mu_0 (h_x \hat{x} + h_y \hat{y}) \quad (\text{E.27})$$

or

$$\frac{\partial e_z}{\partial x} + \gamma_z e_x = j\omega\mu_0 h_y \quad (\text{E.28})$$

$$\frac{\partial e_z}{\partial y} + \gamma_z e_y = -j\omega\mu_0 h_x. \quad (\text{E.29})$$

Equation (E.28) holds at any point and therefore in region (1)

$$\frac{\partial e_z^{(1)}}{\partial x} + \gamma_z e_x^{(1)} = j\omega\mu_0 h_y^{(1)}, \quad (\text{E.30})$$

and in region (2)

$$\frac{\partial e_z^{(2)}}{\partial x} + \gamma_z e_x^{(2)} = j\omega\mu_0 h_y^{(2)}. \quad (\text{E.31})$$

Using (E.7) at the interface $x = x_0$, we can write

$$\left(\frac{\partial \mathbf{e}_z^{(2)}}{\partial x} - \frac{\partial \mathbf{e}_z^{(1)}}{\partial x} \right) = \gamma_z \left(1 - \frac{\epsilon_1}{\epsilon_2} \right) \mathbf{e}_x^{(1)} + j\omega\mu_0 (\mathbf{h}_y^{(2)} - \mathbf{h}_y^{(1)}). \quad (\text{E.32})$$

From the continuity of the magnetic field intensity (E.5), we obtain

$$\boxed{\frac{\partial}{\partial x} \mathbf{e}_z^{(2)} - \frac{\partial}{\partial x} \mathbf{e}_z^{(1)} = \gamma_z \left(1 - \frac{\epsilon_1}{\epsilon_2} \right) \mathbf{e}_x^{(1)}}.$$

Now, from Gauss's law in source-free regions,

$$\vec{\nabla} \cdot \vec{D} = 0 \quad (\text{E.33})$$

we can find a relationship between the derivatives of the x-component of the electric field

$$\vec{\nabla} \cdot \epsilon_1 \vec{E}^{(1)} = 0, \text{ in region (1)} \quad (\text{E.34})$$

$$\vec{\nabla} \cdot \epsilon_2 \vec{E}^{(2)} = 0, \text{ in region (2)}. \quad (\text{E.35})$$

Assuming homogeneous and isotropic materials, we get

$$\epsilon_1 \vec{\nabla} \cdot \vec{E}^{(1)} = \epsilon_2 \vec{\nabla} \cdot \vec{E}^{(2)} = 0 \quad (\text{E.36})$$

from which we obtain, at $x = x_0$

$$\epsilon_1 \left(\frac{\partial e_x^{(1)}}{\partial x} + \frac{\partial e_y^{(1)}}{\partial y} + \frac{\partial e_z^{(1)}}{\partial z} \right) = \epsilon_2 \left(\frac{\partial e_x^{(2)}}{\partial x} + \frac{\partial e_y^{(2)}}{\partial y} + \frac{\partial e_z^{(2)}}{\partial z} \right) \quad (\text{E.37})$$

or

$$\frac{\partial e_x^{(2)}}{\partial x} = \frac{\epsilon_1}{\epsilon_2} \frac{\partial e_x^{(1)}}{\partial x} + \frac{\epsilon_1}{\epsilon_2} \left(\frac{\partial e_y^{(1)}}{\partial y} + \frac{\partial e_z^{(1)}}{\partial z} \right) - \left(\frac{\partial e_y^{(2)}}{\partial y} + \frac{\partial e_z^{(2)}}{\partial z} \right). \quad (\text{E.38})$$

In view of (E.24) and (E.25),

$$\frac{\partial e_x^{(2)}}{\partial x} = \frac{\epsilon_1}{\epsilon_2} \frac{\partial e_x^{(1)}}{\partial x} + \left(\frac{\epsilon_1}{\epsilon_2} - 1 \right) \left(\frac{\partial e_y^{(1)}}{\partial y} + \frac{\partial e_z^{(1)}}{\partial z} \right) \quad (\text{E.39})$$

$$= \frac{\epsilon_1}{\epsilon_2} \frac{\partial e_x^{(1)}}{\partial x} - \left(\frac{\epsilon_1}{\epsilon_2} - 1 \right) \frac{\partial e_x^{(1)}}{\partial x} \quad (\text{E.40})$$

or

$$\boxed{\frac{\partial e_x^{(2)}}{\partial x} = \frac{\partial e_x^{(1)}}{\partial x}.}$$

E.3 Higher-order boundary conditions

To evaluate the boundary condition of the second-order derivative of the electric field, we will make use of the wave equation which can be written, in terms of transverse and longitudinal components of the electric field, as

$$\begin{aligned}\vec{\nabla}_t^2 \vec{e}_t - (\gamma^2 - \gamma_z^2) \vec{e}_t &= 0 \\ \vec{\nabla}_z^2 \vec{e}_z - (\gamma^2 - \gamma_z^2) \vec{e}_z &= 0.\end{aligned}\quad (\text{E.41})$$

The wave equation is general and holds at any point in space at any time. Therefore, Equation (E.41) can be written in region (1) as

$$\frac{\partial^2 e_\xi^{(1)}}{\partial x^2} + \frac{\partial^2 e_\xi^{(1)}}{\partial y^2} + (k_1^2 - k_z^2) e_\xi^{(1)} = 0, \quad (\text{E.42})$$

and in region (2) as

$$\frac{\partial^2 e_\xi^{(2)}}{\partial x^2} + \frac{\partial^2 e_\xi^{(2)}}{\partial y^2} + (k_2^2 - k_z^2) e_\xi^{(2)} = 0. \quad (\text{E.43})$$

At the interface $x = x_o$, subtraction of (E.42) from (E.43) yields

$$\left(\frac{\partial^2 e_\xi^{(2)}}{\partial x^2} - \frac{\partial^2 e_\xi^{(1)}}{\partial x^2} \right) + \left(\frac{\partial^2 e_\xi^{(2)}}{\partial y^2} - \frac{\partial^2 e_\xi^{(1)}}{\partial y^2} \right) + (k_2^2 - k_z^2) e_\xi^{(2)} - (k_1^2 - k_z^2) e_\xi^{(1)} = 0. \quad (\text{E.44})$$

Hence, recalling (E.8)-(E.9), Equation (E.44) becomes

$$\frac{\partial^2 e_\xi^{(2)}}{\partial x^2} - \frac{\partial^2 e_\xi^{(1)}}{\partial x^2} = (k_1^2 - k_z^2) e_\xi^{(1)} - (k_2^2 - k_z^2) e_\xi^{(2)} \quad (\text{E.45})$$

$$= (k_1^2 - k_z^2) e_\xi^{(1)} + (k_2^2 - k_z^2) (e_\xi^{(1)} - e_\xi^{(2)}) \quad (\text{E.46})$$

$$= (k_1^2 - k_z^2) e_\xi^{(1)}. \quad (\text{E.47})$$

Now, taking the x-derivative of (E.42) and (E.43), we get

$$\frac{\partial^3 e_\xi^{(1)}}{\partial x^3} + \frac{\partial^3 e_\xi^{(1)}}{\partial x \partial y^2} + (k_1^2 - k_z^2) \frac{\partial e_\xi^{(1)}}{\partial x} = 0, \text{ in region (1)} \quad (\text{E.48})$$

$$\frac{\partial^3 e_\xi^{(2)}}{\partial x^3} + \frac{\partial^3 e_\xi^{(2)}}{\partial x \partial y^2} + (k_2^2 - k_z^2) \frac{\partial e_\xi^{(2)}}{\partial x} = 0, \text{ in region (2)} \quad (\text{E.49})$$

leading to

$$\frac{\partial^3 \mathbf{e}_\xi^{(2)}}{\partial x^3} - \frac{\partial^3 \mathbf{e}_\xi^{(1)}}{\partial x^3} = (k_1^2 - k_2^2) \frac{\partial \mathbf{e}_\xi^{(1)}}{\partial x} + (k_2^2 - k_z^2 + \frac{\partial^2}{\partial y^2}) \left(\frac{\partial \mathbf{e}_\xi^{(1)}}{\partial x} - \frac{\partial \mathbf{e}_\xi^{(2)}}{\partial x} \right) \quad (\text{E.50})$$

$$= (k_1^2 - k_2^2) \frac{\partial \mathbf{e}_\xi^{(1)}}{\partial x} + (k_{x_2}^2) \left(\frac{\epsilon_1}{\epsilon_2} - 1 \right) \frac{\partial \mathbf{e}_x^{(1)}}{\partial \xi}. \quad (\text{E.51})$$

Generalizing this procedure to the n th-order derivative,

$$\frac{\partial^n \mathbf{e}_\xi^{(1)}}{\partial x^n} + \frac{\partial^n \mathbf{e}_\xi^{(1)}}{\partial x^{n-2} \partial y^2} + (k_1^2 - k_z^2) \frac{\partial^{n-2} \mathbf{e}_\xi^{(1)}}{\partial x^{n-2}} = 0, \text{ in region (1)} \quad (\text{E.52})$$

$$\frac{\partial^n \mathbf{e}_\xi^{(2)}}{\partial x^n} + \frac{\partial^n \mathbf{e}_\xi^{(2)}}{\partial x^{n-2} \partial y^2} + (k_2^2 - k_z^2) \frac{\partial^{n-2} \mathbf{e}_\xi^{(2)}}{\partial x^{n-2}} = 0, \text{ in region (2)} \quad (\text{E.53})$$

from which we get

$$\begin{aligned} \frac{\partial^n \mathbf{e}_\xi^{(2)}}{\partial x^n} - \frac{\partial^n \mathbf{e}_\xi^{(1)}}{\partial x^n} &= -\frac{\partial^2}{\partial y^2} \left(\frac{\partial^{n-2} \mathbf{e}_\xi^{(2)}}{\partial x^{n-2}} - \frac{\partial^{n-2} \mathbf{e}_\xi^{(1)}}{\partial x^{n-2}} \right) \\ &- (k_2^2 - k_z^2) \frac{\partial^{n-2} \mathbf{e}_\xi^{(2)}}{\partial x^{n-2}} + (k_1^2 - k_z^2) \frac{\partial^{n-2} \mathbf{e}_\xi^{(1)}}{\partial x^{n-2}}. \end{aligned} \quad (\text{E.54})$$

The above may be rewritten as

$$\begin{aligned} \frac{\partial^n \mathbf{e}_\xi^{(2)}}{\partial x^n} - \frac{\partial^n \mathbf{e}_\xi^{(1)}}{\partial x^n} &= \\ (k_1^2 - k_2^2) \frac{\partial^{n-2} \mathbf{e}_\xi^{(1)}}{\partial x^{n-2}} - \left(\frac{\partial^2}{\partial y^2} + k_2^2 - k_z^2 \right) \left(\frac{\partial^{n-2} \mathbf{e}_\xi^{(2)}}{\partial x^{n-2}} - \frac{\partial^{n-2} \mathbf{e}_\xi^{(1)}}{\partial x^{n-2}} \right). \end{aligned} \quad (\text{E.55})$$

Now, let us set the following definitions

$$S_n(\xi) \equiv \left(\frac{\partial^n \mathbf{e}_\xi^{(2)}}{\partial x^n} - \frac{\partial^n \mathbf{e}_\xi^{(1)}}{\partial x^n} \right) \Big|_{x=x_0} \quad (\text{E.56})$$

$$R_n(\xi) \equiv \frac{\partial^n \mathbf{e}_\xi^{(1)}}{\partial x^n} \Big|_{x=x_0} \quad (\text{E.57})$$

$$T_n(\xi) \equiv \frac{\partial^n \mathbf{e}_\xi^{(2)}}{\partial x^n} \Big|_{x=x_0} \quad (\text{E.58})$$

and

$$\Delta \equiv k_1^2 - k_2^2 = k_0^2 (\epsilon_1 - \epsilon_2) \quad (\text{E.59})$$

$$F \equiv \frac{\partial^2}{\partial y^2} + k_2^2 - k_z^2 = k_{x_2}^2 \quad (\text{E.60})$$

then (E.55) becomes

$$S_n(\xi) = \Delta R_{n-2}(\xi) - F S_{n-2}(\xi). \quad (\text{E.61})$$

This expression involving S_n and S_{n-2} is a recursion formula [52] and by an iterative process, can be written in the form

$$S_n(\xi) = \Delta R_{n-2}(\xi) - F S_{n-2}(\xi) \quad (\text{E.62})$$

$$= \Delta R_{n-2}(\xi) - F(\Delta R_{n-4}(\xi) - F S_{n-4}(\xi)) \quad (\text{E.63})$$

$$= \Delta(R_{n-2}(\xi) - F R_{n-4}(\xi)) + F^2(\Delta R_{n-6}(\xi) - F S_{n-6}(\xi)) \quad (\text{E.64})$$

$$= \Delta(R_{n-2}(\xi) - F R_{n-4}(\xi) + F^2 R_{n-6}(\xi)) - F^3 S_{n-6}(\xi) \quad (\text{E.65})$$

....

or

$$S_n(\xi) = \begin{cases} \Delta \sum_{\nu=1}^N (-F)^{\nu-1} R_{n-2\nu}(\xi) + (-F)^N S_0(\xi) & , \text{if } n = 2N \\ \Delta \sum_{\nu=1}^N (-F)^{\nu-1} R_{n-2\nu}(\xi) + (-F)^N S_1(\xi) & , \text{if } n = 2N+1. \end{cases} \quad (\text{E.66})$$

Note that in this new nomenclature, the previously derived boundary conditions may be written as

$$S_0(x) = \mathbf{e}_x^{(2)} - \mathbf{e}_x^{(1)} = \left(\frac{\epsilon_1}{\epsilon_2} - 1 \right) \mathbf{e}_x^{(1)} \quad (\text{E.67})$$

$$S_0(y) = \mathbf{e}_y^{(2)} - \mathbf{e}_y^{(1)} = 0 \quad (\text{E.68})$$

$$S_0(z) = \mathbf{e}_z^{(2)} - \mathbf{e}_z^{(1)} = 0 \quad (\text{E.69})$$

$$S_1(x) = \frac{\partial}{\partial x} \mathbf{e}_x^{(2)} - \frac{\partial}{\partial x} \mathbf{e}_x^{(1)} = 0 \quad (\text{E.70})$$

$$S_1(y) = \frac{\partial}{\partial x} \mathbf{e}_y^{(2)} - \frac{\partial}{\partial x} \mathbf{e}_y^{(1)} = \left(\frac{\epsilon_1}{\epsilon_2} - 1 \right) \frac{\partial}{\partial y} \mathbf{e}_x^{(1)} \Big|_{x=x_0} \quad (\text{E.71})$$

$$S_1(z) = \frac{\partial}{\partial x} \mathbf{e}_z^{(2)} - \frac{\partial}{\partial x} \mathbf{e}_z^{(1)} = \left(\frac{\epsilon_1}{\epsilon_2} - 1 \right) \frac{\partial}{\partial z} \mathbf{e}_x^{(1)} \Big|_{x=x_0}. \quad (\text{E.72})$$

Therefore

$$T_n(\xi) = \begin{cases} R_n(\xi) + \Delta \sum_{\nu=1}^N (-F)^{\nu-1} R_{n-2\nu}(\xi) + (-F)^N S_0(\xi) & , \text{if } n = 2N \\ R_n(\xi) + \Delta \sum_{\nu=1}^N (-F)^{\nu-1} R_{n-2\nu}(\xi) + (-F)^N S_1(\xi) & , \text{if } n = 2N+1. \end{cases} \quad (\text{E.73})$$

Alternative expression for the derivatives of the x component

Another formulation is derived below, that takes into account the discontinuity of the electric field at the interface. Proceeding in a similar procedure as above, we recall (E.55)

$$\begin{aligned} \frac{\partial^n \mathbf{e}_\xi^{(2)}}{\partial x^n} - \frac{\partial^n \mathbf{e}_\xi^{(1)}}{\partial x^n} = \\ (k_1^2 - k_2^2) \frac{\partial^{n-2} \mathbf{e}_\xi^{(1)}}{\partial x^{n-2}} - \left(\frac{\partial^2}{\partial y^2} + k_2^2 - k_z^2 \right) \left(\frac{\partial^{n-2} \mathbf{e}_\xi^{(2)}}{\partial x^{n-2}} - \frac{\partial^{n-2} \mathbf{e}_\xi^{(1)}}{\partial x^{n-2}} \right) \end{aligned} \quad (\text{E.74})$$

which may be rewritten as

$$\begin{aligned} \frac{\partial^n \mathbf{e}_x^{(2)}}{\partial x^n} - \frac{\epsilon_1}{\epsilon_2} \frac{\partial^n \mathbf{e}_x^{(1)}}{\partial x^n} = \\ (k_1^2 - k_2^2) \frac{\epsilon_1}{\epsilon_2} \frac{\partial^{n-2} \mathbf{e}_x^{(1)}}{\partial x^{n-2}} - \left(\frac{\partial^2}{\partial y^2} + k_2^2 - k_z^2 \right) \left(\frac{\partial^{n-2} \mathbf{e}_x^{(2)}}{\partial x^{n-2}} - \frac{\epsilon_1}{\epsilon_2} \frac{\partial^{n-2} \mathbf{e}_x^{(1)}}{\partial x^{n-2}} \right) \\ + \left(1 - \frac{\epsilon_1}{\epsilon_2} \right) \left[\frac{\partial^n \mathbf{e}_x^{(1)}}{\partial x^n} + (k_1^2 - k_2^2) \frac{\partial^{n-2} \mathbf{e}_x^{(1)}}{\partial x^{n-2}} + \left(\frac{\partial^2}{\partial y^2} + k_2^2 - k_z^2 \right) \frac{\partial^{n-2} \mathbf{e}_x^{(1)}}{\partial x^{n-2}} \right] \\ = (k_1^2 - k_2^2) \frac{\epsilon_1}{\epsilon_2} \frac{\partial^{n-2} \mathbf{e}_x^{(1)}}{\partial x^{n-2}} + \left(k_z^2 - k_2^2 - \frac{\partial^2}{\partial y^2} \right) \left(\frac{\partial^{n-2} \mathbf{e}_x^{(2)}}{\partial x^{n-2}} - \frac{\epsilon_1}{\epsilon_2} \frac{\partial^{n-2} \mathbf{e}_x^{(1)}}{\partial x^{n-2}} \right) \\ + \left(1 - \frac{\epsilon_1}{\epsilon_2} \right) \frac{\partial^{n-2}}{\partial x^{n-2}} \left(\frac{\partial^2}{\partial x^2} + \frac{\partial^2}{\partial y^2} + k_1^2 - k_z^2 \right) \mathbf{e}_x^{(1)}. \end{aligned} \quad (\text{E.75})$$

Since the eigenvalues are related by

$$k_1^2 = k_{x1}^2 + k_y^2 + k_z^2 \quad (\text{E.76})$$

$$k_2^2 = k_{x2}^2 + k_y^2 + k_z^2, \quad (\text{E.77})$$

equation (E.75) simplifies to

$$\frac{\partial^n \mathbf{e}_x^{(2)}}{\partial x^n} - \frac{\epsilon_1}{\epsilon_2} \frac{\partial^n \mathbf{e}_x^{(1)}}{\partial x^n} = (k_1^2 - k_2^2) \frac{\epsilon_1}{\epsilon_2} \frac{\partial^{n-2} \mathbf{e}_x^{(1)}}{\partial x^{n-2}} + (-k_{x2}^2) \left(\frac{\partial^{n-2} \mathbf{e}_x^{(2)}}{\partial x^{n-2}} - \frac{\epsilon_1}{\epsilon_2} \frac{\partial^{n-2} \mathbf{e}_x^{(1)}}{\partial x^{n-2}} \right) \quad (\text{E.78})$$

Setting the following definitions

$$S'_n(x) \equiv \left(\frac{\partial^n \mathbf{e}_x^{(2)}}{\partial x^n} - \frac{\epsilon_1}{\epsilon_2} \frac{\partial^n \mathbf{e}_x^{(1)}}{\partial x^n} \right) \Big|_{x=x_0} \quad (\text{E.79})$$

$$R'_n(x) \equiv \frac{\epsilon_1}{\epsilon_2} \frac{\partial^n \mathbf{e}_x^{(1)}}{\partial x^n} \Big|_{x=x_0}, \quad (\text{E.80})$$

we find the same type of recurrence formula as in (E.66)

$$S'_n(x) = \begin{cases} \Delta \sum_{\nu=1}^N (-F)^{\nu-1} R'_{n-2\nu}(x) + (-F)^N S'_0(x) & , \text{if } n = 2N \\ \Delta \sum_{\nu=1}^N (-F)^{\nu-1} R'_{n-2\nu}(x) + (-F)^N S'_1(x) & , \text{if } n = 2N+1 \end{cases} \quad (\text{E.81})$$

where, now,

$$S'_0(x) = \mathbf{e}_x^{(2)} - \frac{\epsilon_1}{\epsilon_2} \mathbf{e}_x^{(1)} \Big|_{x=x_0} = 0 \quad (\text{E.82})$$

$$S'_1(x) = \left(\frac{\partial \mathbf{e}_x^{(2)}}{\partial x} - \frac{\epsilon_1}{\epsilon_2} \frac{\partial \mathbf{e}_x^{(1)}}{\partial x} \right) \Big|_{x=x_0} = -\left(\frac{\epsilon_1}{\epsilon_2} - 1 \right) \frac{\partial \mathbf{e}_x^{(1)}}{\partial x}. \quad (\text{E.83})$$

Thus

$$T_n(x) = \begin{cases} R'_n(x) + \Delta \sum_{\nu=1}^N (-F)^{\nu-1} R_{n-2\nu}(x) & , \text{if } n = 2N \\ R'_n(x) + \Delta \sum_{\nu=1}^N (-F)^{\nu-1} R_{n-2\nu}(x) + (-F)^N S'_1(x) & , \text{if } n = 2N+1. \end{cases} \quad (\text{E.84})$$

E.4 SUMMARY

In summary, the generalized boundary conditions at the interface between two media are summarized below,

$$\frac{\partial^n \mathbf{e}_x^{(2)}}{\partial x^n} = \frac{\epsilon_1}{\epsilon_2} \frac{\partial^n \mathbf{e}_x^{(1)}}{\partial x^n} + \Delta \sum_{\nu=1}^{\lfloor \frac{n}{2} \rfloor} (-F)^{\nu-1} \frac{\partial^{n-2\nu}}{\partial x^{n-2\nu}} \mathbf{e}_x^{(1)} + (-F)^{\lfloor \frac{n}{2} \rfloor} \left(\frac{\epsilon_2}{\epsilon_1} - 1 \right) \frac{\partial}{\partial x} \mathbf{e}_x^{(1)} \kappa_n \quad (\text{E.85})$$

and

$$\frac{\partial^n \mathbf{e}_{y,z}^{(2)}}{\partial x^n} = \frac{\partial^n \mathbf{e}_{y,z}^{(1)}}{\partial x^n} + \Delta \sum_{\nu=1}^{\lfloor \frac{n}{2} \rfloor} (-F)^{\nu-1} \frac{\partial^{n-2\nu}}{\partial x^{n-2\nu}} \mathbf{e}_{y,z}^{(1)} + (-F)^{\lfloor \frac{n}{2} \rfloor} \left(\frac{\epsilon_1}{\epsilon_2} - 1 \right) \frac{\partial}{\partial y, z} \mathbf{e}_x^{(1)} \kappa_n \quad (\text{E.86})$$

with

$$\kappa_n = \begin{cases} 1 & , \text{ n odd} \\ 0 & , \text{ n even} \end{cases} \quad (\text{E.87})$$

and

$$\begin{cases} \Delta = k_0^2(\epsilon_1 - \epsilon_2) \\ F = k_{x_2}^2 \end{cases} \quad (\text{E.88})$$

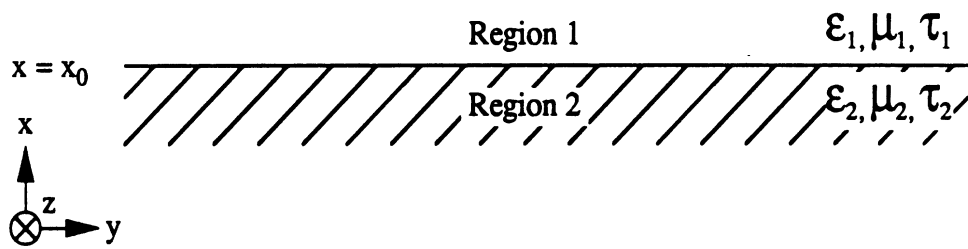


Figure E.1: Geometry of the problem

APPENDIX F

REFLECTION AND TRANSMISSION BY AN INFINITE SLAB

To verify the generalized impedance boundary conditions (GIBC's) between two homogeneous, isotropic media, the expressions given in Chapter 6 and derived in Appendix E are used here to calculate the reflection and transmission coefficients of a uniform plane wave impinging on a slab. This incident plane wave with any polarization may be decomposed into TE and TM wave components. Figure F.1 depicts the case of a TM wave (also called parallel or vertically polarized wave) incident upon the slab, where the electric field is parallel to the plane of incidence, i.e. has both x and y components. This case was chosen to verify both boundary conditions (E.85) and (E.86). Results are compared to the classical derivation which can be found in many electromagnetics textbooks, e.g. [113].

F.1 Classical Derivation

Consider a plane wave incident from region 1 of permittivity ϵ_1 and permeability μ_1 onto a dielectric slab of electrical parameters ϵ_2 and permeability μ_2 with boundaries at $x = 0$ and $-h$. The plane of incidence is parallel to the $x - y$ plane. The third region is semi-infinite and its permittivity and permeability are denoted by ϵ_3 and μ_3 . By the phase-matching conditions the \vec{k} vectors of all plane waves will be in the

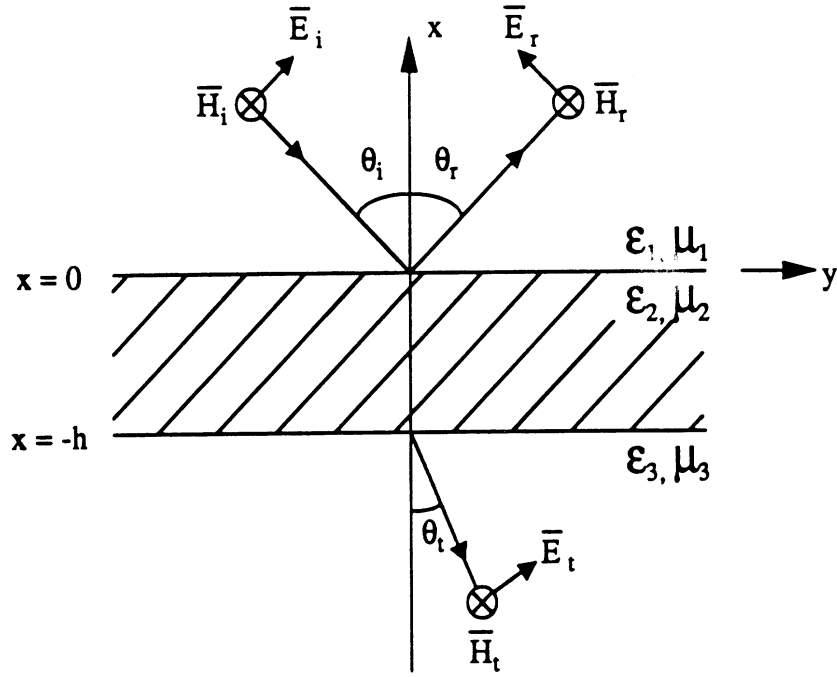


Figure F.1: Reflection and transmission of a vertically polarized plane wave in a slab $x-y$ plane. Thus all field vectors will be dependent on x and y only and independent of z . Since $\frac{\partial}{\partial z} = 0$, the Maxwell's equations may be written as

$$H_x = -\frac{1}{j\omega\mu} \frac{\partial}{\partial y} E_z \quad (\text{F.1})$$

$$H_y = \frac{1}{j\omega\mu} \frac{\partial}{\partial x} E_z \quad (\text{F.2})$$

$$H_z = -\frac{1}{j\omega\mu} \left(\frac{\partial}{\partial x} E_y - \frac{\partial}{\partial y} E_x \right). \quad (\text{F.3})$$

For a TM plane wave incident on medium 2, the electric and magnetic fields in region 1 are the sum of the reflected and incident components, and may be written as

$$\begin{aligned} H_z^{(1)} &= E_0 (R e^{jk_{x1}x} + e^{-jk_{x1}x}) e^{jk_y y} \\ E_x^{(1)} &= \frac{k_y}{\omega\epsilon_1} E_0 (R e^{jk_{x1}x} + e^{-jk_{x1}x}) e^{jk_y y} \\ E_y^{(1)} &= -\frac{k_{x1}}{\omega\epsilon_1} E_0 (R e^{jk_{x1}x} - e^{-jk_{x1}x}) e^{jk_y y} \end{aligned} \quad (\text{F.4})$$

where E_0 is the incident wave amplitude and R is the total reflection coefficient for the electric field. In region 3, there is only a TM transmitted wave which takes the form

$$\begin{aligned} H_z^{(3)} &= T E_0 e^{-jk_{z3}x} e^{jk_y y} \\ E_x^{(3)} &= \frac{k_y}{\omega \epsilon_3} T E_0 e^{-jk_{z3}x} e^{jk_y y} \\ E_y^{(3)} &= \frac{k_{z3}}{\omega \epsilon_3} T E_0 e^{-jk_{z3}x} e^{jk_y y} \end{aligned} \quad (\text{F.5})$$

where T is the transmission coefficient for the electric field. By applying the boundary conditions of continuity of the tangential E and H fields at the interfaces, the reflection and transmission coefficients can be determined as

$$R_{ij} = \frac{1 - p_{ij}}{1 + p_{ij}} \quad (\text{F.6})$$

$$T_{ij} = \frac{2}{1 + p_{ij}} \quad (\text{F.7})$$

where R_{ij} and T_{ij} are the reflection and transmission coefficients from region i to region j respectively, and where p_{ij} is given, for TM waves, by

$$p_{ij} = \frac{\epsilon_i k_{xj}}{\epsilon_j k_{xi}}. \quad (\text{F.8})$$

General relations have been derived for layered media with any given number of layers [113]. For the slab problem, the reflection and transmission coefficients can be cast in the following form

$$R = \frac{R_{12} + R_{23} e^{j2k_{z2}h}}{1 + R_{12} R_{23} e^{j2k_{z2}h}} \quad (\text{F.9})$$

$$T = \frac{4 e^{j(k_{z2} - k_{z3})h}}{(1 + p_{12})(1 + p_{23})(1 + R_{12} R_{23} e^{j2k_{z2}h})}. \quad (\text{F.10})$$

F.2 Alternate Derivation

We shall now derive the reflection and transmission coefficient for a plane wave impinging on a slab using the higher-order impedance boundary conditions. The first

step is to expand the electric field in the slab region in a Taylor's series with respect to the $x = 0$ interface for the top half of the slab, and to $x = -h$ for the bottom half of the slab. In region 2, the fields are as follows

$$\vec{E}^{(2)}(x, y) = \begin{cases} \sum_{n=0}^{\infty} \frac{1}{n!} \left[\frac{\partial^n}{\partial x^n} \vec{E}^{(2)}(x, y) \right]_{x=0} x^n & , \text{if } -\frac{h}{2} \leq x \leq 0 \\ \sum_{n=0}^{\infty} \frac{1}{n!} \left[\frac{\partial^n}{\partial x^n} \vec{E}^{(2)}(x, y) \right]_{x=-h} (x+h)^n & , \text{if } -h \leq x \leq -\frac{h}{2} . \end{cases} \quad (\text{F.11})$$

Next, the generalized impedance boundary conditions described in Chapter 6 can be used to relate the fields in the slab to the fields in the regions outside the slab. These relations involve the higher-order derivatives of the electric field with respect to the direction perpendicular to the interface, and are restated here for convenience

$$\frac{\partial^n E_x^{(2)}}{\partial x^n} = \frac{\epsilon_1}{\epsilon_2} \frac{\partial^n}{\partial x^n} E_x^{(1)} + \Delta \sum_{\nu=1}^{\lfloor \frac{n}{2} \rfloor} (-F)^{\nu-1} \frac{\partial^{n-2\nu}}{\partial x^{n-2\nu}} E_x^{(1)} + (-F)^{\lfloor \frac{n}{2} \rfloor} \left(\frac{\epsilon_2}{\epsilon_1} - 1 \right) \frac{\partial}{\partial x} E_x^{(1)} \kappa_n \quad (\text{F.12})$$

and

$$\frac{\partial^n E_{y,z}^{(2)}}{\partial x^n} = \frac{\partial^n}{\partial x^n} e_{y,z}^{(1)} + \Delta \sum_{\nu=1}^{\lfloor \frac{n}{2} \rfloor} (-F)^{\nu-1} \frac{\partial^{n-2\nu}}{\partial x^{n-2\nu}} E_{y,z}^{(1)} + (-F)^{\lfloor \frac{n}{2} \rfloor} \left(\frac{\epsilon_1}{\epsilon_2} - 1 \right) \frac{\partial}{\partial y, z} E_x^{(1)} \kappa_n \quad (\text{F.13})$$

with

$$\kappa_n = \begin{cases} 1 & , n \text{ odd} \\ 0 & , n \text{ even} \end{cases} \quad (\text{F.14})$$

and

$$\begin{cases} \Delta & = k_0^2 (\epsilon_1 - \epsilon_2) \\ F & = k_{x_2}^2 \end{cases} \quad (\text{F.15})$$

From the continuity of the electric field in the slab at $x = -\frac{h}{2}$, we get the following relations

$$\vec{E}_x^+ = \vec{E}_x^- \quad , x = -\frac{h}{2} \quad (\text{F.16})$$

$$\vec{E}_y^+ = \vec{E}_y^- \quad , x = -\frac{h}{2} \quad (\text{F.17})$$

where (+) and (-) represent the fields just above and below $x = -\frac{h}{2}$, respectively.

Making use of (F.12) and (F.13) in (F.16)-(F.17), it follows that

$$\begin{aligned}
& \sum_{n=0}^{\infty} \frac{(-\frac{h}{2})^n}{n!} \frac{\epsilon_1}{\epsilon_2} \frac{\partial^n E_x^{(1)}}{\partial x^n} \Big|_{x=0} + k_o^2 (\epsilon_1 - \epsilon_2) \frac{\epsilon_1}{\epsilon_2} \sum_{n=2}^{\infty} \frac{(-\frac{h}{2})^n}{n!} \sum_{\nu=1}^{\lfloor \frac{n}{2} \rfloor} (-k_{x_2}^2)^{\nu-1} \frac{\partial^{n-2\nu} E_x^{(1)}}{\partial x^{n-2\nu}} \Big|_{x=0} \\
& + \left(1 - \frac{\epsilon_1}{\epsilon_2}\right) \frac{\partial E_x^{(1)}}{\partial x} \Big|_{x=0} \sum_{n=1,3,5}^{\infty} \frac{(-\frac{h}{2})^n}{n!} (-k_{x_2}^2)^{\lfloor \frac{n}{2} \rfloor} \\
& = \sum_{n=0}^{\infty} \frac{(\frac{h}{2})^n}{n!} \frac{\epsilon_3}{\epsilon_2} \frac{\partial^n E_x^{(3)}}{\partial x^n} \Big|_{x=-h} + k_o^2 (\epsilon_3 - \epsilon_2) \frac{\epsilon_3}{\epsilon_2} \sum_{n=2}^{\infty} \frac{(\frac{h}{2})^n}{n!} \sum_{\nu=1}^{\lfloor \frac{n}{2} \rfloor} (-k_{x_2}^2)^{\nu-1} \frac{\partial^{n-2\nu} E_x^{(3)}}{\partial x^{n-2\nu}} \Big|_{x=-h} \\
& + \left(1 - \frac{\epsilon_3}{\epsilon_2}\right) \frac{\partial E_x^{(3)}}{\partial x} \Big|_{x=-h} \sum_{n=1,3,5}^{\infty} \frac{(\frac{h}{2})^n}{n!} (-k_{x_2}^2)^{\lfloor \frac{n}{2} \rfloor}, \tag{F.18}
\end{aligned}$$

$$\begin{aligned}
& \sum_{n=0}^{\infty} \frac{(-\frac{h}{2})^n}{n!} \frac{\partial^n E_x^{(1)}}{\partial x^n} \Big|_{x=0} + k_o^2 (\epsilon_1 - \epsilon_2) \sum_{n=2}^{\infty} \frac{(-\frac{h}{2})^n}{n!} \sum_{\nu=1}^{\lfloor \frac{n}{2} \rfloor} (-k_{x_2}^2)^{\nu-1} \frac{\partial^{n-2\nu} E_x^{(1)}}{\partial x^{n-2\nu}} \Big|_{x=0} \\
& + \left(\frac{\epsilon_1}{\epsilon_2} - 1\right) \frac{\partial E_x^{(1)}}{\partial y} \Big|_{x=0} \sum_{n=1,3,5}^{\infty} \frac{(-\frac{h}{2})^n}{n!} (-k_{x_2}^2)^{\lfloor \frac{n}{2} \rfloor} \\
& = \sum_{n=0}^{\infty} \frac{(\frac{h}{2})^n}{n!} \frac{\partial^n E_x^{(3)}}{\partial x^n} \Big|_{x=-h} + k_o^2 (\epsilon_3 - \epsilon_2) \sum_{n=2}^{\infty} \frac{(\frac{h}{2})^n}{n!} \sum_{\nu=1}^{\lfloor \frac{n}{2} \rfloor} (-k_{x_2}^2)^{\nu-1} \frac{\partial^{n-2\nu} E_x^{(3)}}{\partial x^{n-2\nu}} \Big|_{x=-h} \\
& + \left(\frac{\epsilon_3}{\epsilon_2} - 1\right) \frac{\partial E_x^{(3)}}{\partial y} \Big|_{x=-h} \sum_{n=1,3,5}^{\infty} \frac{(\frac{h}{2})^n}{n!} (-k_{x_2}^2)^{\lfloor \frac{n}{2} \rfloor}. \tag{F.19}
\end{aligned}$$

To find R and T , the expressions for $\vec{E}^{(1)}$ and $\vec{E}^{(3)}$ given by (F.4), (F.5) are substituted into (F.18), (F.19). Closed-form expressions may be found for the three types of summations that are encountered in these equations, i.e. first the infinite summation over n

$$\sum_{n=0}^{\infty} \frac{(-\frac{h}{2})^n}{n!} \frac{\partial^n E_x^{(1)}}{\partial x^n} \Big|_{x=0} = E_0 e^{jk_y y} \frac{k_y}{\omega \epsilon_1} e^{jk_{x1} \frac{h}{2}} (1 + R e^{-jk_{x1} h}) \tag{F.20}$$

$$\sum_{n=0}^{\infty} \frac{(\frac{h}{2})^n}{n!} \frac{\partial^n E_x^{(3)}}{\partial x^n} \Big|_{x=-h} = E_0 T e^{jk_y y} \frac{k_y}{\omega \epsilon_3} e^{jk_{x3} \frac{h}{2}}, \tag{F.21}$$

second, the double summation given by

$$\sum_{n=2}^{\infty} \frac{(-\frac{h}{2})^n}{n!} \sum_{\nu=1}^{\lfloor \frac{n}{2} \rfloor} (-k_{x_2}^2)^{\nu-1} \frac{\partial^{n-2\nu} E_x^{(1)}}{\partial x^{n-2\nu}} \Big|_{x=0} = E_0 e^{jk_y y} \frac{k_y}{\omega \epsilon_1} \frac{1}{k_o^2 (\epsilon_1 - \epsilon_2)}$$

$$\left[(1 + R) \cos k_{x2} \frac{h}{2} + j(1 - R) \frac{k_{x1}}{k_{x2}} \sin k_{x2} \frac{h}{2} - e^{jk_{x1} \frac{h}{2}} (1 + R e^{-jk_{x1} h}) \right] \quad (\text{F.22})$$

$$\sum_{n=2}^{\infty} \frac{\left(\frac{h}{2}\right)^n \left[\frac{n}{2}\right]}{n!} \sum_{\nu=1}^{\left[\frac{n}{2}\right]} (-k_{x2}^2)^{\nu-1} \left. \frac{\partial^{n-2\nu} E_x^{(3)}}{\partial x^{n-2\nu}} \right|_{x=0} = E_0 T e^{jk_y y} \frac{k_y}{\omega \epsilon_3} e^{jk_{x3} \frac{h}{2}} \frac{1}{k_o^2 (\epsilon_1 - \epsilon_2)} \left[\cos k_{x2} \frac{h}{2} - j \frac{k_{x3}}{k_{x2}} \sin k_{x2} \frac{h}{2} - e^{-jk_{x3} \frac{h}{2}} \right], \quad (\text{F.23})$$

and third, the summation over the odd values of n

$$\sum_{n=1,3,5}^{\infty} \frac{\left(\pm \frac{h}{2}\right)^n}{n!} (-k_{x2}^2)^{\left[\frac{n}{2}\right]} = \pm \frac{\sin k_{x2} \frac{h}{2}}{k_{x2}}. \quad (\text{F.24})$$

After some algebra, the system of two equations for the two unknowns R and T reduces to

$$\begin{aligned} R \left\{ \cos k_{x2} \frac{h}{2} - j p_{21} \sin k_{x2} \frac{h}{2} \right\} + T \left\{ -\cos k_{x2} \frac{h}{2} + j p_{23} \sin k_{x2} \frac{h}{2} \right\} e^{jk_{x3} h} \\ = -\cos k_{x2} \frac{h}{2} - j p_{21} \sin k_{x2} \frac{h}{2} \end{aligned} \quad (\text{F.25})$$

$$\begin{aligned} R \left\{ -\cos k_{x2} \frac{h}{2} + j p_{12} \sin k_{x2} \frac{h}{2} \right\} + T \left\{ -p_{13} \cos k_{x2} \frac{h}{2} + j p_{12} \sin k_{x2} \frac{h}{2} \right\} e^{jk_{x3} h} \\ = -\cos k_{x2} \frac{h}{2} - j p_{12} \sin k_{x2} \frac{h}{2} \end{aligned} \quad (\text{F.26})$$

and may be solved in a straightforward manner to yield

$$R = \frac{(1 - p_{13}) \cos k_{x2} h - j (p_{23} - p_{12}) \sin k_{x2} h}{(1 + p_{13}) \cos k_{x2} h - j (p_{23} + p_{12}) \sin k_{x2} h} \quad (\text{F.27})$$

$$T = \frac{2 \exp(-jk_{x3} h)}{(1 + p_{13}) \cos k_{x2} h - j (p_{23} + p_{12}) \sin k_{x2} h} \quad (\text{F.28})$$

which may be cast in the form of (F.9) and (F.10) using Euler's identities.

APPENDIX G

HARMONIC CLOSED FORM EXPRESSIONS

In this appendix, we derive closed-form expressions for the infinite harmonic summations encountered in the theoretical formulation given in Chapter 6.

- For the (A) term,

$$\sum_{n=0}^{\infty} (\pm 1)^{n+2} \frac{\left(\frac{h}{2}\right)^{n+1}}{\Gamma(n+2)} \frac{\partial^n}{\partial x^n} \left(\begin{array}{c} \sin u(x+v) \\ \cos u(x+v) \end{array} \right) \Bigg|_{x=x_0} \quad (\text{G.1})$$

- For the (B) term,

$$\sum_{n=2}^{\infty} (\pm 1)^{n+2} \frac{\left(\frac{h}{2}\right)^{n+1}}{\Gamma(n+2)} \sum_{\nu=1}^{\lfloor \frac{n}{2} \rfloor} (-w^2)^{\nu-1} \frac{\partial^{n-2\nu}}{\partial x^{n-2\nu}} \left(\begin{array}{c} \sin u(x+v) \\ \cos u(x+v) \end{array} \right) \Bigg|_{x=x_0} \quad (\text{G.2})$$

- For the (C) term,

$$\sum_{n=1,3,5}^{\infty} (\pm 1)^{n+2} \frac{\left(\frac{h}{2}\right)^{n+1}}{\Gamma(n+2)} (-u^2)^{\lfloor \frac{n}{2} \rfloor} \quad (\text{G.3})$$

In the above, the \pm signs correspond to the expressions for the bottom and top interfaces of the strip, respectively. To simplify the notation, let us define the following trigonometric functions as

$$h_s = \sin u(x+v) \quad (\text{G.4})$$

$$h_c = \cos u(x+v) \quad (\text{G.5})$$

and note that an infinite sum of trigonometric derivatives can be decomposed as follows

$$\sum_{n=0}^{\infty} \frac{\partial^n}{\partial x^n} \begin{pmatrix} h_s \\ h_c \end{pmatrix} = \sum_{n=0,2,4}^{\infty} (-1)^{\frac{n}{2}} u^n \begin{pmatrix} h_s \\ h_c \end{pmatrix} + \sum_{n=1,3,5}^{\infty} (-1)^{\frac{n}{2}} u^n \begin{pmatrix} h_c \\ -h_s \end{pmatrix}. \quad (\text{G.6})$$

G.1 Evaluation of the (A) term

For the (A) term, we consider (G.1)

$$\begin{aligned} & \sum_{n=0}^{\infty} (\pm 1)^{n+2} \frac{\left(\frac{h}{2}\right)^{n+1}}{\Gamma(n+2)} \frac{\partial^n}{\partial x^n} \begin{pmatrix} \sin u(x+v) \\ \cos u(x+v) \end{pmatrix} \Big|_{x=x_0} \\ &= \sum_{n=0,2,4}^{\infty} (\pm 1)^{n+2} \frac{\left(\frac{h}{2}\right)^{n+1}}{\Gamma(n+2)} (u)^n (-1)^{\lfloor \frac{n}{2} \rfloor} \begin{pmatrix} h_s \\ h_c \end{pmatrix} \Big|_{x=x_0} \\ &+ \sum_{n=1,3,5}^{\infty} (\pm 1)^{n+2} \frac{\left(\frac{h}{2}\right)^{n+1}}{\Gamma(n+2)} (u)^n (-1)^{\lfloor \frac{n}{2} \rfloor} \begin{pmatrix} h_c \\ -h_s \end{pmatrix} \Big|_{x=x_0} \\ &= \begin{pmatrix} h_s \\ h_c \end{pmatrix} \Big|_{x=x_0} \frac{1}{u} \sum_{n=0,2,4}^{\infty} \frac{\left(u\frac{h}{2}\right)^{n+1}}{\Gamma(n+2)} (-1)^{\lfloor \frac{n}{2} \rfloor} \pm \begin{pmatrix} h_c \\ -h_s \end{pmatrix} \Big|_{x=x_0} \frac{1}{u} \sum_{n=1,3,5}^{\infty} \frac{\left(u\frac{h}{2}\right)^{n+1}}{\Gamma(n+2)} (-1)^{\lfloor \frac{n}{2} \rfloor} \\ &= \begin{pmatrix} h_s \\ h_c \end{pmatrix} \Big|_{x=x_0} \frac{1}{u} \sum_{l=0}^{\infty} (-1)^l \frac{\left(u\frac{h}{2}\right)^{2l+1}}{\Gamma(2l+2)} \pm \begin{pmatrix} h_c \\ -h_s \end{pmatrix} \Big|_{x=x_0} \frac{1}{u} \sum_{m=1}^{\infty} (-1)^{m-1} \frac{\left(u\frac{h}{2}\right)^{2m}}{\Gamma(2m+1)} \end{aligned}$$

where

$$\begin{cases} 2l = n \\ 2m = n + 1 \end{cases}. \quad (\text{G.7})$$

Recognizing that

$$\begin{aligned} \sin x &= \sum_{k=0}^{\infty} (-1)^k \frac{x^{2k+1}}{\Gamma(2k+2)} \\ \cos x &= \sum_{k=0}^{\infty} (-1)^k \frac{x^{2k}}{\Gamma(2k+1)}, \end{aligned} \quad (\text{G.8})$$

we can write

$$\begin{aligned} & \sum_{n=0}^{\infty} (\pm 1)^{n+2} \frac{\left(\frac{h}{2}\right)^{n+1}}{\Gamma(n+2)} \frac{\partial^n}{\partial x^n} \begin{pmatrix} \sin u(x+v) \\ \cos u(x+v) \end{pmatrix} \Big|_{x=x_0} = \\ & \frac{\sin u\frac{h}{2}}{u} \begin{pmatrix} \sin u(x+v) \\ \cos u(x+v) \end{pmatrix} \Big|_{x=x_0} \mp \frac{(\cos u\frac{h}{2} - 1)}{u} \begin{pmatrix} \cos u(x+v) \\ -\sin u(x+v) \end{pmatrix} \Big|_{x=x_0} \end{aligned} \quad (\text{G.9})$$

G.2 Evaluation of the (B) term

Using (G.6) in (G.2) yields

$$\begin{aligned}
& \sum_{n=2}^{\infty} (\pm 1)^{n+2} \frac{\left(\frac{h}{2}\right)^{n+1}}{\Gamma(n+2)} \sum_{\nu=1}^{\lfloor \frac{n}{2} \rfloor} (-w^2)^{\nu-1} \frac{\partial^{n-2\nu}}{\partial x^{n-2\nu}} \left(\begin{array}{c} \sin u(x+v) \\ \cos u(x+v) \end{array} \right) \Big|_{x=x_0} \\
&= \sum_{n=2,4,6}^{\infty} (\pm 1)^{n+2} \frac{\left(\frac{h}{2}\right)^{n+1}}{\Gamma(n+2)} \sum_{\nu=1}^{\lfloor \frac{n}{2} \rfloor} (-w^2)^{\nu-1} (-1)^{\lfloor \frac{n-2\nu}{2} \rfloor} (u)^{n-2\nu} \left(\begin{array}{c} h_s \\ h_c \end{array} \right) \Big|_{x=x_0} \\
&+ \sum_{n=3,5,7}^{\infty} (\pm 1)^{n+2} \frac{\left(\frac{h}{2}\right)^{n+1}}{\Gamma(n+2)} \sum_{\nu=1}^{\lfloor \frac{n}{2} \rfloor} (-w^2)^{\nu-1} (-1)^{\lfloor \frac{n-2\nu}{2} \rfloor} (u)^{n-2\nu} \left(\begin{array}{c} h_c \\ -h_s \end{array} \right) \Big|_{x=x_0} \quad (G.10)
\end{aligned}$$

After some manipulation, the above may be rewritten as

$$\begin{aligned}
& \left(\begin{array}{c} h_s \\ h_c \end{array} \right) \Big|_{x=x_0} \sum_{n=2,4,6}^{\infty} (-1)^{\frac{n}{2}-1} \frac{\left(\frac{h}{2}\right)^{n+1}}{\Gamma(n+2)} \left(\frac{u}{w^2}\right)^n \sum_{\nu=1}^{\lfloor \frac{n}{2} \rfloor} \left(\frac{w}{u}\right)^{2\nu} \\
& \pm \left(\begin{array}{c} h_c \\ -h_s \end{array} \right) \Big|_{x=x_0} \sum_{n=3,5,7}^{\infty} (-1)^{\lfloor \frac{n}{2} \rfloor - 1} \frac{\left(\frac{h}{2}\right)^{n+1}}{\Gamma(n+2)} \left(\frac{u}{w^2}\right)^n \sum_{\nu=1}^{\lfloor \frac{n}{2} \rfloor} \left(\frac{w}{u}\right)^{2\nu}. \quad (G.11)
\end{aligned}$$

Using the following geometric progression formula [111]

$$\sum_{k=1}^n aq^{k-1} = \frac{a(q^n - 1)}{q - 1}, \quad q \neq 1 \quad (G.12)$$

we obtain

$$\begin{aligned}
& \left(\begin{array}{c} h_s \\ h_c \end{array} \right) \Big|_{x=x_0} \sum_{n=2,4,6}^{\infty} (-1)^{\frac{n}{2}-1} \frac{\left(\frac{h}{2}\right)^{n+1}}{\Gamma(n+2)} u^{n-2} \left[\frac{\left(\frac{w}{u}\right)^{2\lfloor \frac{n}{2} \rfloor} - 1}{\left(\frac{w}{u}\right)^2 - 1} \right] \\
& \pm \left(\begin{array}{c} h_c \\ -h_s \end{array} \right) \Big|_{x=x_0} \sum_{n=3,5,7}^{\infty} (-1)^{\lfloor \frac{n}{2} \rfloor - 1} \frac{\left(\frac{h}{2}\right)^{n+1}}{\Gamma(n+2)} u^{n-2} \left[\frac{\left(\frac{w}{u}\right)^{2\lfloor \frac{n}{2} \rfloor} - 1}{\left(\frac{w}{u}\right)^2 - 1} \right]. \quad (G.13)
\end{aligned}$$

Substitution from (G.7) into (G.13) yields

$$\begin{aligned}
& \frac{1}{w^2 - u^2} \left\{ - \left(\begin{array}{c} h_s \\ h_c \end{array} \right) \Big|_{x=x_0} \sum_{l=1}^{\infty} (-1)^l \frac{\left(\frac{h}{2}\right)^{2l+1}}{\Gamma(2l+2)} u^{2l} \left[\left(\frac{w}{u}\right)^{2l} - 1 \right] \right. \\
& \left. \pm \left(\begin{array}{c} h_c \\ -h_s \end{array} \right) \Big|_{x=x_0} \sum_{m=2}^{\infty} (-1)^{m-2} \frac{\left(\frac{h}{2}\right)^{2m}}{\Gamma(2m+1)} u^{2m-1} \left[\left(\frac{w}{u}\right)^{2(m-1)} - 1 \right] \right\}. \quad (G.14)
\end{aligned}$$

After some manipulation we may write

$$\begin{aligned}
& \sum_{n=2}^{\infty} (\pm 1)^{n+2} \frac{\left(\frac{h}{2}\right)^{n+1}}{\Gamma(n+2)} \sum_{\nu=1}^{\lfloor \frac{n}{2} \rfloor} (-w^2)^{\nu-1} \frac{\partial^{n-2\nu}}{\partial x^{n-2\nu}} \begin{pmatrix} h_s \\ h_c \end{pmatrix} \Big|_{x=x_0} = \\
& \frac{1}{w^2 - u^2} \left\{ - \begin{pmatrix} h_s \\ h_c \end{pmatrix} \Big|_{x=x_0} \left[\frac{\sin w \frac{h}{2}}{w} - \frac{\sin u \frac{h}{2}}{u} \right] \right. \\
& \left. \pm \begin{pmatrix} h_c \\ -h_s \end{pmatrix} \Big|_{x=x_0} u \left[\frac{\cos w \frac{h}{2} - 1}{w^2} - \frac{\cos u \frac{h}{2} - 1}{u^2} \right] \right\}. \tag{G.15}
\end{aligned}$$

G.3 Evaluation of the (C) term

For the (C) term, the summations used are of the form shown below

$$\begin{aligned}
\sum_{n=1,3,5}^{\infty} (\pm 1)^{n+2} \frac{\left(\frac{h}{2}\right)^{n+1}}{\Gamma(n+2)} (-u^2)^{\lfloor \frac{n}{2} \rfloor} &= \sum_{m=1}^{\infty} (\pm 1)^{2m+1} \frac{\left(\frac{h}{2}\right)^{2m}}{\Gamma(2m+1)} (-u^2)^{m-1} \\
&= \sum_{m=1}^{\infty} \mp (-1)^m \frac{\left(\frac{h}{2}\right)^{2m}}{\Gamma(2m+1)} (u^2)^{m-1} \\
&= \frac{1}{u^2} \sum_{m=1}^{\infty} \mp (-1)^m \frac{\left(\frac{h}{2}\right)^{2m}}{\Gamma(2m+1)},
\end{aligned}$$

leading to

$$\sum_{n=1,3,5}^{\infty} (\pm 1)^{n+2} \frac{\left(\frac{h}{2}\right)^{n+1}}{\Gamma(n+2)} (-u^2)^{\lfloor \frac{n}{2} \rfloor} = \mp \frac{1}{u^2} (\cos u \frac{h}{2} - 1). \tag{G.16}$$

BIBLIOGRAPHY

BIBLIOGRAPHY

- [1] A.G. Engel Jr., P.B. Katehi, "Low-loss Monolithic Transmission Lines for Sub-Mm and Terahertz Frequency Applications," *IEEE Trans. Microwave Theory Tech.*, vol. MTT-39, No. 11, pp 1847-1854, 1991.
- [2] H. A. Wheeler, "Transmission Line Properties of Parallel Strips Separated by a Dielectric Sheet," *IEEE Trans. Microwave Theory Tech.*, vol. MTT-13, No. 3, pp 172-185, March 1965.
- [3] H.E. Stinehelfer, "An Accurate Calculation of Uniform Microstrip Transmission Lines," *IEEE Trans. Microwave Theory Tech.*, vol. MTT-16, No. 7, pp 439-444, July 1968.
- [4] P. Sylvester, "TEM Properties of Microstrip Transmission Lines," *Proc. Inst. Elec. Eng. (London)*, vol. 115, pp 43-48, January 1968.
- [5] G. Kompa, R. Mehran, "Planar Waveguide Model for Calculating Microstrip Components," *Electron. Lett.*, vol. 11, 1975.
- [6] W.J. Getsinger, "Microstrip Dispersion," *IEEE Trans. Microwave Theory Tech.*, vol. MTT-21, No. 1, pp 34-39, Jan. 1973.
- [7] J.S. Hornsby, A. Gopinath, "Numerical Analysis of a Dielectrically Loaded Waveguide with a Microstrip Line - Finite Difference Methods," *IEEE Trans. Microwave Theory Tech.*, vol. MTT-17, No. 9, pp 684-690, Sept. 1969.
- [8] W.P. Harokopus, P.B. Katehi, "Characterization of Microstrip Discontinuities on Multilayer Dielectric Substrates Including Radiation Losses," *IEEE Trans. Microwave Theory Tech.*, vol. MTT-37, No. 12, pp. 2058-2066, December 1989.
- [9] T. Itoh, R. Mittra, "Spectral-Domain Calculation of Microstrip Characteristic Impedance," *IEEE Trans. Microwave Theory Tech.*, vol. MTT-21, No. 7, pp. 496-498, July 1973.
- [10] C.T. Tai, Dyadic Green's Functions in Electromagnetic Theory, International Textbook Company, Scranton, Pennsylvania, 1971.
- [11] N.L. VandenBerg, "Full-Wave Analysis of Microstrip Slot Antennas and Couplers," *Ph.D. Dissertation*, The University of Michigan, 1991.

- [12] T.G. Livernois, P.B. Katehi, "A Generalized Method for Deriving the Space-Domain Green's Function in a Shielded, Multilayer Substrate Structure with Applications to MIS Slow-Wave Transmission Lines," *IEEE Trans. Microwave Theory Tech.*, vol. MTT-21, No. 1, pp 34-39, Jan. 1973.
- [13] M.E. Coluzzi, P.B. Katehi, "Theoretical Characterization of Air-Bridges," Radiation Laboratory Report No. 024562-1-T, The University of Michigan, Ann Arbor, MI, June 1988.
- [14] J.R. Mosig, Numerical Techniques for Microwave and Millimeter-Wave Passive Structures, John Wiley & Sons, 1989.
- [15] J.A. Stratton, Electromagnetic Theory, McGraw-Hill Book Company, London, 1941.
- [16] A. Sommerfeld, Partial Differential Equations in Physics, Academic Press, 1964.
- [17] N.K. Das, D.M. Pozar, "A Generalized Spectral-Domain Green's Function for Multilayer Dielectric Substrates with Application to Multilayer Transmission Lines," *IEEE Trans. Microwave Theory Tech.*, vol. MTT-35, No. 3, pp 326-335, March 1987.
- [18] R.E. Collin, Foundations for Microwave Engineering, McGraw-Hill Book Co., 1966.
- [19] L. Beyne, D. de Zutter, "Green's Function for Layered Lossy Media with Special Application to Microstrip Antennas," *IEEE Trans. Microwave Theory Tech.*, vol. MTT-36, No. 5, pp 875-881, May 1988.
- [20] R.F. Harrington Time-Harmonic Electromagnetic Fields, McGraw-Hill Book Co., Inc. 1961.
- [21] Balanis, Field Computation by Moment Methods, Robert E. Krieger Publishing Co., Inc. 1987.
- [22] R.F. Harrington, Field Computation by Moment Methods, Robert E. Krieger Publishing Co., Inc. 1987.
- [23] T.Itoh, Numerical Techniques for Microwave and Millimeter-Wave Passive Structures, John Wiley & Sons, 1989.
- [24] H. A. Wheeler, "Formulas for the Skin Effect," *Proc. IRE*, vol. 30, pp 412-424, Sept. 1942.
- [25] R. A. Pucel, D. J. Masse, C. P. Hartwig, "Losses in Microstrip," *IEEE Trans. Microwave Theory Tech.*, vol. MTT-16, No. 6, pp 342-350, June 1968.

- [26] M.V. Schneider, "Microstrip Lines for Microwave Integrated Circuits," *The Bell System Technical Journal*, pp 1421-1444, May-June 1969.
- [27] H. A. Wheeler, "Transmission-Line Properties of a Strip on a Dielectric Sheet on a Plane," *IEEE Trans. Microwave Theory Tech.*, vol. MTT-25, No. 8, pp 631-647, August 1977.
- [28] B.E. Spielman, "Dissipation Loss Effects in Isolated and Coupled Transmission Lines," *IEEE Trans. Microwave Theory Tech.*, vol. MTT-25, No. 8, pp 648-655, August 1977.
- [29] Z. Pantic-Tanner, R. Mittra, "Finite-Element Matrices for Loss Calculation in Quasi-TEM Analysis of Microwave Transmission Lines," *Microwave and Optical Technology Letters*, vol. 1, No. 4, pp 142-146, June 1988.
- [30] D. Mirshekar-Syahkal, J. B. Davies, "Accurate Solution of Microstrip and Coplanar Structures for Dispersion and for Dielectric and Conductor Losses," *IEEE Trans. Microwave Theory Tech.*, vol. MTT-27, No. 7, pp 694-699, July 1979.
- [31] C.M. Crowne, "Microstrip Conductor Losses Calculated by Full Wave and Perturbational Approaches," *Electronics Letters*, vol. 24, No. 9, pp 552-553, April 1988.
- [32] R.H. Jansen, "High Speed Computation of Single and Coupled Microstrip Parameters Including Dispersion, High-Order Modes, Loss and Finite Strip Thickness," *IEEE Trans. Microwave Theory Tech.*, vol. MTT-26, No. 2, pp 75-82, February 1978.
- [33] P. Waldow, I. Wolff, "The Skin-Effect at High Frequencies," *IEEE Trans. Microwave Theory Tech.*, vol. MTT-33, No. 10, pp 1076-1082, October 1985.
- [34] G.I. Costache, "Finite Element Method Applied to Skin-Effect Problems in Strip Transmission Lines," *IEEE Trans. Microwave Theory Tech.*, vol. MTT-35, No. 11, pp 1009-1013, November 1987.
- [35] T.E. van Deventer, P.B. Katehi, A.C. Cangellaris, "High Frequency Conductor and Dielectric Losses in Shielded Microstrip," *IEEE MTT-International Symposium Digest*, pp 919-922, June 1989.
- [36] T.E. van Deventer, P.B. Katehi, A.C. Cangellaris, "An Integral Equation Method for the Evaluation of Conductor and Dielectric Losses in High Frequency Interconnects," *IEEE Trans. Microwave Theory Tech.*, vol. MTT-37, No. 12, pp 1964-1972, December 1989.
- [37] R. Faraji-Dana, Y.L. Chow, "The Current Distribution and AC Resistance of a Microstrip Structure," *IEEE Trans. Microwave Theory Tech.*, vol. MTT-38, No. 9, pp 1268-1277, September 1990.

- [38] H.Y. Lee, T. Itoh, "Phenomenological Loss Equivalence Method for Planar Quasi-TEM Transmission Lines with a Thin Normal Conductor or Superconductor," *IEEE Trans. Microwave Theory Tech.*, vol. MTT-37, No. 12, December 1989.
- [39] W. Heinrich, "Full-Wave Analysis of Conductor Losses on MMIC transmission lines," *IEEE Trans. Microwave Theory Tech.*, vol. MTT-38, No. 10, pp 1468-1472, October 1990.
- [40] D. Hollmann, S. Haffa, W. Wiesbeck, "Full-Wave Analysis for S-Parameter Calculation of Arbitrary Three-Dimensional Lossy Structures," *1990 European Microwave Conference Digest*, pp 1065-1070.
- [41] F.J. Schmuckle, R. Pregla, "The Method of Lines for the Analysis of Lossy Planar Waveguides," *IEEE Trans. Microwave Theory Tech.*, vol. MTT-38, No. 10, pp 1473-1479, October 1990.
- [42] A.C. Cangellaris, "The Importance of Skin-Effect in Microstrip Lines at High Frequencies," *IEEE MTT-International Symposium Digest*, pp 197-198, May 1988.
- [43] A.C. Cangellaris, J.L. Prince, O.A. Palusinski, "Modeling of High-Speed Interconnects; An Integral Equation Approach to Inductance Computation," *Proceedings of the 1988 Summer Computer Simulation Conference*, pp. 33-36, July 1988.
- [44] G.L. Matthaei, K. Kiziloglu, N. Dagli, S.I. Long, "The Nature of the Charges, Currents and Fields in and about Conductors Having Cross-Sectional Dimensions of the Order of a Skin Depth" *IEEE Trans. Microwave Theory Tech.*, vol. MTT-38, No. 8, pp 1031-1036, August 1990.
- [45] L.P. Vakanas, A.C. Cangellaris, J.L. Prince, "Frequency-Dependent [L] and [R] Matrices for Lossy Microstrip Lines", University of Arizona, 1991.
- [46] E.T. Whittaker, G.N. Watson, A Course of Modern Analysis, Cambridge University Press, 1927, pp. 65-66.
- [47] J. C. Maxwell, A Treatise on Electricity and Magnetism, 3rd. ed., vol.1, New York: Dover, 1954, pp 296-297.
- [48] E.J. Denlinger, "A Frequency Dependent Solution for Microstrip Transmission Lines," *IEEE Trans. Microwave Theory Tech.*, vol. MTT-19, No. 1, pp 30-39, January 1971.
- [49] E.F. Kuester, D.C. Chang, "Closed-Form Expressions for the Current or Charge Distribution on Parallel Strips or Microstrip," *IEEE Trans. Microwave Theory Tech.*, vol. MTT-28, NO. 3, pp 254-259, March 1980.

- [50] M. Kobayashi, "Longitudinal and Transverse Current Distributions on Microstriplines and Their Closed-Form Expression," *IEEE Trans. Microwave Theory Tech.*, vol. MTT-33, No. 9, pp 784-788, September 1985.
- [51] T.K. Sarkar, "A Note on the Choice Weighting Functions in the Method of Moments," *IEEE Trans. Antennas Propagat.*, vol. AP-33, No. 3, pp 436-441, April 1985.
- [52] Dahlquist G., A. Björck, Numerical Methods, Prentice-Hall, Inc., Englewood Cliffs, New Jersey, 1961.
- [53] R.H Jansen, "Unified User-oriented Computation of Shielded, Covered and Open Planar Microwave and Millimeter-wave Transmission-line Characteristics," *IEE Journal of Microwaves, Opt. and Acoust.*, vol. 3, pp 14-22, January 1979.
- [54] W.J. Getsinger, "Measurement and Modelling of the Apparent Characteristic Impedance of Microstrip," *IEEE Trans. Microwave Theory Tech.*, vol. MTT-31, No. 8, pp 624-632, August 1983.
- [55] L. Wiemer, R.H Jansen, "Reciprocity Related Definition of Strip Characteristic Impedance for Multiconductor Hybrid-Mode Transmission Lines," *Microwave and Optical Tech. Letters*, vol. 1, No. 1, pp 22-25, March 1988.
- [56] L. Carin, K.J. Webb, "An Equivalent Circuit Model for Terminated Hybrid-Mode Multiconductor Transmission Lines," *IEEE Trans. Microwave Theory Tech.*, vol. MTT-37, No. 11, pp 1784-1793, November 1989.
- [57] D. J. Sooke, "Bessel Functions I and J of Complex Argument and Integer order," *Journal of Research B of the National Bureau of Standards* , vol 77b, 1973, pp 111-114.
- [58] Abramowitz, I.A. Segun, Handbook of Mathematical Functions, Dover Publications, Inc., New York, 1968.
- [59] E. Yamashita, R. Mittra, "Variational Method for the Analysis of Microstrip Lines," *IEEE Trans. Microwave Theory Tech.*, vol. MTT-16, p 251, April 1968.
- [60] R.H. Jansen, R.G. Arnold, I.G. Eddison, "A Comprehensive CAD Approach to the Design of MMIC's up to MM-Wave Frequencies," *IEEE Trans. Microwave Theory Tech.*, vol. MTT-36, pp 208-219, February 1988.
- [61] L. Su, T. Itoh, J. Rivera, "Design of an Overlay Directional Coupler by a Full-Wave Analysis," *IEEE Trans. Microwave Theory Tech.*, vol. MTT-31, pp 1017-1022, December 1983.
- [62] R.E. Diaz, "The Discrete Variational Conformal Technique for the Calculation of Strip Transmission-Line Parameters," *IEEE Trans. Microwave Theory Tech.*, vol. MTT-34, No. 6, pp 714-722, June 1986.

- [63] L. Carin, K.J. Webb, "An Equivalent Circuit Model for Terminated Hybrid-Mode Multiconductor Transmission Lines," *IEEE Trans. Microwave Theory Tech.*, vol. MTT-37, No. 11, pp 1784-1793, November 1989.
- [64] M.V. Schneider, "Dielectric Loss in Integrated Microwave Circuits," *Bell Syst. Tech. Journal*, vol. 48, pp 2325-2332, September 1969.
- [65] T.L. Simpson, B. Tseng, "Dielectric Loss in Microstrip Lines," *IEEE Trans. Microwave Theory Tech.*, vol. MTT-24, No. 2, pp 106-108, Feb. 1976.
- [66] D. Mirshekar-Syahkal, "An Accurate Determination of Dielectric Loss Effect in Monolithic Microwave Integrated Circuits Including Microstrip and Coupled Microstrip Lines," *IEEE Trans. Microwave Theory Tech.*, vol. MTT-31, No. 11, pp 950-954, November 1983.
- [67] Andreas Cangellaris, Private communication.
- [68] R. Horton, "Loss Calculations of Coupled Microstrip Lines," *IEEE Trans. Microwave Theory Tech.*, No. 5, pp 359-360, May 1973.
- [69] B.R. Rao, "Effect of Loss and Frequency Dispersion on the Performance of Microstrip Directional Couplers and Coupled Line Filters," *IEEE Trans. Microwave Theory Tech.*, No. 7, pp 747-750, July 1974.
- [70] E.M.T. Jones, J.T. Bolljahn "Coupled-Strip-Transmission-Line Filters and Directional Couplers," *IRE Trans. Microwave Theory Tech.*, vol. MTT-4, No. 2, pp 75-81, April 1956.
- [71] J.M. Pond, C.M. Krowne, W.L. Carter, "On the Application of Complex Resistive Boundary Conditions to Model Transmission Lines Consisting of Very Thin Superconductors," *IEEE Trans. Microwave Theory Tech.*, vol. MTT-37, No. 1, pp 181-190, January 1989.
- [72] A.C. Cangellaris, "Propagation Characteristics of Superconductive Interconnects," *Microwave and Optical Tech. Letters*, vol. 1, No. 5, pp 153-156, July 1988.
- [73] O.K. Kwon, B.W. Langley, R.F.W. Pease, M.R. Beasley, "Superconductors as Very High-Speed System-level Interconnects," *IEEE Electron Device Letters*, vol. EDL-8, No. 12, pp 582-585, December 1987.
- [74] H.Y. Lee, T. Itoh, "Phenomenological Loss Equivalence Method for Planar Quasi-TEM Transmission Lines with a Thin Normal Conductor or Superconductor," *IEEE Trans. Microwave Theory Tech.*, vol. MTT-37, No. 12, pp 1904-1909, December 1989.
- [75] M.C. Nuss, P.M. Mankiewich, R.E. Howard, B.L. Straughn, T.E. Harvey, C.D. Brandle, G.W. Berkstresser, K.W. Goossen, P.R. Smith, "Propagation of Terahertz Bandwidth Electrical Pulses on $YBa_2Cu_3O_{7-\delta}$ Transmission Lines on Lanthanum Aluminate," *Applied Physics Letters*, vol. 54, pp 2265-2267, 1989.

- [76] F.A. Miranda, W.L. Gordon, K.B. Bhasin, B.T. Ebihara, V.O. Heinen, C.M. Chorey, "Complex Permittivity of Lanthanum Aluminate in the 20 to 300K Temperature Range from 26.5 to 40 GHz," *Microwave and Optical Technology Letters*, vol. 3, No. 1, pp 11-13, January 1990.
- [77] D.W. Cooke, E.R. Gray, R.J. Houlton, B. Rusnak, E.A. Meyer, J.G. Beery, D.R. Brown, F.H. Garzon, I.D. Raistrick, A.D. Rollet, R. Bolmaro, submitted to *Appl. Phys. Lett.*
- [78] D.E. Oates, A.C. Anderson, "Stripline Measurements of Surface Resistance Relation to HTSC film Properties and Deposition Methods," *presented at SPIE*, Santa Clara, CA, October 1989.
- [79] L. Drabeck, G. Gruner, J.J. Chang, A. Inam, X.D. Wu, L. Nazar, T. Venkatesan, D.J. Scalapino, " Millimeter-Wave Surface Impedance of $YBa_2Cu_3O_7$," *Physical Review B*, vol. 40, No. 10, p 7350, October 1989
- [80] H. Chaloupka, G. Muller, U. Klein, H. Piel, "New Experimental Results for Microwave Conductivity of High- T_c Superconductors and Consequences for Applications to Linear Devices," *IEEE MTT-International Symposium Digest*, pp 547-550, June 1989.
- [81] A.T. Fiory, A.F. Hebard, P.M. Mankiewich, R.E. Howard, "Penetration Depths of High T_c Films measured by Two-Coil Mutual Inductances," *Applied Physics Letters*, vol. 52, No. 25, pp 2165-2167, 20 June 1988.
- [82] L.A. Hornak, M. Hatamian, S.K. Tewksbury, E.G Burkhardt, "Experiments with a 31-cm High- T_c Superconducting Thin Film Transmission Line," *IEEE MTT-International Symposium Digest*, pp 623-626, June 1989.
- [83] N. Klein, G. Muller, H. Piel, B. Roas, L. Schultz, U. Klein, M. Peiniger, "Millimeter Wave Surface Resistance of Epitaxially Grown $YBa_2Cu_3O_{7-x}$ Thin Films," *Applied Physics Letters*, vol. 54, No. 8, pp 757-759, 20 February 1989.
- [84] R.W. Simon, C.E. Platt, A.E. Lee, G.S. Lee, K.P. Daly, M.S. Wire, J.A. Luine, "Low-loss Substrate for Epitaxial Growth of High-Temperature Superconductor Thin Films," *Applied Physics Letters*, vol. 53, No. 26, pp 2677-2679, 26 December 1988.
- [85] A.G. Engel Jr., T.E. van Deventer, P.B. Katehi, "Low-loss Guiding Structures for THz Frequency Applications," *Proc. 2nd Int. Symp. Space Terahertz Technology*, pp 545-557, Pasadena, CA, Feb. 1991.
- [86] E.A.J. Marcatili, "Slab-Coupled Waveguides," *Bell Syst. Tech. Journal*, vol. 53, pp 645-674, 1974.
- [87] G.B. Hocker, W.K. Burns, "Mode Dispersion in Diffused Channel Waveguides by the Effective Index Method," *Applied Optics*, vol. 16, pp 113-118, 1977.

- [88] C.M. Kim, B.G. Jung, C.W. Lee, "Analysis of Dielectric Rectangular Waveguide by Modified Effective-Index Method," *Electronics Letters*, vol. 22, pp 296-298, 1986.
- [89] P.K. Mishra, A. Sharma, S. Labroo, A.K. Ghatak, "Scalar Variational Analysis of Single-Mode Waveguides with Rectangular Cross-Section," *IEEE Trans. Microwave Theory Tech.*, vol. MTT-33, pp 282-286, 1985.
- [90] B.M.A. Davies, J.B. Davies, "Finite-Element Solution of Integrated Optical Waveguides," *IEEE Journal of Lightwave Technology*, LT-2, pp 682-688, 1984.
- [91] T.G. Livernois, D.P. Nyquist, "Integral-Equation Formulation for Scattering by Dielectric Discontinuities Along Open-Boundary Dielectric Waveguides," *Journal of Optical Society of America*, A-4, pp 1289-1295, July 1987.
- [92] B.J. Rubin, "Full-Wave Analysis of Waveguides involving Finite-Size Dielectric Regions," *IEEE MTT-International Symposium Digest*, Dallas, pp 705-708, May 1990.
- [93] J. Kane, S.N. Karp, "Generalized Impedance Boundary Conditions with Applications to Surface Wave Structures," *Electromagnetic Wave Theory*, Part 1, ed. J. Brown, pp 479-483, Pergamon: New York, 1965.
- [94] T.B.A. Senior, J.L. Volakis, "Generalized Impedance Boundary Conditions in Scattering," *Proceedings of the IEEE*, vol. 79, No. 10, pp 1413-1420, October 1991.
- [95] T.B.A. Senior, , "Impedance Boundary Conditions for Imperfectly Conducting Surfaces," *Appl. Sci. Res.*, vol. 8(B), pp 418-436, 1960.
- [96] J.H. Richmond, "Scattering by a Dielectric Cylinder of Arbitrary Cross-Section Shape," *IEEE Trans. Antennas Propagat.*, vol. AP-13, No. 3, pp 334-341, March 1965.
- [97] T.K. Sarkar, E. Arvas, S. Ponnappalli, "Electromagnetic Scattering from Dielectric Bodies," *IEEE Trans. Antennas Propagat.*, vol. AP-37, No. 5, pp 673-676, May 1989.
- [98] T.E. van Deventer, P.B. Katehi, "Computer Program for Mode Search in Partially-filled Waveguide," Radiation Laboratory Report No. 024562-3-T, The University of Michigan, Ann Arbor, MI, March 1990.
- [99] J.L. Volakis, "Numerical Implementation of Generalized Impedance Boundary Conditions," *IEEE Trans. Microwave Theory Tech.*, vol. MTT-24, No. 11, pp 821-827, November 1976.
- [100] T. Itoh, "Inverted Strip Dielectric Waveguide for Millimeter-Wave Integrated Circuits," *IEEE Trans. Microwave Theory Tech.*, vol. MTT-24, No. 11, pp 821-827, November 1976.

- [101] T. Trinh, R. Mittra, "Coupling Characteristics of Planar Dielectric Waveguides of Rectangular Cross Section," *IEEE Trans. Microwave Theory Tech.*, vol. MTT-29, No. 9, pp 875-880, September 1981.
- [102] U. Crombach, "Analysis of Single and Coupled Rectangular Dielectric Waveguides," *IEEE Trans. Microwave Theory Tech.*, vol. MTT-29, No. 9, pp 870-874, September 1981.
- [103] K. Hayata, M. Koshiha, M. Eguchi, M. Suzuki "Vectorial Finite-Element Method without any Spurious Solutions for Dielectric Waveguiding Problems using Transverse Magnetic-field Component," *IEEE Trans. Microwave Theory Tech.*, vol. MTT-34, No. 10, pp 1120-1124, November 1986.
- [104] J.S. Bagby, D.P. Nyquist, and B.C. Drachman, "Integral Formulation for Analysis of Integrated Dielectric Waveguides," *IEEE Trans. Microwave Theory Tech.*, vol. MTT-33, No. 10, pp 906-915, October 1985.
- [105] J.F. Kiang, S.M. Ali, J.A. Kong, "Integral Equation Solution to the Guidance and Leakage Properties of Coupled Dielectric Strip Waveguides," *IEEE Trans. Microwave Theory Tech.*, vol. MTT-38, No. 2, pp 193-203, February 1990.
- [106] T.E. van Deventer, P.B. Katehi, "A Planar Integral Equation for the analysis of Dielectric Ridge Structures Using Generalized Boundary Conditions," *IEEE MTT-International Symposium Digest*, pp 647-650, June 1991, Boston, MA.
- [107] D. Marcuse, Theory of Dielectric Optical Waveguides, 2nd edition, Academic Press, Inc., 1991.
- [108] T.E. van Deventer, P.B. Katehi, "A Study of Sub-Millimeter Wave Coupled Dielectric Waveguides Using the GIE Method," *IEEE MTT-International Symposium Digest*, pp 1115-1118, June 1992, Albuquerque, NM.
- [109] B.M.A. Rahman, J.B. Davies, "Penalty function Improvement of Waveguide Solution by Finite Elements," *IEEE Trans. Microwave Theory Tech.*, vol. MTT-32, No. 8, pp 922-928, August 1984.
- [110] L.B. Felsen, N. Markuvitz, Radiation and Scattering of Waves, Prentice-Hall, Inc., 1973.
- [111] Gradshteyn I.S., Ryzhik, Table of Integrals, Series, and Products, 4th edition, Academic Press, 1980.
- [112] Cheng D.K., Field and Wave Electromagnetics, Addison-Wesley Publishing Company, Inc., 1983.
- [113] Kong J.A., Electromagnetic Wave Theory, chapter 3, 2nd edition, Wiley & Sons, Inc., 1990.